THE UNIVERSITY OF CHICAGO

USE, OPTIMIZATION, AND EXPANSION OF QUANTITATIVE MAGNETIC RESONANCE PERFUSION IMAGING IN CEREBROVASCULAR DISEASE

A DISSERTATION SUBMITTED TO
THE FACULTY OF THE DIVISION OF THE BIOLOGICAL SCIENCES
AND THE PRITZKER SCHOOL OF MEDICINE
IN CANDIDACY FOR THE DEGREE OF
DOCTOR OF PHILOSOPHY

COMMITTEE ON MEDICAL PHYSICS

BY

MIRABAI M. LIU

CHICAGO, ILLINOIS

AUGUST 2023

To my mom, Mini Liu, and my grandparents, An-Hwa Liu and Ann Ling Liu.

TABLE OF CONTENTS

LIST OF FIGURES

LIST OF TABLES

ACKNOWLEDGMENTS

I am thankful to my Ph.D. advisor, Dr. Timothy Carroll, for his knowledge, guidance, and time throughout my graduate school journey. In addition, Dr. Gregory Christoforidis and his pedagogy were invaluable to me as I transitioned to pre-clinical medical physics. My sincere thanks to Dr. Patrick La Riviere, Chair of my committee, for introducing me to Medical Physics and for his support throughout my Ph.D. My gratitude to my dissertation committee members Drs. Sean Foxley, Zheng Feng Lu, and Michael Hurley for their knowledge, feedback, and advice throughout the process. I would also like to thank Drs. Steven Roth, Marek Niekrasz, Donovan Gorre, Xiaodong Guo, Yonglin Pu, and Mihai Giurcanu for their work on the experiments presented in this thesis. This work was possible with financial support from the National Science Foundation Graduate Fellowship (DGE1746045) and the National Institutes of Health (R01NS093908, R01NS114632).

I am deeply grateful to Julian Bertini for his friendship in the lab working through physics equations and literature reviews at odd hours, and Chisondi Warioba for his friendship and patience in the lab. Along with Drs. Alexey Dimov, Adam Hasse, Yong Jeong, and Niloufar Saadat, they created a lab that was a joy for me to work in. My gratitude to my colleagues Drs. Inna, Brittany, Lindsay, Isabelle and Jordan for their mentorship, Gia for being a phenomenal fellow co-president and friend, and to Dr. Lili Gonzalez, our incredible graduate education administrator. I would also like to thank my GPMP cohort Natalie, Hadley, Linnea, and Mena, and other current and former members, for their friendship and camaraderie throughout graduate school during a pandemic. In addition, my gratitude to incredible mentors throughout my time in academia; Ms. Marissa Maggio, and Drs. Jamal Ali, Ritoban Basu Thakur, Zhaodi Pan, Stephen Meyer, and David Reid all helped introduce me to the intersection of biology, physics, and medicine that shape me today.

Lastly, the biggest thanks to my friends and family, raised-by and chosen. To my mom, Mini, this work could not have happened without you and your endless support and patience.

Ari, I could not have gotten this far without your encouragement and resigned disbelief that this is how I elect to spend my twenties. Mena, I am forever grateful for our friendship and our constant intellectual, emotional, and existential inquiry throughout our graduate school journey. To all I lack the space to write to fully (including Monona, Steve, Mike, Shellee, Stephen, Ron, Mark, Amy, JT, Marla, Suhasni, Michelle, Evan, Kathryn, Jake, Kevin, Priya, my cat Maxi), thank you for the love, care, and support shown to me throughout my entire PhD. I promise now I'll actually get a life outside of work and live a little... Maybe.

ABSTRACT

The broad, long-term goal of this dissertation is to improve quantitative perfusion magnetic resonance imaging (MRI) for diagnosis, prognosis, and treatment of cerebrovascular disease. Perfusion MRI can assess delivery of blood to a capillary bed in tissue, and quantify flow. The first aim of this work tests the hypothesis that standardized quantitative dynamic susceptibility contrast (DSC) MR perfusion improves prediction of therapeutic outcome of experimental flow augmentation in acute ischemic stroke. Further, results of the study support evaluating flow augmentation as a method of minimizing infarct growth during the critical "door to needle" time for thrombolysis, demonstrating its use in pre-clinical stroke research. The second aim of this work tests the hypothesis that overestimation of perfusion deficit, due to blocked arteries delaying and dispersing contrast agent as it travels through the vascular system, can be reduced by use of a local arterial input function (AIF) DSC in intracranial atherosclerosis. Preliminary data supports the hypothesis that local-AIF DSC can return more accurate perfusion in intracranial atherosclerosis by adjusting for pial collateral supply that standard DSC does not.

The third aim of this work tests the hypothesis that intravoxel incoherent motion (IVIM) MR perfusion can be quantified in ml/100g/min by derivation from fundamental diffusion principles and agree with gold standard microspheres and DSC at baseline, post-CO2 inhalation, and during acute ischemic stroke. This study returned a 5-minute 10 *b*-value IVIM sequence and post-processing algorithm that supports IVIM as a method of getting simultaneous quantitative bolus-independent perfusion, water transport time, and diffusion in cerebrovascular disease. Lastly the fourth aim tests the hypothesis that difference in IVIM exponential behavior can be used to separate tissue compartments with different water motion, specifically, cerebrospinal fluid (CSF) segmentation. Tri-exponential behavior seems a promising direction and quadratic discriminant analysis segmentation demonstrated a quantifiable divide between bi-exponential behavior of CSF-dominated voxels, and tissue-

perfusion dominated voxels. This further supports IVIM signal not being predominately CSF contamination and being a potential method of measuring quantitative perfusion, diffusion, blood volume, transit time, and cerebrospinal fluid flow of neurovascular disease without contrast agent.

CHAPTER 1

INTRODUCTION

1.1 Magnetic Resonance Imaging (MRI) Overview

Magnetic Resonance Imaging (MRI) is a noninvasive medical imaging technique that can produce detailed image of internal structure and physiology in the human body without ionizing radiation. Using strong magnetic fields and nuclear magnetic resonance the varying molecular structure of a material can be determined by the interaction of nuclear spins. MRI can be used instead of the common computed tomography (CT) for soft organs and soft tissue, as well as for pediatric patients and chronic studies in patients who should be exposed to a minimum amount of ionizing radiation (Copen et al. [2016]).

While MRI is a medical imaging modality that uses magnetic fields and gradients for non-invasive detailed image of organs and tissues in the body, focus is typically on anatomic and morphologic characteristics. As technology advances, imaging function of tissues becomes possible for both research and clinical practice. One such measurement of tissue function is perfusion, delivery of blood to a capillary bed in tissue, typically measured as volume of blood per unit time delivered per unit tissue mass. Perfusion MRI focuses on assessment of this delivery and is a promising tool in assessing cardiovascular disease, brain tumors, and neurodegenerative disease.

While perfusion is an important physiologic parameter used in detection, characterization, and monitoring of central nervous system tumors and neurovascular disease, perfusion MR has not reached wide-spread clinical use (Essig et al. [2013]). For example, cardiovascular disease is the leading cause of death globally, with ischemic stroke causing nearly 1 in 6 such deaths and being the leading cause of serious long- term disability (Tsao et al. [2022]), yet currently the most common predictor of treatment success is time to treatment via clot removal, with delayed removal more than three hours post symptoms leading to a

greater chance of disability and death. The underuse of perfusion imaging in the clinic is due to several factors including lack of standardized quantification, contrast injection, imaging time, and dissemination of knowledge. Therefore, standardization of quantification of blood flow, fast non-contrast imaging, and demonstration of added benefit in clinical trials can improve understanding and treatment of cardiovascular disease.

1.2 Current Imaging Methods

While MR diffusion-weighted imaging (DWI) remains the unequivocal reference standard used to measure infarct volume in stroke, Computed Tomography (CT) perfusion is the most common imaging modality used for acute stroke patient triage as it is quick, widely available, and less costly. However, there are several pitfalls of CT image interpretation such as lack of evidence of reliable patient stratification, and mixed results regarding accurate extent or severity of CT hypoattenuation (Potter et al. [2019]). Further, CT perfusion involves radiation exposure, injection of iodinated contrast, is more error-prone regarding small infarct detection, and is less sensitive compared to MR in acute stroke imaging (Demeestere et al. [2020]). In comparison, perfusion MR is noninvasive with no radiation exposure and non-iodinated contrast offering study of tissue function in cardiovascular disease with minimal health risks. Quantification has the added benefit of enabling multi-site cross-sectional comparison in addition to within-patient longitudinal comparison. Therefore, combined MR DWI and quantitative MR perfusion is an alternative technique to study both core infarct volume and under-perfused tissue surrounding the core infarct that represents salvageable tissue (Mair and Wardlaw [2014]). This application in patient stratification and novel treatment studies allows improvement of diagnosis, deeper study of novel treatment, and potential improved stroke triage.

Further, Dynamic Susceptibility Contrast (DSC), the most common MR perfusion sequence, involves injection of gadolinium-based contrast agent (Gd), a rare earth metal, via

IV. While Gd-contrast is typically considered safe, studies have investigated adverse reactions, retention, potential toxicity, and nephrogenic systemic fibrosis (Neeley et al. [2016], McDonald et al. [2018], Rogosnitzky and Branch [2016], Khawaja et al. [2015]). Further, as renal insufficiency and higher dosage increase potential for negative effects, the observed potential Gd retention over years is cause for concern for patients with chronic disease, under watch-and-wait observational studies, and in longitudinal volunteer studies.

The most common non-contrast perfusion MR sequence is Arterial Spin Labelling (ASL). ASL images perfusion via endogenous tracer (Ferre et al. [2013]). However, the physiologic basis of ASL poses difficulties in patients with cerebrovascular disease, as transit time of spin-labeled molecules varies greatly in obstructive neurovascular disease (Grade et al. [2015]) meaning slow flow is difficult to image (Parkes et al. [2004]). Further, ASL has a limited role in evaluation of ischemic stroke compared to DSC. While it can confirm the presence of hypoperfusion, there have been mixed results regarding sensitivity, and it may not detect small perfusion deficits (Zaharchuk et al. [2012], Golay et al. [2004]). Further, ASL may show false hypoperfusion due to reduced labeling efficiency at the labeling plane and has not been found to consistently agree with standard DWI perfusion-diffusion mismatch in acute stroke(Zaharchuk et al. [2012]).

Intravoxel incoherent motion (IVIM) is a non-contrast perfusion-diffusion MRI scan introduced by Le Bihan (Le Bihan et al. [1988]), and re-emerging the last decade, that uses multiple diffusion gradient strengths and durations (b-values) to simultaneously assess tissue water diffusion and tissue perfusion without the use of gadolinium-based contrast agent and independent of arterial input function. Diffusion-weighting is sensitive to water motion and consequently able identify where in the brain water is sequestered inside cells by cytotoxic edema. Typically, high b-values ($b \geq 800 s/mm^2$) are used for diffusion-weighting, meaning signal loss between gradients is due to water diffusion, which creates the greatest contrast between infarct and viable brain. At very low b-values ($b \leq 200 s/mm^2$), diffusion-weighting

is sensitive to faster water motion, meaning signal loss is predominately from fast moving molecules, such as capillary level blood flow. IVIM scans acquire DWI images with multiple b-values and extract CBF as well as diffusion restriction using mathematical modelling of a bi-exponential. This modelling is necessary to separate perfusion (low b-values) and diffusion components (high b-values) and allows for quantification of CBF with a calibration factor to convert relative IVIM perfusion to quantitative values (ml/100g/min), and a more accurate interstitial water diffusion image.

1.3 Proposed Research

The broad, long-term goal of this dissertation is to improve perfusion MRI for diagnosis and prognosis of neurovascular disease. In this work I will 1) demonstrate the utility of our standardized quantitative DSC perfusion to clinical standard relative perfusion in a study of experimental flow augmentation in acute ischemic stroke, 2) explore the effects of correcting delay and dispersion effects in subjects with intracranial atherosclerotic disease with a local AIF by comparison to single-photon emission computerized tomography (SPECT), 3) validate our optimized non-contrast IVIM sequence and proposed quantification through water transport time against multiple independent imaging methods across a range of physiologic and disease states, and 4) explore methods of CSF removal with machine learning to determine if IVIM can return physiologic parameters important for different disease models such as perfusion, diffusion, transit time, blood volume, and cerebrospinal fluid flow, in one non-contrast five minute scan.

1.4 Summary of Aims

For Aim 1, I demonstrate the utility of our standardized quantitative DSC perfusion to clinical standard relative perfusion in a study of experimental flow augmentation in acute

ischemic stroke. During acute ischemic stroke due to cortical cerebral artery occlusion, an infarction core is surrounded by a decreasing penumbra of viable and potentially salvageable tissue. The salvageability of the penumbral tissue varies as a function of collateral blood flow. Therefore, therapeutic intervention to increase perfusion pressure and modify autoregulation to raise CBF above regulated levels may get blood supply to critical region of ischemic tissue and slow infarct volume growth. This reduction in the rate ischemic penumbra progresses to infarction may serve as a "bridge therapy" prior to thrombolysis or thrombectomy to reduce door-to-needle time. One such therapy is a combination of norepinephrine and hydralazine administered in the acute phase of ischemic stroke. Previous study showed that this novel therapy influenced infarct volume growth dichotomized by pial collateral score measured 30 minutes post-occlusion before treatment administration, but relative cerebral blood flow (CBF) did not explain said dichotomy or infarct growth. In Chapter 3 I investigate if quantitative CBF in ml/100g/min may provide a method of action for the unexplained dichotomy of novel therapeutic outcome of acute ischemic stroke that rCBF cannot.

For Aim 2, I examine the effect of delay and dispersion correction in intracranial atherosclerotic disease compared to SPECT. As the cause of a stroke is vital to targeted therapy of the underlying stroke mechanism, development and assessment of diagnostic tests regarding their ability to differentiate between atherosclerotic plaque and other pathologies can improve treatment outcome. Standard DSC has been shown to overestimate perfusion deficit in stroke with correction of delay and dispersion effects by use of a local arterial input function reducing this overestimation. This suggests that the perfusion deficit observed with standard DSC may be due to the effects of blocked arteries in delaying and dispersing contrast agent as it travels through the vascular system. The effect of correcting for this overestimation by use of a local-AIF can be studied by comparison of standard DSC and the local-AIF DSC to an imaging modality that does not involve bolus tracking such as SPECT. In Chapter 4 I explore in a preliminary study of subjects with intracranial atherosclerotic disease if asym-

metry indicative of perfusion deficit can be will demonstrate if overcall of perfusion deficit can be reduced for improved diagnosis.

For Aim 3, to optimize IVIM as a non-contrast MR perfusion sequence, I use fundamental physics of diffusion and diffusion weighted MRI in Chapter 5 to study the two-compartment model of IVIM and determine an optimal fitting algorithm in Chapter 6. The IVIM sequence and post-processing algorithm presents a clinically feasible scan time of 5-minutes to collect images for calculation of parametric perfusion and diffusion MR images, which can be quantified by historical reference standards of capillary geometry assumptions. As these assumptions limmit use of quantification in other organs, I derive a new method of quantification that is independent of capillary geometry assumptions using a proposed water transport time based on diffusion physics in Chapter 7. I hypothesize that IVIM perfusion values can be quantified (ml/100g/min) With this new method to agree with neutron capture microspheres over a range of physiologic conditions. Using the central volume theorem, the proposed IVIM water transport time should also correlate with DSC mean transit time. Finally, using the same IVIM acquisition I hypothesize that IVIM diffusion positive infarct volumes will be accurate compared to MRI mean diffusivity infarct volumes as a reference standard. In Chapter 8 I assess the accuracy and sensitivity of a novel quantification of five-minute simultaneous IVIM perfusion and diffusion in a canine model across three physiologic states.

Lastly, for Aim 4, I explore different methods of removing Cerebrospinal Fluid (CSF) contamination from IVIM signal. CSF is fluid found within the ventricular system and surrounding the brain and spinal cord. It acts as a shock absorber, provides buoyancy, manages intracranial pressure, and allows for removal of waste through the brain's lymphatic system. CSF flow dynamics are an active area of research, as it acts both through pressure gradients throughout the brain and also through pulsatile flow from either cardiac or respiratory motion (Mehta et al. [2022]). As all water motion will contribute to diffusion weighted imaging,

fast moving free water in the glymphatic system will contaminate IVIM perfusion signal. This is a common issue with IVIM in the brain, specifically in the cortex where grey matter and subarachnoid space lead to mixed voxels. Multiple methods have been suggested to remove CSF from IVIM perfusion signal including removal through Inversion Recovery suppression which some have concluded means perfusion signal is actually just CSF contamination (Kwong et al. [1991]). Chapter 9 explores partial volume contamination, inversion recovery CSF suppression, and machine learning methods of CSF segmentation. The success of CSF removal with an IVIM machine learning algorithm is measured by comparing perfusion agreement to reference standards with CSF-classified voxels segmented. With this comparison, I examine if IVIM can return physiologic parameters important for different disease models such as perfusion, diffusion, blood volume, transit time, and cerebrospinal fluid flow, in one non-contrast scan.

CHAPTER 2

MAGNETIC RESONANCE IMAGING FUNDAMENTALS

2.1 Magnetic Resonance Physics Overview

Spin is a quantum-mechanical property akin to angular momentum of a sphere rotating about an axis in classical physics. Using this quasi-classical 'spin' as the magnetic moment of particles rotating about an axis, a strong magnetic field B_0 along the longitudinal direction will exert a torque on the magnetic moment of a proton. This causes spins to align with the magnetic field and rotate about that axis at a resonance frequency, or "Larmor frequency". This frequency is proportional to the strength of that magnetic field by the gyromagnetic ratio $\omega = \gamma B_0$. The net sum of proton spins aligning with the main magnetic field induces a magnetic moment which is composed of longitudinal and transverse components of signal. When a B_1 field is applied orthogonal to B_0 the magnetic moment is flipped into the transverse plane, precessing at the resonance frequency (RF) which induces an AC current that can be detected with an RF coil. The magnetic moment then precesses about both B_1 and B_0 fields.

After excitation by the B_1 field, the net magnetization undergoes two types of relaxation. The first is the spin-lattice relaxation, as the magnetic moment realigns with B_0 along the longitudinal axis. This regrowth is called T1-relaxation, where T1 represents the time it takes for the longitudinal of the magnetization to return to $(1 - e^{-\frac{t=T1}{T1}}) = .63$ of the maximum value. It represents quantum mechanical release of RF energy as statistically the spins return to the lower energy orientation. The second is spin-spin relaxation, or T2-relaxation, which is the loss of transverse magnetization due to phase decoherence between spins as they rotate about the longitudinal axis. It is simple exponential decay with time constant of T2, or the time required for the transverse magnetization to fall to $e^{-\frac{t=T2}{T2}} = .37$ of the initial value. This is caused both by T1 relaxation and phase decoherence between spins.

2.1.1 MR Physics Excitation

Mathematically, magnetization M is the axis of rotation about which particles spin, which produces angular momentum J parallel to M. When an external magnetic field B exerts a torque orthogonal to J, the change in the angular momentum J is represented by

$$\frac{dJ(t)}{dt} = M(t) \times B(t).$$

As $M = \gamma J$, this becomes

$$\frac{dM(t)}{dt} = \gamma\Big(M(t) \times B(t)\Big).$$

This is the equation for bulk magnetization, and solutions to this differential expression describe MR effects.

$$\frac{dM_x}{dt} = \gamma(M_y B_z - M_z B_y), \quad \frac{dM_y}{dt} = \gamma(M_z B_x - M_x B_z), \quad \frac{dM_z}{dt} = \gamma(M_x B_y - M_y B_x)$$

For free precession in the lab frame, there is one B_0 field along the z direction, so $B_z = B_0\hat{z}, B_x = B_y = 0$.

$$\frac{dM_x}{dt} = \gamma(M_y B_0), \quad \frac{dM_y}{dt} = \gamma(-M_x B_0), \quad \frac{dM_z}{dt} = 0$$

Differentiating the two remaining equations with respect to time will decouple them.

$$\frac{d^2M_x}{dt^2} = \gamma B_0(\frac{dM_y}{dt}) = -(\gamma B_0)^2 M_x$$

$$\frac{d^2M_y}{dt^2} = -\gamma B_0(\frac{dM_x}{dt}) = -(\gamma B_0)^2 M_y$$

The solution to these equations is sinusoidal,

$$M_x(t) = a\cos(\gamma B_0 t) + b\sin(\gamma B_0 t),$$

and solving for a and for b returns the well-known rotation matrix around the z-axis.

$$M_x(t) = M_x^0\cos(\gamma B_0 t) + M_y^0\sin(\gamma B_0 t)$$

$$M_y(t) = -M_x^0\sin(\gamma B_0 t) + M_y^0\cos(\gamma B_0 t)$$

$$M_z(t) = M_z^0$$

If we then apply a 90° B_1 pulse flipping the magnetic moment into the transverse plane to detect signal with the RF coil, we can calculate the signal we expect to measure without any relaxation effects. As signal is collected in the transverse plane, this is "excitation".

$$\begin{bmatrix} M_x(t) \\ M_y(t) \\ M_z(t) \end{bmatrix} = \begin{bmatrix} \cos\omega_0 t & \sin\omega_0 t & 0 \\ -\sin\omega_0 t & \cos\omega_0 t & 0 \\ 0 & 0 & 1 \end{bmatrix} \begin{bmatrix} M_0 \\ 0 \\ 0 \end{bmatrix}$$

$$M_x(t) = M_0\cos\omega_0 t \qquad M_y(t) = -M_0\sin(\omega_0 t) \qquad M_z(t) = 0 \tag{2.1}$$

Combining these equations in the transverse plane using Euler notation returns the following:

$$\begin{aligned} M_{xy} &= M_x + iM_y \\ &= M_0(\cos\omega_0 t) + i\sin(\omega_0 t) \\ &= M_0 e^{i\omega_0 t}. \end{aligned} \tag{2.2}$$

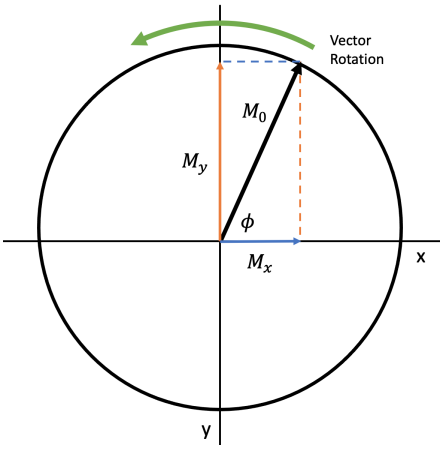

(a) Unit Circle

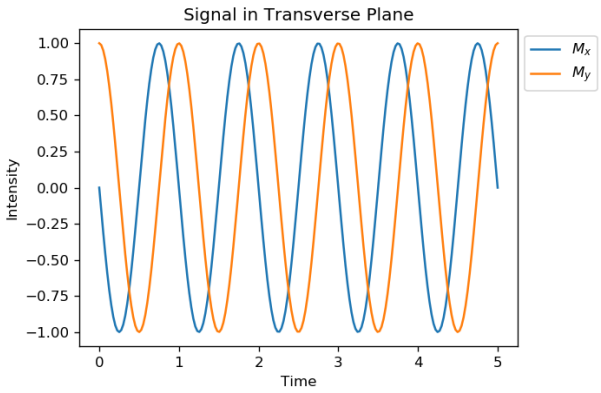

(b) Oscillation in transverse plane

Figure 2.1: These figures demonstrate how the spin rotating within the transverse plane, in the absense of dephasing, after a 90° RF pulse leads to sinusoidal signal readout. Fig. 2.1b represents Eq.(2.1.1) if at time $t = 0, \phi = 0$, and $M_0 = 1$.

2.1.2 MR Physics Relaxation

If we then include relaxation effects, the bulk magnetization equation with relaxation effects R becomes

$$\frac{dM(t)}{dt} = M(t) \times \gamma B(t) - R(M(t) - M_0).$$

Splitting the relaxation effects into those of T1 along the longitudinal axis and T2 in the transverse plane, the three differential equations to solve become

$$\frac{dM_x}{dt} = \gamma(M_y B_z - M_z B_y) - \frac{M_x}{T2}, \qquad \frac{dM_y}{dt} = \gamma(M_z B_x - M_x B_z) - \frac{M_y}{T2},$$

$$\frac{dM_z}{dt} = \gamma(M_x B_y - M_y B_x) - \frac{(M_z - M_0)}{T1}.$$

Solving these for free precession returns the following:

$$\frac{dM_x}{dt} = \gamma(M_y B_0) - \frac{M_x}{T2}, \qquad \frac{dM_y}{dt} = \gamma(-M_x B_0) - \frac{M_y}{T2}, \qquad \frac{dM_z}{dt} = -\frac{(M_z - M_0)}{T1}.$$

This can be differentially solved.

$$M_x(t) = \Big[M_x^0 \cos(\gamma B_0 t) + M_y^0 \sin(\gamma B_0 t)\Big] e^{-\frac{t}{T2}}$$

$$M_y(t) = \Big[-M_x^0 \sin(\gamma B_0 t) + M_y^0 \cos(\gamma B_0 t)\Big] e^{-\frac{t}{T2}}$$

$$M_z(t) = M_0 + \Big[M_z^0 - M_0\Big] e^{-\frac{t}{T1}}$$

After a 90° flip into the transverse plane along the x-direction, $M_x(0) = M_0$ and $M_y(0) = M_z(0) = 0$, resulting in the following signal equations.

$$M_x(t) = \Big[M_x^0 \cos(\gamma B_0 t)\Big] e^{-\frac{t}{T2}}, \qquad M_y(t) = \Big[-M_x^0 \sin(\gamma B_0 t)\Big] e^{-\frac{t}{T2}} \tag{2.3a}$$

$$M_z(t) = M_0\Big[1 - e^{-\frac{t}{T1}}\Big] \tag{2.3b}$$

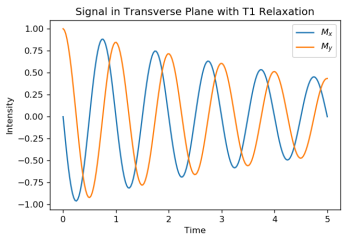

(a) T1 in the transverse plane

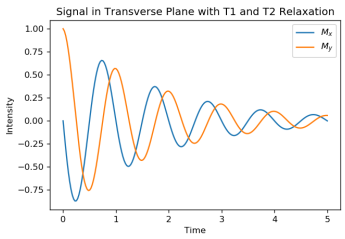

(b) T1 and T2 in the transverse plane

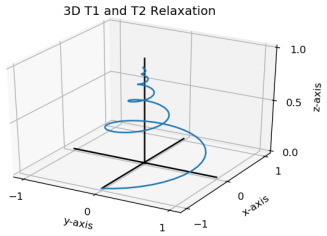

(c) T1 and T2 in 3D lab frame

Figure 2.2: These represent the signal shown in Fig.2.1b and the effects of relaxation in the transverse plane (Fig.2.2a,2.2b) and the combined effect in the 3D lab frame (Fig. 2.2c).

2.2 Signal Acquisition

2.2.1 Slice-encoding

A slice-selecting gradient insert produces a linearly spatially varying magnetic field along B_0 which influences the resonance frequency as a function of location along the z-axis,

$B_z = B_0 + \Delta B(z)$. An RF pulse will only excite spins within a certain range of that frequency. $\omega_{RF} = \omega_0 + \gamma\Delta B$. Therefore with the slice-selecting gradient B_z an RF pulse will excite a specific region along the z-axis with a chosen thickness s.

$$\omega_{RF}(z \pm s) = \omega_0 + \gamma\Delta B(z \pm s)$$

Within this slice that has been excited, frequency and phase of oscillation can then be used to map signal to locations in a 2D plane, i.e. along the x and y dimensions of the transverse plane.

2.2.2 Frequency-encoding

A frequency-encoding gradient along the x-axis produces a linearly spatially varying magnetic field along the x-axis, meaning the effective field B_x at a point along the x-axis is given by

$$B(x) = B_0 + xG_x.$$

From this we can get the transverse resonance frequency, RF, of the spin oscillation $M_{x,y}$ as a function of location along the x-axis, which shows a frequency offset from ω_0 based on position along the gradient.

$$RF(x) = \gamma B(x) = \gamma B_0 + \gamma x G_x = RF_0 + RF_{G_x}(x)$$

2.2.3 Phase-encoding

A phase-encoding gradient along the y-axis produces a linearly spatially varying magnetic field along the y-axis which is applied on and off again for protons to temporarily change precession frequencies. After the phase-encoding gradient is turned off the protons return to the original precession frequencies but have changed phase of their oscillation. The mag-

nitude of the phase shift is proportional to the strength of $G_y(y_i, t)$ at position y_i and the amount of time that the gradient was applied, t.

$$\phi(y) = \gamma G_y(y)t$$

The combined effect of both frequency-encoding and phase-encoding will lead to a transverse magnetic spin M_{xy} for a specific location (x_i, y_i).

$$M_{xy}(x_i, y_i) = M_0 \cos\Big(RF(x_i) + \phi(y_i)\Big)$$

This can be used to assign location of signal along the phase-encoding axis.

The individual phase shifts contributed by a pixel cannot be decoded by Fourier transform, therefore the phase-encoding gradient must be applied sequentially. The change in the resulting signal over time as phase accrues leads to constructive and deconstructive interference which can assign position along the y-axis. The combination of both frequency and phase encoding leads to k-space signal sampling.

2.2.4 k-space signal sampling

Phase and frequency encoding allows for the sampling of the image in the frequency domain, the 2D Fourier Transform of the image, referred to a "k-space". k-space corresponds to the spatial frequency representation of the image. With a gradient applied for a specific amount of time along a certain axis, the spins along that axis experience a varying external B-field; those farther from the origin experience faster precession. The longer that gradient is applied, the longer the spins along that axis have been precessing at different speeds. From this, the spatial frequency of the total signal oscillation along that gradient changes. If a gradient is applied to both x and y axes, this leads to a spatial frequency and phase accrual along both x and y. This changing amplitude of the signal as the frequency increases is

collecting data along a track in k-space. This is demonstrated mathematically below, and shown in Fig. 2.3.

In the rotating frame the non-inertial reference frame is rotating relative to the inertial lab frame. With only a steady B_0 field this rotating frame would have the rotating angular frequency of $\omega_{rot} = \omega_0$. If there is a change in the magnetic field from the influence of a gradient, in the inertial frame the angular frequency would be $\omega = \omega_0 + \gamma\Delta B$, and in the rotating frame it would be $\omega = \gamma\Delta B$. Here, ΔB represents the change in magnetic field due influence of the frequency-encoding gradient, along the x-axis, and this is all now in the transverse plane. Therefore, in the rotating frame in the transverse plane, the x and y components of the magnetization is a function of their location along the x-axis, i.e. ΔB.

$$M_x = \sin(2\pi\gamma\Delta B t) \qquad\qquad M_y = \cos(2\pi\gamma\Delta B t) \tag{2.4}$$

This ΔB will vary linearly along the frequency-encoding axis with G_x, with a stronger end of the gradient leading to a larger ΔB. At time zero, with no gradient, there is a maximum signal amplitude as all spins are aligned. As they begin to precess at different speeds due to ΔB in the gradient, they dephase and signal decreases due to destructive interference. In a homogeneous medium, as Fig. 2.3 shows, this destructive interference of the linearly varying precession frequency is an increase in the frequency of the total signal oscillation along the axis. After 2.5 seconds of the gradient being on, the signal along the axis is now undergoing one oscillation; at 10 seconds the signal is now undergoing 10 oscillations along the axis. In a heterogeneous medium, when the physical spatial frequency of a structural pattern, e.g. a picket fence, and frequency of precession agree, the constructive interference will spike. The amplitude of the signal will peak at that time t, which is the amplitude of the signal of that spatial frequency along the frequency-encoding direction. In 2D Fourier space, this means that as the frequency-encoding gradient is maintained over time, the frequency of spin

alignment is increasing, and the amplitude is the constructive interference of spins arranged at said frequency; this is sampling along k_x of 2D Fourier transform of the heterogeneous image.

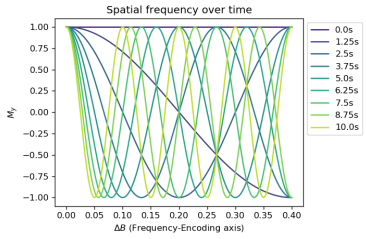

(a) Signal along the frequency-encoding axis at time ts.

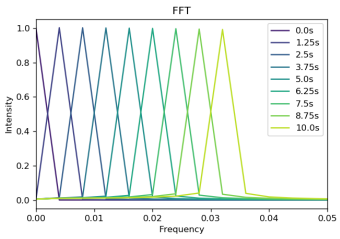

(b) Fast Fourier Transform of the signals in (a) at time ts.

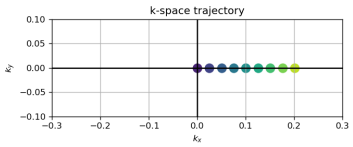

(c) The signals in (b) in k-space. Color is not signal amplitude.

Figure 2.3: These three figures demonstrate a homogeneous medium with a G_x gradient turned on for a period of time. It leads to an increasing spatial frequency along the frequency-encoding direction (ΔB) over time from 0 to 10 seconds. Units are arbitrary in this example, with $\gamma = 1$, $\Delta B = [0, 0.4]$, $t = [0, 10]$. Signals are color-coded matching in a-c and represent changing signal from $t = 0$ to $t = 10$

This is only true for a 1D sinusoid. Incorporating the direction of a 2D sinusoid requires use of the phase-encoding gradient along the y-direction. Application of the phase-encoding gradient means horizontal shifting of a wave of a given frequency by $\phi(y)$ where $\phi(y)$ is a function of location along the y-axis. In other words, by turning on the phase-encoding gradient, spins further along the y-axis precess at a faster frequency until it is turned off again. This means that there is a greater amount of phase accrued for those further away, i.e. one application of the phase-encoding gradient applies a shift in phase $\phi(y)$ as a function of location along y. As demonstrated in Fig. 2.4 this increasing shift in phase along the y-axis is actually 2D rotation of the wave of the original frequency. This is represented rotation about the origin in k-space, as shown in Fig. 2.5 with subsequent phase-encoding gradient applications leading to greater and greater phase accrual along the y-axis, further rotating the 2D wave.

$$M(y,t) = \cos(2\pi\gamma\Delta Bt) \rightarrow \cos(2\pi\gamma\Delta Bt + \phi(y)) \tag{2.5}$$

Here in Eq. (2.5) $\phi(y) = \gamma G_y(y) n t_\phi$ where t_ϕ is the duration of the gradient, G_y is the phase-encoding gradient at y, and n is the number of times the phase-encoding gradient has been applied. As the phase encoding step n increases, ϕ accumulated increases, which further rotates the planar wave. In Fig. 2.4, continuing the phase accumulation would continue to rotate the planar wave clockwise with each n step. Once enough phase has accumulated, the planar wave will have rotated by 90° and will be travelling in the vertical direction. This means that just due to phase accumulation from n phase-encoding steps the frequency along the y-axis has gone from zero (i.e. the original horizontally propagating wave) to ω_0 for the now vertically propagating wave. This is the same as travelling from the origin and along the k_y in k-space.

Looking at just the increase in frequency along the y-axis due to the phase-encoding gradient, this is sampling along k_y with every step n. Notice so far that the phase ϕ of the 2D wave is not included in location in k-space. This is shown in Fig. 2.5 where when phase is added, the complex portion increases while the real portion is unchanged.

Demonstrating the effect of both frequency and phase ϕ of a 1D wave mathematically, we take the Fourier transform ($\mathfrak{F}$) of M_y with the phase encoding ϕ included. In Eq. (2.6) that added phase term $e^{i\phi}$in the 2D wave is a shift along the imaginary component of a point in k-space.

$$\mathfrak{F}[M_y] = \mathfrak{F}[A\cos(2\pi\gamma\Delta Bt + \phi)] = \mathfrak{F}[A\cos(\omega_0 t + \phi)]$$

$$= \frac{1}{2\pi}\int_{-\infty}^{\infty} A\cos(\omega_0 t + \phi)e^{i\omega t}dt$$

$$= \frac{1}{2\pi}\int_{-\infty}^{\infty} A\left[\frac{e^{i(\omega_0 t+\phi)} + e^{-i(\omega_0 t+\phi)}}{2}\right]e^{i\omega t}dt$$

$$= \frac{1}{2\pi}\frac{A}{2}\left(\int_{-\infty}^{\infty}\left[e^{i(\omega_0 t+\phi)}e^{i\omega t}\right]dt + \int_{-\infty}^{\infty}\left[e^{-i(\omega_0 t+\phi)}e^{i\omega t}\right]dt\right)$$

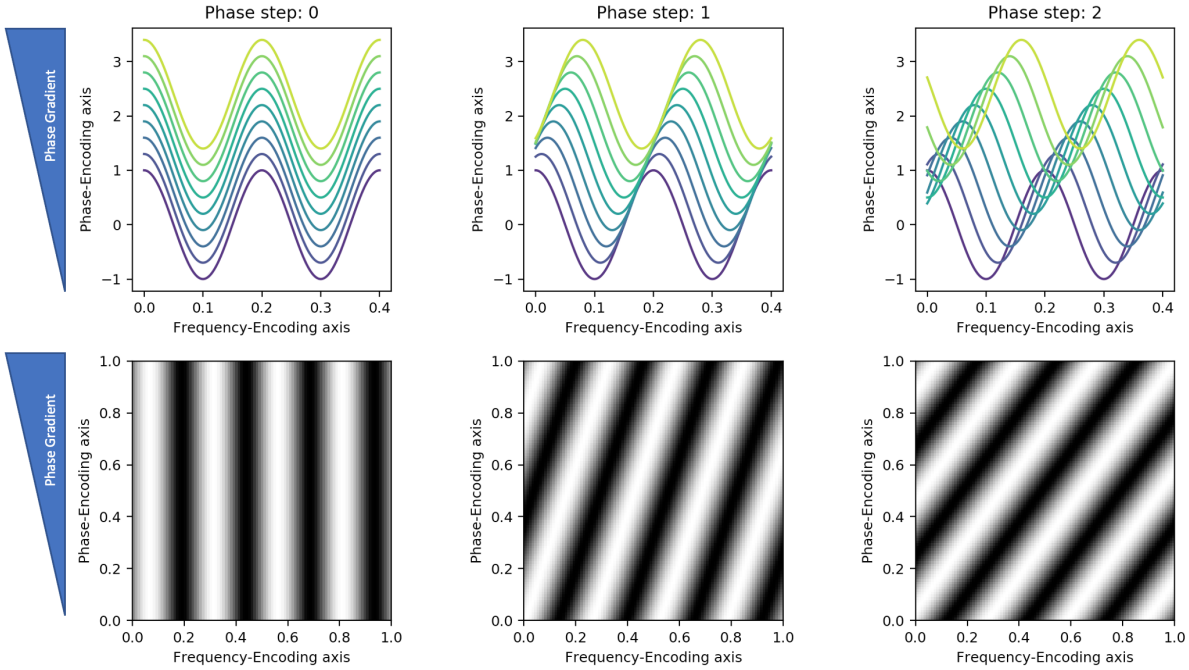

Figure 2.4: Demonstration of phase encoding gradient in spatial domain and k-space. At phase step 0 the Gy gradient has not been applied showing a 2D planar wave travelling horizontally along the x-axis. However, at phase step 1 the phase-encoding gradient has been turned on and off again for a certain amount of time meaning that phase as accrued as a function of location long the y-axis. The increasing phase shift of the wave as it experiences more of the phase gradient can be seen in the bottom image 2D space as rotation of the original wave of the same frequency.

$$= \frac{A}{2}\left(\frac{1}{2\pi}\int_{-\infty}^{\infty}\left[e^{i(\omega+\omega_0)t}e^{i\phi}\right]dt + \frac{1}{2\pi}\int_{-\infty}^{\infty}\left[e^{i(\omega-\omega_0)t}e^{i\phi}\right]dt\right)$$

$$= \frac{A}{2}e^{i\phi}\left(\delta(\omega+\omega_0)+\delta(\omega-\omega_0)\right) \tag{2.6}$$

Finally, combining these parameters and including amplitude we get the following equation for the 2D planar wave produced by a homogeneous medium of spins under frequency and phase-encoding gradients:

$$Z(x,y) = Acos(k\cos\theta x + k\sin\theta y + \phi) \tag{2.7}$$

Absolute distance from the origin of k-space is the frequency $k = \sqrt{k_x^2 + k_y^2}$, direction

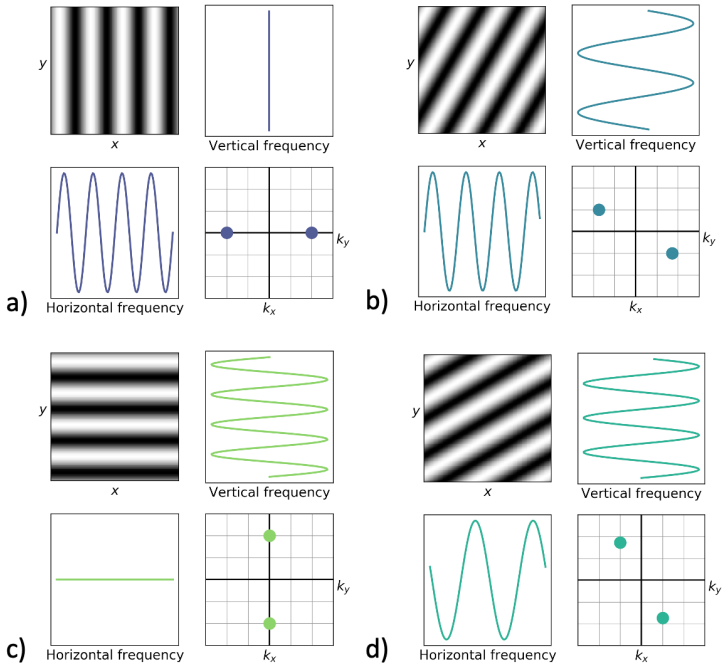

Figure 2.5: This shows that as the n phase-encoding steps are collected and the 2D wave of a certain frequency rotates clockwise that the frequency along the x-axis and along the y-axis change. This is shown in the bottom left figure of a) to d) as the spatial frequency k_x and k_y of the rotating wave also rotates.

of propagation is the angle from the origin $\theta = \arctan \frac{k_y}{k_x}$, amplitude of the wave is the real signal at k_x, k_y and phase of the 2D wave is the complex component. The change in ΔB from Eq. (2.4) due to the frequency-encoding gradient will increase the frequency along the x-axis, i.e. travelling along the k_x axis; this is affecting the $k \cos\theta$ in Eq. (2.7). This shift of the delta function due to the ΔB experienced by the spin is the shift along k_x. Phase-encoding will rotate the 2D wave about the origin in n-steps, which is synonymous with increasing the frequency along the y-axis, i.e. travelling along the k_y axis. This is affecting the $k \sin\theta$ in Eq. (2.7). Therefore, with both frequency and phase encoding gradients applied, data can be collected along k_x and k_y, i.e. with varying frequency k and direction θ, allowing sampling of all of k-space. The timing of the waves will determine the phase ϕ of the 2D wave and is stored as the complex component of k-space. This k-space collection is direct acquisition of the 2D Fourier transform of the image of interest. From this, the inverse Fourier transform

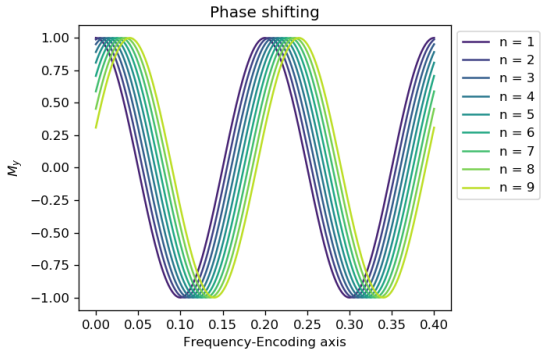

(a) Change in phase along frequency encoding axis

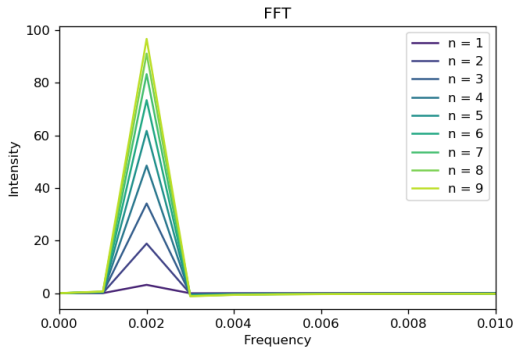

(b) Complex portion of Fast Fourier Transform of the signals in (a).

Figure 2.6: These two figures demonstrate how phase of the 2D waves is encoded in the complex space of the Fourier transform.

of this collected k-space is the true image.

2.2.5 k-space trajectories

k-space trajectories can be written as equation of phase encoding and frequency encoding gradients turned on for a certain amount of time.

$$k_x(t) = \gamma \int_0^t G_x(\tau) d\tau$$

$$k_y(t) = \gamma \int_0^t G_y(\tau) d\tau$$

The simplest, and most common acquisition is the Cartesian 2DFT/spin warp. This is a single line raster acquisition in which an initial negative G_x and G_y begins data collection in the bottom left corner of the k-space of interest. With G_y turned off, and G_x kept on, data collection begins along k_x at $-k_y^{max}$. Once one line along k_x has been collected, G_y is turned on and off again, as a phase step, and G_x is turned on again so that data collection begins again along k_x at $-k_y^{max} + 1$. An example of this starting at $(-k_x^{max}, -k_y^{max}) = (-0.25, -0.25)$ is shown in Figure 2.7a. As each line in k-space requires a different phase-

encoding step, this acquisition is time consuming and therefore prone to motion artifacts. Faster sampling with Echo Planar Imaging (EPI) can minimize these effects, which is critical for sequences that require signal from particle motion like diffusion and perfusion which will be discussed in detail in later chapters.

EPI involves a strong switching frequency-encoding gradient applied simultaneously with a low phase-encoding gradient blipped over time during one RF acquisition. The result is shown in Figure 2.7b in which the initial trajectory begins at $(-k_x^{max}, -k_y^{max}) = (-0.25, -0.25)$. G_x leads to acquisition along the k_x and after this, a small phase blip G_y and a switched negative G_x leads to that first zig-zag. This is followed again by a phase blip G_y and a positive G_x. This can be done rapidly allowing collection of all k-space with one RF pulse.

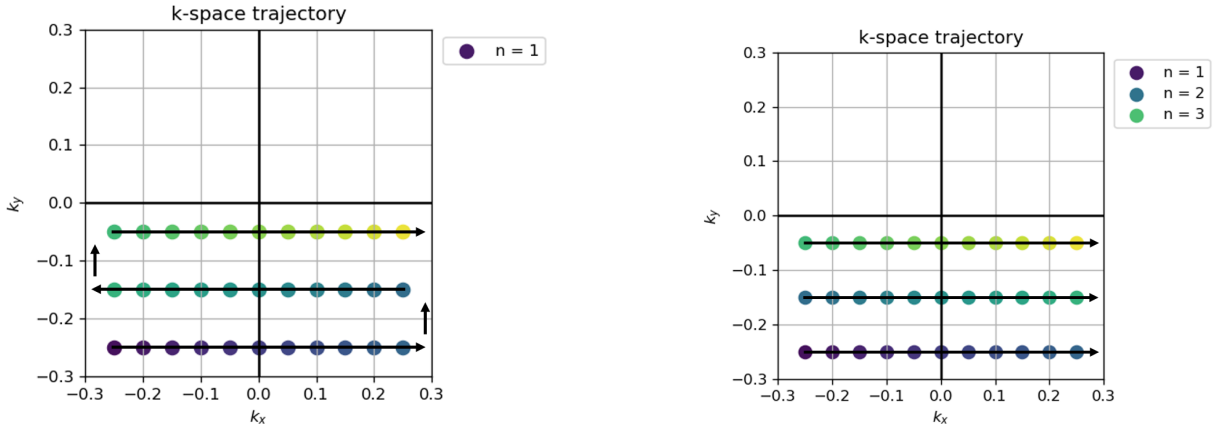

(a) Cartesian k-space trajectory for spin-warp.

(b) Cartesian k-space trajectory for echo-planar imaging.

Figure 2.7: These figures represent two common k-space trajectories. Arrows represent the order of acquisitions in k-space over time. n represents the phase-encoding step number.

With k-space acquired, sampling rate Δk and k-space sampled k_{max} can determine resolution and field of view of the resulting image.

$$\Delta x = \frac{1}{2k_x^{max}}$$

$$FOV_x = \frac{1}{\Delta k_x}$$

In other words, a larger FOV in image domain requires a higher sampling rate in k-space. A higher resolution in the image domain requires a larger FOV in k-space. Intuitively, this is because higher resolution is information stored in higher frequencies, i.e. further edges of k-space. Similarly, high contrast information is in the center of k-space, as those large changes in signal are large frequency waves.

2.3 Basic Pulse Sequences

At the most basic level, MR pulse sequences are composed of echo time (TE), repetition time (TR), and inversion time (TI). TE is the time between excitation and readout, TR is the time between repeated excitations of the same slice, and TI is the time between an inverting 180° pulse and the 90° pulse. A simple RF pulse involves a first flip into the transverse plane with a B_1 field with slice selection gradient on. After TE has passed, signal is acquired from that transverse magnetization with frequency and phase encoding gradients, and at TR, the sequence is repeated. The signal of interest can be the signal regrowth in the longitudinal direction (T1) or the signal decay in the transverse plane (T2), and the two most common acquisitions are gradient echo and spin echo.

2.3.1 T1-weighting

$M_z(t) = M_0 \left[1 - e^{-\frac{t}{T1}}\right]$ from Eq.(2.3b) represents the signal equation for T1-relaxation, with the T1 of a voxel being the time t at which the exponent is -1. This is equivalent to the time at which the longitudinal magnitude has returned to roughly 63% of its initial magnitude prior to the RF pulse. One form of T1-weighting involves collecting images along the regrowth curve and fitting the data to Eq.(2.3b) to extract T_1. A variable TR will mean that the signal is flipped into the transverse plane and measured at different times after the

previous 90° pulse, meaning a collection of varying points on a voxel-by-voxel basis along the regrowth curve. Contrast in an image is generated from different regrowth curves for voxels of different organs and tissues of interest. To maximize this difference, short TR is required to ensure that it has not fully regrown upon the 90° flip, and a short TE is required to minimize T2 relaxation effects. The signal acquisition at varying TR times to get data to fit T1 regrowth curves is shown in Fig. 2.8a.

2.3.2 T2-weighting

M_x and M_y in Eq.(2.3a) represent the signal equation for T2-relaxation, with the T2 of a voxel similarly being the time t at which the exponent is -1. This is when the transverse magnitude has lost roughly 63% of its initial magnitude. For ease, switch $M_x(t)$ and $M_y(t)$ into the rotating frame, where $\omega_0 = -\omega_{rot}$ in the following equation.

$$\omega_{eff} = \omega_0 + \omega_{rot} = \gamma(B_0 + B_{rot}) = \gamma B_{eff}$$

With $\omega_0 = -\omega_{rot}$ there is a $B_{eff} = 0$. Therefore, with a 90° RF pulse, $\phi_0 = 0$, and $M_x = M_0$, the transverse signal in the rotating frame will be $M_x \propto M_0 \cos(0)$ and $M_y \propto M_0 \sin(0)$. This returns the following equations over time.

$$M_x(t) = M_0 e^{-\frac{t}{T2}} \qquad\qquad M_y(t) = 0$$

This rotating frame allows the T2 relaxation to be observed along the x-axis. The T2 relaxation is faster ($T2 < T1$) but longitudinal relaxation will still affect it in the transverse plane. Contrary to T1-weighting, T2-weighting requires a long TR and a long TE to exploit T2 relaxation. A long TR is required such that longitudinal signal has fully regrown before being flipped back into the transverse plane, i.e. minimize T1 effects. A variable and long

TE is used to get the decay of transverse signal within one RF pulse. The signal acquisition at varying TE times to get data to fit T2 regrowth curves is shown in Fig. 2.8b.

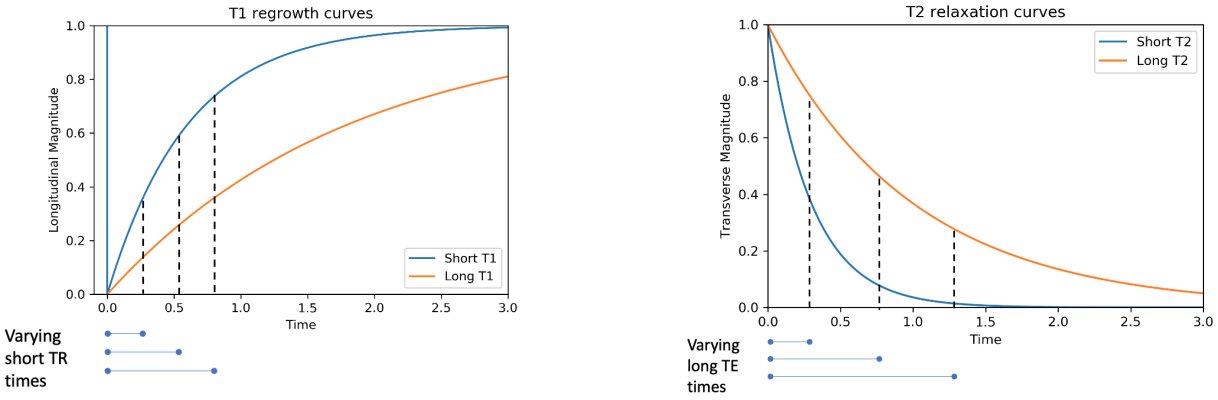

(a) T1-weighting

(b) T2-weighting

Figure 2.8: These figures represent T1 and T2 weighted acquisition. a) represents longitudinal growth and images taken at different TR to get data for the T1 regrowth curve. b) represents the transverse decay and images taken at different TE within a single TR to get data for the T2 decay curve.

2.3.3 Gradient Echo

Gradient Echo sequence (GRE) consists of an RF pulse with slice selection followed by acquisition at TE with frequency and phase encoding gradients. The different combinations of the frequency and phase encoding gradients correspond to different k-space trajectories, and image signal depends on TR and TE. The transverse signal decay is dependent on free induction decay, which is due to T2*.

$$\frac{1}{T2^*} = \frac{1}{T2} + \frac{1}{T2'}$$

After the 90° RF pulse, the transverse signal decays at the rate of T2*, faster than T2 because of dephasing effects. In the rotating frame of reference, this is the equation

$$M_x(t) = M_0 e^{-\frac{t}{T2^*}}.$$

In Fig. 2.9a this is shown as the solid blue line that becomes the dashed blue line in simple exponential decay at the rate of $T2^*$ starting at $t = 0$. GRE can be repeated at time TR: in Fig. 2.9a at $t = 4$ with another 90° pulse.

2.3.4 Spin Echo

Spin-Echo sequence (SE) consists of a 90° pulse and 180° pulse at $\frac{TE}{2}$, followed by an echo at time TE, and a repeated sequence at time TR. The 90° pulse will flip the spins into the transverse plane and a subsequent 180° pulse at $\frac{TE}{2}$ will flip the spins within the transverse plan to cancel out dephasing of spins by magnetic field inhomogeneities. The spin-echo when the spins rephase lead to a signal echo meaning the decay measured will be due to T2, rather than T2*. With SE the T2 decay is recoverable, and multi-echo Spin-Echo can be used to get T2 relaxation with additional 180° echoes whose peaks will decay according to T2. While this sequence has higher signal, it takes longer than GRE. Further, depending on TE, the signal will decrease at further echos due to the decay.

The signal during SE is shown in Fig. 2.9a with the $90° - 180°$ and the solid blue line. The echo occurs at TE, showing how that echo returns signal along the T2 decay line shown in green, as opposed to the T2* decay which continues as the dashed line. After that echo it continues decaying at T2*, but if another 180° pulse is applied in a multi-echo SE, the echos at each subsequent TE would be along the green T2 decay curve. SE can be repeated at time TR with another 90° pulse.

2.3.5 Inversion Recovery

Inversion recovery sequence (IR) consists of a spin-echo sequence that has been preceded by a 180° pulse. The time between this preparatory pulse and the 90° excitation RF pulse is TI. By choosing the appropriate TI, signal from different tissues can be suppressed. This is because the preparatory pulse inverts longitudinal magnetization, and the spins begin to

realign with the main B_0 field, at the rate of $T1$. If the excitation pulse is applied at the null point of a certain tissue, where the longitudinal magnetization crossing zero, the signal from this tissue is suppressed. This value can be solved for using the equation $M_z = 1 - 2e^{-\frac{t}{T1}}$ and solving for t when $M_z = 0$, and is typically $t_{null} \approx \ln(2) \times T1$.

More specifically though, after that first inversion recovery 180° pulse, the IR signal equation at the 90° RF pulse is

$$M_z = M_0 \left(1 - 2e^{-\frac{TI}{T1}} + e^{-\frac{TR}{T1}}\right). \tag{2.8}$$

This comes from solving the equation $\frac{dM_z}{dt} = -\frac{(M_z - M_0)}{T1}$ in Chapter 2.1.2 by separating terms and integrating from $t = 0$ to $t = TI$. In other words, and shown in Fig. 2.9b, at the first 180° pulse, at $t = 0$ the initial $M_z = -M_z$, however for future pulses this will not be the case. Instead, the M_z will be equal to the negative of the regrowth allowed between the 90° of the previous TR and 180° pulse of the current TR. This is the signal at $t = TR - TI$, which given the T1 regrowth equation is $M_z = M_0(1 - e^{-\frac{(TR-TI)}{T1}})$.

Therefore, solving for M_z in the equation from $t = 0$ to $t = TI$ and $M_z = -M_0(1 - e^{\frac{-(TR-T1)}{T1}})$ to M_z:

$$\int_{-M_0(1-e^{-\frac{TR-TI}{T1}})}^{M_z} \frac{dM_z}{M_z - M_0} = -\frac{1}{T1}\int_0^{TI} dt$$

$$\ln(M_z - M_0)\Big|_{-M_0(1-e^{-\frac{TR-TI}{T1}})}^{M_z} = -\frac{t}{T1}\Big|_0^{TI}$$

$$\ln(M_z - M_0) - \ln\left[-M_0\big(1 - e^{-\frac{TR-TI}{T1}}\big) - M_0\right] = -\frac{TI}{T1}$$

$$\ln\left[\frac{M_z - M_0}{-2M_0 - M_0 e^{-\frac{TR-TI}{T1}}}\right] = -\frac{TI}{T1}$$

$$\frac{M_z - M_0}{-2M_0 - M_0 e^{-\frac{TR-TI}{T1}}} = e^{-\frac{TI}{T1}}$$

$$M_z = M_0(1 - 2e^{-\frac{TI}{T1}} + e^{-\frac{TR}{T1}})$$

An example of an IR-GRE pulse and the longitudinal signal is shown in Fig. 2.9b.

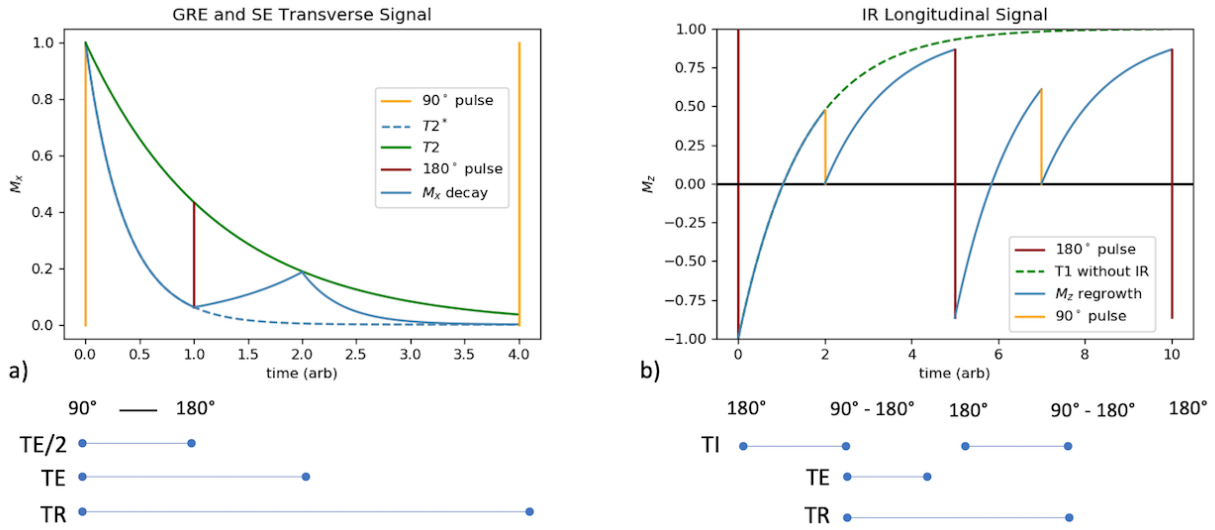

Figure 2.9: a) Transverse signal in the rotating frame during a GRE and SE sequence in the transverse plane. The GRE is shown as the dashed line, decaying at T2* after a single 90 degree pulse. The SE is shown as the solid line and the echo at TE after the 180 pulse. b) Longitudinal signal during an IR sequence. The standard T1 regrowth without IR is shown as a green dashed line. The signal with IR and the SE between the inversion pulses is shown in blue. 180° pulses are shown in red, and 90° pulses are shown in orange.

If this is then a Inversion Recovery Spin Echo (IRSE) sequence, with $180° - 90° - 180°$, this signal decays with time constant T2 in the transverse plane following this equation:

$$M_z = M_0 \left(1 - 2e^{-\frac{TI}{T1}} + e^{-\frac{TR}{T1}}\right) e^{-\frac{TE}{T2}} \tag{2.9}$$

While IRSE can remove signal from tissues and fluids that are not wanted, it does lengthen scan times and can lead to a reduction in SNR due to signal suppression.

2.3.6 Signal-to-Noise Ratio

Signal-to-noise in imaging is one measure of image quality. Higher SNR leads to a clearer image and a better ability to distinguish important features in radiology. In MRI, this SNR is related to the pulse sequence used, the voxel volume, the field strength, the time of acquisition, the coil sensitivity, acquisition number, and patient movement.

$$SNR \propto B_0 C \times (\Delta x \Delta y \Delta z) \times \sqrt{N_{PE} N_{3D} N_{ave} T_{shot}}$$

It can be increased with higher B_0, higher coil sensitivity C, and increased voxel dimensions ($\Delta x \Delta y \Delta z$). A greater number images taken, such as of measurements taken with phase encoding (N_{PE}), planes in 3D acquisition (N_{3D}), images for averaging (N_{ave}), and greater time during acquisition T_{shot} will also increase SNR. SE tends to have higher SNR than GRE because the rephasing of transverse spins leads to a signal peak. This comes at the cost of a longer scan due to the needed 180° pulse.

2.4 Perfusion and Flow

Perfusion refers to the rate of blood flow through capillaries of a tissue bed and is commonly assumed to be related to metabolic demand in the brain. Perfusion is an important physiologic parameter used in detection, characterization, and monitoring of central nervous system tumors and neurovascular disease and can be imaged with contrast and non-contrast sequences, both relative and quantitative in ml/100g/min (Essig et al. [2013]). This is different from blood flow via angiography which involves imaging of blood in large blood vessels $>$ 1mm, rather than blood in tissues.

2.4.1 Dynamic Susceptibility Contrast (DSC)

With DSC perfusion imaging of the brain, rapid T2*-weighted images are obtained immediately following contrast bolus. The contrast used is gadolinium-based contrast agent (GBCA), and during the first pass through circulation it remains largely within the vascular space. The strongly paramagnetic gadolinium produces a local magnetic field distortion (susceptibility effect) by the unpaired electron spins aligning parallel to the field. This facilitates a change in the Larmor frequency of local protons, leading to T2-dephasing in DSC SE (or T2*-dephasing in DSC GRE) sequences and a drop in T2-weighted signal during transit. This drop in signal is a way of tracking the contrast as it travels through the brain via the blood stream.

The rapid T2-weighted images taken over the duration of the bolus result in a time series of change in signal on a voxel-wise basis as the GBCA travels through the circulatory system. This signal over time is used to calculate perfusion in ml/100g/min for each voxel, returning a perfusion map. As this sequence only images during the first bolus passage it takes roughly two minutes.

2.4.2 Dynamic Contrast Enhanced (DCE)

With DCE perfusion imaging of the brain, T1-weighted images are obtained over an extended period of time as GBCA accumulates within the tissue extracellular space. GBCA shortens T1 meaning that GBCA will increase signal over time in a T1-weighted acquisition. By applying a compartmental model to this change in dynamic signal physiological parameters can be derived. This is typically used to measure blood leakage and disruption of the blood brain barrier in cases such as tumors and may have utility in the imaging of brain aneurysms.

2.4.3 Arterial Spin Labeling (ASL)

Rather than using an exogenous IV injected GBCA, ASL images perfusion using endogenous tracer (Ferre et al. [2013]). Water molecules in a certain location upstream of a region of interest are 'labeled' with a selective RF pulse to invert the spins. Over the next few seconds these spin-labeled water molecules in the blood travel downstream and transfer the spin-label to interstitial water in proportion to perfusion. Tissue contrast, post-label, reflects the residual spin-label in the tissue and consequently tissue perfusion. The change in signal before and after these labeled molecules have traveled from their initial location is thus perfusion weighted. For imaging of the brain, molecules are typically labeled at the neck vessels with blood flow bringing the inverted protons up to the brain.

However, there are several limitations of ASL. The spin-labeled inflow causes only 1% percent signal change leading to low SNR (Golay et al. [2004]), meaning many images must be taken to improve SNR at the cost of increased motion artifact. Increased transit time due to circuitous blood flow around an occlusion and labeled blood that doesn't perfuse can confound perfusion signal (Grade et al. [2015], Zaharchuk [2014]) and prevents quantification in disease states as parameters derived from normal subjects are not applicable. Therefore, the physiologic basis of ASL poses difficulties in patients with cerebrovascular disease, as transit time of spin-labeled molecules varies greatly in disease states (Grade et al. [2015]) and slow flow is difficult to image (Parkes et al. [2004]). Further, ASL has a limited role in evaluation of ischemic stroke compared to DSC. While it can confirm the presence of hypoperfusion, there have been mixed results regarding sensitivity, it may not detect small perfusion deficits. ASL may show false hypoperfusion due to reduced labeling efficiency at the labeling plane and has not been found to consistently agree with standard DWI perfusion-diffusion mismatch in acute stroke (Zaharchuk et al. [2012])

2.4.4 Intravoxel Incoherent Motion (IVIM)

Intravoxel incoherent motion (IVIM) is a non-contrast perfusion-diffusion MRI scan introduced in 1987 (Le Bihan et al. [1988]), and re-emerging the last decade (Le Bihan [2019]), that uses diffusion weighted imaging (DWI) to image fast and slow water motion. DWI is a form of MR imaging that measures how easily water can diffuse in a region; using a strong gradient (b-value) the distance a spin has moved can be connected to the signal lost. With multiple gradient strengths and durations, b-values, to simultaneously assess tissue water diffusion and tissue perfusion without the use of gadolinium-based contrast agent and independent of arterial input function. Diffusion-weighting with varying b-values is sensitive to water motion and consequently able identify where in the brain water is sequestered inside cells by cytotoxic edema (Iima and Le Bihan [2016]).

Typically, high b-values ($b \geq 800 s/mm^2$) are used for diffusion-weighting, meaning signal loss between gradients is due to water diffusion, which creates the greatest contrast between infarct and viable brain. At very low b-values ($b \leq 200 s/mm^2$), diffusion-weighting is sensitive to faster water motion, meaning signal loss is predominately from fast moving molecules, such as capillary level blood flow (Le Bihan and Turner [1992], Le Bihan et al. [1988], Le Bihan [2019], Federau et al. [2012], Jalnefjord et al. [2018]). IVIM scans acquire DWI images with multiple b-values and extract CBF as well as diffusion restriction using mathematical modelling of a bi-exponential (Le Bihan et al. [1988]). This modelling is necessary to separate perfusion (low b-values) and diffusion components (high b-values) and allows for quantification of CBF with a calibration factor to convert relative IVIM perfusion to quantitative values (ml/100g/min), and a more accurate interstitial water diffusion image (Le Bihan and Turner [1992], Wirestam et al. [2001]). Diffusion and IVIM perfusion is laid out in more detail in Chapters 5-7.

CHAPTER 3

QUANTIFICATION OF DSC-MR PERFUSION IN NOVEL FLOW AUGMENTATION THERAPY

3.1 Neurovascular Disease: Stroke

Neurovascular disease represents disorders of blood vessels that supply the brain and spinal cord and is a leading cause of death in the U.S. Stroke, symptoms resulting from damage to brain tissue from interruption of blood supply, is the 5th leading cause of death and long-term disability. Stroke can be hemorrhagic or ischemic, with hemorrhagic stroke occurring due to a ruptured vessel and ischemic stroke occurring from a blocked vessel and accounting for nearly 90% of strokes. The blocked arteries can lead to infarction, the tissue death due to inadequate blood supply. A core of infarcted tissue surrounding core of dead brain (i.e "infarction") forms with under-perfused tissue that has not yet died surrounding that core infarct and at risk of becoming infarcted. This penumbra is tissue that is in danger of progressing to infarction and potentially becoming damaged when blood supply returns to ischemic tissue.

Ischemic stroke is best treated with immediate clot removal. This can be done through drug administration via IV, endovascular thrombolytic drug delivery, or physical removal via stent. However, this is within a narrow window, with successful treatment typically done within 8 hours of occlusion. Bridge therapies may reduce disability by extending the door to needle window, i.e. the time from arriving at the hospital to the time when the clot removal procedure begins, expanding the window of successful treatment. Presented here is analysis of a potential bridge therapy via flow augmentation treatment in a pre-clinical canine model through infarct growth and quantitative MR perfusion.

3.1.1 Autoregulation

Cerebral autoregulation under normal physiologic conditions matches cerebral blood flow to metabolic demand, independent of blood pressure, within a given range of mean arterial pressure. To maintain this regulation, high systemic pressure will cause vessel constriction and low systemic pressure will cause vessel dilation. Therefore, disruption of this autoregulation would disrupt this relation between systemic pressure and vessel constriction. Under these conditions, CBF is expected to vary direction with mean arterial pressure (Edvinsson and Krause [2001]). High systemic pressure without autoregulation will lead to CBF higher than standard regulated limits.

3.1.2 Bridge Therapy: Norepinephrine and Hydralazine

Norepinephrine is an ionotropic pressor which will increase blood pressure without cerebral vasoconstriction while hydralazine is a vasodilator that relaxes blood vessels (Rowe et al. [1962], Smrcka et al. [1998], Dawson et al. [2003], Shin et al. [2008]). The simultaneous combination of the two has been posited to increase perfusion pressure and dilate vasculature thereby modifying autoregulation (Overgaard and Skinhoj [1975], Barry and Strandgaard [1985], Barry [1985]), allowing perfusion to rise above regulated levels and allow blood supply to reach critical regions of ischemic tissue. By disrupting cerebral autoregulation, CBF could vary with mean arterial pressure (MAP) and increase CBF to the ischemic territories during cerebral arterial occlusion and reduce the progression rate of ischemic penumbra to infarction, mitigating infarct growth. Therefore, the combination of the two could be leveraged to disrupt cerebral autoregulation in the setting of acute stroke and possibly augment blood flow to penumbral tissue until the clot is removed or dissolved.

During large vessel occlusion this works through the leptomeningeal collateral supply. These pial collaterals are small blood vessels that connect terminal cortical branches of the middle, anterior, and posterior cerebral arteries along the surface of the brain. While

they are dormant under unimpeded blood flow through the primary circulatory system, if a primary artery is occluded these collaterals can re-route blood flow to the affected area. The distribution, size, number, and capacity of the pial collaterals varies based on individual, but robust collaterals may be associated with reduction of infarct size and effect therapeutic outcome.

As salvageability of the penumbral tissue surrounding an infarct during acute ischemic stroke varies with collateral blood supply, depending heavily on leptomeningeal collateral arterial vasodilation and perfusion pressure (Muhonen et al. [1994], Muhonen et al. [1992]), treatments aimed at augmenting leptomeningeal collateral flow should reduce infarction rate. This flow augmentation therapy would serve as a "bridge therapy" prior to thrombolysis or thrombectomy. In animal models, a combination of norepinephrine and hydralazine administered in the first few hours after occluding a large artery in the brain has been shown to mitigate infarct evolution (Saadat et al. [2020]) suggesting that simultaneous increase in systemic blood pressure and potent vasodilation augmented pial collateral supply (PCS), modulated cerebral blood flow (CBF) autoregulation, and mitigated infarct volume growth.

3.2 Experimental Protocol

The two-day pre-clinical canine study laid out in Fig. 3.1a and 3.1b focused on improving the imaging and treatment of ischemic stroke evaluates cerebral tissue perfusion as defined by MRI-based quantitative cerebral blood flow (qCBF) in response to therapeutic intervention after middle cerebral artery occlusion (MCAO). The infarcted middle cerebral artery territory and contralateral normal hemispheric tissue were compared with and without simultaneous administration of norepinephrine and hydralazine during acute phase of ischemic stroke. Perfusion within the core of the infarct (diffusion positive) and penumbral territories were reported as well as comparison to baseline physiology (day 1 values of qCBF prior to CO2 inhalation). This study tested the hypothesis that simultaneous cerebral blood pres-

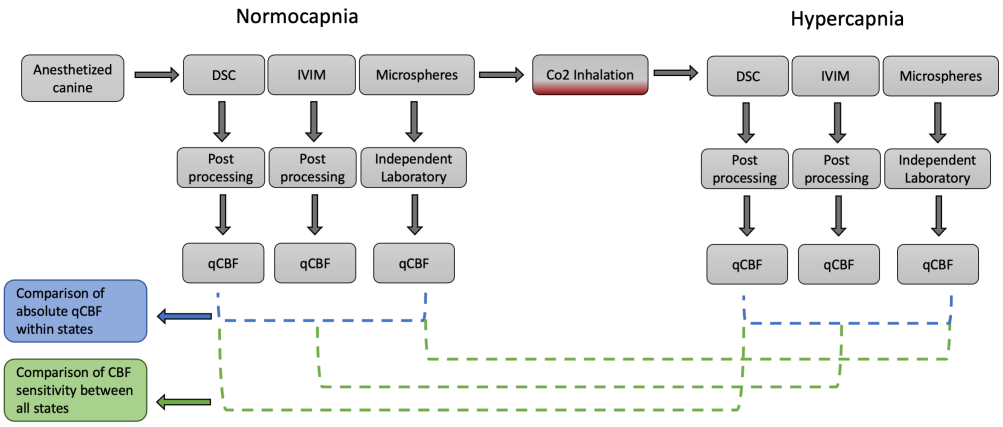

(a) Day 1 Experimental Protocol

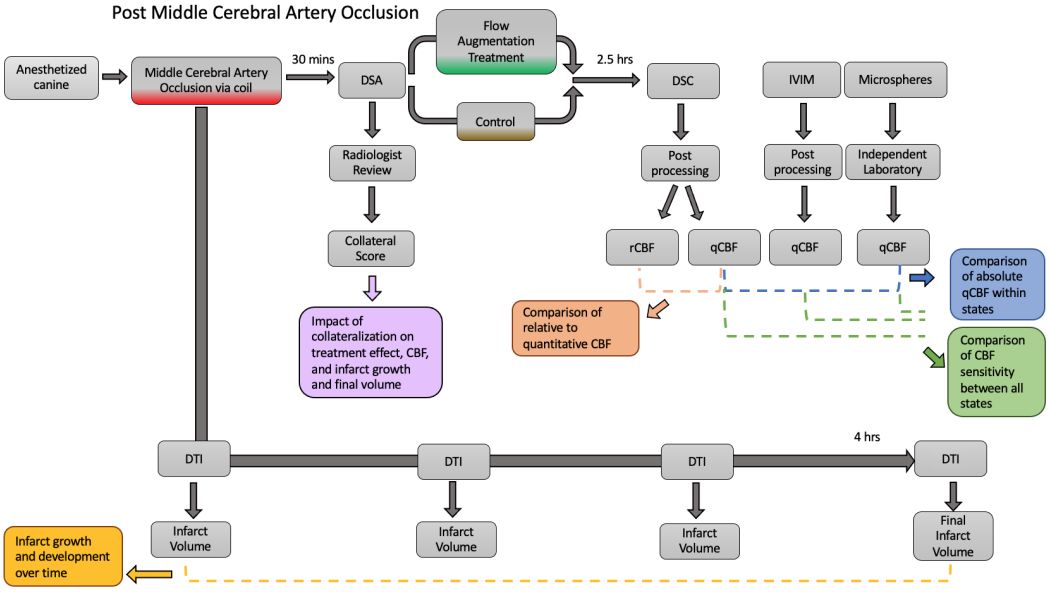

(b) Day 2 Experimental Protocol

Figure 3.1: Flowchart of two day pre-clinical canine model studying cerebrovascular response and flow augmentation therapy via simultaneous norepinephrine and hydralazine.

sure elevation and vasodilation increases cerebral blood flow to ischemic tissue during acute ischemic stroke and that this increase varies by degree of pial collateral recruitment. It compares the perfusion effect due to flow augmentation therapy to the corresponding effect on infarct growth rate.

On the first day of the two day experiment, seventeen mongrel canines (20-30kg, 13F, 4M, 4.22±3.3yr) underwent MRI including anatomic imaging, diffusion and perfusion MRI

at baseline physiologic conditions, under general anesthesia. To minimize influence on tissue perfusion and collateral arterial blood supply, anesthesia was maintained using continuous propofol infusion (25μg/kg/min), intravenous rocuronium (0.4–0.6mg/kg, every 10–30min titrated to effect), and isoflurane (1% end-tidal, 0.75 MAC). On the second day, subjects underwent permanent endovascular middle cerebral artery occlusion (MCAO) at the M1 segment via embolic occlusion coils and underwent post-MCAO perfusion MRI 2.5 hours after occlusion. Physiologic monitoring ensured that cardiac rhythm, end-tidal CO2, and body temperature remained within physiologic limits throughout the procedure. MAP was monitored via 5-French intra-arterial sheath throughout the procedure for all cases. Pial collateral recruitment was measured 30 minutes post-MCAO to record the extent and timing of leptomeningeal collateral recruitment into the ischemic territory prior to treatment.

Starting 30 min post-occlusion, after pial collateral recruitment measurement, seven treatment subjects randomized in advance and independent of collateral score received a continuous infusion of norepinephrine (0.1 – 1.52μg/kg/min) titrated 25-45 mmHg above baseline MAP with systolic blood pressure sub-180 mmHg and a single infusion of 20mg hydralazine. Intra-arterial blood pressure in the control group was maintained within physiologic limits (MAP 80-105 mmHg). Two subjects were excluded from analysis for unanticipated events. In one case, MRI scans were not properly acquired due to human error, and in the second case subarachnoid hemorrhage occurred after MCAO.

All experiments were conducted using a pre-clinical canine model of controlled MCAO (Jeong et al. [2019], Christoforidis et al. [2011]). The two-day experimental protocol was approved by the Institutional Animal Care and Use Committee of the AAALAC International accredited institution, The University of Chicago, and reported in compliance with ARRIVE guidelines. The study adheres to a) Guide for the Care and Use of Laboratory Animals (National Research Council), b) USDA Animal Welfare Act and Animal Welfare Regulations, and c) Public Health Service Policy on Humane Care and Use of Laboratory Animals.

3.3 MRI Protocol

Quantitative MR perfusion scans were acquired on a 3T MRI (Achieva, Philips) on day 1 at baseline and on day 2, 2.5 hours post-occlusion using a T1-bookend dynamic susceptibility method. The scan protocol consisted of a 2D EPI Look-Locker inversion recovery (FOV/Matrix = 220 mm/224, Slice Thickness = 4 mm, single slice) with variable delay time and dynamic susceptibility contrast perfusion (FOV/Matrix = 220 mm/224, single shot, EPI, Fat Saturated, No. of slices = 5, Slice Thickness = 6 mm, TR/TE = 315/40, Flip angle = 75°, 200 time points). A gadolinium-based contrast agent (Multihance, Bracco, Princeton, NJ, USA) was injected followed by a saline flush (Gadolinium: 0.1 mmol/kg, single dose 3 ml at 2 ml/sec, saline: 20 ml at 2 ml/sec).

The MRI CBF maps were calibrated to yield quantitative CBF (in ml/100g/min) via the 'bookend technique' (Carroll et al. [2008]) with custom-made post-processing code in MATLAB 2021b (The Mathworks, Natick, MA). The Arterial Input Function (AIF) was chosen automatically before being fit to a gamma-variate model and CBF calibrated via steady-state CBV calculated from the pre- and post-DSC T1 maps (Carroll et al. [2003]). A water exchange correction factor was applied to account for intra-to-extravascular exchange (Shin et al. [2006]). Delay and dispersion corrections were implemented to mathematically synthesize a "local-AIF" to create a voxel-by-voxel local-AIF for deconvolution analysis. This method of calibration is accurate to 10% and has been validated against O-15 PET in carotid occlusion patient studies (Carroll et al. [2008], Vakil et al. [2013]) and neutron capture microsphere CBF measurements in canine middle cerebral artery occlusion (Jeong et al. [2019]).

3.3.1 Quantitative DSC Post-Processing

With DSC, contrast is injected via I.V. The rate of T2* change is proportional to Gd concentration, and the signal intensity is proportional to

$$S(t) = KH\left(1 - e^{-\frac{TR}{T1(t)}}\right)e^{-\frac{TE}{T2(t)}}.$$

With a long TR and TE, the signal intensity of the Spin Echo sequence becomes predominately T2-weighted, as $e^{-\frac{TR}{T1}} \to 0$, meaning

$$S(t) = S_0 e^{-\frac{TE}{T2(t)}}.$$

The gadolinium concentration [Gd](t) is proportional to the observed change in T2* relaxation rate, which we can solve for using the equation above.

$$[Gd](t) \propto \frac{1}{\Delta T2^*} = -\frac{1}{TE}\ln\left(\frac{S(t)}{S_0}\right)$$

Using this we can calculate perfusion parameters such as CBV, and CBF. Both require knowledge of the shape of the intravenous Gd bolus, or the arterial input function (AIF), after which signal is fit to appropriate mathematical models and parameters of interest are extracted.

The volume of blood in a voxel is proportional to the area under the tissue concentration curve during the first pass of contrast divided by the area under the pure blood curve. If this blood curve is taken from an artery and applied to the entire brain, it is global, i.e. $AIF_G(t)$.

$$rCBV \propto \frac{\int [Gd](t)dt}{\int AIF_G(t)dt}$$

To calculate blood flow, the tissue capillary bed can be modeled as a linear system and the AIF can be modeled as a sum of time-shifted and scaled dirac delta function inputs. The

fraction of injected Gd in the tissue at time t after the delta input is the residue function, $R(t)$. The width of $R(t)$ reflects the distribution of transit times through the tissue. As the AIF is not instantaneous, it is instead dispersed in time as a narrow curve. This curve can be represented as a set of dirac delta functions at different time delays, i.e. a convolution of the AIF with the residue function.

$$[Gd](t) = CBF \times AIF_G(t) \otimes R(t)$$

The AIF is chosen automatically, but there are two unknowns meaning the residue function scaled by CBF is determined by deconvolution via single value decomposition. Mean transit time (MTT), i.e. the average time a particle traveled through the tissue bed, can be calculated from the residual.

$$rCBF_{DSC} \propto max(CBF \times R(t))$$

$$MTT = \int R(t)dt$$

Absolute quantification in ml/100g/min with delay and dispersion corrections is then applied via the T1 bookend method. The DSC scan is bookend-ed by T1 mapping sequences which are used to reduce sensitivity of DSC to AIF selection. Steady-state CBV_{SS} is calculated using the pre and post T1 maps and used as a calibration factor.

$$qCBV_{SS} = \frac{\left(\frac{1}{T1_{post}} - \frac{1}{T1_{pre}}\right)_{tissue}}{\left(\frac{1}{T1_{post}} - \frac{1}{T1_{pre}}\right)_{blood}}$$

For measurement with two gadolinium injections on the same day two WCFs were determined to account for the residual gadolinium in the blood pool arising from these back-to-back perfusion scans (Shin et al. [2006]). The water exchange correction factor for first injection

(WCF_1) and for second injection (WCF_2) are functions of change in T1 of blood (R_1).

$$WCF_1 = 0.35\Delta R_1^2 + 0.11\Delta R_1 + 0.06$$

$$WCF_2 = 0.22\Delta R_1^2 + 2 \bullet 10^{-6}\Delta R_1 + 0.49$$

Combining these returns absolute quantitative $CBF(qCBF)$ in ml/100g/min.

$$qCBF = \frac{1}{\rho}\left(\frac{1 - Hct_{LV}}{1 - Hct_{SV}}\right) \bullet \left(\frac{qCBV_{SS,WM}}{rCBV_{DSC,WM}}\right) \bullet rCBF_{DSC} \bullet WCF_n$$

Here $rCBF_{DSC}$ is the relative CBF calculated from standard deconvolution of the voxel contrast curve deconvolved from the AIF, $rCBV_{DSC,WM}$ is the average relative white matter CBV from the DSC images, $qCBV_{SS,WM}$ as the average white matter steady-state CBV quantified using the T1 maps, and WCF as the water exchange correction factor. ρ is the average density of brain tissue (1.04 g/ml), and Hct_{LV} and Hct_{SV} are the hematocrit levels in large (0.45) and small vessels (0.25), respectively.

3.3.2 Delay and Dispersion Correction

Delay and dispersion effects correct for dispersion of the bolus as well as the delay of bolus arrival time to local voxels compared to the global AIF. Dispersion is corrected for by comparing the bolus shape of the AIF to that of venous outflow at the sagittal sinus.

$$VOF(t + t_D) = \frac{\alpha}{(t_D + 1)} e^{-\frac{\beta t}{t_D}} \otimes AIF_G(t)$$

t_D represents the delay time between global AIF and VOF while α, β are fit to capture dispersion effects. The local-AIF for every voxel with a delay of t_T is found by deconvolving

the global AIF and the residue function of the VOF using the fit parameters α and β.

$$AIF_{local}(t) = AIF_G(t) \otimes \frac{\alpha}{(t_T + 1)} e^{-\frac{\beta t}{t_T}}$$

To apply delay and dispersion correction effects to qCBF this $AIF_{local}(t)$ replaces the $AIF_G(t)$ in deconvolution via SVD for CBV_{DSC} and CBF_{DSC}. More detail regarding the local-AIF is included in Chapter 4.

3.3.3 Arterial Input Function (AIF), Venous Outflow, and White Matter

Global AIF was selected automatically based on simultaneous early arrival time, narrow bolus, and large area under the concentration curve (Carroll et al. [2003]). Local-AIF with delay and dispersion correction is calculated relative to the global AIF by comparing the global AIF to venous outflow measured at the sagittal sinus. The VOF was selected manually based on anatomic location and large T1 difference before and after contrast injection. White matter selection was performed manually based on anatomic location on T1 images and reviewed by an interventional neuroradiologist.

3.3.4 Diffusion Tensor Imaging

MR Diffusion Tensor Imaging (DTI) was taken on day 2 in 30-minute intervals from 1 to 4 hours post-occlusion to track infarct volume progression (FOV/Matrix = 224 mm/128, Slice Thickness = 2mm, TR/TE = 2993/83, *b*-values = 0, 800 s/mm2, 33 directions). Infarct volume was calculated applying an automatic threshold determined via leave-one-out cross-validation with infarct volume manually calculated by an interventional neuroradiologist.

3.4 Data Analysis

3.4.1 Regions of Interest

Eight anatomic regions of interest (ROIs) were drawn to capture average qCBF in 1) superior cortical, 2) middle cortical, 3) inferior cortical, and 4) deep grey nuclei on both hemispheres by a trained operator blinded to experimental group, infarction volume, collateral score, and blood pressure. The middle cortical ROI represents the region centered within the middle cerebral artery (MCA) territory, whereas the superior cortical and inferior cortical ROIs represents a mixed combination of MCA and adjacent anterior (ACA) and posterior (PCA) territories respectively. The deep portion represent deep gray nuclei from MCA, ACA and PCA territories. Separate ROIs shown in Fig. 3.5 were drawn on three consecutive 6 mm coronal slices starting at, and posterior to, the M1 segment relying on the proportional size of the brain sections to the whole brain slice, and any visible anatomical cues.

DTI and DSC were co-registered via Statistical Parametric Mapping (SPM12). Core infarct and penumbra ROIs were assessed via these co-registered mean diffusivity volumes from DTI to the corresponding DSC qCBF volumes acquired at 2.5 hours post MCAO. Infarcted voxels and corresponding infarct volume were calculated by an automatic threshold of $.57e-3mm^2/s$ validated by leave-one-out cross validation with an interventional neuroradiologist. ROIs were drawn to cover the entire MCA territory on the three consecutive 6mm coronal slices starting at, and posterior to, the M1 segment. Penumbra was calculated as the MCA territory that was diffusion negative on the co-registered mean diffusivity maps.

3.4.2 Pial Collateral Supply

Pial collateral recruitment was measured 30 min post-occlusion and prior to treatment by assessing arteriographic images (OEC9800; General Electric Healthcare, Chicago, IL, USA). The 11-point scoring system compares arteriographic images pre- and post-occlusion, with

a higher score representing more pial collateral recruitment distal to an occlusion, assessing transit time and reconstituted occluded MCA territory relative to the opacity of the jugular vein (Christoforidis et al. [2011]).

3.4.3 Statistical Analysis

Expected infarct growth was calculated via previously described nonlinear asymptotic model with $V(t)$ representing the expected volume growth at time t (Christoforidis et al. [2017]).

$$V(t) = \big[-2472.8 \times PCS + 342971 \big] \left(1 - e^{-(0.0179 - 0.0013 \times PCS)t} \right)$$

The parameters were previously derived as a function of pial collateral score (PCS) via linear regression and the resulting equation used to estimate final infarct volume and expected infarct growth as a function of pial collateral score.

The dependence of tissue qCBF on collateral score was assessed via separate linear regression analysis of mean ROI values for control and flow augmented (norepinephrine and hydralazine) experiments for the four anatomic ROIs, split by hemisphere. ROIs of core infarct and penumbra were similarly analyzed. For all ROIs drawn, difference in qCBF between treatment and control groups was compared, dichotomized by hemisphere and pial collateral score ($\geq$ 9 as "good" and $\leq$ 8 as "poor"), with absolute values, percent difference, and a two-sided Wilcoxon rank sum statistic assuming unequal variance. Relative CBF via 1) the ratio of the middle cortical territory of the ipsilateral hemisphere to the corresponding contralateral hemisphere and 2) via the ratio of the middle cortical territory of the infarct hemisphere to the baseline qCBF were also compared between treatment and control groups. All statistical analysis was written using Python 3.0 (Anaconda Software Distribution. Austin, TX, USA).

3.5 Results

3.5.1 Infarct Growth

The treatment effect was found to be dichotomized by collateral score. Infarct volumes and infarct growth were found to be significantly lower in subjects with collateral scores below 9, deemed "poor" collaterals. For subjects with collateral scores 9 and above, no statistical difference between experimental groups was found for final infarct volume.

A previous model predicting infarct growth over time as a function of collateral score was used to predict the expected growth without flow augmentation therapy (Christoforidis et al. [2017]). This is shown in Fig. 3.2 as dashed lines. With flow augmentation therapy, for poor collaterals shown in Fig. 3.2a, the curve is significantly altered, significantly reducing infarct development. Shown in Table 3.1b, infarct volume growth between 1 hours and 4 hours post-MCAO was found to be significantly lower than the predicted growth for the treatment group. For good collaterals shown in Fig. 3.2b, the infarct growth curve is already much shallower, and the infarct growth rate seems minimally affected. This is supported by Table 3.1b showing no significant difference between measured and predicted infarct growth was found for the control group.

This dichotomy of therapeutic outcome is supported by the infarct growth post-augmentation between treatment and control groups in Table 3.1a. For those with poor collaterals, there was a noted -35.7% drop in infarct growth compared to the control group, whereas for those with good collaterals there was a statistically insignificant 9.57% higher infarct growth compared to the control. This dichotomy suggests the influence of collateral supply on therapeutic outcome.

a) Comparison between Experimental Groups			
	PCS	Percent difference	p-val
Infarct growth	Poor (<9)	-35.7%	0.0008
	Good (>8)	+9.57%	0.83
b) Comparison to Predicted Growth			
	PCS	Wilcoxon rank sum	p-val
Treatment	Poor (<9)	-2.19	0.028
	Good (>8)	-1.15	0.25
Control	Poor (<9)	-1.14	0.25
	Good (>8)	-0.65	0.51

Table 3.1: a) Statistical analysis of infarct growth between treatment and control group dichotomized by collateral score. b) Statistical analysis of infarct growth of treatment and control groups compared to predicted values dichotomized by collateral score.

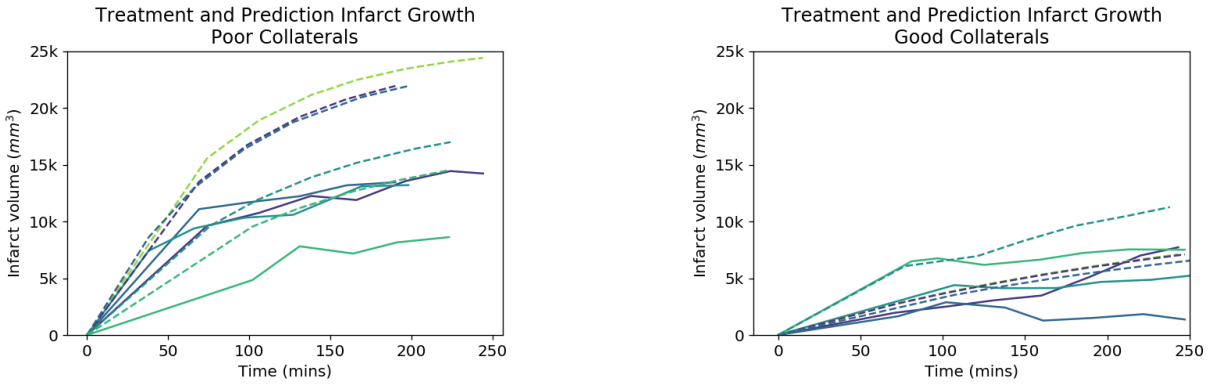

(a) (b)

Figure 3.2: Measured (solid) and predicted (dashed) Infarct growth post-MCAO dichotomized by collateral score.

3.5.2 Cerebral Blood Flow

Randomization into treatment and control groups prior to the determination of collateral score left four control and four experimental subjects with 'good' collaterals, and four control and three experimental subjects with 'poor' collaterals. Student's t-test in relevant subject parameters of treatment group vs. control group subjects returned no significant differences: collateral score (8.4±2.9 vs. 8.7±2.2, p = 0.82), age (4.3±4.2, 3.7±2.9, p = 0.79), weight (26.2±5.1, 25.8±3.3, p = 0.89), MAP (82±29, vs 84±20, p = 0.86), ETCo2 (36±11, 34±4.5, p = 0.63), and time between occlusion and start of the DSC scan (3.2±.9 vs. 2.7±.8, p =

0.48).

A representative qCBF image 2.5 hours post-MCAO for a treatment and control group subject with identical poor pial collateral scores is shown in Fig. 3.3b and Fig. 3.3c demonstrating a visual of flow augmentation. For qCBF of anatomic middle cortical territory, statistical analysis is shown in Table 3.2 and linear regression analysis of qCBF as a function of pial collateral score and experimental group for the anatomic middle cortical ROI split by hemisphere is shown in Fig. 3.5a-b. While the control group shows strong pial collateral dependence, treatment weakened the dependence of ipsilateral qCBF by raising the qCBF of poor pial collateral supply above the ischemic threshold threshold for cell death as defined by Jones et al. [1981], and lowering the qCBF of good pial collateral supply.

Linear regression analysis in inferior and superior cortical regions and deep portions, as a function of pial collateral score and group, is shown in Fig. 3.5. Contralateral to the occlusion we observe higher qCBF of superior cortical and inferior cortical regions in the treatment group compared to the control with poor collaterals (+74.4ml/100g/min (51%), t = 2.12, p = 0.16) and good collaterals (+152.5ml/100g/min (100.2%), t = 2.3, p = 0.02). A similar trend of increased qCBF on the contralateral side is observed in the deep portion (Fig. 3.5c) for both poor collaterals (+40.8ml/100g/min (50%), t = 1.77, p = 0.08) and good collaterals (+123.7ml/100g/min (109.5%), t = 2.02, p = 0.04). Distal to the occlusion, superior cortical and inferior cortical regions show non-significant higher qCBF with treatment of poorly collateralized subjects (+27.7ml/100g/min (59%), t = 1.4, p = 0.15) and good collaterals (+24ml/100g/min (24%), t = 1.2, p = 0.24). Deep portions show no statistically significant difference between control group and treatment group distal to the occlusion for poor collaterals (+.6ml/100g/min (3.3%), t = 0.0, p = 1.0) and good collaterals (+8ml/100g/min (18.5%), t = 0.5, p = 0.60).

Linear regression analysis of the core infarct and penumbra territories determined by DTI is shown in Fig. 3.6. Absolute and percent difference with Wilcoxon rank sum statistic of

qCBF only returned one p-value < 0.10: core infarct for good collaterals (+17ml/100g/min (70.1%), t = 1.9, p = 0.06). Large variability in other territories reduced statistical significance; penumbra for good collaterals (+8.2ml/100g/min (16.5%), t = 1.1, p = 0.24) and poor collaterals (+17.3ml/100g/min (53.1%), t = 1.1, p = 0.28), and core infarct for poor collaterals (+3.4ml/100g/min (21.5%), t = 0.71, p = 0.47). Evaluation of relative CBF (rCBF ratio of ipsilateral to contralateral middle cortical territory post-occlusion) is shown in Fig. 3.4 and Table 3.3. The ratio of qCBF post-occlusion to baseline CBF in the contralateral anatomic middle cortical region was on average 90% higher (t = 1.9, p = 0.05) for the treatment group compared to the control group, while the ratio post-occlusion to baseline CBF of the middle cortical region of the infarcted hemisphere was 72% higher (t = 1.6, p = 0.10) compared to the control group.

qCBF of Middle Cortical Territory						
	PCS	Control qCBF	Treatment qCBF	Percent difference	Wilcoxon rank sum	p-val
Ipsilateral	Poor (<9)	16.4±9.3	21.3±2.9	26.20%	1.06	0.22
	Good (>8)	48.4±7.5	36.3±11.5	-28.62%	-1.44	0.10
Contralateral	Poor (<9)	113.8±28.5	203.0±48.1	56.30%	1.77	0.08
	Good (>8)	75.1±20.5	250.8±114.5	107.20%	2.31	0.02

Table 3.2: Reports qCBF between control and treatment group for both core infarct and non-infarct MCA territory. It compares with percent difference of qCBF between treatment and control group and the Wilcoxon rank sum statistic, dichotomized by pial collateral score.

rCBF (ipsilateral/contralateral) of Middle Cortical Territory						
	PCS	Control rCBF	Treatment rCBF	Percent difference	Wilcoxon rank sum	p-val
Ratio (rCBF)	Poor (<9)	0.16±.12	0.11±.02	-34.60%	0.35	0.72
	Good (>8)	0.67±.10	0.18±.10	-113.20%	-2.31	0.02

Table 3.3: rCBF as ratio of core infarct territory to contralateral non-infarct MCA territory between control and treatment group dichotomized by pial collateral score, showing how the increase in contralateral perfusion with treatment may confound rCBF. Reproduced from "Augmentation of perfusion with simultaneous vasodilator and inotropic agents in experimental acute middle cerebral artery occlusion: a pilot study", Liu et al., 2022 with permission from BMJ Publishing Group Ltd.

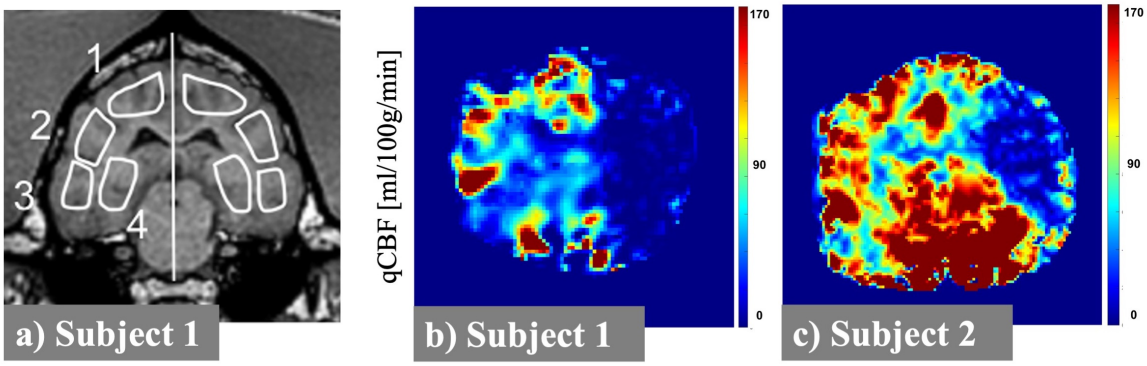

Figure 3.3: a) Representative image showing four labeled ROIs. The middle cortical ROI is shown labeled as ROI 2, while the inferior and superior cortical ROIs are labeled ROI 1 and ROI 3 respectively and contain potential penumbra. The deep grey nuclei portion is labeled ROI 4. Quantitative DSC perfusion maps of b) an example subject in control group with pial collateral score 5 (non-infarct qCBF of 90ml/100g/min, core infarct qCBF of 3.2ml/100g/min) and c) an example subject in treatment group with a matching pial collateral score 5 (non-infarct qCBF of 142.9ml/100g/min, core infarct qCBF of 18.7ml/100g/min). Subsequent infarct volume growth was 11,404mm^3 and 5,781mm^3 between 1hr and 4hrs post-occlusion respectively (both occlusions on the right side). Reproduced from "Augmentation of perfusion with simultaneous vasodilator and inotropic agents in experimental acute middle cerebral artery occlusion: a pilot study", Liu et al., 2022 with permission from BMJ Publishing Group Ltd.

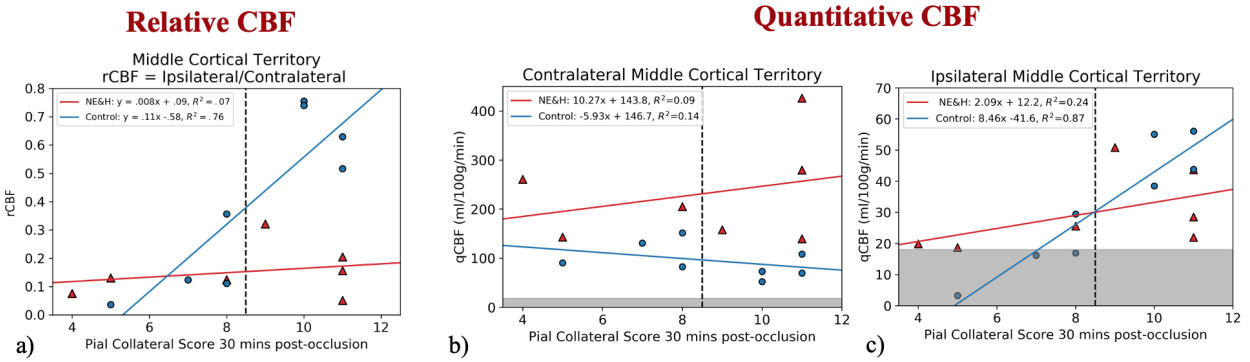

Figure 3.4: a) Linear regression of relative CBF as ratio of middle cortical ROI on the ipsilateral hemisphere to the mirrored region on the contralateral hemisphere (red: treatment, blue: control). Linear regression across collateral score for average quantitative CBF middle cortical territory b) contralateral to occlusion and c) ipsilateral to occlusion (red: treatment, blue: control). This represents qCBF from a middle cortical ROI, labeled ROI 2 in Fig. 3.3a. A black dotted line divides the pial collateral scores into those determined to be 'good' or 'poor' and a grey region represents values below the ischemic threshold 18ml/100g/min. Reproduced from "Augmentation of perfusion with simultaneous vasodilator and inotropic agents in experimental acute middle cerebral artery occlusion: a pilot study", Liu et al., 2022 with permission from BMJ Publishing Group Ltd.

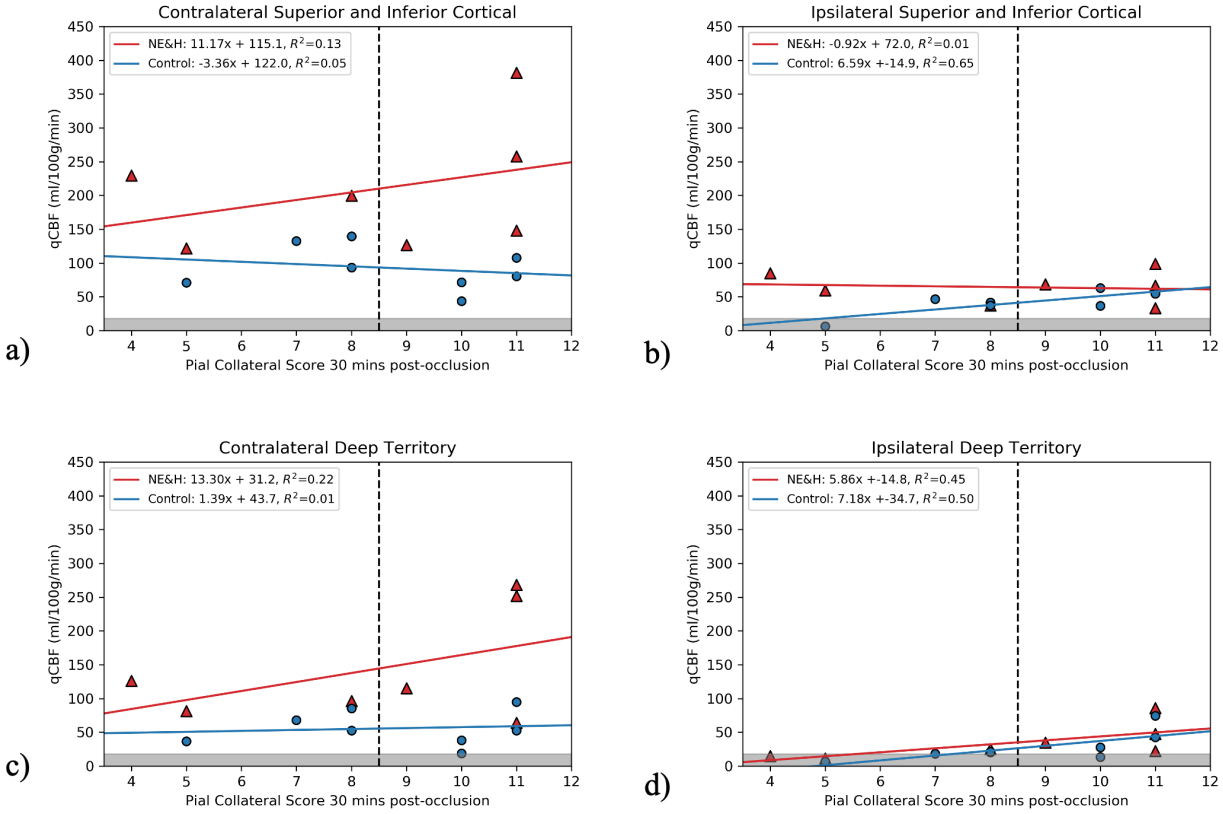

Figure 3.5: (a,b) Linear regression across collateral score for average qCBF of superior and inferior cortical regions on a) contralateral and b) ipsilateral hemisphere, labeled ROI 1 and 3 in Fig. 3.3a. (c,d) Deep territory label ROI 4 in Fig. 3.3a split into ROIs on c) contralateral and d) ipsilateral hemispheres (red: treatment, blue: control). Note that the deep territory is predominantly supplied by lenticulostriate end perforators without immediately available collaterals. A black dotted line divides the pial collateral scores into those determined to be 'good' or 'poor' and a grey region represents values below the ischemic threshold 18ml/100g/min. Reproduced from "Augmentation of perfusion with simultaneous vasodilator and inotropic agents in experimental acute middle cerebral artery occlusion: a pilot study", Liu et al., 2022 with permission from BMJ Publishing Group Ltd.

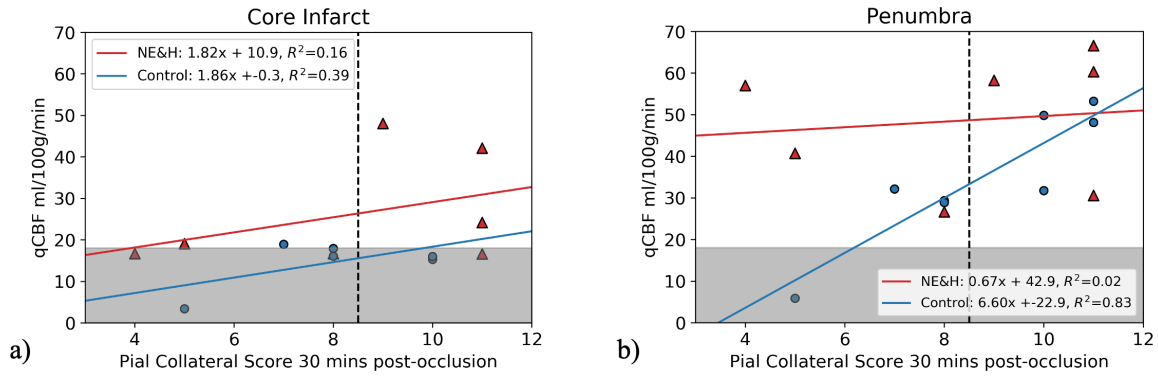

Figure 3.6: a) Linear regression of qCBF in core infarct ROI, b) linear regression of qCBF in penumbra ROI (red: treatment, blue: control). A black dotted line divides the pial collateral score into those determined to be 'good' or 'poor', and grey region represents values below the ischemic threshold 18ml/100g/min. Reproduced from "Augmentation of perfusion with simultaneous vasodilator and inotropic agents in experimental acute middle cerebral artery occlusion: a pilot study", Liu et al., 2022 with permission from BMJ Publishing Group Ltd.

3.6 Discussion

Results from this study show simultaneous administration of inotropic agent and vasodilators results in augmentation of tissue CBF in the unaffected brain hemisphere as well as distal to an occlusion for subjects with poor collateralization. The augmentation of perfusion to ischemic tissue depends on pre-treatment pial collateral recruitment and reduces collateral dependence of qCBF across all collateral scores. We see a paradoxical, decrease in qCBF distal to the occlusion in well-collateralized subjects, supporting the need for further study to understand the effects of therapies intended to mitigate (i.e., bridge) the effects of hypoperfusion in ischemic stroke. Our findings suggest that treatment via an inotropic agent and vasodilators dramatically increases perfusion distal to the occlusion in cases of poorly collateralized subjects. As such, this study provides a method of action for norepinephrine and hydralazine reducing the rate of infarction growth after arterial occlusion in subjects with poor collateral recruitment through the increase in blood pressure leading to an increase in CBF.

In Fig. 3.4a relative CBF shows a paradoxical decrease in rCBF with flow augmentation in red for both good and poor collaterals. This does not agree with the infarct growth curve outcomes shown in Table 3.1. Quantitative CBF in Fig. 3.4b provides an explanation for the paradoxical rCBF, as well as a method of action for the dichotomy of therapeutic outcome. qCBF shows that flow augmentation increased perfusion on the normal un-infarcted hemisphere, and this contralateral increase confounds the rCBF. This meant rCBF did not accurately represent the flow augmentation on the infarcted hemisphere. In Fig. 3.4c we can see a potential method of action for the dichotomy of the therapeutic outcome. Poor collaterals show an increase in qCBF above the ischemic threshold in grey, raising qCBF in potential penumbra and mitigating infarct growth. In comparison those with good collaterals show a decrease in qCBF but all still remain above the ischemic threshold, agreeing with the lack of effect.

In the middle cortical territory contralateral to the occlusion, the quantitative qCBF across all collateral scores is higher with treatment suggesting autoregulatory disruption in the normal hemisphere. Table 3.1a and Fig. 3.4c demonstrate that treatment of subjects with poor collateral supply may raise ipsilateral qCBF above the ischemic threshold despite a $p > 0.05$. The observation of increased perfusion provides a method of action for a significant -35.7% decrease in infarct growth (Saadat et al. [2020]) and reducing the gap between 'poor' and 'good' collaterals. Further, treatment has a paradoxical effect on qCBF in the middle cortical territory in subjects with good collateralization, with a -12ml/100g/min decrease ($p=0.10$) in qCBF distal to the occlusion despite a +175ml/100g/min increase ($p = 0.02$) in qCBF on the contralateral side. This supports studies that have shown trends of oxygen carrier treatment influencing reduction of ischemic growth to a greater extent for those who are fast evolvers (Christoforidis et al. [2021], Shazeeb et al. [2022]). The drop in ipsilateral qCBF and increase in contralateral qCBF for 'good' collaterals provides a method of action for the minor +9.57% increase in infarct growth (Saadat et al. [2020]), and may signify vascular steal (Conklin et al. [2010]). Reduction in linear dependence of qCBF on collateral score with treatment (Fig. 3.4) supports norepinephrine and hydralazine mitigating infarct evolution through increased MAP augmented collateral flow of poorly collateralized subjects and further demonstrates the influence of collaterals in stroke development and treatment.

Quantitative CBF in the ipsilateral superiors and inferior cortical territory showed a similar reduction in linear dependence on collateral score with treatment (Fig. 3.5a-b) and higher qCBF for poor collaterals in these cortical zones distal to the occlusion, though not significant as they are mixed ROIs composed of territories supplied by collaterals and ACA and PCA territories. Regression model fit returns minimal effect of norepinephrine and hydralazine in the ipsilateral deep portion, agreeing with this deep territory being predominantly supplied by lenticulostriate end perforators without immediately available collaterals (Fig. 3.5d), supporting flow augmentation treatment distal to the occlusion acting through

collateral flow.

Statistical analysis of quantitative CBF in core infarct and penumbra determined by DTI returns mixed results. While all dichotomized comparisons returned higher mean qCBF for treatment group, with a greater increase in penumbra qCBF for 'poor' collaterals, all but one returned $p > 0.10$. Factors contributing to this include imperfections in volumetric alignment of DSC and DTI and the highly variable size of core infarct and penumbra 2.5 hours post-occlusion as a function of treatment group and collateral score. As such, the anatomic ROIs may be a better measure of statistical difference as they are consistent sizes across all subjects and still represent influence of treatment on perfusion. Trends observed support previous studies (Saadat et al. [2020], Christoforidis et al. [2021], Shazeeb et al. [2022]) with linear regression show treatment group with a higher core infarct qCBF across all collateral scores (Fig. 3.6a) and higher penumbra qCBF for poor collaterals and minimal difference for good collaterals (Fig. 3.6b) with reduction in linear dependence of penumbra qCBF on collateral score.

The ratio of quantitative CBF post-occlusion to baseline CBF pre-occlusion is higher for the treatment group in both hemispheres, with lower augmentation and lower significance observed on the ipsilateral hemisphere. Given the comparison to both baseline of the prior day through rCBF, and comparison to qCBF of the control group on day two, autoregulation was disrupted by the administration of inotropic agent and vasodilators to some degree. Treatment with norepinephrine and hydralazine led to an average increase in mean arterial pressure (+34.5mmHg) with a greater increase with poor collaterals (+38.75mmHg) compared to good collaterals (+29.75mmHg). In comparison, controls showed a minor increase in mean arterial pressure (+4.88mmHg) with minimal difference between poor collaterals (+4.25mmHg) and good collaterals (+5.5mmHg). Autoregulation has been shown to be disrupted in collateral-dependent tissue resulting in qCBF varying directly with MAP (Muhonen et al. [1994], Muhonen et al. [1992], Smrcka et al. [1998], Dawson et al. [2003]). In this

study, treatment returned an average of higher MAP but only higher qCBF of the middle cortical territory for low collaterals. While perfusion to the ischemic penumbra during acute stroke is thought to be pressure dependent (Fischberg et al. [2000]), the use of pressor agents and vasodilatory treatment has been controversial and returned mixed results in clinical trials (Vitt et al. [2019]). This study suggests that an increase in CBF, and corresponding infarct growth mitigation, due to increased MAP and disruption of cerebral autoregulation with norepinephrine and hydralazine only occurs for subjects with poor collateralization. Although there was no MR evidence that autoregulatory disruption had a significant impact on the normal hemisphere, this study did not assess for any potential subsequent functional impact. In addition, the fact that CBF increased in both hemispheres may confound the assessment of relative cerebral blood flow in a clinical setting (Fig. 3.4c).

This study is not without limitations. There were variable times of qCBF during infarct growth with 2.5hrs post-MCAO being the only constant time available in all fifteen subjects, preventing study of temporal dynamics of quantitative CBF and infarct. Further, collateral score dynamics via conventional angiography could not be assessed simultaneously to MR imaging. However, work previously demonstrated expectation of infarct growth curve from this baseline collateral score, including expected infarct volume at 2.5hours post-MCAO. This study uses collateral score as a predictor of infarct growth prior to treatment and explores qCBF 2 hours later. In addition, intracranial pressure could have influenced perfusion and infarct growth and although care was taken to mitigate the influence of anesthetics used, the anesthetic strategy may have nonetheless influenced results. Furthermore, our population was predominately female so sex effects were not equally distributed and as in all dichotomous studies there is a chance of bias between treatment and control groups despite students t-tests returning no significant difference. Lastly, ideally the study would be extended to look at the inotropic and vasodilatory treatment effects individually. There are, however, prior studies that have evaluated the drugs individually and studying the drug for individual contributions

would have doubled the animal cohort raising AICUC concerns and being beyond the scope of the funded project.

3.7 Conclusion

We have now provided a potential method of action for novel flow augmentation therapy of acute ischemic stroke in a pre-clinical canine model, shown perfusion plays a role in dichotomy of subjects who may benefit from flow augmentation as "bridge therapy" and shown how quantitative MR perfusion in ml/100g/min may provide information that rCBF cannot, and its use in pre-clinical research. Pilot data from this study (Liu et al. [2022]) demonstrates that treatment with norepinephrine and hydralazine administered in the acute phase of ischemic stroke leads to an increase in cerebral perfusion to the ischemic zone only in subjects with poor collateralization and in the unaffected hemisphere in all subjects. Flow augmentation increased tissue qCBF above the ischemic threshold for cell death, confirming prior observations of reduced infarct growth and final infarct volume (Saadat et al. [2020]). However, a paradoxical decrease in qCBF was observed for subjects with good collateralization. Further, relative CBF was influenced by the variable effect on CBF by the collateral score in the normal hemisphere. As such, quantitative perfusion was a more reliable method of measuring augmented collateral blood flow as a biomarker of therapeutic efficacy, and other methods of flow augmentation should be evaluated as methods of minimizing infarct growth during the critical "door to needle" time for thrombolysis. In so far as a potential clinical relevance, findings from this study imply that the combination of vasodilator and inotropic reagent would only have a potential benefit is subjects with poor collateral recruitment in the early hours of cerebral ischemia.

CHAPTER 4

DELAY AND DISPERSION IN NEUROVASCULAR DISEASE

4.1 Introduction

As the cause of a stroke is vital to target therapy of the underlying stroke mechanism, development and assessment of diagnostic tests regarding their ability to differentiate between atherosclerotic plaque and other pathologies can improve treatment outcome. Further, infarct pattern such as watershed infarction, multiple cortical infarcts, and single deep infarct has therapeutic implications regarding response and recurrence. As such, as a technical note towards improving diagnostic images and patient outcome we compare reference standard single-photon emission computerized tomography (SPECT) perfusion to 1) standard dynamic susceptibility contrast (DSC) perfusion maps via $C(t) = AIF_G(t) \otimes R(t)$ and 2) local-AIF (AIF_L) DSC with delay and dispersion effects corrected via $C(t) = AIF_L(t - t_0) \otimes R(t)$ where t_0 represents the time-delay in arrival of the contrast bolus resulting from intracranial atherosclerotic disease (ICAD).

Standard DSC has been shown to overestimate perfusion deficit in stroke with correction of delay and dispersion effects reducing this overestimation (Demeestere et al. [2020], Jeong et al. [2019]). This suggests that the perfusion deficit observed with standard DSC may be due to the effects of blocked arteries in delaying and dispersing contrast agent as it travels through the vascular system. The effect of correcting for this overestimation by use of a local-AIF (Mouannes-Srour et al. [2012]) can be addressed by comparison of standard DSC and the local-AIF DSC to an imaging modality that does not involve bolus tracking such as SPECT. To avoid the inherent bias this study compares standard DSC and local-AIF DSC to SPECT by quantifying asymmetry in automatically segmented vascular territories of the brain (Chatterjee et al. [2015]). Analysis of agreement in subject-wise affected and unaffected territories, determined by a neuroradiologist blinded to perfusion images, allows quantitative

comparison of perfusion asymmetry with and without expected delay and dispersion effects. The effect of the local-AIF was compared to Tmax maps to explore if Tmax was related to the delay and dispersion effects of bolus dynamics. Comparison of asymmetry to SPECT for standard and local-AIF corrected DSC will demonstrate if overcall of perfusion deficit can be reduced for improved diagnosis.

4.2 Materials and Methods

4.2.1 Subjects and Image Acquisition

Presented are preliminary results from an ongoing study involving intracranial hemodynamics with 7 subjects with ICAD scanned for participation in a research study with SPECT and GBCA MR perfusion. This study was performed in accordance with protocols approved by the University of Chicago Medicine institutional review board. Subjects were brought to the hospital for a one day study with SPECT and MRI images acquired back-to-back. All subjects underwent SPECT, DSC, and anatomic T1 imaging protocols. DSC was post-processed into both standard DSC and local-AIF DSC (Jeong et al. [2019]). T1 anatomic scans were co-registered to volumetric vascular segmentation templates (Fig. 4.3) with code developed in-house (Chatterjee et al. [2015], MATLAB [2022]). The SPECT and DSC volumes were co-registered (SPM12 [2022]) to allow the vascular segmentation maps to be automatically applied to the perfusion maps for automatic vascular segmentation. These vascular segments on each side include the middle cerebral artery (MCA) inferior division, MCA superior division, M1 perforator, combined MCA superior and inferior, total MCA territory, posterior cerebral artery (PCA), anterior cerebral artery (ACA), basilar, and hemispheric. A neuroradiologist blinded to both MRI and SPECT perfusion images, interpreted MRA, DWI, T2 and FLAIR results and assigned each of the vascular territories to either be likely 'affected' or 'unaffected' at the time of imaging.

4.2.2 Single-Photon Emission Computed Tomography (SPECT)

Data in this study was acquired with the existing clinical single-photon emission computerized tomography (SPECT) perfusion protocol in Nuclear Medicine of the University of Chicago Medical Center. 25mCi of Tc-99mm exametazime tracer (HMPAO: Ceretec) was injected via IV in the antecubital vein and SPECT scanning run 30 minutes after. Images were acquired with GE Discovery 670 Pro dual head SPECT/CT with CT used for attenuation correction. Reconstructions were done by GE Xeleris version 4, and patient motion was reduced by co-registration (SPM12 [2022]).

SPECT is a form of low-resolution nuclear medicine tomographic imaging in which a gamma-emitting radioisotope is injected into the blood stream. Emissions from the radionuclide indicate capillary blood flow in the tissues. Projections are acquired from multiple angles and tomographic reconstruction can be used to return a 3D volume. As SPECT is performed following injection of a lipophilic radiopharmaceutical with minimal washout, CBF is not affected by delay and dispersion of the bolus and imaging. This makes it independent of the arrival time of the bolus kinetics, i.e. AIF-independent.

4.2.3 Standard DSC

Quantitative MR perfusion scans were acquired on a 3T MRI (Achieva, Philips) using a T1-bookend dynamic susceptibility method. The scan protocol consisted of a 2D EPI Look-Locker inversion recovery (FOV/Matrix = 220 mm/224, Slice Thickness = 4 mm, single slice) with variable delay time and dynamic susceptibility contrast perfusion (FOV/Matrix = 220 mm/224, single shot, EPI, Fat Saturated, No. of slices = 25, Slice Thickness = 4 mm, TR/TE = 1618/40, Flip angle = 75°, 60 time points). A gadolinium-based contrast agent (Multihance, Bracco, Princeton, NJ, USA) was injected followed by a saline flush (Gadolinium: split dose 0.05mmol/kg 3 ml at 2 ml/sec, saline: 20 ml at 2 ml/sec).

The MRI CBF maps were calibrated to yield quantitative CBF (ml/100g/min) via the

'bookend technique' (Carroll et al. [2008]) with custom-made post-processing code in MATLAB 2021b (The Mathworks, Natick, MA). The global AIF_G was chosen automatically before being fit to a gamma-variate model and CBF calibrated via steady-state CBV calculated from the pre- and post-DSC T1 maps (Carroll et al. [2003]). A water exchange correction factor was applied to account for intra-to-extravascular exchange (Shin et al. [2006]), and patient motion was reduced by co-registration (SPM12 [2022]) prior to post-processing.

4.2.4 Local-AIF DSC

Delay and Dispersion correction as described previously in Section 3.3.2 is a method of changing the global AIF into a local-AIF when post-processing DSC into quantitative perfusion. When contrast is injected via IV, it enters the blood stream and travels through the heart and lungs, finally to the circle of Willis before perfusing the brain. This means that perfusing contrast is not instantaneous and instead, it enters the brain through the arteries branching off the circle of Willis, such as the middle cerebral artery. The bolus of contrast agent, a surrogate of unit impulse of blood flow, enters the brain through these arteries and its shape represents an average or "global arterial input function". This can be mathematically represented a series of dirac delta functions, as mentioned in Section 3.3.2. When there is an occlusion of a major artery, blood will have to travel around the occlusion to reach the infarcted hemisphere as shown in Fig. 4.1. This means that the global arterial input function will no longer accurately represent the input to the tissue; the delay and the added dispersion as blood and contrast travel around the occlusion must be taken into account. Our delay and dispersion algorithm corrects for the time-delay associated with the greater path length that the global AIF must take, and the additional dispersion of the shape of the unit impulse resulting from the same path length.

Continuing from the previous section Eq. (3.3.1) $[Gd](t) = CBF \times AIF_G(t) \otimes R(t)$ is used with standard DSC. If contrast could be instantaneously injected into all of the tissue,

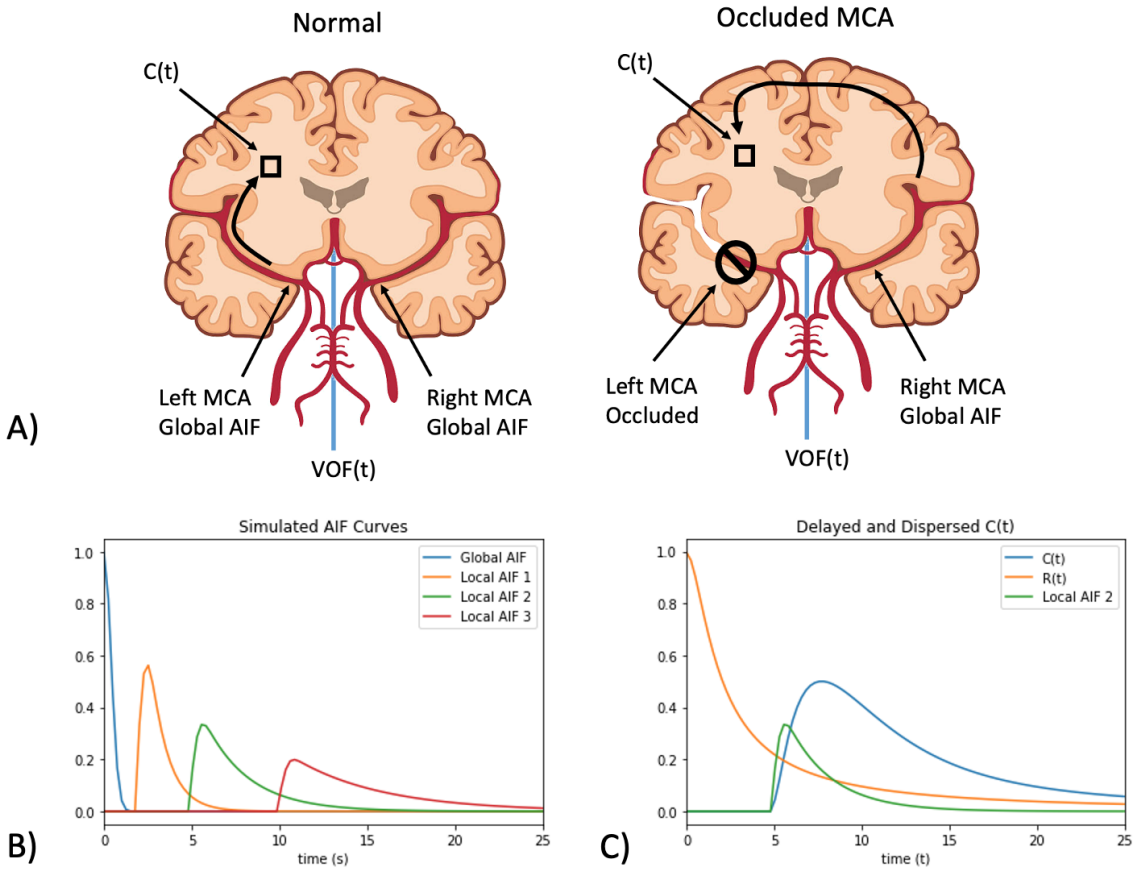

Figure 4.1: Demonstration of Delay and Dispersion effects. A) comparison of blood pathway through the brain from the MCA for a normal (left) and an occluded (right) MCA. B) Examples of simulated local-AIF curves with increasing delay and increasing dispersion. These would be local-AIFs for voxels increasing distances from the normal hemisphere in A). C) The effect of a delayed and dispersed local-AIF on a contrast curve. If one assumed the global AIF and deconvolves the contrast curve C(t), the Residue function R(t) would be artificially delayed and dispersed due to the lack of correction.

avoiding the dispersion effects of the circulatory system, the contrast curve of $\Delta T2^*$ would match the residue function $R(t)$ because AIF_G would be a delta function. Instead, AIF_G is the extended dispersion from the contrast injection via IV to the head. With an occlusion, this AIF_G is further delayed and dispersed by the blocked cerebral artery. This means that $C(t)$ is no longer the residue function convolved by the global AIF_G, but must take into account time shift and further dispersion of the contrast as it traveled through the brain

tissue.

Delay is calculated by a timeshift operator. The local-AIF feeding a voxel with contrast curve $C(t)$ is temporally delayed from the global AIF, as shown in Fig. 4.1B.

$$C(t) = AIF_G(t - \Delta t) \otimes R(t)$$

Dispersion of the contrast agent as it travels through the tissue will lead to a broader local-AIF, also shown in Fig. 4.1B. This dispersion as it travels through the brain will lead to a broader measured contrast curve $C(t)$ that is independent of perfusion in the voxel and instead dependent on the path length that the bolus followed from the global AIF. To correct for this artificial extending of the curve, a local-AIF is estimated. This is done by comparing the bolus shape of the AIF to that of venous outflow at the sagittal sinus (VOF).

$$VOF(t + t_D) = \frac{\alpha}{(t_D + 1)} e^{-\frac{\beta t}{t_D}} \otimes AIF_G(t)$$

t_D represents the delay time between arrival of the global AIF and VOF while α, β are fit to capture the corresponding dispersion effects as the contrast has travelled through the entire brain. These α and β curves are a function of time, meaning a voxel closer to the global AIF will have a local-AIF that is less dispersed than a voxel closer to the sagittal sinus outflow, as expected. Convolving the delayed global AIF by the dispersion $\frac{\alpha}{(t_D+1)} e^{-\frac{\beta t}{t_D}}$ will return a local-AIF with both delayed and dispersion effects. This will return the mathematical equation for the contrast curve $C(t)$ with delay and dispersion effects.

$$
\begin{aligned}
C(t) =& AIF_{local}(t-\Delta t) \otimes R(t) \\
& AIF_{local}(t-\Delta t) = AIF_G(t-\Delta t) \otimes \frac{\alpha}{(\Delta t+1)} e^{-\frac{\beta t}{\Delta t}} \\
[Gd](t) =& CBF_{DD} \times AIF_{local}(t) \otimes R(t)
\end{aligned}
$$

To apply delay and dispersion correction effects to qCBF, this local $AIF_{local}(t)$ replaces the $AIF_G(t)$ in deconvolution via SVD for CBV_{DSC} and CBF_{DSC}. In this study local-AIF with delay and dispersion correction is calculated relative to the global AIF by calculating the dispersion by comparing the global AIF to venous outflow measured at the sagittal sinus. The VOF was selected manually based on anatomic location and large T1 difference before and after contrast injection. White matter selection was performed manually based on anatomic location on T1 images. Not performing this correction may lead to an overestimate of perfusion deficit on the ipsilateral side, an overestimation of hemispheric asymmetry, and false hypoperfusion (Jeong et al. [2019]). Therefore, for a voxel in a certain region, the CBF is now deconvolved from an AIF that has delay and dispersion correction to account for the contrast travelling from the global AIF to the location of the voxel. An example of the influence of using a local-AIF and correcting for the delay and dispersion of contrast agent injection is shown in Fig. 4.2.

4.2.5 Automatic Vascular Territories

For comparison of vascular territory asymmetry, all perfusion images were coregistered. SPECT was resized to match DSC perfusion images by volumetric overlay written in-house (MATLAB [2022]) to ensure correct rotation and FOV before being converted to nifti format and automatically co-registered (SPM12 [2022]). The DSC perfusion image was coregistered to the anatomic T1 map and then the anatomic image was normalized to Montreal Neu-

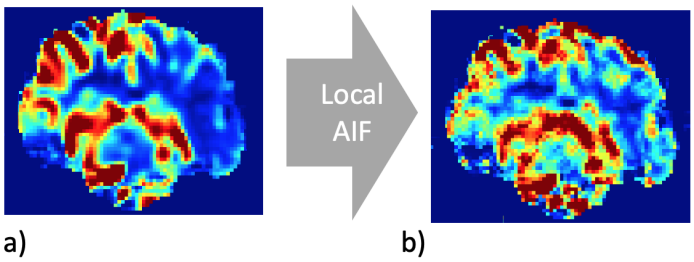

Figure 4.2: An example of perfusion calculated first with a global AIF (a) and a local-AIF (b) in a canine post-MCAO. The global AIF returns a larger perfusion deficit that Local-AIF correction shows to be false hypoperfusion. c) Examples of simulated curves with increasing delay time and their corresponding shift and dispersion

rological Institute (MNI) space for coregistration via (SPM12 [2022]), used to approximate a brain that is representative of the general public. Then the automatic vascular territory template developed by Chatterjee et al. [2015] was applied unsupervised to return average individual vascular territory values. No parameters of automatic vascular segmentation were changed between subjects. Territory maps were visually inspected for each subject to ensure reasonable location. These vascular segments on each side include the middle cerebral artery (MCA) inferior division, MCA superior division, M1 perforator, combined MCA superior and inferior, total MCA territory, posterior cerebral artery (PCA), anterior cerebral artery (ACA), basilar, and hemispheric. An example of the vascular territory template in MNI space used for automatic generation of subject-specific vascular territory maps is shown in Fig. 4.3. A neuroradiologist blinded to perfusion images labeled each of the vascular territories on a subject-wise basis as 'affected' or 'unaffected'.

From the territory map, average perfusion was computed for each vascular territory and asymmetry was calculated as contralateral/ipsilateral in which the further the asymmetry is from 1 the greater the perfusion deficit in that territory. The theoretical normal asymmetry index is 1.0. The extent of asymmetry was therefore calculated as contralateral/ipsilateral - 1.0.

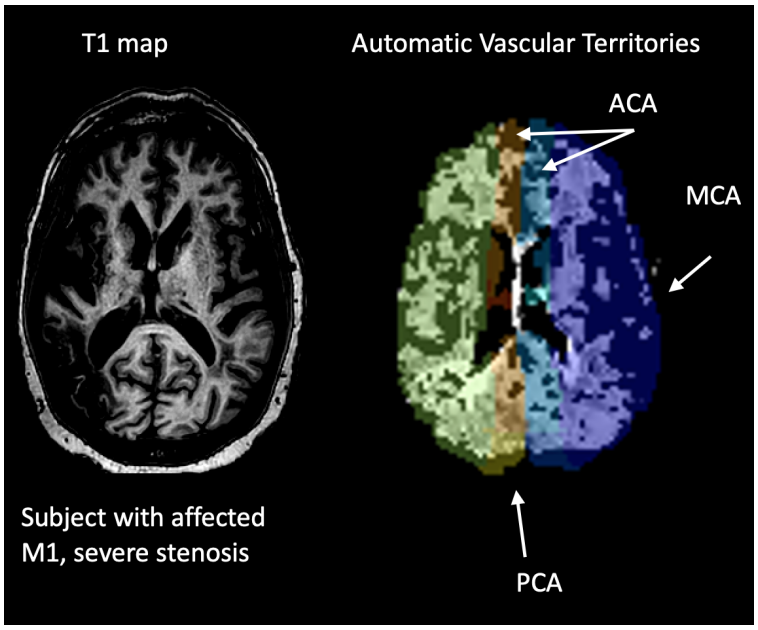

Figure 4.3: An example of the vascular territory template (in MNI space) used for automatic vascular segmentation (Applied template adapted from Chatterjee et al. [2015]).

4.2.6 Data Analysis

For each subject, asymmetry was calculated for the automatically segmented vascular territories and labeled as likely to be 'unaffected' or 'affected' in accordance with the neuroradiologist. Asymmetry (ratio of contralateral/ipsilateral vascular territories) of affected and unaffected territories was compared to SPECT for standard DSC and local-AIF DSC. Asymmetry of vascular territories for each patient were calculated, averaged, and shown as heat maps. The extent of the asymmetry (contra/ipsi - 1.0) was compared via percent error to SPECT of standard DSC and local-AIF DSC and the difference in asymmetry extent analyzed via Wilcoxon signed-rank within the affected and unaffected territory labels. A mixed effects model was applied to the asymmetries with modality as fixed effects and patient and region nested as random effects. Bland-Altman analysis was applied to all territories and all subjects.

The local-AIF effect was calculated on a pixel-by-pixel basis as the difference between the local-AIF and standard DSC. Asymmetry of this effect was calculated for vascular territories and compared to Tmax asymmetry via Wilcoxon signed-rank, Bland-Altman analysis, and a mixed effects model. Tmax in affected territories to Tmax in unaffected territories was analyzed with Wilcoxon Rank Sum. The same analysis was applied for local-AIF effect in affected and unaffected territories.

4.3 Results

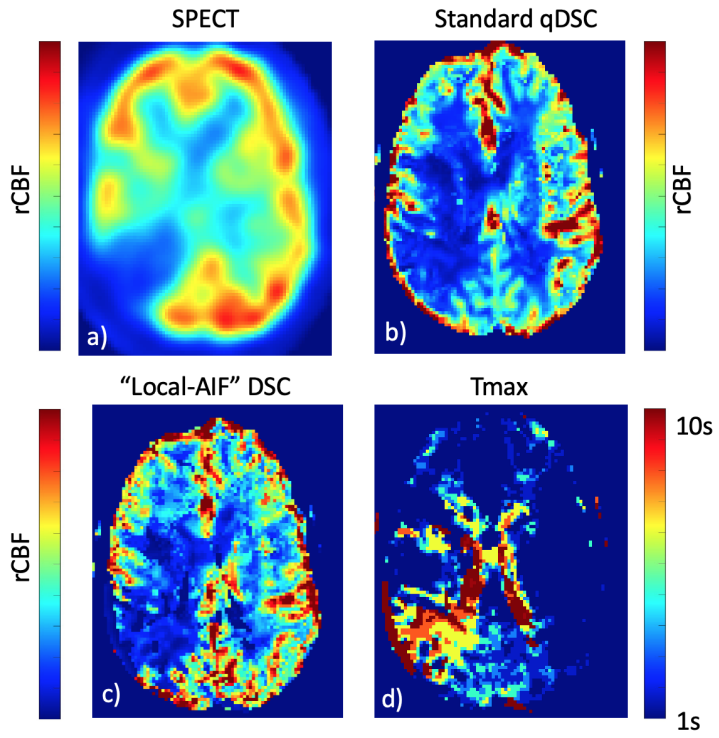

Figure 4.4: Example slice from three perfusion methods: a) relative SPECT, b) standard DSC, c) local-AIF DSC, and d) Tmax of one example case with severe stenosis on left M1 MCA and A2 ACA. In this example affected territories returned SPECT asymmetry of 1.33, standard DSC asymmetry of 1.57, and local-AIF DSC asymmetry of 1.34. This shows a case in which the local-AIF led to much better agreement in the affected territory.

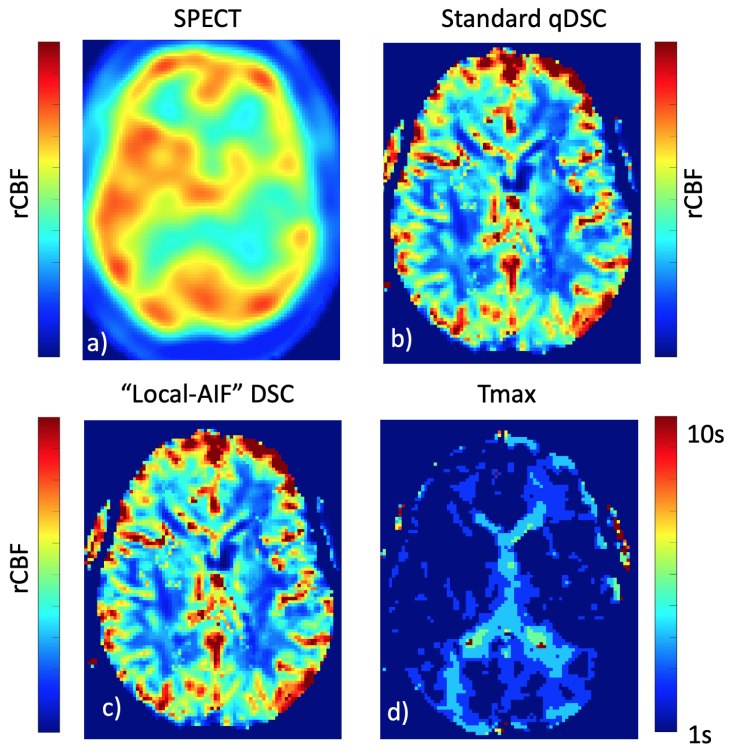

Figure 4.5: Example slice from three perfusion methods: a) relative SPECT, b) standard DSC, c) local-AIF DSC, and d) Tmax of one example case with no significant steno-occlusive lesion, but multifocal mild narrowings in the anterior circulation. In this example affected territories returned SPECT asymmetry of 1.06, standard DSC asymmetry of 1.21, and local-AIF DSC asymmetry of 1.17. This shows a case in which the local-AIF had a minor effect, though Tmax showed no lesion.

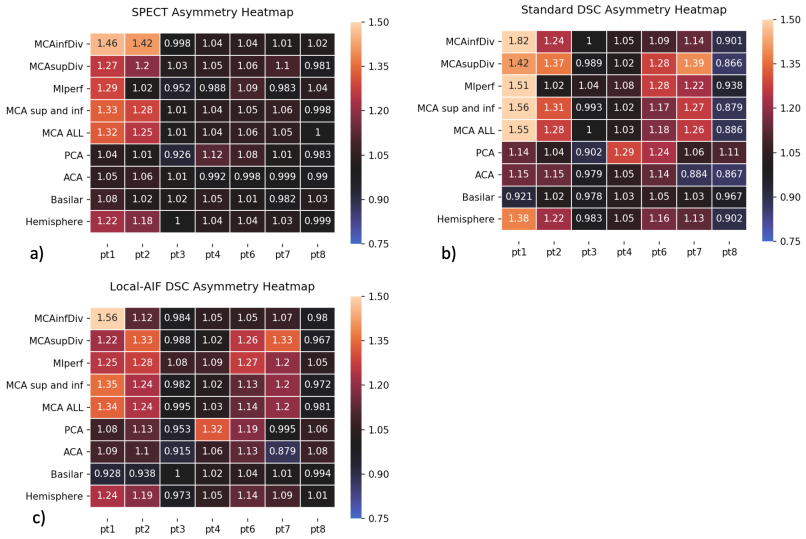

Figure 4.6: Heatmaps of perfusion asymmetry (contralateral/ipsilateral) from a) SPECT, b) standard qDSC, and c) local-AIF DSC in vascular territories for each case. Note: Asymmetry in second column in a-c corresponds to the case shown in Fig. 4.4.

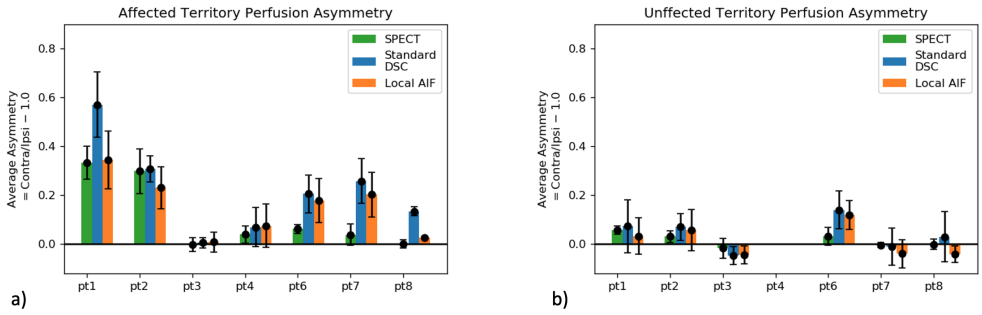

Figure 4.7: a) Plot of average asymmetry per subject as contralateral/ipsilateral - 1.0 across a) affected vascular territories and b) unaffected territories for each case.

All Vascular Territories	Absolute Difference [Percent error]	Wilcoxon signed-rank
Standard DSC:	+0.08 [+111.72%]	304.0, p = 0.000001
Local-AIF DSC:	+0.04 [+45.6%]	630.0, p = 0.01
Affected Vascular Territories	Difference [Percent error]	Wilcoxon signed-rank
Standard DSC:	+0.11 [+101.73%]	61.0, p = 0.0001
Local-AIF DSC:	+0.04 [+42.9%]	146.0, p = 0.027
Unaffected Vascular Territories	Difference [Percent error]	Wilcoxon signed-rank
Standard DSC:	+0.03 [+158.15%]	57.0, p = 0.21
Local-AIF DSC:	-0.002[-12.48%]	82.0, p = 0.88

Table 4.1: Affected and unaffected vascular territories compared to SPECT across all subjects. E.g. Asymmetry effect of average standard DSC of the affected vascular territories was +.11 higher than the average SPECT of those same affected vascular territories with statistical significance at the $p = 0.01$ level.

Mixed Model	Mean Intercept [95% CI]	Mean Slope [95% CI]	Bland-Altman [95% CI]
Standard DSC:	-0.301 [-0.595, 0.007]	1.331 [1.062, 1.600]	0.054 [-0.179, 0.290]
Local-AIF:	0.227 [-0.031, 0.485]	0.819 [0.580, 1.057]	0.033 [-0.153, 0.219]

Table 4.2: Mixed Effects model and Bland-Altman analysis with modalities as fixed effects. E.g. SPECT and standard DSC asymmetry across all territories returned mixed model mean intercept of -0.301 and mean slope 1.33 with a mean difference of asymmetry of 0.054.

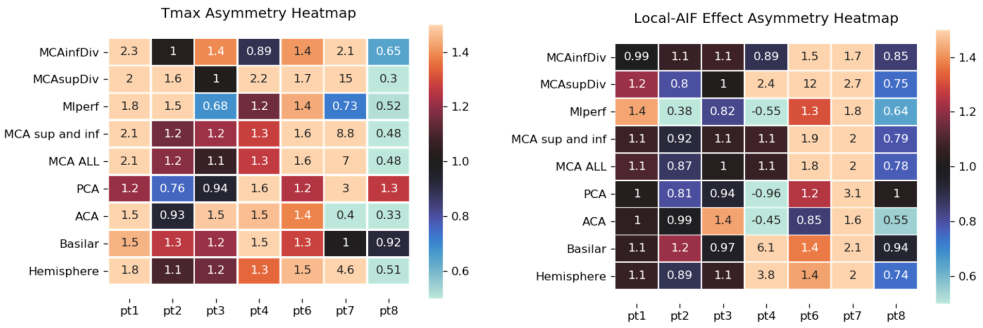

Figure 4.8: Heatmaps of asymmetry (ipsilateral/contralateral) from a) Tmax and b) local-AIF effect (local-AIF DSC − standard DSC) in vascular territories for each case.

Local-AIF effect compared to Tmax	Percent error	Wilcoxon signed-rank
All Vascular Territories:	-18.22%	733.0, p = 0.060
Affected Vascular Territories:	-23.88%	108.0, p = 0.031
Unaffected Vascular Territories:	-0.49%	52.0, p = 0.650

Table 4.3: Local-AIF effect (pixel-wise difference between local-AIF DSC and standard DSC CBF) compared to Tmax in affected and unaffected vascular territory by asymmetry. E.g. Average asymmetry of the local-AIF effect was -23.88% lower than Tmax asymmetry in the affected territories, though it is not a statistically significant difference at the $p = 0.01$ level.

Affected vascular territory compared to unaffected	Percent difference	Wilcoxon Rank Sum
Tmax:	29.26%	-2.06, p = 0.039
Local-AIF effect:	50.41%	-1.40, p = 0.161

Table 4.4: Affected territories compared to unaffected vascular territories for local-AIF effect and Tmax asymmetry E.g. Tmax in the affected territory was +29.26% higher than Tmax in the unaffected territory, though it is not a statistically significant difference at the $p = 0.01$ level.

Mixed Model	Mean Intercept [95% CI]	Mean Slope [95% CI]	Bland-Altman [95% CI]
Local-AIF effect:	-0.574 [0.140, 1.008]	0.223 [-0.066, 0.512]	-0.390 [-1.74, 0.964]

Table 4.5: Mixed Effects model and Bland-Altman analysis with modalities as fixed effects. E.g. Tmax and local-AIF asymmetry across all territories returned mixed model mean intercept of-0.574 and mean slope 0.223 with a mean asymmetry difference of -0.390.

4.4 Discussion

DSC bolus kinetics corrected with a local-AIF showed stronger agreement with SPECT in affected vascular territories of the brain regarding asymmetry of vascular regions in 7 ICAD patients. This effect was not statistically significant in unaffected territories, supporting DSC overcall of perfusion deficit being in part due to delay and dispersion of bolus arriving in affected territories. DSC with a local-AIF may function better for imaging perfusion asymmetry in intracranial stenosis, and Tmax and delay and dispersion effects are not easily untangled.

Shown in Table 4.1 standard DSC asymmetry was higher than SPECT across all vascular territories, affected or not, at the $p = 0.01$ level, agreeing with previous studies (Demeestere et al. [2020]). Correction with a local-AIF reduced the average asymmetry of all territories, an example of which can be seen by eye in Fig. 4.4 leading to no statistically significant difference from SPECT at the $p = 0.01$ level, though not at the $p = 0.05$ level. Heatmaps in Fig. 4.6 show these asymmetries across subjects per vascular territory. Standard DSC asymmetry in Fig. 4.6b is higher than SPECT asymmetry in Fig. 4.6a, while Fig. 4.6c shows that correction with a local-AIF will return patterns closer to those shown in the SPECT heatmap.

Table 4.2 shows the complexity of comparison of all combined vascular territories, and the subject-wise dependence of the local-AIF effect. The location, severity, extent of vascular territories affected, and cause of perfusion deficit will effect the influence of a local-AIF correction. Across all subjects, use of the local-AIF nearly halved the Bland-Altman mean

asymmetry difference compared to SPECT from 0.054 for standard DSC to 0.033 and returned a mean slope closer to unity and mean intercept closer to zero, though both are marginal effects.

Separation into affected and unaffected vascular territories makes the correction clearer; the local-AIF correction effect is predominately in vascular territories labeled 'affected' by the blinded neuroradiologist. Standard DSC overestimated perfusion deficit +0.11 compared to reference standard SPECT with statistical significance at the $p = 0.01$ level in the affected territory. Correction with a local-AIF DSC reduced this overcall to a non-significant +0.04 difference in average asymmetry effect at the $p = 0.01$ level. The unaffected vascular territories show no statistically significant difference between the three measurement types, supporting the perfusion deficit overcall of standard DSC being due to bolus delay and dispersion on the ipsilateral hemisphere.

The study of Tmax and the local-AIF effect (i.e. the difference in perfusion between standard and corrected DSC) is shown in Table 4.3. Most notable is that while the local-AIF effect is on average lower than the Tmax asymmetry, no comparisons return statistical significance at the $p = 0.01$ level. That is, Tmax shows on average greater asymmetry in affected territories than the local-AIF correction can account for but it is not a statistically significant difference. This suggests that Tmax asymmetry in affected territory are not statistically significantly different from effects due to delay and dispersion. Tmax and the local-AIF effect show minimal difference, no statistical significance, in unaffected territories confirming the expectation that both are negligible in those regions. This agrees with the hypothesis that Tmax is influenced by delay and dispersion of pial collateral supply, and correction of this delay and dispersion with a local-AIF will agree better with AIF-independent perfusion..

However, comparing the affected and unaffected territories in Table 4.4, Tmax shows the delay of blood arrival and would be expected to be higher in affected territories that is

statistically significant at the $p = 0.05$ level, though not the $p = 0.01$ level. The local-AIF effect has a non-significant +50.41% percent difference ($p = 0.16$). Mixed model regression in Table 4.5 shows weak correlation between Tmax and local-AIF effect. This also suggests the Tmax is not completely removed by local-AIF corrected delay time. When examining if the local-AIF effect matched Tmax asymmetry patterns, shown in Fig. 4.8, the local-AIF effect asymmetry is smaller than Tmax asymmetry. While local-AIF effect may add to the calculated Tmax, this demonstrates that Tmax and delay and dispersion effects are not easily untangled. Further study of lesion ROIs and surrounding territory may increase the statistical significance of these smaller effects.

There are several limitations of the present study. The small sample size of a complex and variable disease with subtle perfusion abnormalities complicates statistical comparison. It is further limited by the automatic vascular territories used for avoidance of bias; if this analysis was run on specifically the subject-wise lesion and surrounding territory at risk there is likelihood for more prominent effects. Beyond the small preliminary study size, the lesion size relative to vascular territory volume would also effect this significance. In future work this could be minimized by lesion-specific analysis of asymmetry or comparison of lesion volume calculated based on automatic asymmetry thresholds.

4.5 Conclusion

DSC bolus kinetics corrected with a local-AIF showed stronger agreement with SPECT in affected vascular territories of the brain regarding asymmetry of vascular regions in 7 ICAD patients. This effect was notable in affected territories, supporting DSC perfusion deficit overcall being in part due to delay and dispersion of bolus arriving in affected territories. When this delay and dispersion is corrected for with a local-AIF, the affected territories more closely match SPECT asymmetry, though the effect was varied among individuals. While observable trends are seen between the local-AIF effect and Tmax asymmetry, and this delay

and dispersion effect may influence the calculated Tmax, their asymmetry patterns show different patterns though lack of lesion-specific analysis reduces the statistical significance. DSC with a local-AIF may function better for imaging perfusion asymmetry in intracranial stenosis, and the relation between Tmax and delay and dispersion effects are not easily untangled.

CHAPTER 5

DIFFUSION IN MRI

5.1 Diffusion Overview

Molecular diffusion refers to the motion of a molecule in a fluid that is randomly displaced due to thermal energy. The human brain is highly heterogeneous with various architecture and tissue diffusivity. The movement of water in the brain due to diffusion is therefore impeded by compartmental boundaries. Imaging diffusion of water in the brain can be used to differentiate between tissue types, image tissue structure, and examine pathology.

There are two main types of diffusion MRI: Diffusion Weighted Imaging (DWI), and Diffusion Tensor Imaging (DTI). DWI only takes into account the average speed of diffusion in a region by its diffusion coefficient (Apparent Diffusion Coefficient, or ADC) while DTI constructs tensors that include diffusivity (i.e. rate) and directionality with 3D diffusion probability density functions. The tensors can return useful information such as Mean Diffusivity (MD) and Fractional Anisotropy (FA). MD is the average diffusion coefficient D per voxel and represents information about overall tissue integrity, or how fast fluid is diffusion. FA gives a value to indicate how elongated the diffusion ellipsoid is, i.e. how anisotropic it is, or how directional the diffusion is. DTI is useful for highly detailed structural imaging, while DWI is used most commonly in clinical pathology being able to differentiate tumors and necrosis. The main benefit of DWI is the speed of the imaging sequence, which is of extreme importance for the imaging of acute stroke, with more detail in Section 5.4 and Appendix B.

5.2 Diffusion Physics

5.2.1 Derivation of Diffusion Equation

Diffusion MRI uses the diffusion coefficient D, either estimating it in DWI or calculating a directional probability tensor in DTI. The meaning of this diffusion coefficient can be derived from Fick's first law of diffusion,

$$\vec{J} = -D\nabla\psi,$$

where $\vec{J}$ is the flux density, D is the diffusion coefficient, and $\nabla\psi$ is the concentration gradient. Derivation of Fick's second law predicts how diffusion will cause concentration $\nabla\phi$ to change over time. In 1D for simplicity we know from conservation of mass that

$$\frac{\partial}{\partial x}\vec{J} = -\frac{\partial\psi}{\partial t}.$$

This means that the flux density, or the substance flowing through a given area per unit time over time must be equal to the negative of the change in concentration over time. Plugging in Fick's first law we get

$$\frac{\partial\psi}{\partial t} + \frac{\partial}{\partial x}\vec{J} = 0,$$
$$\frac{\partial\psi}{\partial t} - \frac{\partial}{\partial x}\left(D\frac{\partial}{\partial x}\psi\right) = 0.$$

As D is assumed to be constant, the order of partial derivatives can be moved to return Fick's 2nd law of diffusion

$$\frac{\partial\psi}{\partial t} = D\frac{\partial^2}{\partial x^2}\psi.$$

Continuing with Fick's 2nd law of diffusion we can see how this can be solved for ψ in 1D as a Gaussian distribution.

If we assume initial conditions of isotropic diffusion starting at $x = 0$, this can be solved with a random walk. Assuming a one dimensional random walk where a particle can move either left or right for n steps of size $\Delta x = 1$ with equal probability of doing either, the probability for the particle to be at $x = +m$ after n steps means there must have been a net m steps to the right. In other words the steps to the right must be m more steps than those to the left, and the steps to the left plus steps to the right must equal n; $S_R + S_L = n$ and $S_R - S_L = m$. Solving for S_R and S_L returns $S_R = \frac{1}{2}(n + m)$ and $S_L = \frac{1}{2}(n - m)$. Therefore, the chances of getting this combination of left and right steps can be written as a binomial distribution of n choose k with $k = S_R$ and $q = 1 - q = \frac{1}{2}$.

$$p(k, n) = \binom{n}{k}(q)^k(1 - q)^{n-k}$$

$$\binom{n}{k} = \frac{n!}{S_R!S_L!} = \frac{n!}{\left[\frac{1}{2}(n + m)\right]!\left[\frac{1}{2}(n - m)\right]!}$$

With $q = 1 - q = \frac{1}{2}$, step size of $\Delta x = 1$, the mean of the binomial (i.e. the population of walks) is the mean value of all possible random walks.

$$\langle x\rangle = \sum_{i=1}^{n} \langle x_i\rangle = n(q\Delta x - (1 - q)\Delta x) = 0$$

Similarly, the variance of the binomial can be calculated from expectation values of the final positions of all possible random walks.

$$\sigma^2 = \langle x^2\rangle - \langle x\rangle^2 = n\left(\langle x_i\rangle - \langle x_i\rangle^2\right) = n\left(q\Delta x^2 + (1 - q)\Delta x^2 - 0\right) = n\Delta x^2$$

Applying the central limit theorem, that the distribution of sample means for large random samples will be approximately normally distributed with a mean μ and variance σ^2 of the population, the sample means of the possible binomial distributions taken from all

possible random walks can be written as a normal distribution with mean $\mu = 0$, $\sigma^2 = n\Delta x^2$. Mathematically this means that while the probability of each possible random walk follows a binomial distribution, the probability of location from all of the possible random walks is a normal distribution following the central limit theorem:

$$p(x,n) = \binom{n}{k}(q)^k(1-q)^{n-k} \rightarrow \frac{1}{\sqrt{2\pi\sigma^2}}e^{-\frac{(x-\mu)^2}{2\sigma^2}}.$$

With $k = x$, step size of $\Delta x = 1$, and assuming n steps are occurring per time t such that $D = \frac{n\Delta x^2}{2t}$,

$$p(x,t) = \frac{1}{\sqrt{4\pi Dt}}e^{-\frac{x^2}{4Dt}}.$$

This is the standard 1D Gaussian diffusion equation, which can be checked as meeting Fick's 2nd law of diffusion. For a particle at x_0 the probability of the location at time t with diffusivity coefficient D is the following:

$$\psi(x,t) = \frac{1}{\sqrt{4\pi Dt}}e^{-\frac{(x-x_0)^2}{4Dt}}. \tag{5.1}$$

5.2.2 Mean Squared Displacement

From the above Gaussian probability distribution function the mean squared displacement can be calculated using characteristic functions and moments (Papoulis [1991]). Mean Squared Displacement (MSD) is the expected ensemble average of the square of the net displacement travelled from time $t = 0$ to t. Note it is the net displacement, not the total distance travelled.

$$MSD(t) = E\{(x(t) - x_0)^2\}$$

The diffusion equation, Eq. (5.1), is the probability distribution of the location of a single particle at time t. One can use characteristic functions to generate moments represent various traits of a function. The characteristic function of a random variable with probability density

function $p(x)$ is

$$\Phi(\omega) = \int_{-\infty}^{\infty} p(x) e^{i\omega x} dx.$$

The second characteristic function of x is

$$\Psi = \ln \Phi(\omega) = \ln \int_{-\infty}^{\infty} p(x) e^{i\omega x} dx.$$

The derivatives of the characteristic function $\Phi(\omega)$ at the origin are moments of the random variable. Derivatives of the second characteristic function Ψ are the nth cumulants of the random variable,λ_n

$$\frac{d^n \Psi(0)}{ds^n} = \lambda_n.$$

The mean and variance of the random variable are the first and second cumulants, $\lambda_1 = \mu, \lambda_2 = \sigma^2$. Doing this for the Gaussian will confirm what was shown with the central limit theorem, $\lambda_1 = \mu = 0, \lambda_2 = \sigma^2 = 2Dt$ and is demonstrated below:

$$\begin{aligned}
\Phi(\omega) &= \frac{1}{\sqrt{4\pi Dt}} \int_{-\infty}^{\infty} e^{-\frac{x^2}{4Dt}} \cdot e^{i\omega x} dx \\
&= \frac{1}{\sqrt{4\pi Dt}} \int_{-\infty}^{\infty} e^{-\frac{(x^2 - 4Dti\omega x)}{4Dt}} dx \\
&= \frac{1}{\sqrt{4\pi Dt}} \int_{-\infty}^{\infty} e^{\frac{-\left[(x-2Dti\omega)^2 - 4D^2t^2(i\omega)^2\right]}{4Dt}} dx \\
&= \frac{1}{\sqrt{4\pi Dt}} e^{\frac{4D^2t^2(i\omega)^2}{4Dt}} \int_{-\infty}^{\infty} e^{-\frac{(x-2Dti\omega)^2}{4Dt}} dx \\
&= e^{Dt(i\omega)^2}.
\end{aligned}$$

The first and second derivative with respect to $s = i\omega$ of the natural log of this equation returns the cumulants that are the mean and variance.

$$\frac{d\Psi}{ds} = \frac{d}{ds} \ln \Phi = \frac{d}{ds} \ln e^{Dt(i\omega)^2} = 2Dts$$

$$\lambda_1 = \frac{d\Psi(0)}{ds} = 0 = \mu$$

$$\lambda_2 = \frac{d^2\Psi(0)}{ds^2} = 2Dt = \sigma^2 \tag{5.2}$$

5.2.3 Average Particle Speed

Now can see how we can use MSD and its relation to diffusion coefficient D to get the average speed of a molecule, or restricted its movement it is. From Fick's 2nd law and the assumption of a random walk in 1D, the expected average displacement is a function of time, with

$$E\{(x - x_0)^2\} = \sigma^2 = 2Dt. \tag{5.3}$$

In other words root mean squared displacement at time t can be calculated as $\sigma = \sqrt{2Dt}$. This means that from a diffusion coefficient $D = \frac{\sigma}{2t}$ and time t one can calculate the average ensemble movement in 1D in terms of average displacement over time. $v = \frac{\sigma}{t} = \frac{\sqrt{2Dt}}{t} = \sqrt{\frac{2D}{t}}$. This is how diffusion weighted images can generate image contrast based on the different molecular speed in various pathologies such as tumor or infarction.

5.3 3D Diffusion

Now we can apply to this 3 dimensions and get a diffusion ellipsoid described with a diffusion tensor. This can be either derived from above by expanding into multivariate Gaussians, or through the Fokker-Planck equation. The Fokker-Planck equation is as follows for a k dimensional probability distribution p with diffusion D, and drift (or small net flow) u:

$$\frac{\partial p(\vec{x}, t)}{\partial t} = \nabla\left(\vec{u}(\vec{x}, t)p(\vec{x}, t)\right) + \nabla\left(D(\vec{x}, t)\nabla p(\vec{x}t)\right).$$

This describes diffusive particle density over time with an isotropic diffusion tensor, and if we assume initial point of $x_0 = 0$ it can be solved as

$$p(\vec{x}, t; \vec{u}, D) = \frac{1}{\sqrt{(2\pi)^k (2Dt)^k}} e^{-\frac{1}{2}\sum_{i=0}^{k} \frac{(x_i - \vec{u}t)^2}{2D_i t}}.$$

This is the multivariate Gaussian function with the diffusion tensor as the covariance, and the mean $\vec{u}t$ as the shift due to drift. If the diffusion tensor is anisotropic, but drift and diffusion are still constant, the equation must be scaled by the determinant of the tensor $[Dt] = \Pi_{i=0}^{k} 2D_i t$.

$$p(\vec{x}, t; \vec{u}, D) = \frac{1}{\sqrt{(2\pi)^k [Dt]}} e^{-\frac{1}{2}\sum_{i=0}^{k} \frac{(x_i - \vec{u}t)^2}{2D_i t}}$$

Understanding the variance in a k-dimensional Gaussian requires a covariance matrix. If the diffusion directions are aligned with the principal axes, the covariance matrix Σ will be a diagonal, with each variance the expected function of the corresponding diffusion along that direction. $\Sigma_{ii} = \sigma_i^2 = 2D_i t, \Sigma_{ij} = 0$, or

$$\Sigma = \begin{pmatrix} \sigma_1^2 & 0 & 0 \\ 0 & \sigma_2^2 & 0 \\ 0 & 0 & \sigma_3^2 \end{pmatrix}.$$

If, though, the diffusion directions are not aligned along the principal axes, the covariance matrix will not be a diagonal. Instead, it will be a matrix of a rotated ellipsoid whose eigenvalues and eigenvectors will provide information regarding the true variance. The diagonals of the covariance matrix of a rotated ellipsoid will then underestimate the diffusion and the anisotropy. The effect of this is discussed more in Section 5.5.

For a k = 3 multivariate Gaussian, an estimate of the variance of the 3D ellipsoid can be given by the trace of the covariance matrix, assuming the standard $\vec{x} = [x, y, z]$.

$$\Sigma = \begin{pmatrix} 2D_x t & 0 & 0 \\ 0 & 2D_y t & 0 \\ 0 & 0 & 2D_z t \end{pmatrix}$$

$$\sigma_{3D}^2 = tr(\Sigma) = 2D_x t + 2D_y t + 2D_z t$$

$$E\{(x - x_0)^2\} = \sigma_{3D}^2 = 6Dt \tag{5.4}$$

The 3D multivariate Gaussian will be used in MR diffusion imaging with the fundamental equation $S = S_0 e^{-bD}$ in which use of gradients allows fitting to the diffusion coefficient D which is the average of the three diffusions D_x, D_y, D_z. However, it must be noted though that again this 'speed' refers to only average motion of molecules in an ensemble over time; it cannot account for individual speed within each timestep, nor net displacement of a fluid. Further detailed analysis, application, and limitation of this is included in Sections 5.5 and 7.3.

5.4 Diffusion Weighted Imaging

Knowing the mathematical basis of diffusion coefficients, and how they represent the motion of a molecule in a fluid, MRI can return differences in tissues and pathologies based on diffusion restriction as described above. For example, in ischemic stroke the diffusion is greatly reduced in the vicinity of cells that are dead and swelling (cytotoxic edema) which leads to movement of free water into cells restricting its motion. Diffusion weighted images can be used to image core infarction as arterial occlusion leads a decrease in diffusivity before eventual ionic edema and necrosis.

Diffusion-weighting can be performed with a diffusion-weighted spin echo, or a pulsed

gradient. In this case the gradient is not used for position encoding or sampling in k-space, but instead adds two gradients to a standard Spin Echo to track displacement as shown in Fig. 5.1a. The first pulse introduces a phase shift that is dependent on the strength of the gradient at the position of a spin at time 0. After phase has accrued, a 180° RF pulse is then applied to reverse the phase shift induced by the first gradient pulse. The diffusion encoding gradient is applied again, and all spins that have not moved will return to their initial state. This means that at the echo, all stationary spins will have retained their original signal while moving spins will acquire phase information from the first gradient that is not fully reversed upon the second gradient. In other words, spins that have moved will be experiencing a different reversing field strength during the second gradient because they are located physically in a different part of the gradient.

The further the spin has moved between the 90° pulse and the 180° pulse the greater the phase accrual, i.e. the faster the spin is diffusing the greater the decrease in signal intensity. This diffusion gradient is applied along one direction to get signal loss due to motion along a single axis. The gradient strength will determine the sensitivity of the gradient to movement; a higher gradient strength will mean a spin will travel less in a period of time to experience the same difference in gradient strength before and after the 180° pulse as displayed in Fig. 5.1b. Here, the steeper gradient on the bottom demonstrates the greater phase accrual compared to the shallower gradient for a hypothetical particle. In other words, a steeper gradient is more sensitive to movement than a shallower one. The strength of this gradient, or the diffusion weighting, is expressed in terms of the b-value. A lower b-value will capture information on fast-moving fluid while a higher b-value will capture information on slow-moving fluid. Mathematically, this b-value is such that

$$\frac{S(2\tau)}{S_0} = e^{-Db}. \tag{5.5}$$

Here, 2τ is the echo time and D is the diffusion coefficient, while b is

$$b = \gamma^2 \delta^2 \left(\Delta = \frac{1}{3}\delta\right) g^2, \tag{5.6}$$

using the notation in Fig. 5.1a. The derivation of the b-value and its relation to the diffusion weighted spin echo is described in Appendix A.

The simplest DWI would be composed of one diffusion weighted spin echo taken at $b = 0$ and a diffusion weighted spin echo taken at $b = 1000$, or a similarly high b-value, and then fitting that curve to Eq. (5.5) to get D. This D is the diffusion coefficient of diffusing molecules along one direction.

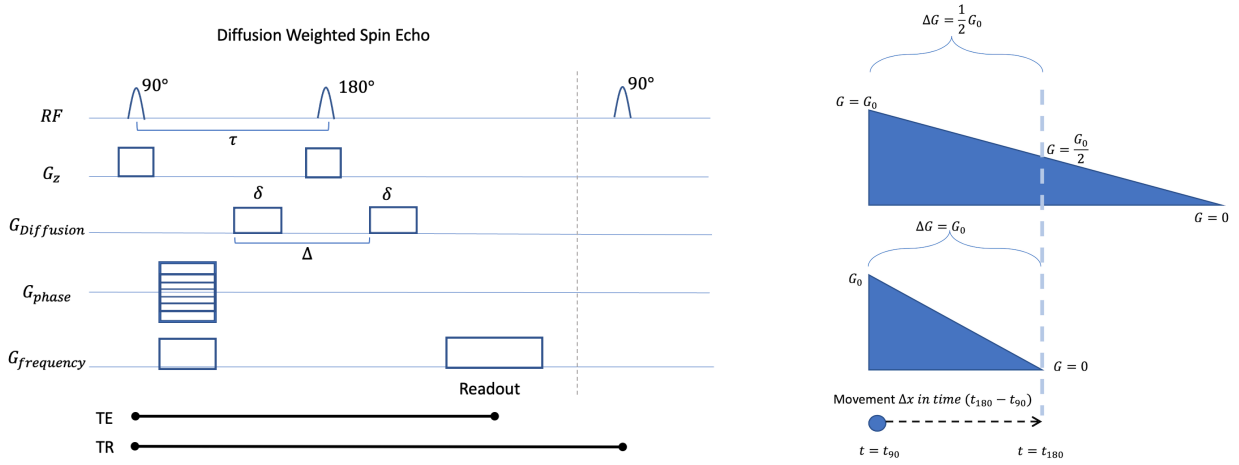

(a) DWI SE (b) b-value sensitivity

Figure 5.1: a) represents a standard MR sequence diagram for a DWI Spin Echo and b) is a graphical representation of a particle that has moved Δx in time $\Delta t = t_{180} - t_{90}$ and the different change in gradient strength that it would experience resulting in a higher sensitivity for a stronger gradient. The steeper gradient is more sensitive to movement than a shallower one, and represents a higher b-value.

5.4.1 Apparent Diffusion Coefficient

The ADC can be calculated as the average diffusion coefficient in three orthogonal directions, which do not have to necessarily be along the major axes of the diffusion ellipsoid. In

clinical settings the ADC can be used as an estimate of diffusion for imaging major diffusive abnormalities such as tumors, or infarct in a stroke.

ADC is the average of diffusion along three Lab Frame orthogonal directions $(\vec{x}, \vec{y}, \vec{z})$. If the diffusion in a voxel is described as a diffusion ellipsoid, described in more detail in the following Section 5.5, the ADC is the average of the diagonal elements of a diffusion tensor in Eq. (5.8), D_{xx}, D_{yy}, D_{zz}. These measured diffusion coefficients will be fit from the signal decay along $(\vec{x}, \vec{y}, \vec{z})$.

$$S_x = S_0 e^{-bDxx}$$
$$S_y = S_0 e^{-bDyy}$$
$$S_z = S_0 e^{-bDzz}$$

From this we can get an apparent diffusion coefficient, the average of these three orthogonal diffusion coefficients.

$$S_{ADC} = \sqrt[3]{S_x S_y S_z} = S_0 e^{-b(Dxx+Dyy+Dzz)/3}$$

$$ADC = -\frac{1}{b} \ln \left(\frac{S_{ADC}}{S_0} \right) = \frac{(D_{xx} + D_{yy} + D_{zz})}{3}$$

5.5 Diffusion Tensor Imaging

While the ADC can be calculated with just three directions, these directions don't necessarily align with the principal axes of an anisotropic 3D diffusion ellipsoid. Therefore, imaging anisotropic diffusion in 3D requires 3 vectors and 3 eigenvalues, i.e. 6 isotropically distributed diffusion images and a $b = 0$ image to fit to a model of interest (Kingsley [2006a,b,c]). With this, though typically more directions are taken, a diffusion ellipsoid can be reconstructed for every voxel to show diffusion preference and view anatomic white matter tractography.

For mean diffusivity of the ellipsoid one can calculate the trace which is the average of the eigenvalues of the diffusion ellipsoid.

The diffusion tensor representing the anisotropic 3D ellipsoid can be written in Cartesian coordinates as

$$x = a\sin(\theta)\cos(\phi),$$

$$y = b\sin(\theta)\sin(\phi),$$

$$z = c\cos(\theta),$$

in which $0 \leq \theta \leq \pi$ and $0 \leq \phi \leq 2\pi$. θ is the polar angle and ϕ is the azimuthal angle. The standard geometric equation of an ellipsoid is commonly

$$\frac{x^2}{a^2} + \frac{y^2}{b^2} + \frac{z^2}{c^2} = 1.$$

Translating this to a diffusion ellipsoid, we know from Eq. (5.2) that the average displacement along a single direction will be $2Dt$. Along the three principal axes of the diffusion gradient this D is $\lambda_1, \lambda_2, \lambda_3$. This means that these will be the coefficients along principal axes of the diffusion ellipsoid within the principal coordinate system, i.e. where the axes are aligned with the three Cartesian coordinates, x', y', z' (Masutani et al. [2003]).

$$\frac{x'^2}{2\lambda_1 t} + \frac{y'^2}{2\lambda_2 t} + \frac{z'^2}{2\lambda_3 t} = 1 \tag{5.7}$$

This ellipsoid can be represented with at minimum a 3×3 diffusion tensor, where the coefficients represent diffusion coefficients measured along the $(\vec{x}, \vec{y}, \vec{z})$ axes and the correlation between each pair.

$$D = \begin{pmatrix} D_{xx} & D_{xy} & D_{xz} \\ D_{yx} & D_{yy} & D_{yz} \\ D_{zx} & D_{zy} & D_{zz} \end{pmatrix} \tag{5.8}$$

From Appendix A we can replace D with this diffusion tensor for each direction k.

$$\frac{S(2\tau)}{S_0} = e^{-bD} \rightarrow \frac{S_k}{S_0} = e^{-b\widehat{g_k}^T D\widehat{g_k}}$$

Here $\vec{g_k}^T D\vec{g_k}$ represents the diffusion coefficient in the direction $\vec{g_k}$. An example given by Westin et al. [2002] shows 6 directions in vector notation.

$$g_0 = \begin{pmatrix} 0 \\ 0 \\ 0 \end{pmatrix}, g_1 = \begin{pmatrix} 1 \\ 1 \\ 0 \end{pmatrix}, g_2 = \begin{pmatrix} 0 \\ 1 \\ 1 \end{pmatrix}, g3 = \begin{pmatrix} 1 \\ 0 \\ 1 \end{pmatrix}, g_4 = \begin{pmatrix} 0 \\ 1 \\ -1 \end{pmatrix}, g_5 = \begin{pmatrix} 1 \\ -1 \\ 0 \end{pmatrix}, g_6 = \begin{pmatrix} -1 \\ 0 \\ 1 \end{pmatrix}$$

Normalizing these to get $\widehat{g_k} = \frac{\vec{g}}{|g|}$ returns a system of six equations from which to calculate the tensor D. On a voxel-by-voxel basis, having multiple diffusion weighted images in 6 directions for b=0 and for a b-value b from the signal loss along that direction from that b-value one can calculate D along that direction.

$$\ln\left(\frac{S_1}{S_0}\right) = -b\widehat{g_1}^T D\widehat{g_1}, \qquad \ln\left(\frac{S_2}{S_0}\right) = -b\widehat{g_2}^T D\widehat{g_2}, \qquad etc...$$

Solving across all 6 directions generates the diffusion tensor matrix shown in Eq. (5.8). While larger tensors can be generated with a greater number of gradient directions, only 6 directions with a baseline S_0 are needed to solve for D tensor using Singular Value Decomposition (SVD) to find the eigenvalues and eigenvectors.

Eigenvalues $\lambda_1, \lambda_2, \lambda_3$ are the strengths of the diffusion displacement along the three orthonormal eigenvectors $\vec{\epsilon_1}, \vec{\epsilon_2}, \vec{\epsilon_3}$ which represent the three principal diffusion directions. In other words the eigenvectors provide the three directions of the major axes, and the eigenvalues give the magnitudes of those corresponding peaks.

$$D\vec{\epsilon_1} = \lambda_1\vec{\epsilon_1} \qquad D\vec{\epsilon_2} = \lambda_2\vec{\epsilon_2} \qquad D\vec{\epsilon_3} = \lambda_3\vec{\epsilon_3}$$

These equations can be expanded to

$$D = \begin{pmatrix} D_{xx} & D_{xy} & D_{xz} \\ D_{yx} & D_{yy} & D_{yz} \\ D_{zx} & D_{zy} & D_{zz} \end{pmatrix} \begin{pmatrix} \epsilon_{ix} \\ \epsilon_{iy} \\ \epsilon_{iz} \end{pmatrix} = \lambda_i \begin{pmatrix} \epsilon_{ix} \\ \epsilon_{iy} \\ \epsilon_{iz} \end{pmatrix}. \tag{5.9}$$

Generalizing this, Eq. (5.8) can be replaced with a diagonalized matrix of eigenvalues, with

$$D = \begin{pmatrix} D_{xx} & D_{xy} & D_{xz} \\ D_{yx} & D_{yy} & D_{yz} \\ D_{zx} & D_{zy} & D_{zz} \end{pmatrix} \begin{pmatrix} \epsilon_{1x} & \epsilon_{2x} & \epsilon_{3x} \\ \epsilon_{1y} & \epsilon_{2y} & \epsilon_{3y} \\ \epsilon_{1z} & \epsilon_{2z} & \epsilon_{3z} \end{pmatrix} = \begin{pmatrix} \lambda_1 & 0 & 0 \\ 0 & \lambda_2 & 0 \\ 0 & 0 & \lambda_3 \end{pmatrix} \begin{pmatrix} \epsilon_{1x} & \epsilon_{2x} & \epsilon_{3x} \\ \epsilon_{1y} & \epsilon_{2y} & \epsilon_{3y} \\ \epsilon_{1z} & \epsilon_{2z} & \epsilon_{3z} \end{pmatrix}. \tag{5.10}$$

5.5.1 Mean Diffusivity

From the calculation of the diffusion tensor in Eq. (5.8) one can find the eigenvalues and eigenvectors via singular value decomposition, and these eigenvalues represent the anisotropic diffusion along the principal axes as shown in Eq. (5.7). This can then be used to calculate the mean diffusivity.

$$MD = \frac{\lambda_1 + \lambda_2 + \lambda_3}{3}$$

However, these eigenvectors $(\vec{\epsilon_1}, \vec{\epsilon_2}, \vec{\epsilon_3})$ do not necessarily align with the lab frame $(\vec{x}, \vec{y}, \vec{z})$. This is why 6 directions, rather than just three directions along the principal axes, are needed to allow calculation of a tensor that can return true anisotropic diffusion ellipsoid through singular value decomposition.

5.5.2 *Fractional Anisotropy*

While a diffusion ellipsoid is completely represented by a diffusion tensor, fractional anisotropy (FA) can be calculated from eigenvalues and eigenvectors of the tensor as a simpler measure of anisotropy.

$$FA = \sqrt{\frac{3}{2}} \frac{\sqrt{(\lambda_1 - \lambda)^2 + (\lambda_2 - \lambda)^2 + (\lambda_3 - \lambda)^2}}{\sqrt{\lambda_1^2 + \lambda_2^2 + \lambda_3^2}}$$

This value can range from 0 to 1, with 0 representing all eigenvalues being equal (isotropic diffusion), and 1 representing only one nonzero eigenvalue (linear diffusion along a single direction). Examples of ellispoids with varying fractional anisotropy are shown in Fig. 5.2.

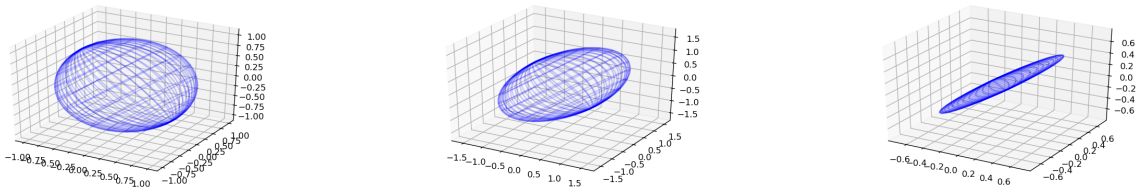

(a) FA = 0 (b) FA = 0.41 (c) FA = 0.89

Figure 5.2: These figures represent 3D anisotropic diffusion ellipsoids with increasing Fractional Anisotropy

The loss of anisotropy measurement is the cost of using diffusion weighted imaging rather than diffusion tensor imaging, with the benefit of needing fewer directions and therefore shorter scan time overall. The effects of the loss of this anisotropy information on ADC compared to true mean diffusivity is presented in Appendix B.

CHAPTER 6

BASICS OF IVIM MRI

Intravoxel incoherent motion (IVIM) as described previously in Section 2.4.4 is a type of diffusion MRI scan introduced by Le Bihan et al. [1988] that uses multiple b-values to simultaneously assess tissue water diffusion and tissue perfusion without the use of gadolinium-based contrast agent. Due to the high number of b-values needed (from 5 to 20+ in literature, Le Bihan et al. [1988, 1986], Federau et al. [2014], Jalnefjord et al. [2018], Wirestam et al. [2001], Iima and Le Bihan [2016], Federau et al. [2012], Wong et al. [2018]), and the focus being on isotropic perfusion, only three directions are taken for each b-value to minimize scan time. In other words, IVIM is composed of multiple DWI scans taken with varying sensitivities to diffusion. The effects of using DWI compared to DTI in estimating diffusion coefficients is presented in Appendix B.

The different b-values will allow separation of compartments with different speeds. That is, loss of signal at low b-values, i.e. less-sensitive gradients, will be due to fast movement; slow movement will return less phase accrual than fast movement. Loss of signal between high b-values, i.e. more-sensitive gradients, will be due to slower movement. This returns two compartments, a 'fast' and a 'slow' compartment discussed in further detail in Section 6.1, and can be done along any number of directions.

As originally conceived, IVIM scans were prohibitory as they were too long for clinical use but recently, newer, faster scanner hardware and software have substantially reduced scan and image processing times which are nominally 5-8 minutes long. As a results, many groups (Zhu et al. [2020], Federau et al. [2017], Fujiwara et al. [2020], Bergamino et al. [2020], Paschoal et al. [2018]) are beginning to revisit IVIM perfusion-diffusion image as a tool for evaluating neurovascular disease. The management of neurovascular diseases, including large artery occlusions, relies on the identification of infarcted tissue volume and the residual tissue perfusion. Thus, conceivably IVIM acquisitions could serve a critical role in the management

of acute stroke and chronic neurovascular disease, particularly when longitudinal imaging is desirable. Furthermore, as a quantitative imaging technique, IVIM has the potential to allow multi-site cross-sectional comparison in addition to within-patient longitudinal comparison.

6.1 Two-compartment IVIM signal model

The two-compartment signal model is based on an assumption of two main types of molecular movement within a voxel, specifically a 'fast' portion (i.e. 'perfusion', or 'pseudo-diffusion'), and a 'slow' portion (i.e. interstitial water motion: diffusion). This means that signal in the voxel will be composed of molecules that have two different diffusion decay curves in the form of the standard diffusion equation Eq. (5.5), or $S = S_0 e^{-bD}$ from Appendix A. This is the standard bi-exponential model of IVIM (Le Bihan et al. [1988]) that signal is assumed to follow on a voxel-by-voxel basis:

$$\frac{S(b)}{S(0)} = f e^{-bD^*} + (1-f)e^{-bD}. \tag{6.1}$$

In Eq. (6.1) the first component fe^{-bD^*} represents the 'fast' movement, ,i.e. motion of water in capillaries, or the 'pseudo-diffusion' component. The second component $(1-f)e^{-bD}$ is the remaining signal in the voxel which is the 'slow' movement, or the diffusion component. This is shown in Fig. 6.1 which had the b=0 signal normalized to 1.

As shown in Fig. 6.1 each voxel is assumed to be composed of two compartments, and the signal in that voxel as a function of b-value is fit to the bi-exponential parameters. The different volume fraction and diffusion coefficient of those components will return f, D, and D^* of that voxel. A voxel in the cortex will have a dense capillary network meaning large cerebral blood volume f and fast blood motion D^*. At hypercapnia, with blood vessels dilating leading to greater fraction of cerebral blood volume in that voxel, f should increase, creating to a larger calculated cerebral blood flow fD^*. A voxel that has infarcted should

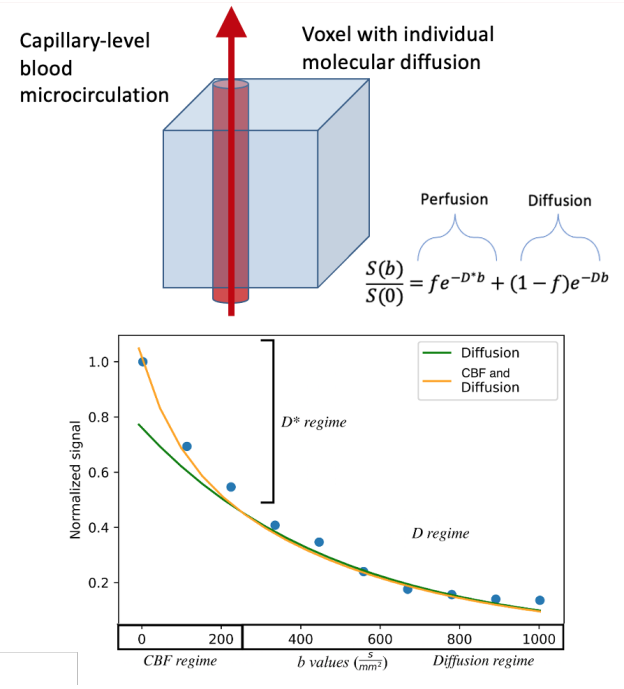

Figure 6.1: A simplified example of a voxel, its pseudo-diffusion and diffusion compartments, and the subsequent IVIM bi-exponential of those compartments with D* and D respectively.

no longer have perfusing blood, and so should fit to a monoexponential or $D^* = D$. An example of a map of these parameters, and the corresponding cerebral blood flow is shown in Fig. 6.2. Note the influence of the left middle cerebral artery occlusion.

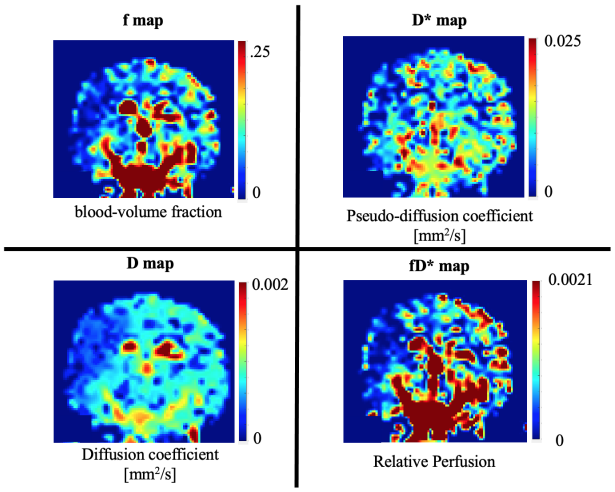

Figure 6.2: An example of a single slice of a coronal IVIM scan of a canine post middle artery occlusion. f, D, D^*, and fD^* are shown with their respective units.

6.2 Simulation of IVIM Fit Algorithm

6.2.1 IVIM Fit Algorithm Setup

As of the beginning of this work, the optimal method of processing IVIM data was an active ongoing area of research (Le Bihan [2019], Gurney-Champion et al. [2018], Conklin et al. [2016]), and this work independently validated the proposed fitting algorithm and mathematical model by simulation and in vivo for a number of physiologic conditions in Chapter 8. the accepted result. To determine the two-component model parameters, the accuracy of fits to the bi-exponential model was simulated and tested with various fit algorithms, fit parameters and noise. The algorithm and fit parameters that returned the lowest mean absolute percentage difference ($MAPD = 200\% \frac{1}{n} \sum_0^n \frac{|True - Measured|}{True + Measured}$) were used to retrieve f, D, and D* from data.

In the simulation the classical bi-exponential model, Eq. (6.1), was given randomly selected 'true' values for f, D^*, and D. f was chosen from a range of 0.01 to 0.09, D^* from a range of 0.003 to 0.01$(mm^2)/s$, and D from a range of 0.0003 to 0.001$(mm^2)/s$. The ranges reflect the expected experimental values of the three parameters and ensure D^* is

one order of magnitude greater than D (Le Bihan and Iima [2015]). Simulated IVIM signal was generated with these randomly selected parameters, different numbers of b-values, and added Rician noise associated with MRI signal noise (Gudbjartsson and Patz [1995]). The Rician noise with the probability distribution of

$$PDF_{Rician} = \frac{x}{\sigma^2} e^{\left(-\frac{(x^2+A^2)}{(2\sigma^2)}\right)} I_0(\frac{xA}{\sigma^2})$$

was approximated by the square root of the sum of squares of two independent and identically distributed Gaussian distributions (Aja-Fernandez and Vegas-Sanchez-Ferrero [2016]),

$$N(b) = \sqrt{g_1^2 + g_2^2},$$

in which σ is the standard deviation and I_0 is a modified Bessel function of the first kind of order zero, and g_n is a value from a Gaussian distribution with $\sigma = 1$ and a mean μ_n. $N(b)$ is then scaled to the appropriate standard deviation and mean of the PDF_{Rician} by a linear factor. With the signal without noise as $S(b)$ and the Rayleigh approximation of background noise as $N(b)$, the simulated MR signal with noise is of the form

$$S(b) + \frac{S(b)}{SNR} \times N(b).$$

SNR of $1, 10, 22, 50, 75, 100, 125, 150$ and ∞ was included in the simulation to test fit algorithm performance.

Fit Algorithms

Three fit algorithms were compared, the first being a simple fit, the second being a split fit, and the third being a two-step fit. All used least-square fit with bounds on variables with the trust region reflective (TRF) algorithm to perform minimization of the cost function.

The 'simple fit' optimized the entire bi-exponential model to fit to the simulated data

using the TRF least square fit where f, D, and D^* were fit simultaneously in Eq. (6.1) to the entire range of $S(b)$. For the other two algorithms the compartments are treated as two separate regimes in the fitting. In 'split fit' the signal from b-values higher than b_t are fit to the second term in Eq. (6.1) to constrain D and then the three-parameter model of Eq. (6.1) is fit with D held as this constant. In ' two-step fit' the signal of b-values higher than b_t is fit to the second term in Eq. (6.1), and f and D are retrieved. The diffusion regime fit is calculated with the returned fit parameters f and D and the residual signal is fit to the CBF regime D^* after subtracting the diffusion component. As D^* is typically an order of magnitude greater than D, the signal has decayed to zero for values above b_t.

Threshold b-value b_t

In both the split fit and the two-step fit Eq. (6.1) is divided into two segments: CBF dominated segment (i.e. lower b-values) and diffusion-dominated segment (i.e. higher b-values), denoted by a specific b threshold, b_t. This b_t has been explored by many different studies (Le Bihan [2019], Wurnig et al. [2015]), and this simulation tested the range of b_t values studied in previous literature $b_t = 200 - 600 s/(mm^2)$.

b-value sets

$$
\begin{aligned}
5\ b\text{-values} &= [0, 120, 350, 575, 800] \\
16\ b\text{-values set 1} &= [0, 10, 20, 40, 80, 110, 140, 170, 200, 300, 400, 500, 600, 700, 800, 900] \\
16\ b\text{-values set 2} &= [0, 20, 40, 80, 110, 140, 170, 200, 300, 400, 500, 600, 700, 800, 900, 1000] \\
10\ b\text{-values} &= [0, 111, 222, 333, 444, 556, 667, 778, 889, 1000]
\end{aligned}
$$

The combination of fitting algorithm, b_t, and the number of b-values used that returned values with lowest percent error was used to process the IVIM signal and calculate the three fit parameters for every voxel. Laid out, the following sets of possibilities were as follows, leading to 36 combinations of possible IVIM fits as shown in Fig. 6.3. MAPD is calculated for

the returned parameters and used to judge the combination of all b-values chosen, threshold b-value, and fit algorithm for a standard SNR.

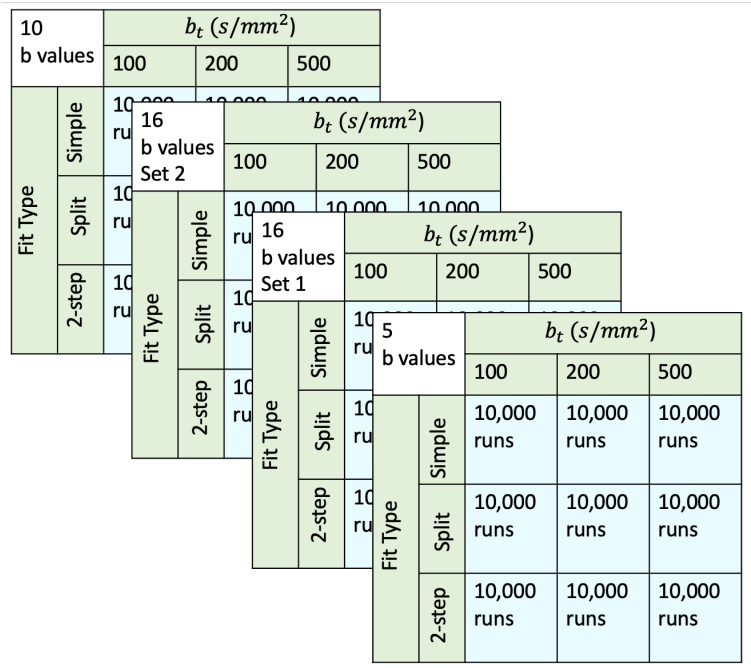

Figure 6.3: Graphic demonstration of the simulations run on various combinations of b-value set, threshold b-value, and fit type.

6.2.2 IVIM Fit Algorithm Results

The results of the simulation and the MAPD of all combinations of protocol is shown in Fig. 6.4b. SNR in the IVIM images was measured as 22 using mean signal intensity of the brain and standard deviation of the difference image at $b = 1000$. The protocol corresponding to minimum mean absolute percent difference (MAPD) of the returned fit parameters is ten b-values, a threshold $b_t = 222s/(mm^2)$, and the two-step fit algorithm. Consequently all IVIM parameters in this study were fit as such. An example of the two-step fit applied to data from a voxel of 10 b-values with the $b_t = 222$ is shown in Fig. 6.1.

This optimized protocol for SNR of 22 was split into a distribution of percent error. D showed the best fit success, with a narrow peak centered around 0% error. f showed an even

distribution similar centered around 0% but with a broad distribution with wide tails from roughly -100% error to 100% error. This suggests the f is more sensitive, but on average is fit within 50% with a mean percent error near 0%. D^* as expected was the most difficult to fit accurately. It has a long tail showing underestimation up to 200%. While the average is still close to zero, overestimation from 0% to 40% is the most likely. The sharp cutoff is due to the hard-coded cutoff on a D^* maximum.

Simulated SNR was run with the best combination of fit algorithm, number of b-values, and b_t, shown in Fig. 6.5. MAPD of three different fits using the best combination retrospectively (10 b-values and $b_t = 222$) as a function of simulated SNR from 0 to 150 and infinity (no noise). At SNR = 22, as measured in the IVIM images, the two-step fit has the lowest MAPD. For SNR between 0 and 10, simple fit is best, but at SNR greater than 10 the two-step fit returns the lowest MAPD. Split fit, used by many to post-process IVIM images, has the highest MAPD in the range of SNR in MR images. As expected, when there is no noise the simple fit has the lowest MAPD.

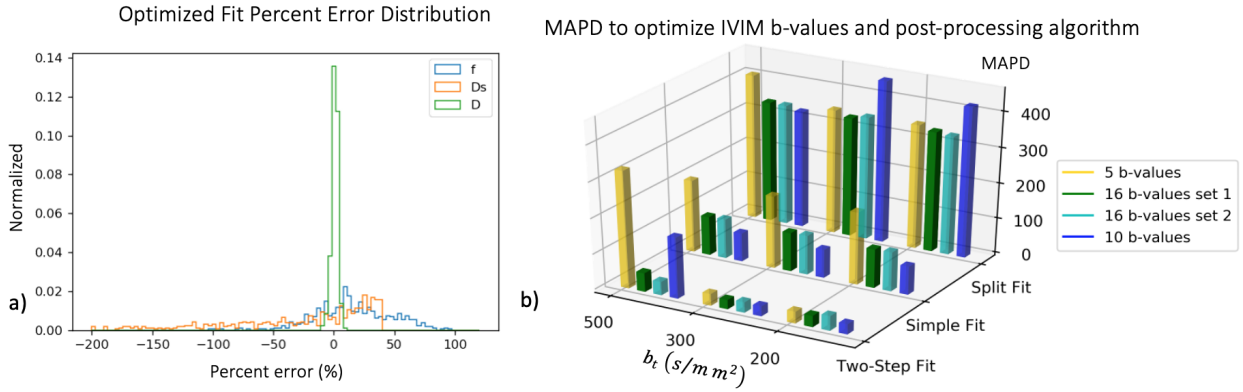

Figure 6.4: Optimized fit algorithm and the percent error distribution across three IVIM parameters. a) Distribution of MAPD of the three different parameters f, D, and D^* for 10,000 runs of the optimized fit. b) MAPD of every combination of three different fit processes, b_t, and sequence of b-values (with SNR = 22). The optimized combination for SNR = 22 was found to be two-step fit with 10 b-values from 0 to $1000 s/mm^2$ and $b_t = 222$.

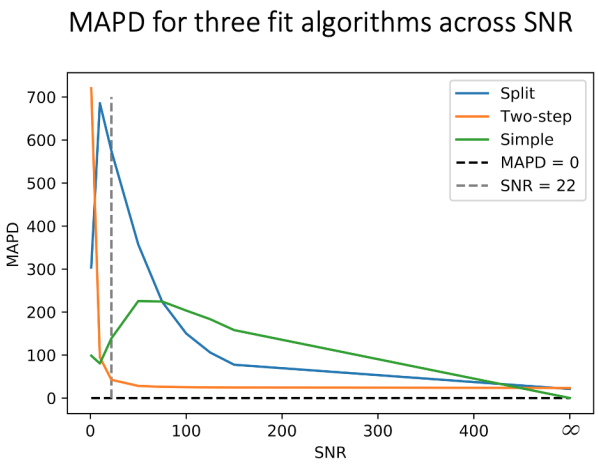

Figure 6.5: Simulation of the three different fit types with the optimized 10 b-values and threshold $b_t = 200$ as a function of SNR. This shows the dependence of fit success on SNR of the images. The two-step fit has the lowest MAPD for the measured SNR of 22.

6.2.3 IVIM Fit Algorithm Discussion

Averaged MAPD of the three bi-exponential parameters f, D, and D^* was used to measure the optimal fit parameters. However, the distribution of error between these parameters did differ. D^* was, as seen in practice, the most error-prone, while D did show higher accuracy. This agrees with studies shown previously which have had close agreement between IVIM D and standard ADC, and shown correlation between CBV and IVIM f, but have often struggled with D^*. This suggests the problems are not merely physiologic, or due to signal compromise, but bi-exponential fitting difficulties.

The optimized algorithm still did return an average MAPD of 24.2%. The mean percent error was -3.1%, suggesting no bias towards over or under calling true parameters. However, when divided into parameter type, D returned a mean percent error of 0.89% while D^* returned -25.4% and f returned 15.3%.

The five b-value sequence returned the second lowest MAPD at 29.1%. It returned a larger distribution of percent errors of f, D, and D^*, though all three parameters do have mean percent errors close to 0. The main benefit of so few b-values is the shortening of the scan. For the 10 b-value sequence to run in three direction, it takes roughly 5 minutes. If

only half as many b-values are taken, the sequence could be run in 2.5 minutes making it less prone to motion artifacts.

There are several limitations to this simulation. First, that the range of true parameters given were based on those observed and expected based on physiology of the brain. This would differ based on organ and fluid flow of interest. Second, it was assumed that the true signal was in fact a bi-exponential, i.e. the two-compartment model was assumed to be correct and all voxels composed of a fraction of blood and a fraction of water. Again this would differ based on organ and fluid flow of interest, with notable different in other organs such as the kidney and the liver. This leads to another limitation being lack of cerebrospinal fluid (CSF) in the simulations. CSF is believed to behave like free water and so would have a high rate of flow and potentially dominate the signal. As such this simulation did not show if there was any optimal combination of fit algorithm, b-value sequence, or b_t to separate between CSF and blood with a potential tri-exponential for a three-compartment model. Further, there was not signal contamination or compromise from subject movement, brain pulsatility, arterial or venous flow, or EPI distortion. Finally, all combinations were run on just 10,000 pseudo-randomly generated parameters for computational efficiency, but similar trends were seen for smaller numbers of runs suggesting this to be an adequate number.

In 2018 the two-step model with a b_t threshold approximately $200 s/mm^2$ became the general fit used in clinical neurology, though this simulation presented here examined the results simultaneously, with a focus on statistical success rather than clinical imaging, and independently of these findings (Paschoal et al. [2018], Le Bihan [2019], Liu et al. [2019]).

CHAPTER 7

IVIM QUANTIFICATION VIA WATER TRANSPORT TIME

The parameters of the bi-exponential, f, D, and D^* are used to calculate cerebral blood flow. In this case it is hypothesized that f represents blood volume, as it is the fraction of the total water signal that is moving more rapidly than interstitial water, allowing us to separate the two signals. D^* is the pseudo-diffusion coefficient, which reflects the speed of motion of this blood volume. From this relative CBF can be calculated as being proportional to fD^*. Different methods of quantification of this blood flow have been studied, most notably by Le Bihan and Turner [1992] and Wirestam et al. [2001] using historical reference values describing representative capillary geometries of the brain. To avoid the capillary assumptions, and the resulting restriction to only quantitative perfusion in the brain, I propose a method quantifying IVIM blood flow to ml/100g/min by deriving pseudo-diffusion water transport time.

7.1 Water Transport Time

Mean transit time is commonly used to refer to the average period of time that blood spends within the blood vessels of a particular of a capillary network in tissue (Copen et al. [2016]). It is typically measured via DSC using the central volume theorem as described in Section 4. As the Gd contrast travels through the blood, blood volume can be calculated from integral over the tissue concentration curve during the first pass divided by the total concentration of the arterial input function. Blood flow can then be calculated by deconvolving the tissue concentration curve from the arterial input function and the residue function. That is, after an instantaneous bolus to tissue one can calculate the blood flow by examining how quickly the flowing blood washed the bolus out of given voxel. As the bolus is not instantaneously delivered, implementing proper delay and dispersion correction is necessary to return the

true amount of blood that flowed through the tissue per unit time. From that mean transit time is calculated with the central volume theorem.

$$MTT = \frac{CBV}{CBF}$$

Unfortunately this means that MTT is measured indirectly as an estimate, using exogenous contrast agent, and depends on AIF chosen and deconvolution method (Orsingher et al. [2014], Zaharchuk [2007]). Further, the order of calculation is flipped, where CBV and CBF are known first, as opposed to using MTT and CBV to calculate CBF. As such, when examining how to solve for quantitative IVIM using a similar idea of transit time various definitions were studied. Further, important assumptions were made where IVIM perfusion was assumed to be approximately uniform and Gaussian distributed over a sphere for ease of calculation (Fig. 7.2c), whereas DSC perfusion does not need to make said assumption as its calculation is solely based on contrast dynamics. Lastly, the fast-moving water is assumed to be related to the fast water in blood flow.

As IVIM uses water as an endogenous tracer, a Water Transport Time (WTT) definition was derived from the fast-moving pseudo-diffusion coefficient to calculate: 1) 50% probability of a water molecule having left the volume of interest, 2) time for mean squared displacement to match volume of interest, and 3) time to leave volume of interest for a particle travelling at average velocity. This WTT was expected to behave similar to the MTT from DSC. The first method was shown to return strong agreement and so was used in the studies. Derivation and results of the two alternate definitions are included in Appendix C.

7.2 Literature Calibration Coefficient

Algorithms for the quantification of perfusion via IVIM has existed since the original proposal, but has always relied on assumptions of capillary geometry limiting its use to healthy

brain tissue. The literature calibration coefficient attempts to quantify perfusion in ml/100g/min with a few assumptions regarding the capillary segments. It essentially views the capillary bed of tissue as a series of tubes oriented randomly, but ultimately results in isotropic movement. This is the 'capillary bed model'. Using the central volume theorem previous work (Wirestam et al. [2001], Le Bihan et al. [1988]) posits the following:

$$qCBF = \frac{CBV}{MTT} = \frac{\text{volume flowing}}{\text{mean transit time}}. \tag{7.1}$$

Also, from the bi-exponential fit, the total cerebral blood volume is the fraction of the voxel that is the capillary blood in a voxel, or the 'fast' component (f), times the water content fraction of the voxel, $f_w = \frac{V_{H_2O}}{V}$. This f_w is the ratio of the total voxel volume of water to the total voxel volume, i.e. the fraction of the voxel that is even water. From this we can calculate the total cerebral blood volume as the fraction of MRI-IVIM signal that was 'fast', times the total fraction of the voxel that is contributing to this MRI-IVIM signal.

$$f = \frac{CBV}{f_w} = \frac{\text{blood volume}}{\text{water fraction per voxel}}$$

$$CBV = f \times f_w$$

Then, to solve for MTT in the denominator of Eq. (7.1) qCBF Le Bihan and Turner [1992] states that the mean transit time in a region of the brain is equal to the total capillary length divided by the average velocity of blood in that region.

$$MTT = \frac{L}{\langle v \rangle} = \frac{\text{total capillary length}}{\text{average velocity}}$$

Further, that the perfusion coefficient follows a diffusion process at a macroscopic scale, meaning that

$$D^* = \frac{\langle l \rangle \langle v \rangle}{6} = \frac{\text{average segment length} \times \text{average velocity}}{6}.$$

This is an assumption in which the diffusion coefficient is equal to the mean capillary segment length times the average blood velocity divided by 6. This will be discussed further in the following Section 7.3. However, if this is assumed to be true, it can be solved for $\langle v \rangle$ which can be plugged into Eq. (7.1) to return their final equation,

$$\langle v \rangle = \frac{6D^*}{\langle l \rangle}.$$

Therefore from this, values from average biological values of capillary networks can be input to the final capillary model equation, with the literature values being $f_w = 0.65$, $\rho = 1.047 g/mL$, $L = 2mm$, $\langle l \rangle = 0.11mm$ returning

$$qCBF = fD^* \frac{6f_w}{\rho L \langle l \rangle} \approx fD^* \times 1.016e5. \tag{7.2}$$

7.3 Proposed Water Transport Time

Proposed here is a method that does not require assumptions regarding capillary network parameters and instead approaches the question from a pure physics-isotropic diffusion on a voxel-by-voxel basis of interpreting movement between voxels. It defines water transport time, rather than mean transit time, as the time at which the 50% of the originally tagged "fast" water is now no longer in the voxel, i.e. 50% will take more time and 50% have taken less time to leave the volume. In other words, to use Gaussian probability distribution for a single water molecule, it is the time at which there is a 50% chance for a single molecule to leave the voxel. Beginning with the 3-dimensional Gaussian derived from the Fokker-Plank equation, and shown in 1D from Fick's first law of diffusion all in Section 5.2 we get the following standard 3D Gaussian equation for the isotropic 'pseudo-diffusion', assuming a

drift $u = 0$ and $\vec{x} = [x, y, z]$:

$$p(\vec{x}, t; \vec{u}, D) = \frac{1}{\sqrt{(2\pi)^3[Dt]}} e^{-\sum_{i=0}^{3} \frac{x_i^2}{4D_i t}}$$
$$= \frac{1}{\sqrt{(2\pi)^3[Dt]}} e^{-\left[\frac{x^2}{4D_x t} + \frac{y^2}{4D_y t} + \frac{z^2}{4D_z t}\right]}.$$

The covariance matrix again would be

$$\Sigma = \begin{pmatrix} 2D_x t & 0 & 0 \\ 0 & 2D_y t & 0 \\ 0 & 0 & 2D_z t \end{pmatrix},$$

and

$$Var(X) = tr(\Sigma) = 2(D_x t + D_y t + D_z t).$$

From this, with $D_x = D_y = D_z = D$ due to the isotropic nature of the perfusion in the voxel

$$\sigma_{3D}^2 = tr(\Sigma) = 6Dt.$$

A demonstration of a) 1D, b) 2D, and c) 3D probability distribution, and its integral within a voxel, is shown in Fig. 7.1.

Now isotropic Gaussian distribution can be used to determine time at which a particle has 50% chance of having left the voxel, which I'll refer to as Water Transport Time. Beginning with 1D for a simpler thought experiment, a voxel is a region on a line with a molecule starting in the middle of the line and diffusing. Particle position can be modeled as a delta function in the center of this 1D voxel, the way tracer is modeled in DSC (Carroll et al. [2008]), and following the law of diffusion the position of particles will spread over time according to a normal distribution as a function of $\sigma = \sqrt{2Dt}$. This is shown in Fig. 7.2a.

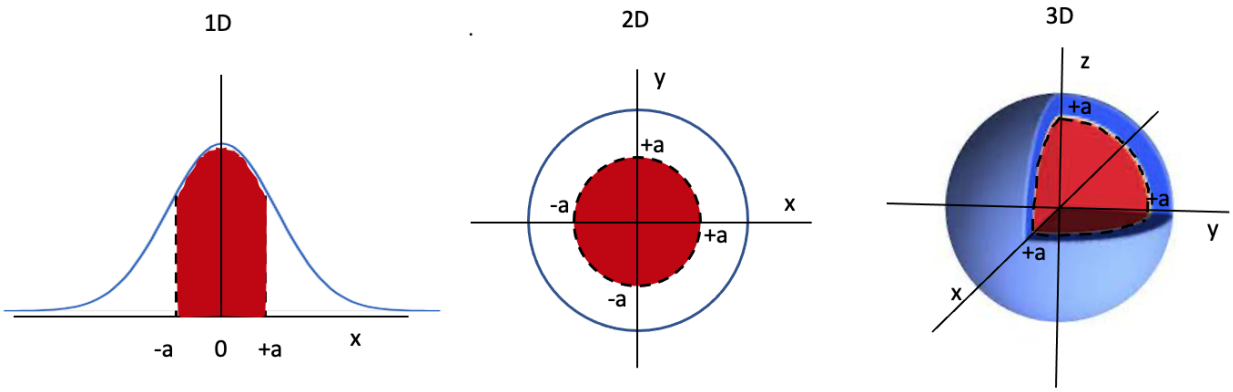

Figure 7.1: An example of diffusion from 1D to 3D. On the left 1D shows the location along the x-axis and the probability of its location along the y-axis. At time t with diffusion coefficient D there is a 50% chance it is within the red range, i.e. has been displaced more or less than a. In the middle, 2D shows again a red circle now along the x and y-axes, with the 2D probability Gaussian not shown. Instead it shows that there is now a 50% chance it is within the red circle, with the blue circle showing where the probability drops close to zero. Lastly, on the right 3D shows this as a sphere, with again a smaller sphere within the 3D Gaussian distribution that represents the radius of a. In other words, again now in 3D the displacement which a molecule has 50% chance of moving past. MTT is finding the time at which

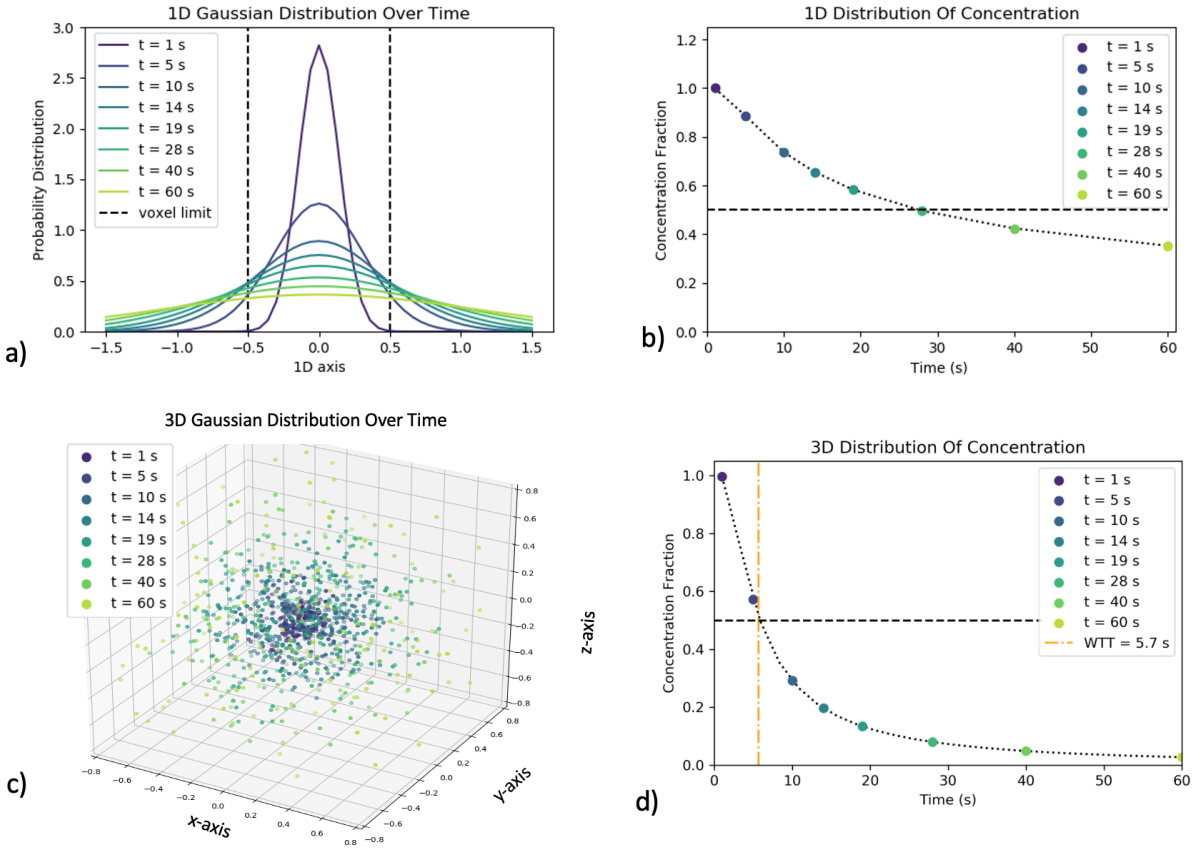

Figure 7.2: An example of diffusion from 1D and 3D. a) Demonstrates the change in the 1D probability density function as a function of time, assuming an instantaneous random walk from the center of the voxel, where a voxel is a range along a single line. b) Demonstrates the change in the concentration in the 1D voxel as a function of time, as expected as particles diffuse, the concentration drops. c) Demonstrates the change in the 3D density as a function of time, where the voxel would be within the limits of-0.5 and 0.5 on all three axes. d) Demonstrates the change in that 3D concentration as a function of time from isotropic diffusion.

Just as mean transit time of blood is the time it would take for a certain ml of blood per 100g of tissue to travel through a capillary bed, water transport time is the median time it takes for water to travel out of a cubic mm of tissue. This is shown in Fig. 7.2b as the horizontal dashed line where 50% of the initial water molecules have diffused out of the sphere. In 1D this can be solved as follows.

$$\int_{-.5}^{.5} \frac{1}{\sqrt{2\pi}\sigma} e^{-\frac{x^2}{2\sigma^2}} = \int_{-.5}^{.5} \frac{1}{\sqrt{4\pi D \times WTT}} e^{-\frac{x^2}{4D \times WTT}} = .50$$

$$0.5 = 0.6745\sigma = 0.6745\sqrt{2D \times WTT}$$

$$WTT = \frac{(0.741)^2}{2D}$$

In other words, for an ensemble of molecules diffusing along a line with diffusion coefficient D over time t, when $t = WTT$ half of them will have moved outside of the 1D voxel and half will still be within the 1D voxel.

For diffusion in 3D, which is shown visually in Fig.7.2c) we get the following:

$$\int_{-.5}^{.5}\int_{-.5}^{.5}\int_{-.5}^{.5} \frac{1}{\sqrt{(2\pi)^3(2D \times WTT)^3}} e^{-\frac{x^2}{4D_x \times WTT}} e^{-\frac{y^2}{4D_y \times WTT}} e^{-\frac{z^2}{4D_z \times WTT}} dxdydz = 0.5.$$

In spherical coordinates, this is written as

$$\int_0^{2\pi}\int_0^{\pi}\int_0^{.5} \frac{1}{\sqrt{(2\pi)^3(2D \times WTT)^3}} e^{-\frac{r^2}{4D \times WTT}} r^2 \sin\theta dr d\theta d\phi = 0.5.$$

This simplifies to

$$\frac{4\pi}{(\sqrt{4\pi D \times WTT})^3} \int_0^{.5} e^{-r^2/4D \times WTT} r^2 dr = 0.5. \tag{7.3}$$

The concentration over time will decrease as water diffuses out of the sphere, as shown in Fig. 7.2d. Solving for the time at which this concentration is 50%, i.e. the WTT, is

shown below. For simplicity I substitute s for $4D \times WTT$, and solve the resulting integral by integration of parts as follows.

$$\int e^{-r^2/s} r^2 dr$$

$$\int udv = uv - \int vdu$$

$$u = r, du = dr$$

$$v = -\frac{s}{2}e^{-r^2/s}, dv = -\frac{s}{2}\Big(-\frac{2r}{s}\Big)e^{-r^2/s} = re^{-r^2/s}$$

$$= -r\Big(\frac{s}{2}e^{-r^2/s}\Big) + \int \frac{s}{2}e^{-r^2/s}dr.$$

Putting in the limits of integration from 0 to .5 returns the following

$$\int_0^{.5} e^{-r^2/s} r^2 dr$$

$$= -r\Big(\frac{s}{2}e^{-r^2 r/s}\Big)\Big|_0^{.5} + \int_0^{.5} \frac{s}{2}e^{-r^2/s}dr$$

$$= -0.5\Big(\frac{s}{2}e^{-.5^2/s}\Big) + \frac{s}{2}\frac{\sqrt{\pi s}}{2}\operatorname{erf}\Big(\frac{r}{\sqrt{s}}\Big)\Big|_0^{.5}$$

$$= -0.25s\Big(e^{-.25/s}\Big) + \frac{\sqrt{\pi}}{4}s^{3/2}\operatorname{erf}\Big(\frac{.5}{\sqrt{s}}\Big).$$

Plugging this back into Eq. (7.3) returns the following

$$\frac{4\pi}{(\pi s)^{3/2}}\left[-.25s\Big(e^{-.25/s}\Big) + \frac{\sqrt{\pi}}{4}s^{3/2}\operatorname{erf}\Big(\frac{.5}{\sqrt{s}}\Big)\right] = 0.5$$

$$-\frac{1}{\sqrt{\pi s}}e^{-.25/s} + \operatorname{erf}\Big(\frac{.5}{\sqrt{s}}\Big) = 0.5.$$

$$\operatorname{erf}(x) = \frac{2}{\sqrt{\pi}}\int_0^x e^{-t^2}dt \quad = 1 - \Big(1 + 0.278393x + 0.230389x^2 + 0.000972x^3 + 0.078108x^4\Big)^{-4}$$

Plugging this in returns the following equation which can be solved for s.

$$-\frac{1}{\sqrt{\pi s}}e^{-.25/s} + \left[1-\left(1+0.278393\Big(\frac{.5}{\sqrt{s}}\Big)+0.230389\Big(\frac{.5}{\sqrt{s}}\Big)^2 + 0.000972\Big(\frac{.5}{\sqrt{s}}\Big)^3+0.078108\Big(\frac{.5}{\sqrt{s}}\Big)^4\right)^{-4}\right] = 0.5$$

$$s \approx 0.21$$

This can be checked by plugging $4Dt = s \approx 0.21$ into Eq. (7.3),

$$\frac{4\pi}{(\sqrt{.21\pi})^3}\int_0^{.5} e^{-r^2/.21}r^2 dr = 0.50281 \approx 0.5.$$

Returning to Gaussian diffusion, if we substitute $\sigma = \sqrt{2D \times WTT} = \frac{\sqrt{s}}{\sqrt{2}}$ we can solve for $\sigma = \frac{\sqrt{.21}}{\sqrt{2}}$, and get $\sigma \approx 0.32$. Solving this for WTT$[s]$ in terms of D$[s/mm^2]$ returns

$$WTT = \frac{(0.32)^2}{2D}.$$

This is the same as if we solved for WTT in terms of D straight from the approximation of $s = 4D \times WTT$, but in terms of σ of the the 3D Gaussian for easier comparison to an intuitive spread.

This value can be understood intuitively as follows. With the water transport time as the time after which a molecule has a 50% chance of passing, in 3D $WTT_{3D} = \frac{(.32)^2}{2D}$ whereas for 1D $WTT_{1D} = \frac{(.741)^2}{2D}$. This is because if a molecule is restricted to 1D it can move either left or right. This means that say it took one step left at $t = 1$, at $t = 2$ it can either take a step further left or a step back to the right. That means it has a 50/50 chance of ending up back where it started. On the other hand, if it is in 2D, it can move left, right, up, or down. This means that if a molecule first took a step left at $t = 1$, at $t = 2$ it can now move either back to the right, or up or down. That means now only 1/4 chance of ending up back

where it started. This is the intuitive explanation of why the radius of 3D median absolute displacement is a larger portion of variance than the 1D median absolute displacement. Or in other words, it explains why Fig. 7.2d is a steeper curve than Fig. 7.2b.

With this water transport time derived and explained intuitively, we can plug this into the central volume equation to return the calibration coefficient

$$qCBF = \frac{CBV}{MTT} = \frac{f \times f_w}{\rho} \frac{2D^*}{(.32)^2}. \tag{7.4}$$

With tissue density unity $\rho = 1.0g/mL$ and water content fraction $f_w = 0.79$ (Madelin et al. [2014]), and converting to 100g/min, we get the following

$$qCBF \approx fD^* \times 9.3e4. \tag{7.5}$$

It should be emphasized that this is an approximation. The water content fraction of a voxel, the density ρ, the numerical estimation used for solving the $\text{erf}(x)$, and the assumption of it being a sphere all contribute to the quantification factor above. This is the trade-off in assumptions compared to capillary segment assumptions. Below is side-by-side comparison of the two equations to demonstrate the differences clearly.

From 7.2 the capillary bed network model with their reported values (Wirestam et al. [2001], Le Bihan et al. [1988]):

$$\begin{aligned} qCBF_{Capillaries} &= fD^* \frac{6f_w}{\rho L \langle l \rangle} \\ &= fD^* \frac{6(.65)}{(1.047g/mL)(2mm)(.11mm)} \times 100g \times 60s/min \\ &\approx fD^* \times 101600. \end{aligned}$$

Using a WTT based perfusion model with $f_w = 0.79$ and assuming tissue density unity:

$$\begin{aligned} qCBF_{WTT} &= fD^* \times \frac{2f_w}{\rho(.32)^2} \\ &= fD^* \times \frac{2(.79)}{(1.0g/mL)(.32mm)^2} \times 100g \times 60s/min \\ &\approx fD^* \times 93000 \end{aligned}$$

The benefit of the voxel- based diffusion model is that first it does not assume any capillary architecture or any biologic constrains such as average segment length or total capillary length. Second, it does not assume that the variance of a molecule undergoing diffusion in a voxel is a function of the assumed capillary segment length $\langle l \rangle$. As mentioned in Section 7.2, to use the capillary bed network model, the diffusion coefficient D^* is assumed to be a function of the literature value capillary segment lengths.

$$D^* = \frac{\langle l \rangle \langle v \rangle}{6} = \frac{\text{average segment length} \times \text{average velocity}}{6}$$

The capillary geometry mimics the Gaussian equation

$$\sigma^2 = 6D^*t,$$

where if one solves for D^* one gets

$$D^* = \frac{\sigma^2}{6t}.$$

To make this applicable to the assumed capillary bed, the variance is set equal to the average capillary segment length times the average distance a molecule travels per time. If instead of assuming known capillary bed values, we treat signal loss from blood flow on a voxel-by-voxel basis, we avoid this assumption and instead can treat the diffusion coefficient fit as an estimation of the concentration decrease per cubic mm, and the mean transit time as the

time after which there is a 50% chance that a molecule has left this region. This will then estimate the time it takes for a ml of blood to travel through 100g tissue.

7.4 IVIM Quantification Limitations

IVIM quantification in ml/100g/min presented here makes several assumptions to provide an estimate. First, for IVIM to measure blood perfusion it must assume that the blood perfusion separated by f and D^* are purely Gaussian and accurately captured by a bi-exponential. That is, it works under the assumption of a two-compartment model: fast-flowing water, and slow-flowing water, and assumes that the fast-flowing water is from blood perfusion while the slow-flowing water is from stationary tissue. The implications of this assumption are studied further in Chapter 9.

Further, it makes the assumption that the bi-exponential model successfully fits and removes diffusion, assuming it to be Gaussian, and that the effects of Rician noise are minimal. The effect of diffusion misfitting has been explored previously (Le Bihan [2019]) with notable effects occurring at b-values higher than those studied in this work (Jensen et al. [2005]). Diffusion Kurtosis was explored by comparing the IVIM D, i.e. 'Apparent Diffusion Coefficient' to diffusion tensor ellipsoid, which does not assume isotropic diffusion, returning a median 11% lower diffusivity bias (Appendix B). This would affect the diffusion component of the bi-exponential. In addition Rician noise was included when building the simulation of an IVIM fit algorithm to optimize the fit returning an average underestimation of D^* and an overestimation of f (Section 6.2).

However, these cannot remove the issues of exponential fitting error, noise and subject movement, or motion coming from multiple sources such as respiration, heart beat, or brain pulsatility. Further, a significant limitation is that with an endogenous tracer all water signal is measured as opposed to exogenous tracer in which fluid it injected solely into the blood. Therefore, while fluid can be separated based on its movement, there will be signal from

alternate sources such as intracellular fluid, extracellular fluid, and CSF. Further, while the water content fraction was assumed to be 79% based on historical reference values (Madelin et al. [2014]), water content fraction of different tissue type will vary. This assumption of a constant water content fraction will decrease the differentiation of perfusion across brain tissue types.

CHAPTER 8

IVIM QUANTIFICATION VALIDATION STUDY

8.1 Introduction

Many groups (Zhu et al. [2020], Federau et al. [2017], Fujiwara et al. [2020], Bergamino et al. [2020], Paschoal et al. [2018]) are beginning to revisit IVIM perfusion-diffusion image as a tool for evaluating neurovascular disease. IVIM acquisitions could serve a prominent role in the management of neurovascular disease, particularly when longitudinal imaging is desirable. Furthermore, if cerebral blood flow can be quantified in ml/100g/min (qCBF) without organ-dependent capillary geometry assumptions, IVIM has the potential to allow multi-site cross-sectional comparison in addition to within-patient longitudinal comparison in organs besides the brain (Wirestam et al. [2001], Le Bihan and Turner [1992]).

There is some question of what IVIM signal changes correspond to, with potential that observed "perfusion" changes are reflecting flow of the perivascular cerebrospinal fluid (CSF) (Kwong et al. [1991]). This study uses a previously reported canine model of acute ischemia (Christoforidis et al. [2011, 2021], Liu et al. [2022], Saadat et al. [2020], Jeong et al. [2019]) to examine if quantified IVIM in ml/100g/min agrees with reference standard quantitative values of blood flow and demonstrates similar sensitivity to physiologic changes (both predicted and directly measured). IVIM cerebral perfusion is compared to neutron capture microsphere deposition, an established reference standard for tissue perfusion, at normocapnia (PaCO2 = 30-35 mmHg), hypercapnia (PaCO2 60-70mmHg), and focal ischemia resulting from middle cerebral artery occlusion (MCAO). IVIM water transport time used to quantify perfusion was compared to the similar dynamic susceptibility (DSC) mean transit time via the central volume theorem. Lastly, the accuracy of an IVIM-based infarct volume was compared to the infarct volume determined by standard mean diffusivity (MD) at 2 hours post-occlusion. The model is a clinically viable diagnostic tool for identifying perfusion/diffusion changes

and allowed for precise control over physiologic conditions and direct comparison to invasive reference standard values of perfusion.

The IVIM sequence and post-processing presented here presents a clinically feasible scan time of 5-minutes to collect images for calculation of parametric perfusion, diffusion, and water transport time MR images. We hypothesize that IVIM perfusion values can be quantified (ml/100g/min) using water transport time and agree over a range of physiologic conditions when compared directly to neutron capture microspheres. Using the central volume theorem, IVIM water transport time should correlate with DSC mean transit time. Further, using the same IVIM acquisition we hypothesize that IVIM diffusion positive infarct volumes will be accurate compared to MRI mean diffusivity infarct volumes as a reference standard. The purpose of this study was thus to assess the accuracy and sensitivity of a novel quantification of five-minute simultaneous IVIM perfusion and diffusion across three physiologic states.

8.2 Materials and Methods

8.2.1 IVIM Quantification via Water Transport Time

Perfusion and diffusion values are calculated from the multiple b-value IVIM scan using software developed in-house with a two-step fitting algorithm built using previous literature (Le Bihan et al. [1988], Wirestam et al. [2001], Le Bihan and Turner [1992]) and as laid out in more detail in Chapters 6 and 7.

The diffusion regime ($b > 222 s/mm^2$) is fit to the mono-exponential $(1-f)e^{-bD}$and the perfusion regime is fit to the remainder fe^{-bD^*}, resulting in the bi-exponential

$$\frac{S_b}{S_0} = fe^{-bD^*} + (1-f)e^{-bD}.$$

D^* is the pseudo-diffusion coefficient, f is the cebral blood volume fraction, and D is the diffusion coefficient. With the bi-exponential fit returning an approximation of a pseudo-

diffusion coefficient D^*. The movement of this water can be written as a 1D gaussian $\int_{-.5}^{.5} \frac{1}{\sqrt{4\pi D^* t}} e^{-\frac{x^2}{4D^* t}} dx$. Water transport time is defined as the time time for concentration of perfusing water in a capillary bed to drop to 50% of its original value. With three directions taken this can be written in spherical coordinates for 3D pseudo-diffusion and solved for Water Transport Time as described in Chapter 7.

$$\frac{1}{\left(\sqrt{4\pi D^* WTT}\right)^3} \int_0^{.5} e^{-\frac{r^2}{4D^* WTT}} r^2 dr = 0.50$$

Quantitative CBF can be calculated by substituting this definition of water transport time into the central volume equation, where water transport time is solved as a function of $D^*[mm^2/s]$. Fast-water fraction (f) per water transport time (t) is proportional to cerebral blood flow in ml/100g/min returning Eq. (7.5) with assumed values of $\rho = 1.04 g/mL$, water content fraction $f_w = 0.79$, and converted to 100g/min.

$$\begin{aligned} qCBF = \frac{CBV}{MTT} &= \frac{CBV}{WTT}[ml/100g/min] \\ &= \frac{f \times f_w}{\rho} \frac{2D^*}{(.32)^2} \approx fD^* \times 93,000 \end{aligned}$$

Applying this to IVIM bi-exponential parameters determined by the fitting algorithms returns IVIM maps of qCBF in ml/100g/min for comparison to reference standard values.

8.2.2 Pre-clinical Model

All experiments were conducted using a pre-clinical canine model of both controlled hypercapnia and MCAO (Christoforidis et al. [2011, 2021], Saadat et al. [2020], Liu et al. [2022], Jeong et al. [2019]). The two-day experimental protocol was approved by the University of Chicago Institutional Animal Care and Use Committee and reported in compliance with

ARRIVE guidelines. The University of Chicago is an AAALAC International accredited institution adhering to the following guidelines, regulations, and policies: a) Guide for the Care and Use of Laboratory Animals (National Research Council), b) USDA Animal Welfare Act and Animal Welfare Regulations, and c) Public Health Service Policy on Humane Care and Use of Laboratory Animals. The canine model has several advantages compared to rodents as a model for assessment of infarct progression using perfusion and diffusion imaging studies. Canines have a gyrencephalic neocortex with similar ratio of white to grey matter (Thomsen et al. [2017], Zhang and Sejnowski [2000], Traystman [2003]) as well as comparable pial arteriolar network organization (McHedlishvili and Kuridze [1984]), critical in modeling collateral arterial blood supply and predicting infarct evolution (Saadat et al. [2020]), to humans. In addition, the canine model provides tissue volumes necessary to evaluate both core and penumbra during ischemia using microsphere deposition. The neurovascular structure of canines also allows a range of endovascular devices and interventional radiology techniques allowing minimal invasion with real-time visualization of occlusion preventing imaging artifacts and traumatic cerebrovascular reaction from open surgical occlusion. Lastly, the middle cerebral artery occlusion proposed is a relatively inexpensive alternative to nonhuman primate models of acute ischemia.

8.2.3 Experimental Protocol

In each animal, two experiments were performed on consecutive days to validate our algorithm in a setting of cerebrovascular response to hypercapnia and MCAO and the effect of flow augmentation on collateral arterial networks after MCAO(Jeong et al. [2019], Saadat et al. [2020]). We present an analysis of these experiments in which neutron capture microspheres and IVIM were acquired during quiescent physiologic conditions. On the first day, canines were imaged at baseline (i.e., normocapnia) (target PaCO2 = 30-35 mmHg) and hypercapnia (5-7% carbogen respiration, target PaCO2 60-70mmHg) induced by carbogen gas

inhalation (5-7% CO2 95% O2). End Tidal CO2 was monitored to assess minute to minute variations in exhaled CO2 levels, and true arterial PaCO2 was measured through direct arterial blood sampled from the descending aorta at the time of perfusion measurements.

On the second day, canines underwent permanent endovascular middle cerebral artery occlusion under fluoroscopic guidance. Occlusion was then verified via selective ipsilateral and contralateral internal carotid and vertebral arteriography (Jeong et al. [2019]). Subjects were transported to the MRI suite for imaging studies within 60 minutes of occlusion. We evaluated experimental flow augmentation during MCAO via simultaneous administration of a vasopressor and vasodilator intended to augment CBF (Liu et al. [2022]); therefore, highly dynamic, and abnormally high perfusion throughout the brain post-occlusion is expected by experimental design. Throughout experiments physiologic parameters were maintained within normal range (excluding PaCO2 for experiments involving intentional hypercapnia and blood pressure for experiments involving flow augmentation).

IVIM and microspheres included in the study were taken less than 30 minutes apart on day two post-occlusion to mitigate perfusion fluctuation. Furthermore, differences induced by physiologic fluctuations (heart rate, blood pressure, ETCO2) between microsphere and IVIM imaging was monitored. Large variance in physiologic parameters within these timing windows is noted.

8.2.4 Microsphere Acquisition

Stable-isotope microsphere quantitative CBF was acquired in a subset of cases with microspheres injected immediately prior to DSC acquisition using a previously reported technique (Jeong et al. [2019]). Each injection consisted of 4ml of stable isotope (gold, samarium, lutetium, terbium, lanthanum, and ytterbium) labeled 15μm microspheres (STERIspheres, BioPal Inc, Medford, MA) into the left ventricle over 10s. Reference blood (20ml) was withdrawn at 10ml/min for analysis from the mid abdominal aorta with an MRI compatible

withdrawal pump (PHD 2200, Harvard Apparatus, Holliston, MA, USA). Brains were excised and sliced by a calibrated brain cutting matrix (Canine Brain Matrix, Stoelting Co., Wood Dale, IL, USA) at 6mm intervals and matched MRI slices in orientation and thickness. Each slice was sectioned into eight regions of interest (3 cortical regions and one deep region per hemisphere, Fig. 8.1c which were weighed. Each section was analyzed through neutron activation for CBF at an independent laboratory (BioPal Inc. Medford, MA, USA) blinded to the MRI result and laterality of the infarct, and reported as

$$qCBF = \frac{N_t R_b}{N_b m_t} \qquad [ml/g/min].$$

Here N_t is microsphere count of the brain tissue sample in decay per minute, N_b is the microsphere count in reference blood draw, R_b is the reference withdrawal rate in ml/min and m_t is the mass of the tissue sample.

8.2.5 MRI Acquisition

All MRI scans were performed on a 3T MRI scanner (Ingenia, Philips) with canines in a headfirst, prone position using a 15 channel receive-only coil. Diffusion weighted images (DWI) for IVIM were collected with 10 b-values from 0 to 1000 s/mm^2 (0,111, 222, 333, 444, 556, 667, 778, 889, 1000) and 3 orthogonal directions to ensure a clinically feasible scan time (5:38 min). IVIM scans were prescribed to cover the entire head (2D single shot EPI, TR/TE= 3056/91ms, 50 slices, 2mm, FOV = 160 mm, total scan time = 332s, SENSE Factor=2).

Dynamic Susceptibility Contrast (DSC) images were acquired using a T1-Bookend method (Jeong et al. [2019]) within 30 minutes of IVIM (FOV/Matrix = $220mm/224$, single shot, EPI, Fat Saturated, No. of slices = 5, Slice Thickness = 6 mm, TR/TE = 315/40, Flip angle = 75°, 200 time points) and delay and dispersion corrected (Mouannes-Srour et al. [2012]) to return qCBF and Mean Transit Time (MTT) as described in Section 3.3.1.

Diffusion tensor imaging (DTI) for infarct volume progression was prescribed to cover the entire head (TR/TE = 2993/83ms, FA = 90°, BW = 1790Hz/pixel, FOV =160 mm, voxel size = $1.75 \times 1.75 \times 2mm^3$, b-values = $0, 800s/mm^2$, slices = 50, 32 directions).

8.3 Statistical Analysis

Linear regression was analyzed, pooled across all physiologic states and the coefficient of determination (R^2), p-values (p), slopes (m), offsets, and corresponding Bland-Altman mean differences and 95% CIs are reported. A mixed effects model was applied with modality as fixed effects, and the case and region nested as random effects. Tukey's boxplots per physiologic state with mean, first and third quartiles, and whiskers were produced with hemispheric paired comparison. Statistical agreement within physiologic states was studied with Wilcoxon signed-rank test. Lin's concordance correlation coefficient (CCC) and its 95% CI was used to determine agreement between multiple quantitative measures incorporating both accuracy and precision between two readings along the 45 degree line through the origin (Lin [1989], Steichen and Cox [2002]). In addition, Lin's CCC variability across subjects was shown with the reported subject-wise CCC. All statistical significance was determined at the 1% ($p < .01$) level for hypothesis testing.

8.3.1 Perfusion Comparison

Hemispheric regions-of-interest (ROIs), shown in Fig. 8.1, were manually drawn on three central slices on the diffusion image by a trained operator who was blinded to all perfusion values for comparison to microsphere perfusion and DSC perfusion. IVIM slices were averaged to match microsphere thickness (6mm). To remove high values from misfitting as demonstrated in previous studies (Federau et al. [2014]), $D^* \geq 0.10$ were removed. Manual avoidance of subarachnoid space and ventricles, along with leave-one-out cross validation T2 map thresholds, were used to remove CSF-dominated voxels from analysis. Kwong et al.

[1991] suggests using an inversion recovery saturation pulse to remove proposed artifactually high perfusion values in the brain from the glymphatic system. In this study, a simulation was written to explore the effects of this saturation pulse on blood signal.

8.3.2 Transit Time Comparison

Anatomic middle cortical ROIs post-MCAO were drawn by an operator blinded to physiologic status on pre-processed images of IVIM and DSC ipsilateral and contralateral to the occlusion.

8.3.3 Infarct Volume Comparison

Mean Diffusivity (MD) analogous to the more widely used Apparent Diffusion Coefficient (ADC), was used to determine true infarct volume with the automatic threshold of 5.7e-4 (Christoforidis et al. [2011]). A previously determined automatic IVIM D infarct threshold of 5.15e-4 was applied calculate IVIM infarct volume.

8.4 Results

8.4.1 IVIM v. Microspheres

A total of n=6 (mean age = 0.72y, mean weight = 25.1kg, 5 female, 1 male) experiments were analyzed with further detail in Table 8.1 for IVIM and microspheres. Representative images are shown in Fig. 8.2A for quantitative IVIM perfusion images during normocapnia, hypercapnia and post-MCAO, in Fig. 8.2C for transit time post-MCAO, and in Fig. 8.2D for diffusion-positive maps post-MCAO. Average sum squared residuals (SSR) of the IVIM bi-exponential fits shows higher average error at hypercapnia ($SSR = 0.91 \pm 2.0$) compared to normocapnia ($SSR = 0.07 \pm 0.3$) or post-MCAO ($SSR = 0.002 \pm 0.004$)

Fig. 8.3A-B shows linear regression, Lin's CCC, and corresponding Bland-Altman of IVIM and microsphere perfusion. Tukey's Box Plots in Fig. 8.3C demonstrate average and range of perfusion at normocapnia, hypercapnia, and post-MCAO split into ipsilateral and contralateral hemispheres, Wilxocon signed-rank statistic across all states is 506 with $p = 0.02$. There were no significant differences in hypercapnia or post-occlusion hemispheres, but a statistically significant difference was seen at normocapnia ($p = 0.0005$). Linear regression of middle cortical asymmetry of IVIM water transport time post-occlusion returned correlation to DSC mean transit time (Fig. 8.4A) and Tukey's Box plots show expected increase in transit time on the ipsilateral hemispheres, though with a different mean and range of values (Fig. 8.4B). Using IVIM to determine infarct volume from these 6 cases showed strong linear correlation to truth (slope = 1.01, intercept= 0.58, R^2= 0.71, CCC= 0.79 [.35, 0.94]). Subject-wise Lin's CCC for cases with all slices analyzed ranged from 0.26 to 0.86, with a mean of 0.56. Simulation of inversion recovery spin echo to suppress CSF signal in IVIM showed the optimal TI for suppression would also suppress blood signal to 18% of its original (Fig. 9.10).

Quantification by capillary geometry assumptions as laid out in Section 7.2 returns linear regression (slope = 0.60, intercept = 57.2, $R^2 = 0.64$, Lin's CCC = 0.68 [0.59, 0.75]) with a Wilcoxon signed-rank statistic across all states equal to 308 and p = 0.0006.

	Normocapnia	Hypercapnia	Post-Occlusion
Number: IVIM & Microspheres	5 (Case 1 IVIM incomplete)	5 (Case 4 IVIM incomplete)	5 (Case 5 subarachnoid hemorrhage)

Table 8.1: Of the 6 cases studied with microspheres, shown is the number of cases available for each physiologic states, with all measurements within 30 minutes of each other. Two cases post-MCAO had slices removed from analysis due to zeros returned by the microsphere vendors.

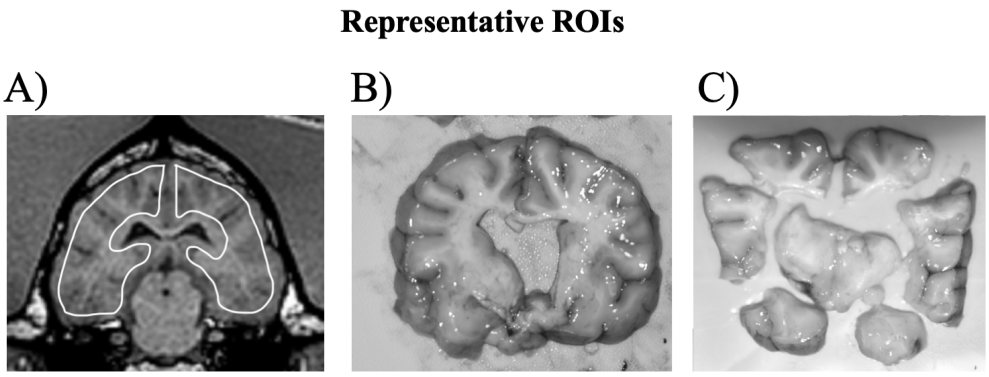

Figure 8.1: Representative images for hemispheric ROIs on one of three slices drawn on IVIM and on DSC on an Anatomic T1 weighted MRI (A). Edges are avoided to avoid subarachnoid CSF and DSC susceptibility artifacts. The brain slice (B) is cut into eight regions (C) for microsphere analysis and averaged for hemispheric qCBF.

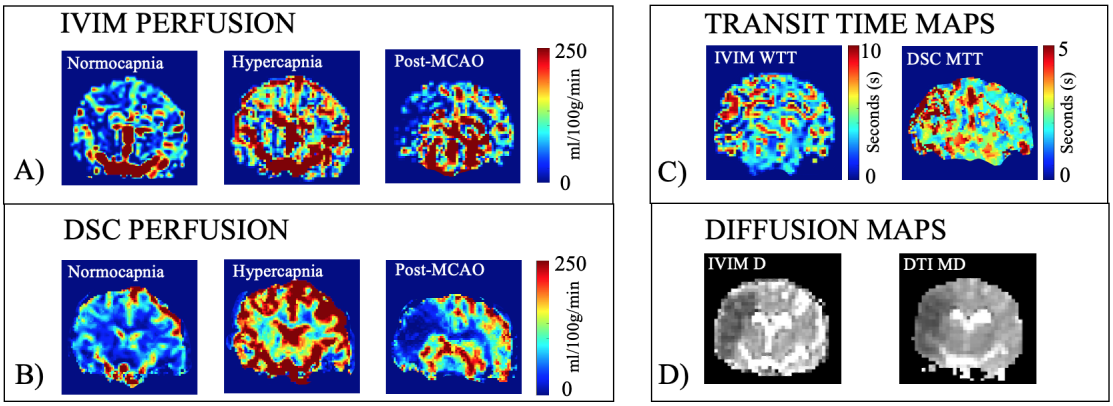

Figure 8.2: A) Representative quantitative IVIM perfusion for normocapnia, hypercapnia, and post-MCAO respectively. The qCBF images are shown with a dynamic range of 0 to 250 ml/100g/min. B) Corresponding DSC perfusion. C) Transit time maps post-MCAO for (right) delay and dispersion corrected DSC MTT and (right) IVIM water transport time. D) Diffusion images with a Mean Diffusivity map (right) compared to IVIM diffusion coefficient image (left) post-MCAO used for calculation of infarct volume. A case without flow augmentation treatment is provided to highlight diffusion abnormality post-MCAO.

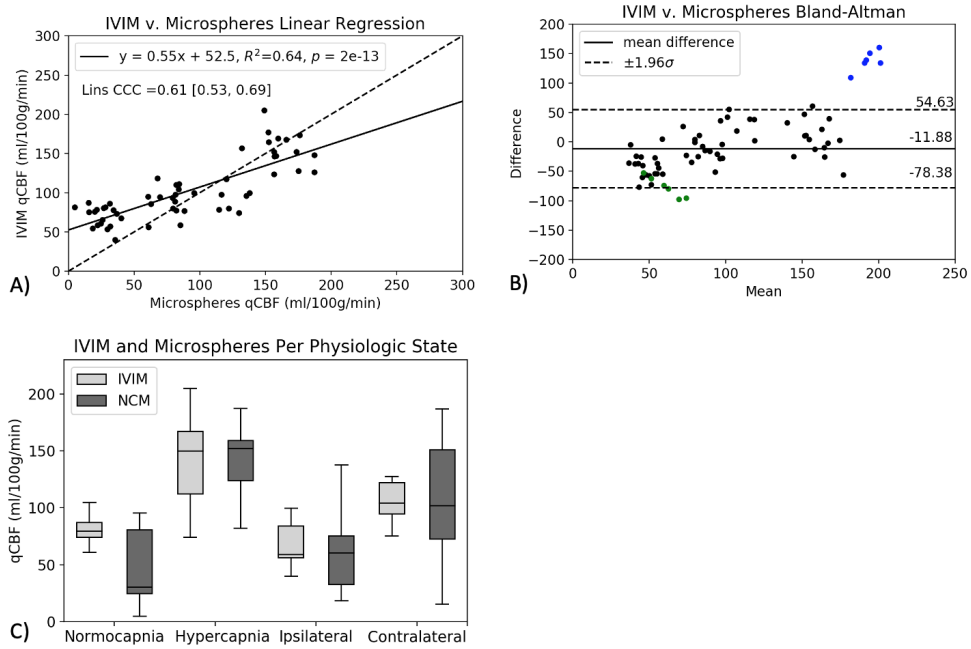

Figure 8.3: A) Hemispheric correlation of microsphere qCBF vs. quantitative IVIM qCBF across all physiologic states. Solid lines in linear regression plots represent the line of regression and a dashed line of unity is shown for reference. B) Bland-Altman plot with mean difference as a solid line and dashed lines representing 95% CI. Blue and green data in Bland-Altman represent two cases with large physiologic change between IVIM and microsphere injection. Due to the instability in physiology these cases are not included in statistical analysis. C) Tukey's box-whisker plots of hemispheric values for all physiologic states. Microspheres are called 'NCM' for brevity. Normocapnia and hypercapnia include both left and right hemisphere while occlusion and contralateral are split into corresponding hemispheres. Note: values are considerably higher in the MCAO model due to the use of aggressive flow augmentation(Liu et al. [2022]).

IVIM v. Microspheres per physiologic state	Mean Paired Difference (ml/100g/min)	Wilcoxon signed-rank
Normocapnia:	+34.32	6.0, p = 0.0005
Hypercapnia:	-1.85	79.0, p = 0.78
Post-MCAO:	+4.02	95.0, p = 0.71
Mixed Effects Model	Mean Intercept [95% CI]	Mean Slope [95% CI]
IVIM v. Microspheres:	54.6 [41.6, 67.7]	0.52 [0.40, 0.64]

Table 8.2: Wilcoxon signed-rank comparing IVIM to microsphere perfusion within each physiologic state and mixed effects model with subject as random effect. Normocapnia disagreement may be influenced by to CSF contamination or microsphere vendor error.

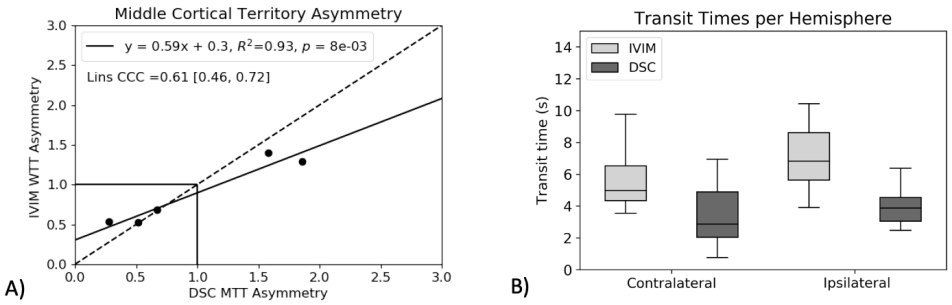

Figure 8.4: A) Hemispheric correlation of middle cortical territory asymmetry (Left/Right) of the transit time (MTT or WTT) for the five subjects post-MCAO. B) Tukey's box blots of the middle cortical territories post-MCAO showing mean and range of transit times from IVIM and DSC, split into contralateral and ipsilateral hemispheres.

8.4.2 IVIM v. DSC

A total of n=11 (mean age = 1.98y, mean weight = 26.76kg, 7 female, 4 male) experiments were analyzed with IVIM and DSC quantitative perfusion for at least one physiologic state, with further detail in Table 8.3. Fig. 8.2B shows representative quantitative DSC perfusion images. Cerebrovascular reserve calculated as $CVR(\%) = \frac{CBF_H - CBF_N}{CBF_N} \times \frac{100}{\Delta CO_2}$ returned linear regression $y = 1.15x - 0.70$ with an $R^2 = 0.85$, $p = 0.008$, and Lin's CCC $= 0.63\,[0.37, 0.80]$ for the 6 cases that had both normocapnia and hypercapnia available for IVIM and DSC analysis. Fig. 8.5A-B shows linear regression, Lin's CCC, and corresponding Bland-Altman of IVIM and DSC perfusion. Wilcoxon signed-rank returned a statistic of 2525 and $p = 0.01$. Using IVIM to determine infarct volume from these 11 cases showed strong linear correlation to MD infarct volume (slope = 0.81, intercept = 2.0, $R^2 = 0.76$, CCC = 0.86 [0.70, 0.94]).

Quantification by capillary geometry assumptions as laid out in Section 7.2 returns linear regression (slope = 0.70, intercept = 34.5, $R^2 = 0.66$, Lin's CCC = 0.78 [0.72, 0.82]) with a Wilcoxon signed-rank statistic across all states equal to 3195 and p = 0.32.

	Normocapnia	Hypercapnia	Post-Occlusion
Number: IVIM & DSC	8 (Case 1 IVIM incomplete) (Case 3 BP spike) (Case 6 no DSC)	8 (Case 4 IVIM incomplete) (Case 8 IVIM incomplete) (Case 6 no DSC)	7 (Case 5 subarachnoid hemorrhage) (Case 7, 10 early expiration) (Case 9 DSC error)

Table 8.3: Of the 11 cases studied with DSC, shown is the number of cases available for each physiologic states, with all measurements within 30 minutes of each other. Two cases were removed from the study due to early expiration.

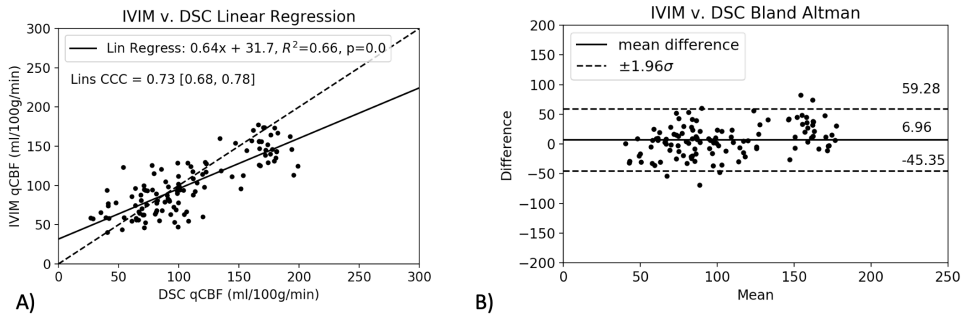

Figure 8.5: A) Correlation of DSC T1-bookend qCBF vs. quantitative IVIM qCBF across all physiologic states in 11 cases. Solid lines in linear regression plots represent the line of regression and a dashed line of unity is shown for reference. B) Bland-Altman plot with mean difference as a solid line and dashed lines representing 95% CI.

IVIM v. DSC per physiologic state	Mean Paired Difference (ml/100g/min)	Wilcoxon Signed-Rank
Normocapnia:	+0.11	560.0, p = 0.77
Hypercapnia:	-18.3	258.0, p = 0.0007
Post-MCAO:	+22.3	317.0, p = 0.09
Mixed Effects Model	Mean Intercept [95% CI]	Mean Slope [95% CI]
IVIM v. DSC:	34.5 [23.5, 45.4]	0.62 [0.54, 0.70]

Table 8.4: Wilcoxon signed-rank comparing IVIM to DSC perfusion within each physiologic state and mixed effects model with subject as random effect.

8.5 Discussion

This study found that a 5-minute IVIM 10 *b*-value sequence can produce quantitative cerebral perfusion via water transport time in a clinically acceptable scan time that demonstrates sensitivity over a range of relevant physiologic conditions. The sensitivity of CBF to normocapnia, hypercapnia, and acute ischemia post-MCAO suggest IVIM images can have impact in the management of cerebrovascular disease. Furthermore, IVIM images can predict qCBF in response to controlled changes in CO2 (cerebrovascular reactivity), without repeated administration of contrast agent, an advantage in the evaluation of chronic disease (Wirestam et al. [2001], Federau et al. [2012]). Further, the study suggests a possible quantification factor that relies solely on pseudo-diffusion water transport, and not on organ-dependent

capillary geometry. IVIM and microspheres across three physiologic states returned strong correlation and were further supported by agreement shown with Lin's CCC analysis.

Prior studies compare IVIM cerebral perfusion to MR CBF measurements with varying levels of success (Wirestam et al. [2001], Wu et al. [2015], Federau et al. [2014]). Several studies compare DSC CBV and IVIM f (Wirestam et al. [2001], Wu et al. [2015]), while one study ($R^2 = 0.42$) compares relative IVIM CBF fD^* and relative DSC CBF (Federau et al. [2014]). In comparison, this study found a strong correlation ($R^2 = 0.64$, Lin's CCC = 0.61) of quantitative IVIM CBF fD^* in ml/100g/min to neutron capture microsphere qCBF in ml/100g/min, as well as to DSC ($R^2 = 0.66$, Lin's CCc = 0.73). Mixed model effects holding modality as fixed and subject as random supports this correlation within subjects and Wilcoxon signed-rank shows agreement within physiologic state (Table 8.2. Comparison to DSC in Table 8.4 showed IVIM returning lower perfusion at hypercapnia compared to DSC. This may be due to susceptibility distortion increasing DSC perfusion at the edges of the cortex despite hemispheric ROIs drawn to minimize this. Further, the higher residuals at hypercapnia show increased perfusion causing poorer bi-exponential fit, a potential factor in the lower sensitivity of IVIM to increased perfusion.

Sensitivity to physiologic state is lower for IVIM with linear regression lower than unity, and a lower average perfusion at hypercapnia. However, paired agreement within physiologic states and observed change in measured perfusion between states supports quantification of hemispheric perfusion without capillary geometry assumptions in a multi-day controlled pre-clinical model, which to the best of our knowledge, has not been published previously. However, it also highlights examples of the remaining difficulty of CSF removal: partial volume contamination of CSF may falsely add to perfusion signal at all normocapnia shown in Fig. 8.3C) and with $p < 0.01$ at normocapnia compared to microspheres. Further, the higher residuals at hypercapnia show increased perfusion causing poorer bi-exponential fit, a potential factor in the lower sensitivity of IVIM to increased perfusion.

Comparison of statistical results of quantification via a previous capillary geometry quantification factor shows that the pseudo-diffusion water transport quantification returns better statistical agreement of IVIM perfusion to microspheres. As expected, as the capillary geometry factor is a higher multiplicative constant, it leads to a higher slope, higher intercept, and higher mean difference. This study shows that quantification derived from Gaussian approximation of perfusion returns comparable agreement with reference standard quantitative perfusion.

Water transport time used to quantify perfusion showed linear correlation with delay and dispersion corrected DSC mean transit time. Comparison to DSC requires delay and dispersion correction, i.e., a local-AIF, to account for IVIM AIF-independence. Difference in transit time range observed is notable (Fig. 8.3B), potentially due to the difference in properties being measured and endogenous vs. exogenous measurement. Further, zeroes are noted where D^* is small making its inverse (WTT) is inversely proportionally high. To prevent influencing results, these voxels are assigned 0 in Fig. 8.2, rather than being assigned an estimated WTT, and are not included in analysis. It could also be an effect of diffusion kurtosis leading to an overestimation of D (i.e. an underestimation of D^*), though the b-values in this study were $< 1500 s/mm^2$ (Jensen et al. [2005]).

Previous studies have also reported positive correlation between ADC and IVIM D in ischemic and normal regions ($R^2 = 1$,$R^2 = 1$) (Suo et al. [2016]) and ($R^2 = .98$,$R^2 = 0.81$) (Gao et al. [2017]). Although this study's agreement was lower than prior studies (slope $= 1.01$, $R^2 = 0.79$), it should be noted that the IVIM and DTI scans that were compared were taken from separate MR scans during a period of dynamic infarct expansion while the previous studies used the same images to get ADC and IVIM D. Use of two separate scans and sequences for IVIM D and MD infarct volume was chosen to best compare IVIM D and a separate standard clinical infarct volume. This combined with the IVIM qCBF from the same IVIM scan, not included in previous studies, demonstrates that the simultaneous perfusion

and diffusion components from a single IVIM bi-exponential fit agreed with corresponding perfusion and diffusion reference standard values.

IVIM imaging exploits the fact that diffusion-weighting is sensitive to water motion and consequently able identify where in the brain water is sequestered inside cells by cytotoxic edema (Iima and Le Bihan [2016]). At very low b-values ($b \leq 200$ s/mm^2), diffusion-weighting is predominantly sensitive to faster water motion such as capillary level blood flow (Le Bihan and Turner [1992], Federau et al. [2012], Le Bihan [2019], Jalnefjord et al. [2018], Le Bihan et al. [1988]). Questions remain regarding the origin of fast water motion signal, with Kwong et al. [1991] showing that use of an inversion recovery pulse significantly reduced cortical gray matter pseudo-diffusion fraction suggesting that much of the bi-exponential behavior resulted from CSF contamination rather than perfusion. In the following Chapter 9, Fig. 9.10 shows inversion recovery spin echo suppression will suppress both CSF and blood. This means signal loss with CSF suppression may come from inversion recovery, reducing signal from both CSF and blood from both T1 and T2 effects with the inverted blood contributing less than 10% of its IVIM signal, which may be incorrectly interpreted as CSF signal suppression. Further, following the Monro-Kellie hypothesis, at hypercapnia the dilation of cerebral capillaries prompts an increase in cerebral blood volume and CBF, and a decrease in CSF to maintain intracranial pressure (van der Kleij et al. [2020]). If fast-flow IVIM signal were due solely to CSF contamination, fD^* should decrease after CO2 inhalation, which was not observed in this study (Fig. 8.3C). Use of an absolute T2 threshold to remove CSF-dominated voxels in the ventricles and subarachnoid space reduced the effect of human bias in region selection. However, endogenous contrast prevents proof of signal origin and partial volume effects require further study especially in disease states. This study provides evidence that observed IVIM signal changes reflect cytotoxic edema and tissue perfusion.

Arterial spin labelling (ASL) is well-established, widely available, and a fully quantitative

means of imaging cerebral perfusion noninvasively (Detre and Alsop [1999]). However, with ASL, delayed arterial arrival times due to proximal vessel occlusion in stroke studies remains a challenge (Haller et al. [2016], Yao et al. [2016]). As such, IVIM being independent of arterial input functions or bolus kinetics is a singificant benefit of the sequence in comparison to both ASL and DSC-MRI when measuring neurovascular disease. Futher, IVIM is able to provide simultaneous identification of cytotoxic edema unlike both ASL and DSC-MRI.

This study is not without limitations. The highly dynamic physiology created challenges for acquisition of normocapnia, hypercapnia, and post-MCAO with MRI and invasive neutron capture microspheres within tight timing windows. Two cases showing large disagreement between IVIM and microsphere perfusion also show rapid change in BP and CO2 that agrees with the discrepancy shown, though the causality cannot be proven. While sensitivity to physiologic change is observed, IVIM sensitivity appears weaker than the perfusion effects observed with microspheres. Notably normocapnia returns higher IVIM perfusion, possibly due to partial volume contamination from CSF. Exponential fitting error especially regarding pseudo-diffusion coefficient is a continuing problem. While limits were placed to maintain pseudo-diffusion coefficients in the expected range following historical references (Federau et al. [2014]), pseudo-diffusion error will have large effects due to the inverse relation to water transport time. Further, some data was lost beyond our control due to vendor error and dynamic physiology, highlighting the complexity of microsphere perfusion. Finally, translatability of this perfusion to humans is not known.

8.6 Conclusion

In conclusion, this study found that a 5-minute IVIM 10 b-value sequence can produce quantitative cerebral perfusion via water transport time independent of capillary geometric assumptions in a clinically acceptable scan time that demonstrates sensitivity over a range of relevant physiologic conditions. The sensitivity of CBF to normocapnia, hypercapnia, and

acute ischemia post-MCAO suggest IVIM images can have impact in the management of cerebrovascular disease. IVIM diffusion positive volumes and quantitative cerebral perfusion sensitivity agreed with reference standard values over a range of physiologic conditions. Subarachnoid CSF contamination may affect quantitative agreement within physiologic states, but inversion recovery for CSF suppression will suppress blood signal along with CSF making it unideal for CSF contamination removal. The sensitivity of IVIM provides evidence that observed signal changes reflect cytotoxic edema and tissue perfusion. This supports the further development and refinement of IVIM for measuring noninvasive quantitative perfusion and diffusion.

CHAPTER 9

CEREBROSPINAL FLUID SIGNAL CONTAMINATION

9.1 Cerebrospinal Fluid (CSF)

Cerebrospinal Fluid (CSF) is fluid found within the ventricular system and surrounding the brain and spinal cord. It acts as a shock absorber, provides buoyancy, manages intracranial pressure, and allows for removal of waste through the brain's lymphatic system. CSF flow dynamics are an active area of research, as it acts both through pressure gradients throughout the brain and also through pulsatile flow from either cardiac or respiratory motion (Mehta et al. [2022]). For CSF in the ventricular spaces the fluid is unrestricted, unlike blood travelling through capillary beds for example, and so behaves like high free water diffusion.

As all water motion will contribute to diffusion weighted imaging, fast moving free water in the glymphatic system will add to signal observed at low b-values. This is a common issue with IVIM in the brain, specifically in the cortex where grey matter and subarachnoid space lead to mixed voxels. Multiple methods have been suggested to remove CSF from IVIM perfusion signal (Le Bihan et al. [1991], Scott et al. [2021], Wong et al. [2018]). Further, it has been suggested that if CSF signal is removed through Inversion Recovery (IR) suppression, IVIM perfusion signal is reduced leading to a conclusion that the perfusion signal is actually just CSF contamination (Kwong et al. [1991]).

Analysis presented in Chapter 8 found values higher than reference values which may have been from artificially high values from the glymphatic system (Kwong et al. [1991]). Chapter 8 used literature value thresholds of f and D^* to limit CSF contamination (Wirestam et al. [2001]), and ventricles and subarachnoid space were manually avoided in ROIs. However, despite these thresholds, variable partial volume with CSF in deep sulci that avoids the threshold may still contribute to perfusion signal if the standard bi-exponential is assumed.

However, this does not mean that all IVIM perfusion signal is due to CSF contamination.

An example of this is seen with the increase in perfusion signal at hypercapnia in Chapter 8. In a recent study of vasodilation van der Kleij et al. [2020] observed an increase in parenchyma and a decrease in CSF volume in T1 weighted MRI after increased arterial CO2. Vasodilation during hypercapnia would increase the blood volume and decrease CSF volume. Specifically noted was accordance with the Monro-Kellie doctrine in which CSF displacement is caused by increased cerebral blood volume during hypercapnia to maintain intracranial pressure. This supports the hypothesis that the observed increase in fast moving spins at hypercapnia in Chapter 8 being due to the blood and not CSF. If IVIM perfusion signal was due solely to CSF contamination, the fast-moving signal at hypercapnia would be expected to decrease.

Nonetheless, as IVIM uses endogenous tracer and CSF and blood both contain fast-moving and diffusing water molecules that will contribute to signal, the signal will be composed of both blood and CSF movement. This is an issue that exogenous tracers such as DSC and microspheres are not affected by. As these are the two perfusion methods IVIM is compared to in this work, potential CSF signal contamination and its removal is studied in this chapter by comparing quantitative IVIM perfusion with CSF removal through various methods to quantitative microsphere perfusion ground truth.

9.1.1 CSF Study Overview

CSF signal contamination is explored through potential partial volume separation and CSF-dominated voxel segmentation. Multi-exponential behavior of grey matter (GM), white matter (WM), infarct, and CSF is explored for potential significant differences in partial volume components, and independent component analysis examined as a possible method of separation (Section 9.2). Inversion Recovery posited by Kwong et al. [1991] was tested in a healthy volunteer as a method of removing CSF signal, and a simulation written to explore its effects on blood signal (Section 9.3). Removal of CSF-dominated voxels was explored

with leave-one-out cross-validation thresholding of T2 and diffusion (Section 9.4 and with supervised machine learning via discriminant analysis of IVIM bi-exponential parameters (Section 9.5). The results of these methods of CSF segmentation were compared to manual avoidance of CSF in ventricles and subarachnoid space in IVIM perfusion agreement to microspheres from Chapter 8.

9.2 CSF Exponentials

To examine partial volume contamination, ROIs of different tissue types were drawn to elucidate respective average multi-exponential curves. Different anatomic regions and tissue types will have different fluid compartments with varying blood volumes and velocities. In a diffusion weighted image of a brain post-MCAO there are typically three major sources of contrast: grey matter, white matter, infarct and CSF. To interrogate the signal response of CSF to IVIM analysis, a series of ROIs were drawn on three slices of one canine subject from Chapter 8 post-MCAO. Guided by T2 images WM, GM and CSF ROIs were used to elucidate average curve shapes of their respective tissue types. By eye, arterial blood and venous outflow can also be observed within arteries, draining veins and the sagittal sinus, but the small size of these make it difficult to get an ROI without partial volume effects. If we have various b-values with different sensitivities to fluid displacement (Section5.4), we can examine the average exponential decay of different regions of interest. The result of these averaged ROI curves is shown in Fig. 9.1.

The curves behave as expected for their partial volume components. Infarcted tissue will have only diffusion, and hence be a slow mono-exponential. The Gray matter ROI has both a greater cerebral blood volume, and faster average pseudo-diffusion in comparison to white matter ROI. This is shown by the larger slope and the larger intercept. The CSF ROI is composed of both ventricles and subarachnoid space with bright T2-weighted signal. Shown in Fig. 9.1b this ROI returns a potential tri-exponential pattern suggesting

three components. This suggests that the ventricles and subarachnoid space ROI may be composed of diffusion, capillary perfusion from cortical partial volume, and CSF. When examining the ventricle ROI of voxels in the center of a ventricle, free diffusion is observed as expected. The different speeds of the fast component of CSF and tissue ROIs suggests it would be possible to remove CSF-dominated voxels through automatic thresholding or machine learning of bi-exponential parameters.

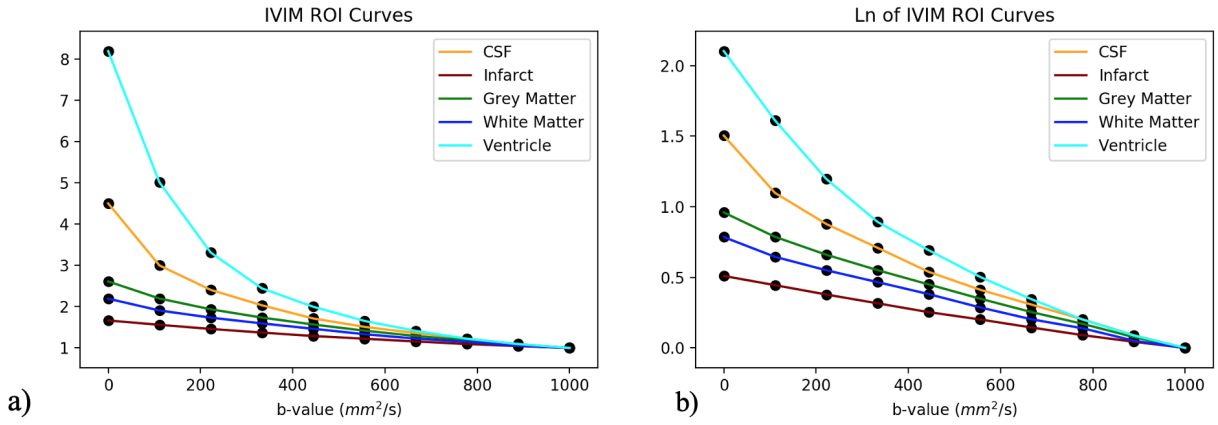

Figure 9.1: An example of average IVIM curves in CSF, infarct, grey matter, white matter, and deep in the center of a ventricle a) Demonstrates the exponential curves for average ROI signal across different b-values. CSF is composed of ventricles and subarachnoid space drawn from T2 images. Infarct is composed of automatically thresholded ADC masks, grey matter and white matter were drawn on T2 images. b) Demonstrates the natural log of a) to show the varying exponential behavior.

9.2.1 Tri-exponential partial volume contamination

Comparison of signal between ROIs in Fig. 9.1b show potential partial volume contamination affecting the exponential curves. This means that partial volume contamination will influence the bi-exponential fit parameters, and so the perfusion fD^* measured. The bi-exponential fits of the IVIM signal decay for four ROIs a) infarct, b) grey matter, c) white matter, and d) pure ventricles are shown in Figure. 9.2.

Shown with the fits, CSF in the ventricles demonstrates behavior like free diffusion.

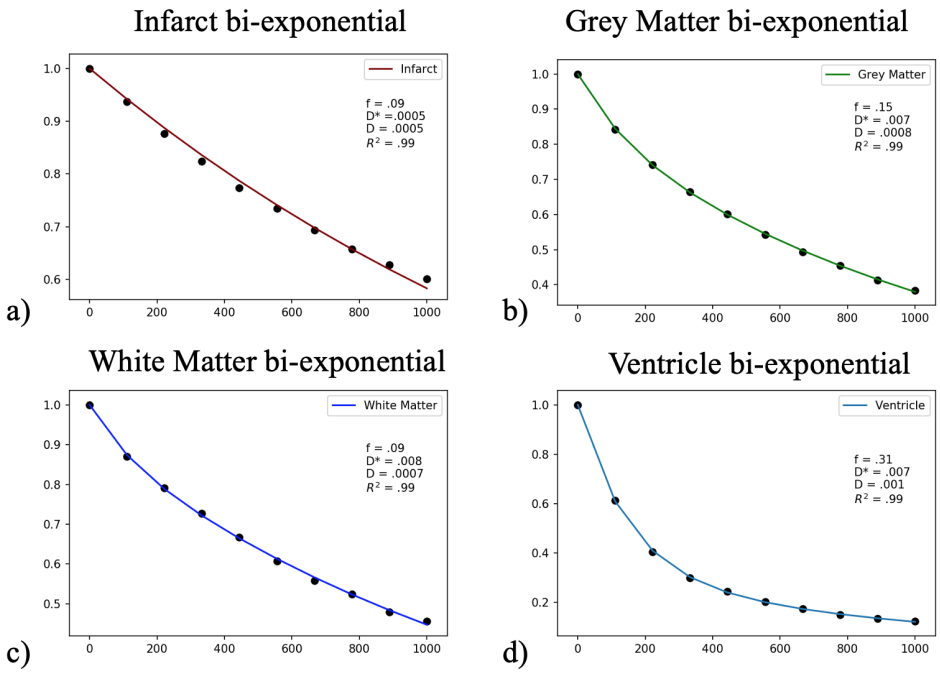

Figure 9.2: Average IVIM bi-exponential fits in a) infarct, b) grey matter, c) white matter, and d) pure ventricles from Fig. 9.1.

However, the subarachnoid space includes voxels with partial volume contamination from cortical tissue as well. The signal is composed of three exponentials potentially representing free CSF flow (D_{csf}, f_{csf}) , tissue perfusion (f, D^*), and tissue diffusion (f_{slow}, D) though this work does not explore this further. The bi-exponential fit of the CSF ROI also behaves differently from a cortical ROI with a much larger fast flowing fraction ($f = .40$), supporting previous literature that removes high f voxels (Federau et al. [2014]).

It should be noted that segmentation of CSF based on exponential behavior will only remove CSF that is diffusing differently compared to blood. Exogenous contrast allows measurement of the CSF lining the capillaries because it is separated physically by the blood-CSF barrier. Endogenous contrast though will measure signal from both blood and CSF lining the capillaries. If those two behave following similar diffusive properties they are difficult to untangle. Fig. 9.1 shows that CSF lining the cortex and in the ventricles definitely demonstrates different fluid behavior from perfusion. Removal of these high values

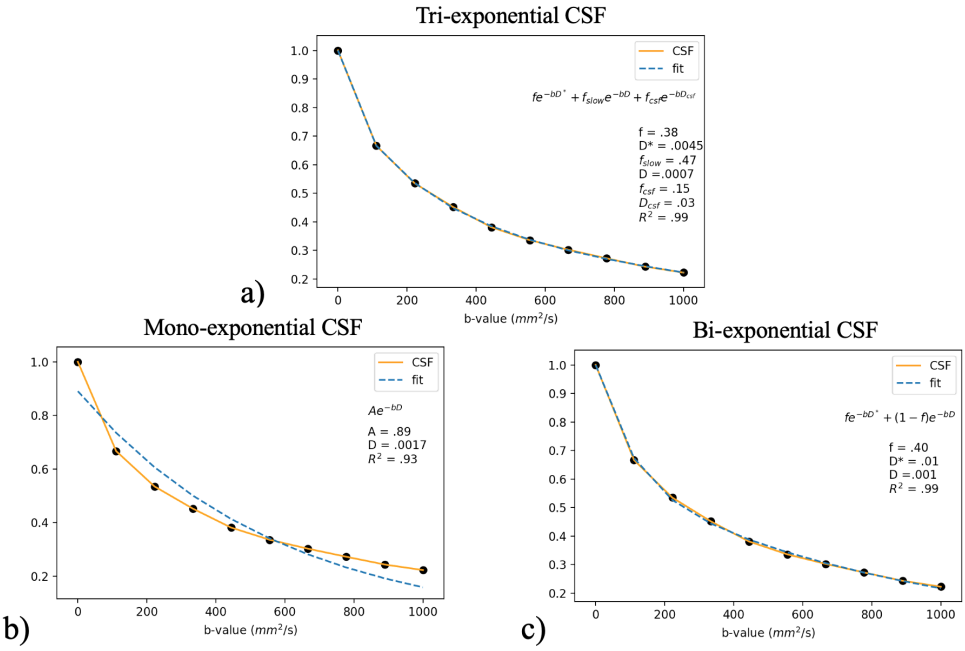

Figure 9.3: IVIM mono-exponential, bi-exponential, and tri-exponential fits in all CSF from Fig. 9.1. Tri-exponential fits return the minimum error and may demonstrate the partial volume contamination of subarachnoid space.

of fluid motion based on differing exponential behavior may be a step towards removing CSF automatically during post-processing. Further physiology of CSF is needed to study how CSF lining the capillaries could be removed, and if it is necessary.

9.2.2 Independent Component Analysis

Separation of the IVIM tri-exponential into three compartments with differing diffusion coefficients could return a method of measuring partial volumes of voxels. Independent component analysis (ICA) was applied as a source separation technique (Tharwat [2021]). ICA is typically used to separate a mixture of independent sources without knowing about the source signals. The tri-exponential behavior is assumed to be a sum of weighted mono-exponentials from independent sources of moving fluid within a voxel. In other words the IVIM signal curve is the 'mixed signal' in which each exponential is its own source and is multiplied by a mixing matrix.

$$\mathbf{X} = \begin{pmatrix} x_1 \\ x_2 \\ x_3 \end{pmatrix} = \begin{pmatrix} a & b & c \\ d & e & f \\ g & h & i \end{pmatrix} \begin{pmatrix} s_1 \\ s_2 \\ s_3 \end{pmatrix}$$

To study the feasibility of using ICA in three component separation, a simulation was written. First, three signals were written with $s_1(b) = e^{-Ab} + c$, $s_2(b) = A\sin(.5b)$ and $S_3 = \text{rect}(b)$, multiplied by the mixing array, and reconstructed via FastICA (Pedregosa et al. [2011]).

$$\begin{pmatrix} 1 & 1 & 1 \\ 0.5 & 2 & 1.0 \\ 1.5 & 1.0 & 2.0 \end{pmatrix}$$

Then a tri-exponential of three compartments, A) perfusion, B) diffusion, and C) CSF, was built with the diffusion coefficients retrieved from the average IVIM curves from anatomic ROIs. The average diffusion coefficient values were A) $D^* = 0.0087$, B) $D = 0.0008$, C) $D_{csf} = 0.003$. These were then summed with various weights that would sum to 1.

$$Ae^{-bD*} + Be^{-bD} + Ce^{-bD_{csf}}$$

The two simulated ICA results are shown in Figure 9.4. While ICA did work for clearly independent signals with significantly different original signal patterns (left column), it did not reconstruct the three compartment exponentials of IVIM (right column). This suggests ICA would not be ideal for CSF separation of partial volume contamination in a tri-exponential IVIM model. A tri-exponential model could be used as shown in the one test case presented, but further work regarding proposed compartments, a reference standard truth to compare CSF to, and computational load of tens of thousands of tri-exponentials is beyond the scope of this work.

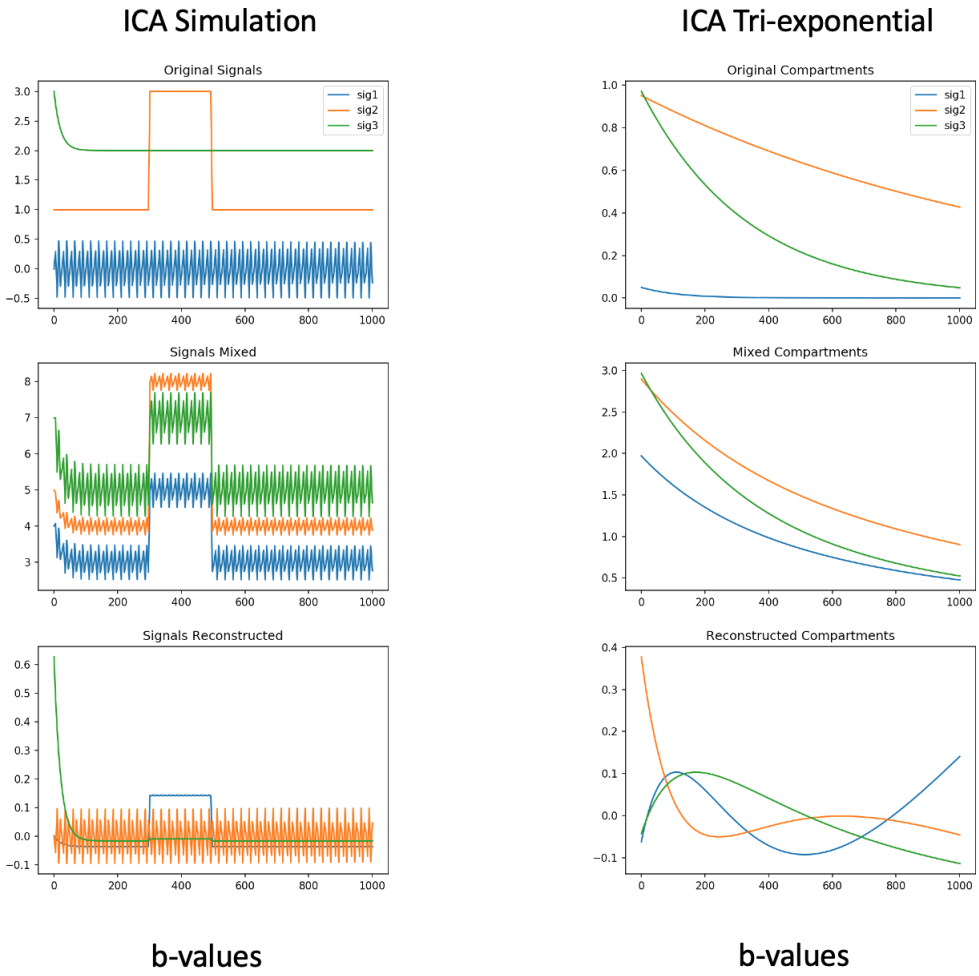

Figure 9.4: Left column: ICA simulation with three independent original signals s_n, them mixed, and then the reconstruction of the original signals from the mixed signals via ICA. Right column: ICA simulation with three mono-exponential curves for three fluid compartments (perfusion, diffusion, and CSF respectively). The mixing with different weights as tri-exponential IVIM curves for a voxel and then the last row showing the reconstruction of the exponentials via ICA

9.3 Inversion Recovery for CSF Suppression

As described in Section 2.3.5, inversion recovery consists of a spin-echo sequence (90° - 180°) that has been preceded by a 180° pulse. The preparatory pulse inverts longitudinal magnetization, and as the spins begin to realign with the main B_0 field, at the rate of T1, and flip from being antiparallel to parallel to the main B_0 field. If the excitation pulse is applied at the null point of a certain tissue, where the longitudinal magnetization is crossing zero, the signal from this tissue is suppressed. Once it is knocked into the transverse plane by the 90° pulse it is subject to both T1 and T2 effects until the 180°.

Questions remain regarding the origin of fast water motion signal, with Kwong et al. [1991] showing that use of an inversion recovery pulse designed to null CSF significantly reduced cortical gray matter pseudo-diffusion fraction. Further, after noting the pseudo-diffusion coefficient without the inversion recovery pulse was seen in some regions to approximate free water such as CSF, authors concluded that for cortical gray matter much of the bi-exponential behavior resulted from CSF contamination rather than perfusion. An inversion recovery spin echo sequence was run to, null CSF, and test the IVIM sequence on a healthy human volunteer. Simulations were performed with an inversion recovery spin echo sequence applied to literature values of T1 and T2. The effect of inversion recovery on CSF, white matter, grey matter, arterial blood, venous blood, and gd contrast was studied. This simulation was expanded to demonstrate the effect of the inversion recovery pulse on blood and examine if the loss of blood signal in human studies with inversion recovery IVIM may be due to confounding effects of inversion rather than proof of all IVIM signal being from CSF.

9.3.1 Inversion Recovery Human Volunteer Results

To compare expected T_{null} using Eq. (9.1), $b0$ scans were run on a healthy volunteer with varying inversion times from 1600 to 3000ms. Multiple DWI with $b = 0$ were run and signal

was measured as the ratio of an ROI centered in the lateral left ventricle to an ROI of the deep white matter with minimal CSF. The results are shown in Fig. 9.5a, with a visual comparison of the $b0$ images with the literature value and the null point value determined by varying inversion time (TI). TE was set to the shortest possible time allowed by the scanner at $TE = 37ms$. One ROI was drawn at the center of the left ventricle to capture CSF signal and applied to all images. The average signal as a function of inversion time is shown in Fig. 9.5a, with the minimum shown at 1850ms.

The IVIM sequence we determined optimized human imaging was then written to include an IR pulse at $TI = 2000$ and an identical sequence with $TI = 1850ms$. These were written with the shortest possible $TE = 108ms$. The images were post-processed using the standard bi-exponential and it was found that much of the signal was lost for both inversion times, Fig. 9.5b, agreeing with Kwong et al. [1991]. Signal in grey matter with inversion recovery $TI = 1850ms$ and $TI = 2000ms$ is much lower than the standard IVIM. Highlighted with the comparison between slice 2 with $TI = 1850ms$ and no IR in Fig. 9.5b, there is clear loss of fast signal with the inversion pulse. The common conclusion reached from these prior studies has been that IVIM predominately measures CSF.

9.3.2 Inversion Recovery Spin Echo Simulation

A simulation of an Inversion Recovery Spin Echo (IRSE) was written to examine transverse signal subject to diffusion weighting spin echo if a CSF-nulling inversion recovery pulse were introduced. This presented a possible explanation for the signal loss beyond CSF contamination. The sequence is shown in Fig. 9.6. After the first 180° inversion pulse as the signal regrows along the longitudinal axis it crosses the axis flipping from antiparallel to parallel to the main B_0 field as shown in Fig. 2.9b. If the spin echo is played as a T1 curve crosses the axis, the signal flipped into the transverse plane by the 90° pulse will be zero for that specific tissue type. The remaining diffusion weighted sequence and signal decay in the

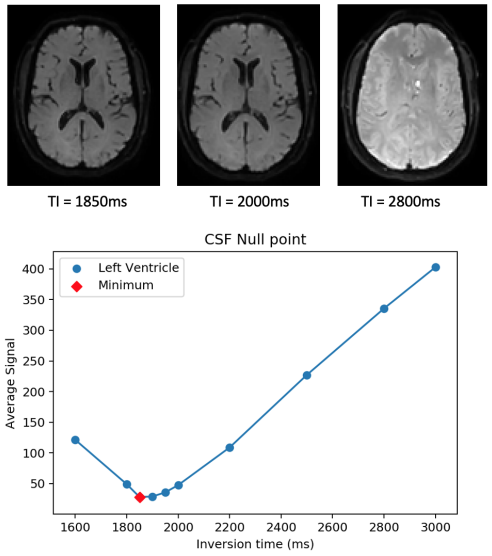

(a) Comparison of same slice same sequence with two IR times and one without IR.

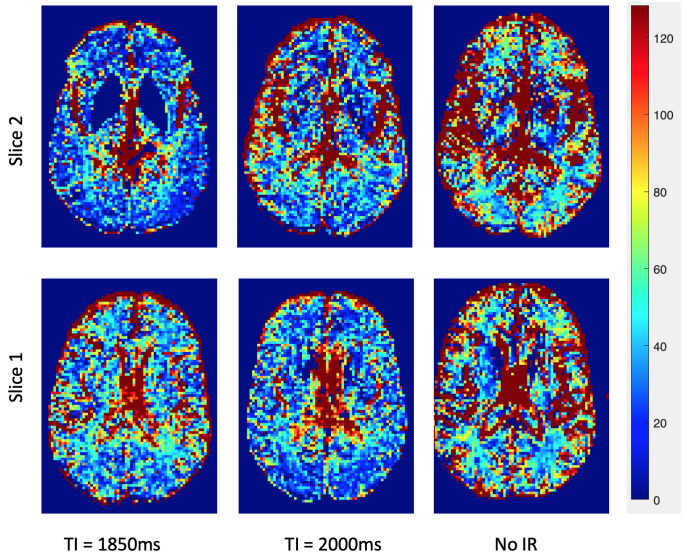

(b) Comparison of IVIM qCBF with two IR times and one without IR.

Figure 9.5: To note, in 9.5b the ventricles and subarachnoid space didn't have all signal removed. This means that these areas were still normalized to the b0 and fit with a bi-exponential and the corresponding parameters fD^* shown. The bright values in the ventricles are therefore not proportional to the amount of CSF signal.

transverse plane will now only be applied to the tissue type that has not been nulled.

An approximation of IRSE with T1 effects can be used to calculate the T_{null} of CSF. This involves setting $M_z = 1 - e^{-t/T1}$ to $\frac{1}{2}$ and solving for t. Using literature value of CSF T1 for 3.0T being roughly 4000ms, the inversion time estimated as $\ln(2) \times 4000 = 2800$ms. However, when using this number CSF signal remained dominant (see Fig. 9.5a).

The limits of the approximation can be explained through Eq. (2.8), $M_z = M_0 \left(1 - 2e^{-\frac{TI}{T1}} + e^{-\frac{TR}{T1}}\right)$. If $TR << T1$, this equation returns the previous approximation of $T_{null} \approx \ln 2 \times T1$ as $e^{-\frac{TR}{T1}} \to 0$. However, if TR is close to T1, solving for t_{null} returns

$$0 = 1 - 2e^{-\frac{T_{null}}{T1}} + e^{-\frac{TR}{T1}}$$

$$2e^{-\frac{T_{null}}{T1}} = 1 + e^{-\frac{TR}{T1}}$$

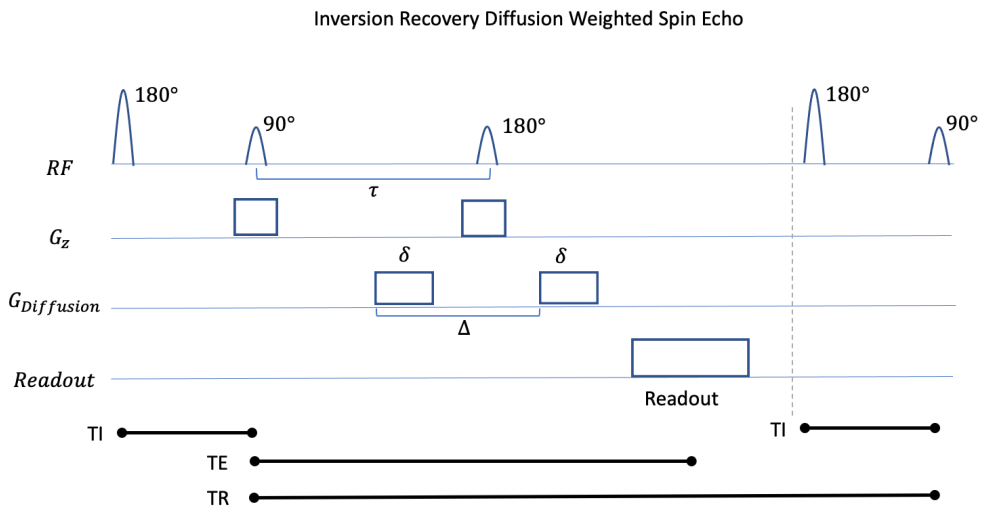

Figure 9.6: Example of Inversion Recovery Diffusion Weighted Spin Echo sequence.

T1 and T2 Simulated Values		
Biological Tissues	T1	T2
CSF	4500	50
Arterial blood	1650	100
Venous blood	1650	20
GBCA blood	500	50
White Matter	790	237
Grey Matter	1495	160

Table 9.1: T1 and T2 values assumed for various biological tissues and fluids (Zhang et al. [2013], Wansapura et al. [1999], Daoust et al. [2017], Lin et al. [2012], Rohrer et al. [2005])

$$-\frac{T_{null}}{T1} = \ln\frac{1}{2} + \ln\left(1 + e^{-\frac{TR}{T1}}\right)$$

$$T_{null} = T1 \times \left[\ln 2 + \ln\left(1 + e^{-\frac{TR}{T1}}\right)\right]. \tag{9.1}$$

This T_{null} is the time to play the IR pulse to have as close to zero signal flipped into the transverse plane as shown in Fig. 9.7, while maximizing the signal of other tissues of interest. For CSF with a T1 = 4000 - 5000ms, and our sequence with TR = 5000, this returns $T_{null} = 1770 - 1900ms$. This is shown in Fig. 9.7b and does agree with the experimental results laid out in Section 9.3.1.

The signal amplitude flipped into the transverse plane at a given inversion time is the

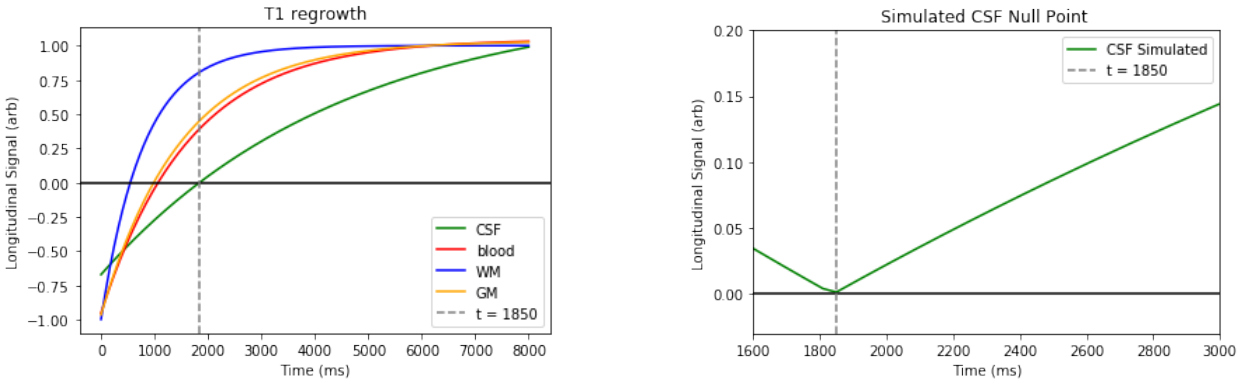

(a) (b)

Figure 9.7: a) Simulated longitudinal signal given standard T1 values for a 3.0T MRI of various biological tissues and fluids. b) The simulated longitudinal CSF signal over time within the range of likely inversion times.

M_0 in the T2 equation $M_0 e^{-\frac{t}{T2}}$. Setting the inversion time TI $= T_{null}$ means the transverse signal in the rotating frame is then the same as Eq. (2.9), ignoring diffusion effects:

$$M_x(t) = \left(1 - 2e^{-\frac{TI=T_{null}}{T1}} + e^{-\frac{TR}{T1}}\right) e^{-\frac{TE}{T2}}.$$

This equation is plotted in Fig. 9.8 as a function of TI. Fig. 9.8 shows the signal that would be available before diffusion weighted decay using the values in Table 9.1. It is set with $TI = 180ms$, $TR = 5000ms$, and $TE = 37ms$ as the shortest possible at $b0$ or $TE = 108ms$, which was the shortest for an IVIM sequence with multiple b-values.

Seen in Fig. 9.8 the IR pulse at the CSF null point of $T_{null} = 1850ms$ suppresses both CSF as well as arterial and venous blood when the T2 weighting effects are taken into account. As approximately 75% of the blood signal results in a dramatic underestimation of perfusion, the effect could also be misinterpreted as "supressing CSF reduces CBF, therefore IVIM CBF signal must be due to CSF". This is particularly true for a longer $TE = 108ms$. This is because despite the T1 and T2 of CSF and blood being different, the combination of both effects effectively nulls both with a suppression pulse intended to only null CSF based on T1. The simulation does suggest that this effect can be mitigated if there is GBCA in

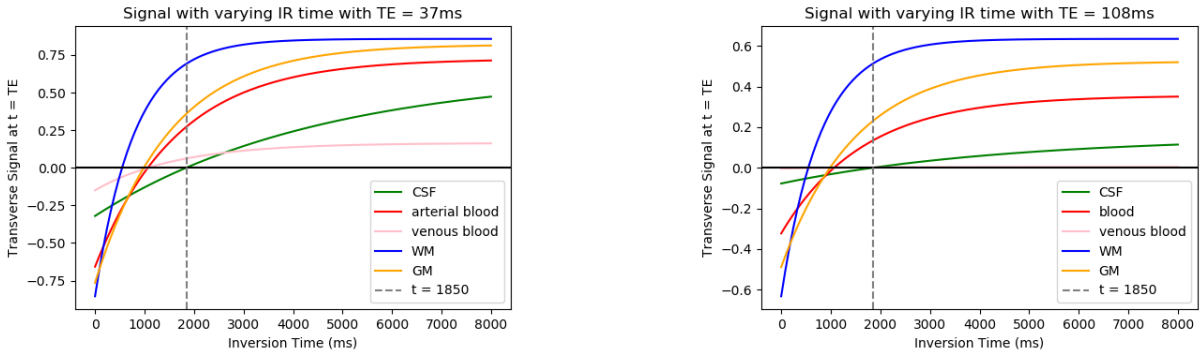

(a) (b)

Figure 9.8: a) Simulated transverse signal given standard T1 and T2 values for a 3.0T MRI of various biological tissues and fluids with TR = 5000ms, TE = 37ms. b) Simulated transverse signal given standard T1 and T2 values for a 3.0T MRI of various biological tissues and fluids with TR = 5000ms, TE = 108ms.

the system effectively shortening the T1 of the blood, as demonstrated in Fig. 9.9, with values from Table 9.1. In Fig. 9.9, especially at $TE = 37ms$, there is still a large portion of arterial blood signal remaining with an inversion time at $T_{null} = 1850$ compared to blood without GBCA. At $TE = 108ms$, there is again a smaller portion of arterial blood signal, but still remaining signal compared to CSF suppressed. Venous blood is essentially completely suppressed for all $TE = 108$, but for a short $TE = 37ms$ there is still some signal. It should be noted that the blood signal is suppressed significantly for all simulated IR sequences.

9.3.3 Blood Signal Suppression

Focusing on separating between CSF suppression and blood signal suppression is Fig. 9.10. With $TR = 5000ms$, $TE = 108ms$, the solid lines show remaining signal from CSF (blue) and blood (red) if only longitudinal decay is considered. The combined T1 and T2 effects on transverse signal are shown with dashed lines and represent the signal within the transverse plane as it undergoes T2 decay. At $TI = 1850ms$ (vertical dotted line), the best time for CSF suppression (blue circle) shows the cost of blood signal suppressed (red circle). While only T1 effects (dashed) suggest reasonable regrowth, when considering both T1 and T2

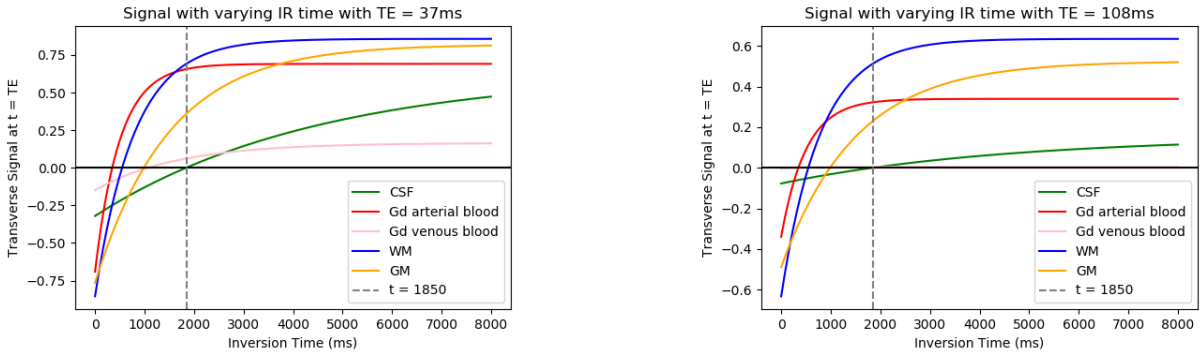

(a) (b)

Figure 9.9: a) Simulated transverse signal with GBCA modified blood T1 with TR = 5000ms, TE = 37ms. b) Simulated transverse signal with GBCA modified blood T1 with TR = 5000ms, TE = 108ms.

(solid) blood signal is not recovered (red circle).

The inclusion of T2 effects may explain part of the loss of blood signal observed with inversion recovery IVIM. Breaking down the IRSE recovery curve into T1 and T2 effects, simulation inversion recovery spin echo to suppress CSF signal in IVIM showed the optimal TI=1850 for CSF-suppression would also suppress blood signal to 13% of its original. This suggests that CSF may be better removed during post-processing to avoid loss of blood signal.

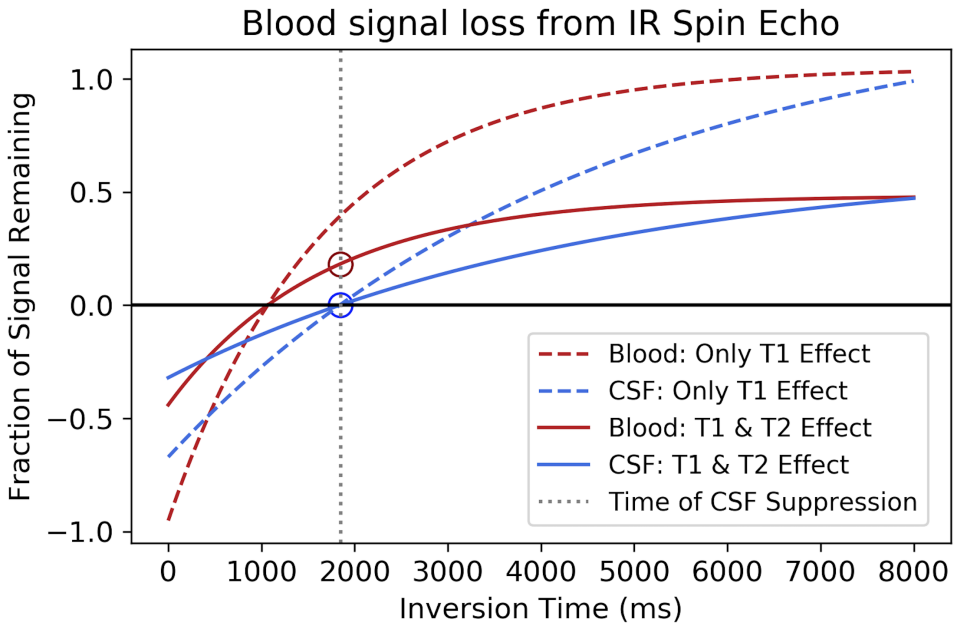

Figure 9.10: Simulated Inversion Recovery Spin Echo with T1 effects only (dashed), and T1 and T2 effects (solid), for CSF and blood signal. Shown blood signal suppressed to 13% of the original signal with inversion recovery due to T1 and T2 combined effects.

9.4 CSF Removal via Automatic Thresholding

9.4.1 Leave-One-Out Cross-Validation

Leave-One-Out Cross-Validation (LOOCV) is used to evaluate the performance of a model on a data set and to measure the accuracy of predictions made by the model to the observed data. In practice, typically a model is tested on data by splitting the data of size n into a training set and a testing set. The model will be trained by the training set, and this model's accuracy in predicting on new data will be tested on data that the model has not seen before, i.e., with the testing set. If there is a large amount of data, the data is typically split into training and testing sets which should in theory be random without any bias and equal predictors of the data as a whole. If, however, the data set is small, it may be difficult, if not impossible, for the data to be split into a training and testing set with sufficient size. LOOCV is one way of minimizing this problem.

LOOCV is computationally expensive, and involves dividing a finite data set into varying divisions of testing and training data. For each division, a subset of the data will be the 'training' data, while the remaining data is the 'testing' data. With LOOCV, with each partition of the data one data is 'left out' as the testing data and a new model is generated and tested on the corresponding left-out data. k-fold cross validation is when instead of one data point being left out, k-data are left out as a testing set. This makes it less computationally expensive or time consuming. The model is evaluated by the average of the test set results. An example of the data division is shown in Fig. 9.11a, and a work schematic of k-fold CV is shown in Fig. 9.11b.

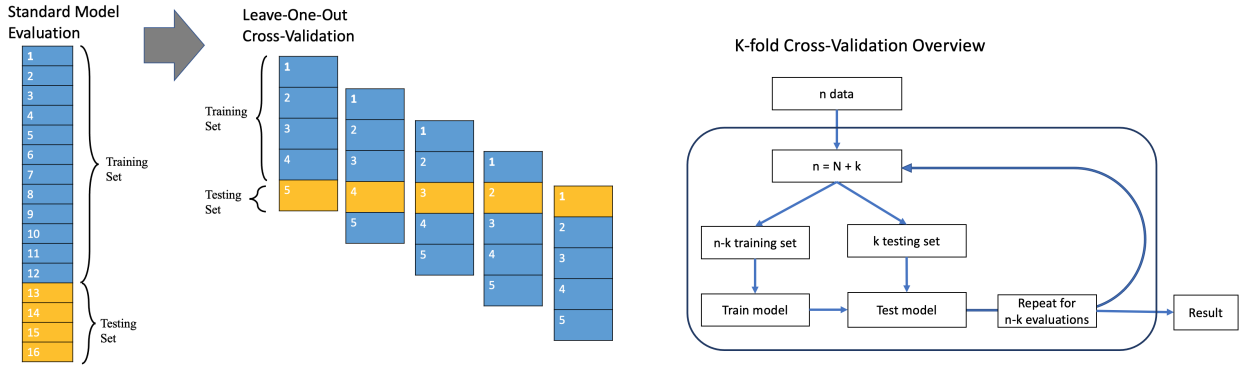

(a) (b)

Figure 9.11: a) Leave-One-Out Cross-Validation data division. Shows an example of typical training testing, as well as a LOOCV with 5 subjects and the 5 different possible training and testing set combinations. b) k-fold CV work schematic showing input and output result.

9.4.2 Nested Leave-One-Out Cross-Validation

For a comparison of segmentation across three physiologic states, nested LOOCV is used to both determine a model as well as measure the model's predictive ability independently of each other to avoid underestimating error and overfitting data. The inner LOOCV loop uses the training set of the outerloop. That training set is split into model training and model validation and LOOCV is used on those different divisions of data to create an ensemble. That is, on every model training set, the model is trained and then validated against the

validation set, and the best model is determined by that validation set. This inner loop is done for every possible iteration of the outer loop. The best validation set from every outer loop is averaged to create an ensemble, which is then tested against the testing set of the outer loop. A diagram of the division of data into an inner and outer LOOCV loop independently is shown in Fig. 9.12. Here, there are 5 total subjects. The outer loop is LOOCV $k = 1$, so there are 5 possible training set and testing set divisions. Of each of those 5 possible training sets composed of 4 subjects each, there are 4 possible divisions into different training and validation sets in the inner loop. Three of the subjects within the inner loop will be used to fit a model of interest. One of the subjects will be used to validate the model. Across all 4 inner loops, the best predictor will be chosen. This means one model is fit per outer loop. The models are averaged into an ensemble and then tested in the outer loop to determine the model metric, i.e., how well the model does perform.

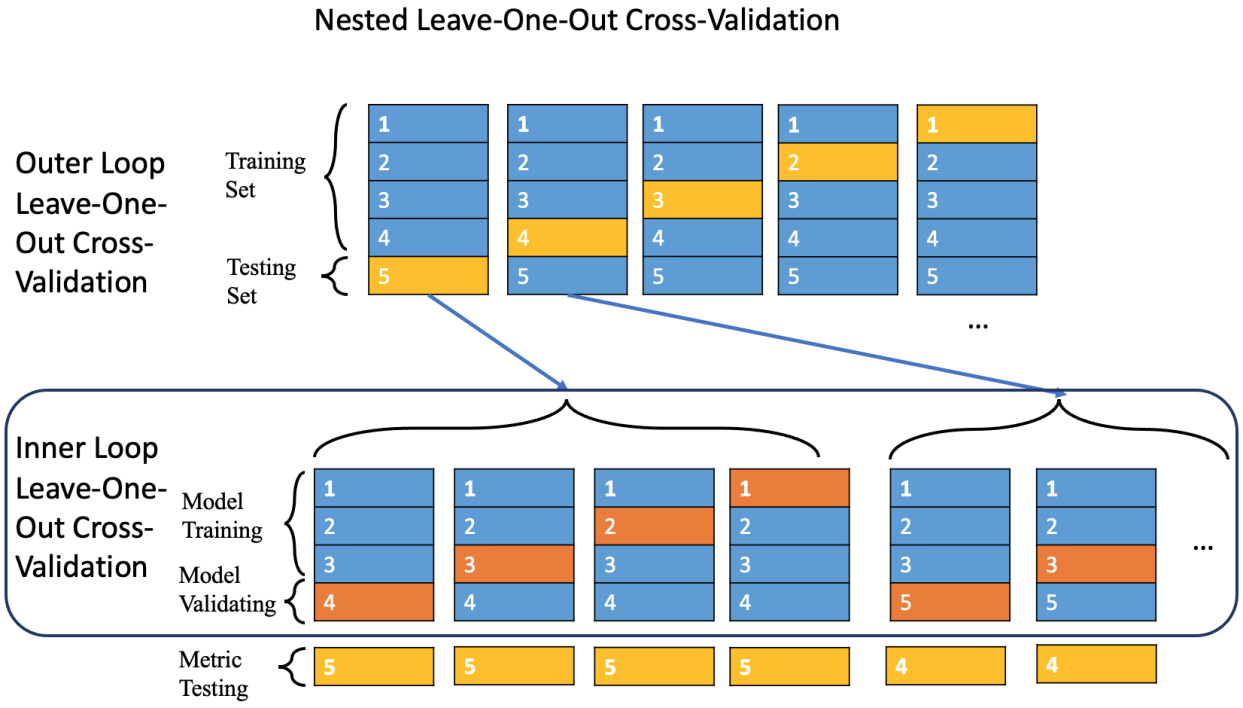

Figure 9.12: An example of a data set split into training, validation, and testing groups for inner and outer loop of a nested LOOCV.

9.4.3 Results

CSF is bright in T2 weighted images, which are equivalent to the $b0$ images of IVIM without IR suppression. Therefore, ROIs can be drawn in the ventricles and the subarachnoid space to remove CSF-dominated voxels from the IVIM diffusion images. An example of this in a canine coronal T2 image is shown in Fig. 9.13. Automatic thresholds on 1) T2 signal and 2) monoexponential diffusion DWI (D_{mono}) were tested and compared as potential classifiers via LOOCV at three physiologic states 1) normocapnia, 2) hypercapnia, and 3) post-MCAO. These automatic threshold CSF masks were trained on hand-drawn segmentations on T2 weighted $b0$ images in 11 cases, 3 slices each, of coronal canine images. Success was gauged by the Dice similarity coefficient. Results of nested LOOCV thresholding is shown in Table 9.2. An example of the masking is shown in Fig. 9.13.

	T2 Threshold	T2 Dice	D_{mono} Threshold	D_{mono} dice
Normocapnia	323	$.72 \pm .05$	0.0015	$.56 \pm .10$
Hypercapnia	337	$.67 \pm .05$	0.0097	$.42 \pm .03$
Post-MCAO	331	$.62 \pm .07$	0.0010	$.42 \pm .05$

Table 9.2: Thresholds and corresponding Dice coefficients compared to hand-drawn CSF segmentation.

CSF segmentation is simple in the ventricles, but subarachnoid space is more variable due to partial volume effects. To highlight this variability, at normocapnia a second set of hand-drawn masks were drawn blinded to the originals with a focus on subarachnoid space. These returned an average Dice coefficient of $.63 \pm 0.12$ emphasizing the difficulty of agreement. Automatic thresholding via nested LOOCV and hand-drawn ROIs return a wide range of Dice scores emphasizing the difficulty of removing CSF from partial volume contamination.

A higher threshold was found to optimize CSF segmentation at hypercapnia compared to normocapnia for both T2 and D_{mono} thresholding. The increase in both thresholds is likely due to the increase in blood volume at hypercapnia (van der Kleij et al. [2020]). Hypercapnia thresholding also returned a lower Dice coefficient than normocapnia for both thresholds.

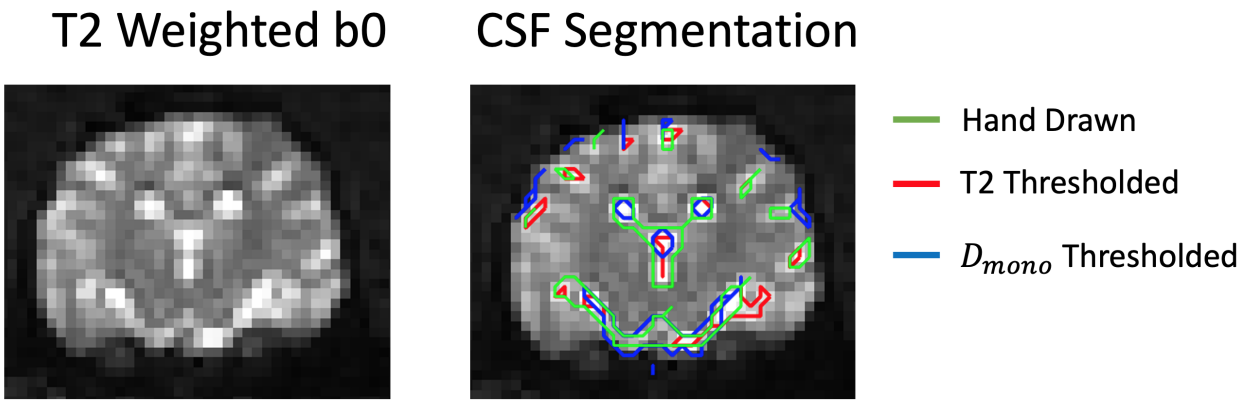

Figure 9.13: An example of a T2 weighted $b0$ image (left) with a hand-drawn mask, a T2 thresholding mask, and a D_{mono} mask superimposed (right). The Dice coefficients compared to the hand drawn mask for this image are 0.58 for T2 thresholding and 0.40 for D_{mono}. Images appear pixelated due to the low resolution that is not smoothed to preserve the thresholding masks

This suggests that at hypercapnia, the increase blood volume may make CSF partial volume effects more difficult.

Post-MCAO returned a T2 threshold between normocapnia and hypercapnia thresholds potentially due to the increase in blood volume and flow on the contralateral hemisphere, dependent on collateralization. Further, infarction decreased the blood flow on the ipsilateral side, while CSF would still remain in the ventricles and subarachnoid space with movement due to brain pulsatility. The varied behavior between hemispheres may contribute to the lower Dice score.

T2 weighted $b0$ thresholding outperformed diffusion weighted D_{mono} at all physiologic states. This is expected as the CSF segmentations were drawn on the standard T2 weighted images. However, use of D_{mono} and their Dice coefficients $> .40$ shows voxels do contain statistical difference in diffusivity in CSF-dominated regions and supports future study of diffusion parameters for CSF removal.

9.4.4 Conclusions

A threshold applied to either a T2 weighted image or a mono-exponential diffusion coefficient of IVIM could return a CSF mask with varying degrees of success. T2 thresholding of a normocapnic brain returned the highest outerloop dice coefficient of .72. Average outerloop Dice coefficients ranged from 0.42 to 0.72, with T2 thresholding returning higher Dice coefficients than D_{mono} thresholding. Average Dice scores between hand-drawn segmentations was 0.63, emphasizing the difficulty of CSF separation specifically in the subarachnoid space. While not reported, an inner loop with k-fold CV, rather than LOOCV, was tested as a method of reducing computational load; however, due to the small number of subjects LOOCV was ultimately determined to be required.

Dice scores of automatic T2 weighted $b0$ images were expected to be highest, as those were the base images used for hand-segmentation. This was shown to be the case across all physiologic states. However, T2 weighted images may have varying signal as a function of FOV, voxel size, and automatic range determined by the scanner. In comparison, the mono-exponential maps were determined by the fit of 10 b-values normalized to $b0$ to an exponential. This normalization would, in theory, allow for the same threshold to be used across different scans. The cost of this would be fit error and effect of high b-value diffusion which was not taken into account for the hand-segmentation. This allows potential overlap of mono-exponential CSF estimation with fast perfusion which could be a confounding effect especially at hypercapnia. Further exploration of this involves training on an IVIM bi-exponential which would include diffusion at both high and low b-values.

9.5 Supervised Machine Learning Segmentation via IVIM

As described in Section 9.4, CSF is typically observed as bright on T2 weighted $b0$ images. However, CSF is not only differentiated by its T2 decay, but also by its movement. CSF physiology is complex and an active area of research; there are multiple effects including

pressure gradients, pulsatile flow from cardiac and respiratory motion, and unrestricted flow in ventricles. In comparison, tissue diffusion is restricted, and tissue perfusion is constrained by the capillary bed. Therefore, difference in IVIM exponential signal behavior between CSF and non-CSF (9.2) could be used to segment CSF during IVIM post-processing. This would avoid the difficulty of blood suppression from inversion recovery (9.3.3), and the question of human bias when removing bright signal. Further, with LOOCV seeming to be a fair method of removing CSF-dominated pixels, by applying machine learning to IVIM bi-exponential parameters we can explore if the IVIM signal and fits can separate between perfusion and CSF fluid flow. If bi-exponential parameters are statistically different enough in CSF regions, this would further validate IVIM signal in cortical and deep white matter tissue being from blood perfusion and not only CSF contamination. However, again it could not remove signal from CSF in the perivascular space that moves similar to blood in the capillaries.

Supervised machine learning involves using labeled data sets to train algorithms that classify data. Classification involves developing an algorithm to assign data to specific categories or labels. One such method is discriminant analysis. Discriminant analysis classification is a dimensionality reduction technique commonly used in supervised classification to separate groups or classes. Linear discriminant analysis draws a linear line between all possible axes to maximize the distance between means of the two classes and minimize the variation within each class. It assumes normal distribution of classes with different means but equal covariance. Quadratic discriminant analysis does so with quadratic discriminant curves along all possible feature axes, and does not assume equal covariance. For classification with multiple features, feature weights rank the features in order of importance for the classification decision. A demonstration of quadratic discriminant analysis across 3 features is shown in Figure 9.14.

Supervised discriminant analysis success was analyzed via precision, F1 Score (i.e. Dice similarity coefficient), and sensitivity calculated from true positives (TP), true negatives

(TN), false positives (FP) and false negatives (FN). Accuracy was not included due to uneven class distribution.

$$Precision = \frac{TP}{TP + FP}$$

$$Sensitivity = \frac{TP}{TP + FN}$$

$$F1 = 2\frac{Precision * Sensitivity}{Precision + Sensitivity}$$

9.5.1 Training

With the IVIM bi-exponential model returning three features (f, D, D^*) for each voxel (6.1), these three values are used to train a classifier with linear and quadratic discriminant analysis. As a substudy, IVIM bi-exponential parameters used for multi-class segmentation between CSF, cortical gray matter, white matter, and infarct post-MCAO were studied. CSF, grey matter, and white matter ROIs were drawn on T2 weighted images, and infarct was calculated by applying a co-registered ADC maps with an automatic infarct threshold applied. These regions of interest were produced on randomly chosen central slices of nine cases post-occlusion. The number of labeled voxels per each training test are shown in Table 9.3.

Label/State	Normocapnia	Hypercapnia	Post-MCAO
CSF	1745	927	1364
Cortex	2368	1731	1419
Deep WM	1261	845	650
Infarct	0	0	804
Total = 13114	5347	3503	4237

Table 9.3: Number of voxel types at each physiologic state.

With 13,114 voxels labeled either CSF, grey matter, white matter, or infarct, across three physiologic states, discriminant analysis classification was trained on 75% of the cases and

tested on the remaining 25%. This was performed with 5-fold cross-validation.

9.5.2 Analysis

Discriminant analysis was run with five random seeds used to separate the voxels into a training set (75%) and testing set (25%). Linear (circle) and quadratic (triangle) discriminant analysis was trained and tested with these five random seeds. The precision (green), sensitivity (purple), and F1 score (red) were calculated for each of the five runs with average and standard deviation of the performance measures shown. Results are plotted with the markers described and shown with comparison to a dashed line of .72 which was the highest Dice coefficient from automatic thresholding of a T2 weighted image.

9.5.3 Results

Binary CSF segmentation comparing across the three states, as well as all data combined, is shown in Fig. 9.15a. A comparison between using bi-exponential parameters or raw b-value signal for binary segmentation at normocapnia is shown in Fig. 9.15b. Multiclass segmentation at the three separate states is shown in Fig. 9.16a-c. Application of trained baseline model, hypercapnic model, and post-occlusion model to the three physiologic states is shown in Fig. 9.16d-f respectively.

9.5.4 Binary vs. Multiclass

For post-occlusion maps, multiclass discriminant analysis was run to test if bi-exponential parameters could segment CSF, infarct, cortex, and deep white matter. They were trained on labeled data, and processed with both linear and quadratic discriminant analysis. Discriminant analysis was run both on multi-class labels, and on binary CSF. In binary CSF all other classes are treated as "not-CSF", and all that is tested is the ability to classify CSF voxels.

Multiclass:

Shown in Fig. 9.16c, for linear discriminant analysis (circles) on post-occlusion images, CSF and infarct segmentation were strongest with $F1 = 0.70 \pm .02$ and $F1 = .75 \pm .03$ respectively. Precision (green) is higher ($> .80$) while sensitivity (purple) is lower ($< .60$). Grey matter returned slightly lower F1 scores ($F1 = .64 \pm .01$). White matter was poor ($F1 = 0.02 \pm .02$). Cortex was the only classification that returned higher sensitivity than precision ($P = 0.50 \pm .02, S = 0.91 \pm .01$). Quadratic multi-class discriminant analysis (triangles) returned slightly lower F1 score for CSF, and higher F1 scores for the other three classifications compared to linear multi-class discriminant analysis. Most notable increase in F1 score is white matter ($F1 = 0.50 \pm .06$) classification by quadratic discriminant analysis.

Fig. 9.16a-b demonstrate that at baseline and hypercapnia, CSF and cortical gray matter return high F1 scores with quadratic discriminant analysis $F1 > 0.72$ (dashed line). White matter could only be segmented with quadratic discriminant analysis; linear discriminant analysis returned $F1 = 0.004 \pm .006$ at baseline and $F1 = 0 \pm 0$ at hypercapnia. In comparison, with quadratic discriminant analysis, normocapnia returned $F1 = 0.69 \pm .02$, and hypercapnia returned $F1 = 0.65 \pm .01$.

Binary:

Shown in Fig. 9.15a is the binary CSF segmentation. For the post-occlusion model linear discriminant analysis showed high precision, but low sensitivity ($P = 0.96 \pm .02, S = 0.51 \pm .03, F1 = 0.67 \pm .03$). Quadratic discriminant analysis showed lower precision but higher sensitivity ($P = 0.89 \pm .01, S = 0.56 \pm .03, F1 = 0.69 \pm .03$) returning a marginally higher F1 score. Cases at baseline returned the highest F1 score for binary CSF segmentation, specifically via quadratic discriminant analysis ($P = 0.90 \pm .02, S = 0.62 \pm .04, F1 = 0.74 \pm .02$). Hyperpcania quadratic discriminant analysis was also high ($P = 0.91 \pm .01, S = 0.62 \pm .04, F1 = 0.74 \pm .03$)

9.5.5 Linear vs. quadratic

This trend of lower precision and higher sensitivity, yet a higher overall $F1$ with quadratic analysis compared to linear analysis is seen at all states. Fig. 9.15a demonstrates a binary discriminant analysis in which training set and testing set were from the same physiologic state (baseline, hypercapnia, post-occlusion), or all 13,114 voxels from all physiologic states were combined into global data set (All States). Baseline showed the highest F1 scores (red), and quadratic discriminant analysis (triangles) outperformed linear discriminant analysis (circles) across all four data sets. Combined with linear discriminant analysis being unable to segment deep white matter, quadratic discriminant analysis seems optimal for both binary and multiclass CSF segmentation.

9.5.6 Physiologic State Dependence

Shown in Fig. 9.15b performance measures varied across physiologic models, with normocapnia and hypercapnia performing similarly, but post-occlusion returning poorer metrics. This pattern is observed in automatic thresholding (Section 9.4) as well, suggesting it is a factor of the complex physiology post-occlusion.

Application of various models to differing physiologic states was explored to study differences in the models and potential generalizability across physiologic states. Quadratic discriminant analysis again outperformed linear discriminant analysis. The normocapnia model returned reasonable metrics at hypercapnia and post-occlusion (Fig. 9.16d). The hypercapnia model performed poorly post-occlusion (Fig. 9.16e). Interestingly, the post-occlusion model performed better at hypercapnia than at post-occlusion with $F1 = 0.74 \pm .02$ compared to $F1 = 0.69 \pm .03$. This further suggests that the difficulty in post-occlusion segmentation is the complex physiology.

The normocapnia model performed best across all three states suggesting if a model were to be generalized, a quadratic discriminant analysis trained on normocapnia would be

optimal. However, as expected, a discriminant model trained on all states would perform best on all states (Fig. 9.15a).

9.5.7 IVIM Bi-exponential Parameters vs. Raw Values

Shown in Fig. 9.15b linear discriminant analysis of the 10 raw DWI SE values across 10 b-values performed more poorly than use of the three bi-exponential models with $F1 = 0.57 \pm .04$ and $F1 = 0.72 \pm .03$ respectively. Quadratic analysis performed similarly for both types of data with an overlap of standard deviation with $F1 = 0.69 \pm .03$ and $F1 = 0.74 \pm .02$. This suggests feature reduction by use of bi-exponential parameters rather than raw 10 b-value DWI signal is valid for CSF segmentation.

9.5.8 Thresholding vs. Discriminant Analysis

Supervised binary classification via quadratic discriminant analysis of bi-exponential parameters returned higher F1 scores than LOOCV thresholds of D_{mono}, as shown in Table 9.4. Use of QDA on bi-exponential parameters demonstrated several benefits compared to automatic thresholding via LOOCV. First, while automatic thresholding of T2 weighted images did return reasonable dice scores, this is not easily generalizable. T2 weighted images may have varying signal as a function of FOV, voxel size, and automatic range determined by the scanner per experiment. This may vary even within the study, let alone across multiple studies, scanners, and hospitals. Second, while D_{mono} attempted to remove these effects with a normalized signal fit to a mono-exponential, thresholding of the mono-exponential returned the lowest performance metrics. This may be due to the loss of the fast-behavior at low b-values due to CSF, or the difference in diffusing behavior at high b-values. By treating every voxel as a single compartment, data regarding various components is lost. Finally, QDA of the bi-exponential model captures the benefits of both T2 weighting thresholds and D_{mono} thresholds. It is normalized to remove scanner range, FOV, and voxel size effects,

and it includes both fast-behavior and slow-behavior. Further the use of three parameters with quadratic discriminant analysis allows classification of different variances, which is to be expected when separating CSF and non-CSF. Separation based on tri-exponential parameters was not explored. Shown in Table 9.4, quadratic discriminant analysis did return higher dice coefficients than D_{mono} across all states. It performed similarly to a T2-threshold with standard deviation overlap.

State/Analysis	T2-threshold	D_{mono}-threshold	QDA bi-exp
Normocapnia	$.72 \pm .05$	$.56 \pm .10$	$.74 \pm .02$
Hypercapnia	$.67 \pm .05$	$.42 \pm .03$	$.74 \pm .03$
Post-MCAO	$.62 \pm .07$	$.42 \pm .05$	$.67 \pm .03$

Table 9.4: Dice score for automatic thresholding and F1 score for supervised machine learning algorithm compared to hand-drawn segmentation at three different physiologic states.

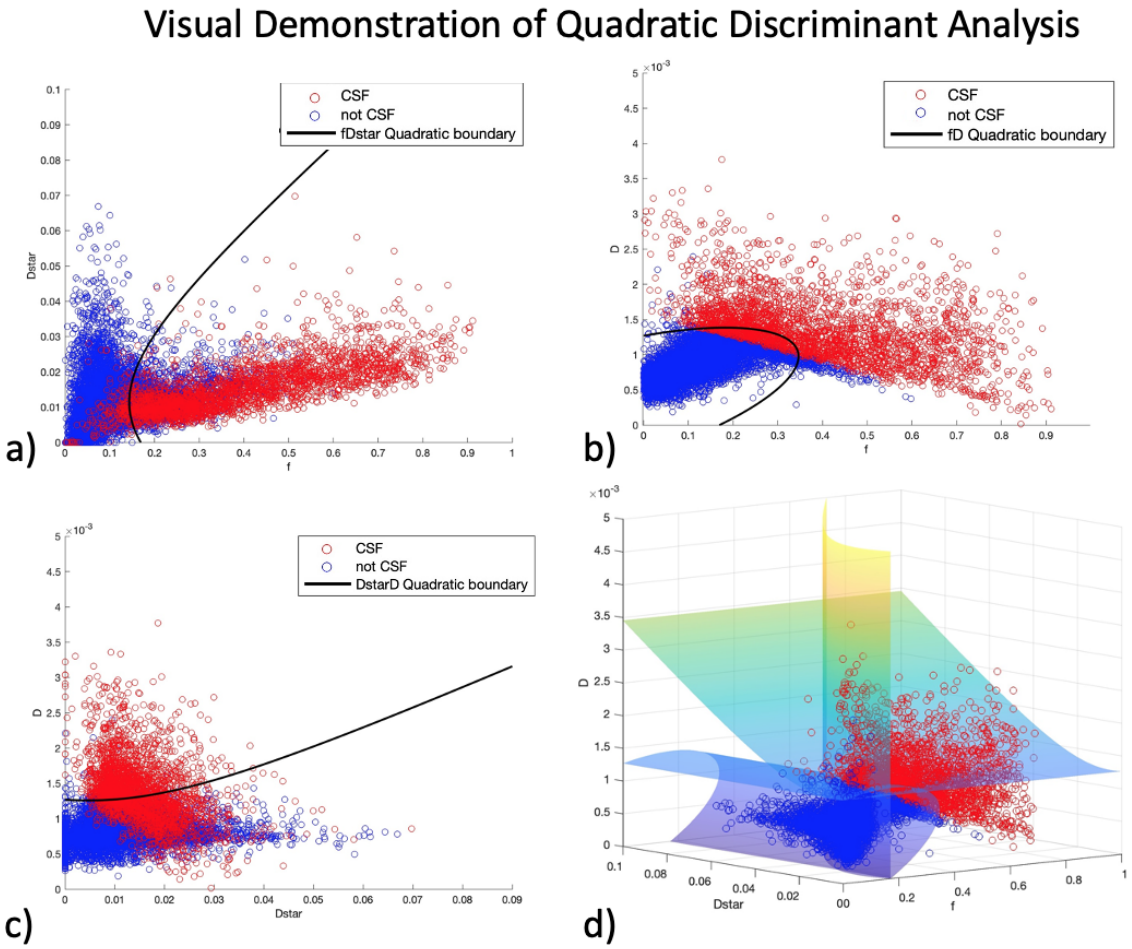

Figure 9.14: Supervised Machine learning via binary quadratic discriminant analysis of CSF (red) and non-CSF (blue) with boundaries between three IVIM parameters ($f, D*, D$). Figures a-c show projections of the quadratic discriminant lines between the three combinations of parameters. Figure d) shows the 3D discriminant planes.

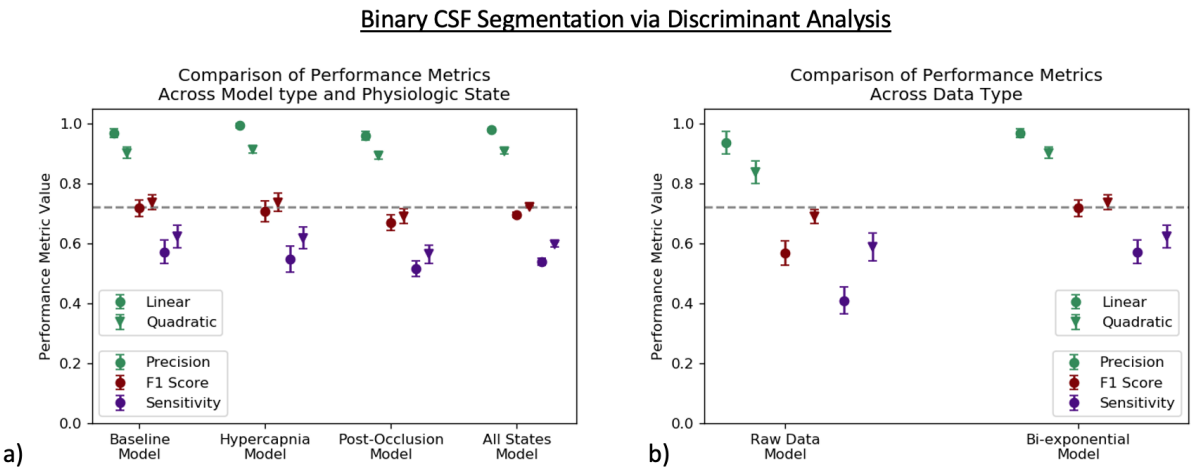

Figure 9.15: a) Binary discriminant analysis at three physiologic states and all combined states. b) Binary discriminant analysis comparing using the 10 b-value raw DWI SE signal $S_{b=0}, S_{b=100}, ...S_{b=1000}$ versus bi-exponential parameters f, D, D^* as features. A horizontal line at 0.72 is included for ease of comparison between plots.

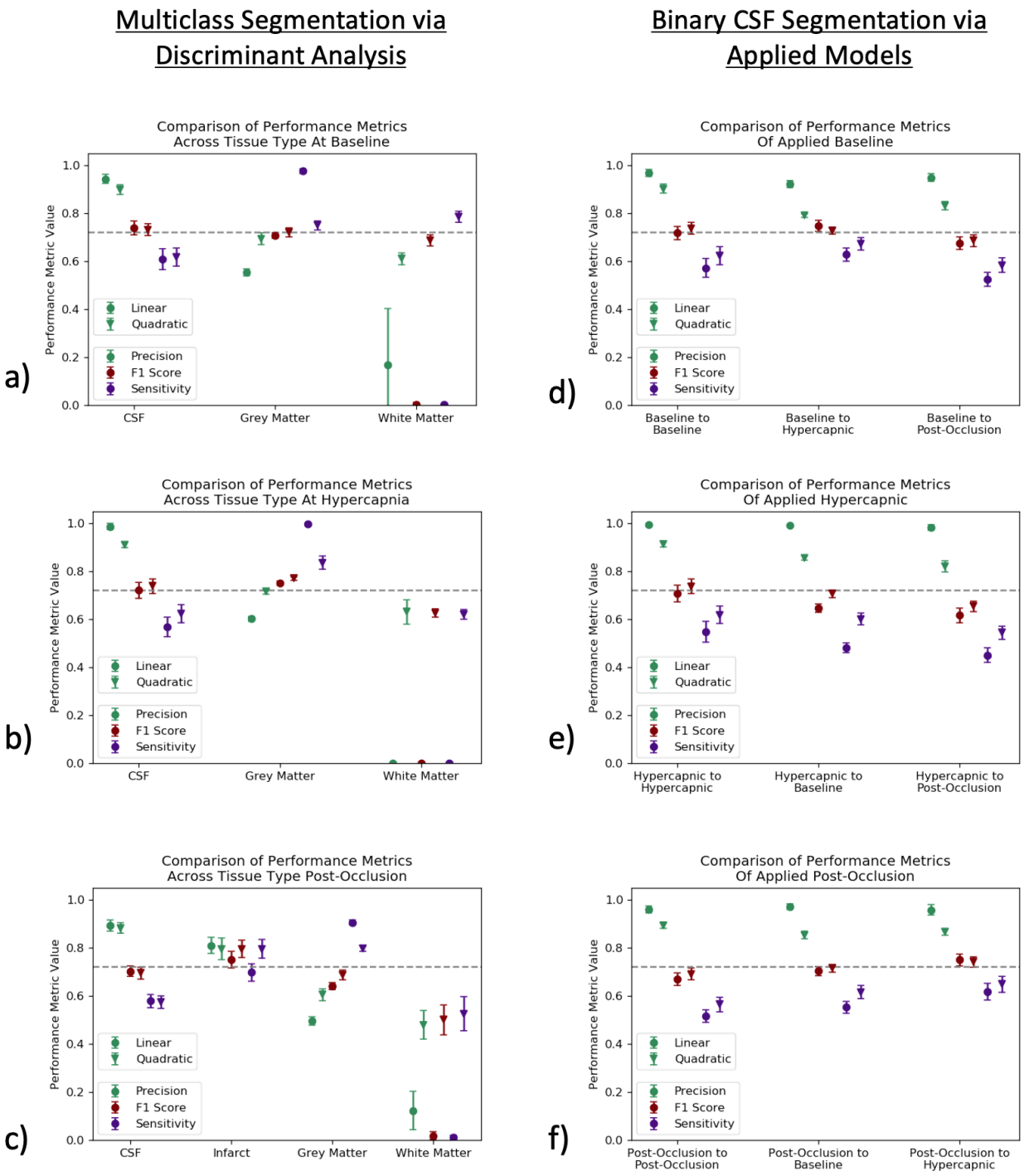

Figure 9.16: a-c) Multiclass segmentation at each of the three physiologic states into CSF, grey matter, white matter, and infarct. d-f) Binary segmentation of models trained on one physiologic state and applied to other testing sets to explore differences in success. A horizontal line at 0.72 is included for ease of comparison between plots.

9.6 Applied Supervised Machine Learning Classification

9.6.1 Introduction

Study of supervised machine learning (ML) on bi-exponential parameters was used to determine if discriminant analysis could be applied to just bi-exponential parameters and return perfusion that agreed with reference standard values. Automatic removal of CSF-dominated voxels would remove the effect of human bias in region selection. Further, unlike T2 weighted thresholds or mono-exponential thresholds, the supervised ML on the bi-exponential parameters supports a pattern observed that is expected from fast CSF flow. As seen in section 9.2, CSF will return a larger fast-component fraction (f) and speed D^* than tissue voxels. The use of these parameters in training discriminant analysis quantifies this divide between voxel type. Due to the success of quadratic discriminant analysis (QDA), removal of those by automatic thresholding is hypothesized to return perfusion that agrees with standard perfusion and its sensitivity to physiologic change.

9.6.2 Methods and Materials

From the same canine model described in Chapter 8, 11 subjects underwent a two-day controlled experiment of a pre-clinical canine model of normocapnia, CO2 induced hypercapnia, and middle cerebral artery occlusion (ischemic stroke) with IVIM. IVIM and microsphere perfusion for six subjects were measured and quantified following Chapter 8 while DSC perfusion was measured and quantified following Section 3.3.1 with delay and dispersion correction.

Two types of hemispheric ROIs were drawn: 1) hemispheric ROIs manually avoiding the subarachnoid space and ventricles as described in 8, and 2) hemispheric ROIs without manual avoidance of CSF. CSF was also removed automatically via QDA per physiologic state as described in Section 9.5.

Two methods of CSF segmentation were applied to the hemispheric ROIs: 1) T2 thresholding from Section 9.4 by physiologic state and 2) QDA segmentation from Section 9.5 by physiologic state. Hemispheric quantitative perfusion agreement with CSF removed by these two methods is compared to microspheres. It should be noted that some of the six cases analyzed in this experiment did contribute to the data set used to train both the T2 thresholding and the QDA, but many other subjects were included in that large data set that do not have microsphere perfusion with which to be compared.

9.6.3 Results

Fig. 9.17 demonstrates a QDA mask from IVIM parameters of a baseline coronal canine image and superimposes it on the corresponding T2 weighted $b0$ image. Comparison to alternate methods is included for reference. Fig. 9.18 shows the same QDA mask superimposed on the corresponding IVIM perfusion image quantified via water transport time (Eq. (7.5)), alongside the hand-drawn CSF mask for comparison. Fig. 9.19 shows the linear regression analysis of the four post-processing methods of hemispheric IVIM compared to microspheres, and Fig. 9.20 shows the corresponding Bland-Altman analysis. Combination of both manual avoidance and the QDA segmentation was analyzed with linear regression (slope = 0.41, intercept = 59.9, $R^2 = 0.49$, $p = 0.0$) and Bland-Altman (-2.38[-77.95, 73.18]), as well as Lin's CCC (CCC = 0.43 [0.34, 0.51]) and Wilcoxon signed-rank (statistic = 581.0, p = 0.59). Combination of manual avoidance and T2 thresholding was presented in Chapter 8 and returned linear regression (slope = 0.55, intercept = 52.5, $R^2 = 0.64$, $p = 0.0$) and Bland-Altman (-11.88 [-78.38, 54.63]), as well as Lin's CCC (CCC = 0.61 [0.53, 0.69]) and Wilcoxon signed-rank (statistic = 506, $p = 0.02$).

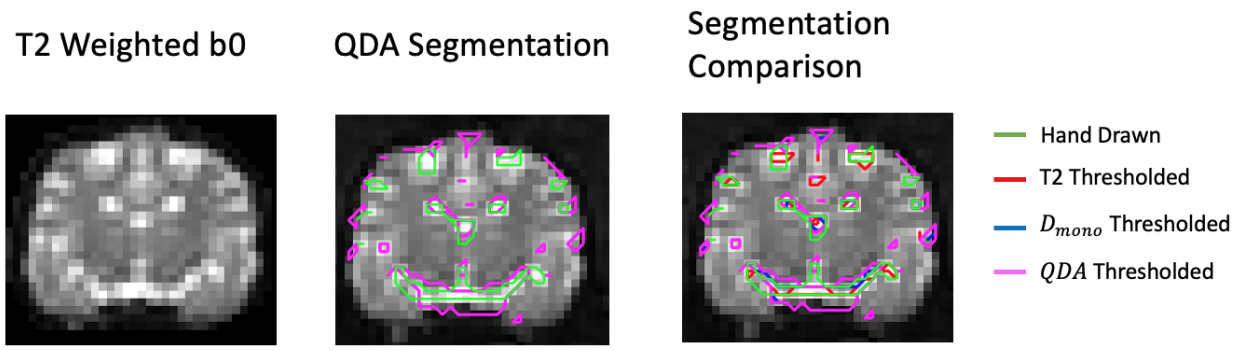

Figure 9.17: An example of a T2 weighted $b0$ image (left) with a QDA mask and a hand-drawn mask superimposed (center), and with a QDA mask, hand-drawn mask, T2 thresholding mask, and a D_{mono} mask superimposed (right). The Dice coefficients compared to the hand drawn mask for this image are 0.40 for QDA, 0.68 for T2 thresholding, and 0.40 for D_{mono}.

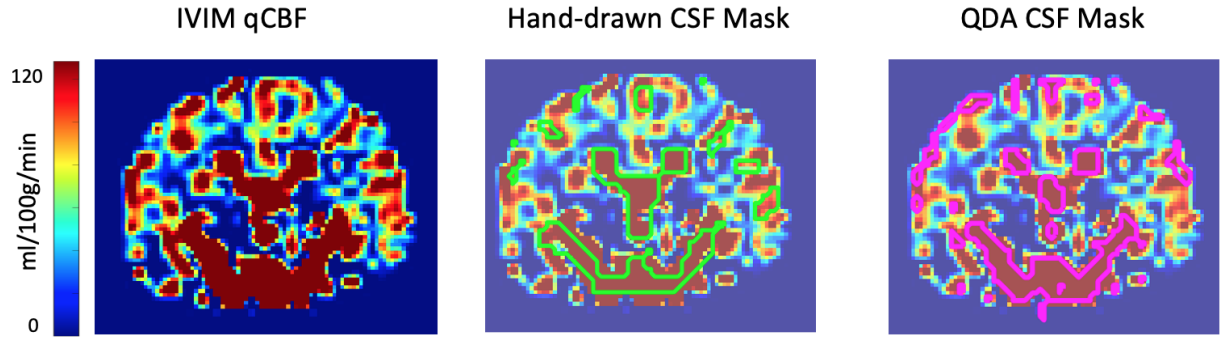

Figure 9.18: An example of a baseline IVIM quantitative perfusion image (left) with a hand-drawn mask superimposed (center), and a QDA mask superimposed (right).

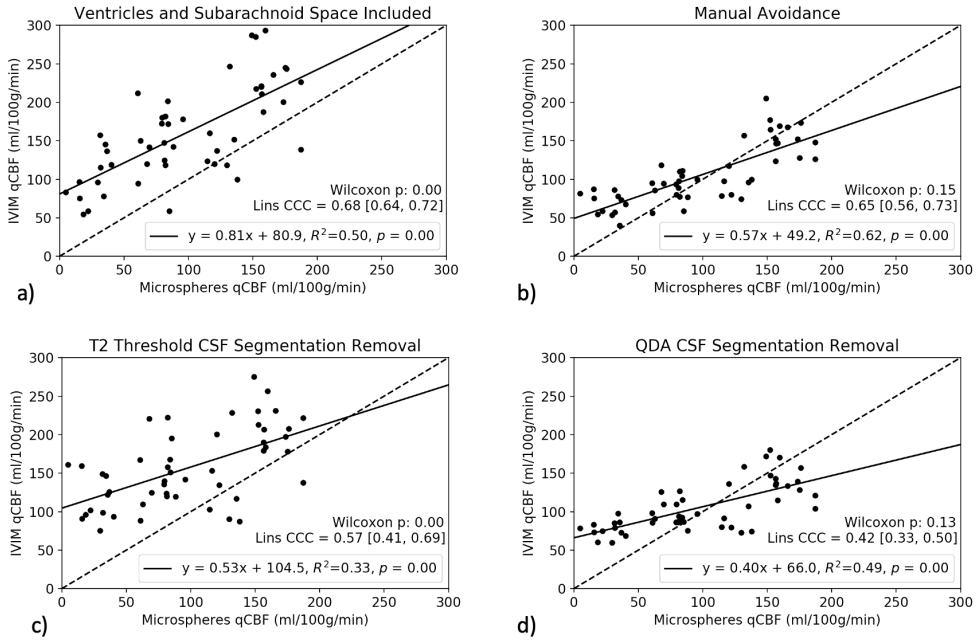

Figure 9.19: Hemispheric IVIM perfusion linearly correlated with microsphere perfusion with a) included ventricles and subarachnoid space, b) manual avoidance of ventricles and subarachnoid space, c) automatic T2 thresholding, and d) QDA CSF removal.

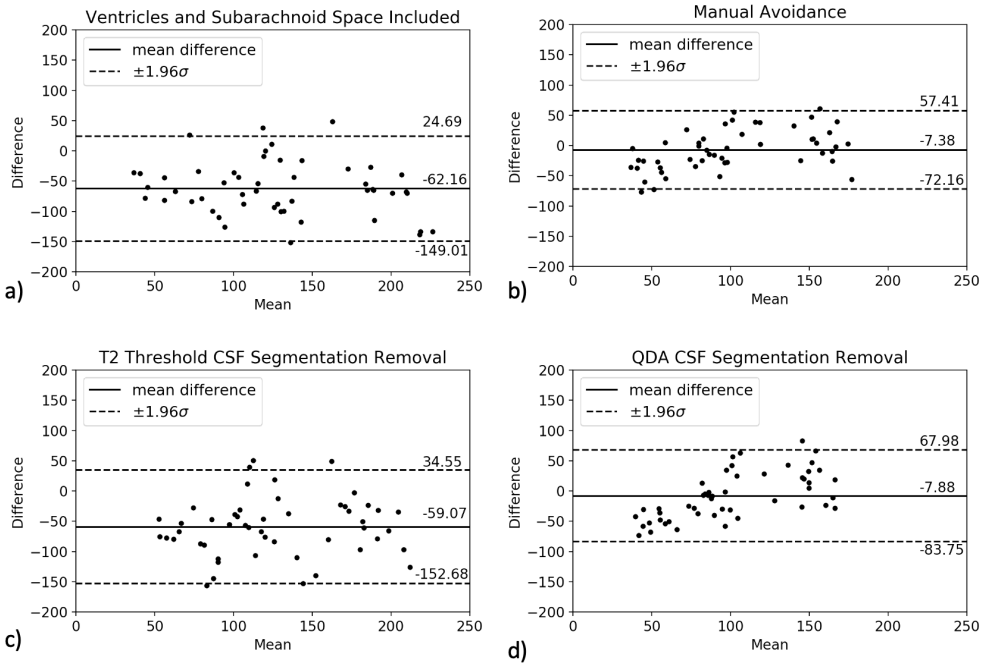

Figure 9.20: Bland-Altman analysis of IVIM perfusion and microsphere perfusion with a) included ventricles and subarachnoid space, b) manual avoidance of ventricles and subarachnoid space, c) automatic T2 thresholding, and d) QDA CSF removal.

9.6.4 Discussion

Overall, the applied QDA hemispheric perfusion correlation, and absolute agreement, returned better agreement to microspheres than if ventricles and subarachnoid space were not avoided. However, manual avoidance of CSF returned the closest perfusion agreement to microspheres. QDA CSF removal returned better agreement than automatic T2 thresholding, and if QDA was combined with manual agreement it reduced the sensitivity but reduced the Bland-Altman mean difference.

The effect of CSF contamination is seen in the offset of Fig. 9.19a without CSF removal, but a slope closest to 1.0. This suggests good sensitivity to physiologic change, but an offset of 80 ml/100g/min and the largest Bland-Altman mean difference, potentially due to CSF signal in ventricles and subarachnoid space contaminating the signal. Automatic T2 thresholding performed well against hand-drawn T2 CSF masks, but returned poor results in Fig. 9.19c on perfusion with a lower slope and the second largest Bland-Altman 95% CI. The similarity to Fig. 9.19a suggests some CSF was removed, but not all, and to different degrees based on physiologic state. The changed slope suggests more CSF was removed in hypercapnia and less removed at baseline. Further, despite a high Dice score, the T2 mask is more conservative than the hand-drawn avoidance, which permits more voxels with CSF contamination to be included in analysis. Total hemispheres and T2 thresholding showed a mean different centered at -62 and -59 ml/100g/min respectively. This further supports T2 automatic thresholding not successfully removing all CSF voxels, allowing voxels with partial volume contamination to be included in analysis.

In comparison, applied QDA returns a smaller 95% CI that is centered at -7.88 ml/100g/min, but a slope furthest from unity and the lowest Lin's CCC. This suggests both CSF and perfusion voxels were removed, especially at hypercapnia and post-MCAO, which reduced the offset at the cost of a reduced sensitivity. This demonstrates limits of QDA. As perfusion increases under physiologic stress such as an occlusion or CO2 inhalation, the very parameters

that the model uses to segment begin to overlap. When vessels dilate, CBV (or f) increases, and as heart rate and blood pressure increases it's possible that the speed (D^*) increases. This follows the Monro-Kellie hypothesis that the dilation of cerebral capillaries prompts an increase in CBF and a decrease in CSF (van der Kleij et al. [2020]). With a quadratic line separating between perfusion and CSF just based on these parameters, under physiologic stress, the line between CSF and CBF will become less distinct. This is a potential reason for the increased removal of higher perfusion at hypercapnia compared to normocapnia with QDA. While QDA did perform better than linear discriminant analysis, and T2 automatic thresholding, the application of QDA applies a hard division for segmentation that may underperform as parameters begin to overlap. Nonetheless, the moderate success does show statistical discrimination between CSF-dominated and perfusion-dominated voxels, further supporting IVIM signal not solely being due to CSF contamination. A deep learning model that can take into account higher-order features could potentially perform better.

Manual avoidance of anatomic regions performed best returning the smallest Bland-Altman and 95% CI, the highest R^2, the highest Wilcoxon p-value, and the highest Lin's CCC. Linear regression shows lower sensitivity to perfusion change than no avoidance. This could be potentially due to excessive exclusion of high perfusion voxels from human error as the speed and volume of tissue voxels begins to overlap more with fast-flowing CSF. With manual avoidance, anatomic location could be considered when drawing ROIs, which T2 thresholding and QDA does not. Combination of manual avoidance and machine learning returned moderate improvement. Manual avoidance and QDA segmentation returned the smallest mean difference with the greatest number of voxels removed. However, automatic removal of high perfusion at hypercapnia and contralateral post-MCAO artificially reduced the sensitivity. Manual avoidance and T2 thresholding returned reasonable sensitivity and a small Bland-Altman mean difference. The combination of the two allows both automatic thresholding to reduce bias between subjects or physiologic states, while also taking into

account higher-order features that a human would consider when examining a perfusion image.

These segmentation results support post-processing IVIM to remove CSF, rather than using and inversion recovery pulse that suppresses blood signal as shown in Section 9.3.3. They also demonstrate the difficulty of determining the optimal CSF removal algorithm. The $F1$ scores demonstrated in Section 9.5 show removal of voxels that have high perfusion in hypercapnia, and admission of voxels with CSF contamination at normocapnia. This could explain the lower linear regression slope of Fig. 9.19c. There are multiple limitations of this study including small sample size, possible training set contamination, and microsphere vendor error. Further, given current limitations on quantitative CSF imaging, comparison could only be made to microsphere perfusion. A larger study with contrast-based perfusion imaging and quantitative CSF flow at different physiologic states would provide greater evidence for IVIM signal origin, and segmentation success.

9.6.5 Conclusion

While tri-exponential separation of partial volume effects remains a possibility for partial volume analysis (Section 9.2.1), automatic removal of CSF-dominated voxels via QDA, and combined manual avoidance and T2 thresholding returns cortical and deep tissue perfusion of interest that agrees better with reference standard quantitative perfusion. The results of applied supervised machine learning approach the results drawn from manually avoiding ventricles and subarachnoid space, with human bias minimized, but there remain voxels and partial volume effects that are not corrected for. Even with moderate agreement, the result of QDA segmentation demonstrates a more quantifiable divide between bi-exponential behavior of CSF-dominated voxels and tissue-perfusion dominated voxels. This further supports IVIM signal not being predominately CSF contamination and a potential method of measuring quantitative perfusion of neurovascular disease without contrast agent.

CHAPTER 10

CONCLUSION

The broad, long-term goal of this dissertation is to improve quantitative perfusion MRI for diagnosis and prognosis of neurovascular disease. After an introduction and overview in Chapters 1 and 2, Chapter 3 demonstrates the utility of a standardized quantitative DSC perfusion to clinical standard relative perfusion in a study of experimental flow augmentation in acute ischemic stroke. Use of delay and dispersion corrected quantitative DSC perfusion provides a potential method of action for novel flow augmentation therapy of ischemic stroke and its effect in infarct growth that standard relative DSC could not. This demonstrates the importance of development and improvement of reliable perfusion quantification in clinical studies. Chapter 4 continues exploration of DSC perfusion by examining the difference between DSC with a standard global AIF and DSC with the delay and dispersion corrected local-AIF. This chapter agrees with historic trends showing standard DSC overcalls perfusion deficit, and demonstrates that using a local-AIF may reduce this overcall in intracranial atherosclerotic disease. By comparison to the ground truth of single-photon emission computerized tomography it further shows that the effect is localized to territories labeled as 'affected' by a neuroradiologist blinded to the perfusion results. Local-AIF is a method of correcting standard DSC perfusion deficit in affected territories to more closely agree with reference standards in ICAD imaging studies.

IVIM, a non-contrast perfusion method via multi b-value diffusion weighting, is explored from Chapter 5 and on. Beginning with fundamental physics of diffusion and diffusion weighted MRI, Chapter 6 applies diffusion physics to optimize IVIM as a non-contrast MR perfusion sequence and determines an optimal fitting algorithm. For the standard bi-exponential two-compartment model of perfusion and diffusion, a ten b-value sequence in three directions fit in two-steps was optimal. Chapter 7 lays out a derivation of a new method of IVIM perfusion quantification in ml/100g/min that is independent of capillary geometry

assumptions, and Chapter 8 validates its use and a post-processing algorithm against neutron capture microspheres, and DSC perfusion. It returns strong agreement of the derived IVIM water transport time to delay and dispersion corrected DSC Mean Transit Time, and DTI mean diffusivity. This work provides a method of scanning, post-processing, and quantifying non-contrast perfusion that doesn't require known capillary geometry, which could be used in organs beyond the brain.

Lastly, Chapter 9 studies different methods of removing CSF contamination from IVIM signal including showing tri-exponential behavior, simulation of inversion recovery CSF suppression, application of inversion recovery in a healthy human volunteer, manual avoidance of anatomic regions with CSF, automatic thresholding of T2 and Diffusion coefficients, and supervised machine learning via discriminant analysis of bi-exponential parameters. Tri-exponential behavior seems a promising direction but determining the parameters necessary for compartment modeling and computational load proved beyond the scope of this work. The simulation of inversion recovery shows that CSF suppression also suppressed blood signal if T1 and T2 effects are taken into account providing an explanation of why IVIM perfusion signal is lost when CSF is suppressed. For CSF segmentation, manual avoidance on T2 maps returns perfusion that agrees most closely with microspheres, while quadratic discriminant analysis is second best. Chapter 7, 8, and 9 demonstrate that IVIM can return physiologic parameters important for different disease models such as perfusion, diffusion, blood volume, transit time, and cerebrospinal fluid flow, in one non-contrast scan. However, due to the limitations of endogenous contrast, the separation of multiple types of fast-fluid and partial volume contamination must be considered carefully.

APPENDICES

A. b-VALUE DERIVATION

The diffusion weighting is expressed in terms of the b-value, which is the variable used to fit for the diffusion coefficient D as originally laid out by Stejskal and Tanner [1965] with the full derivation laid out by Kuchel et al. [2012]. The b-value affects the sensitivity of the signal to water diffusion with a lower b-value losing signal from fast flow and a higher b-value losing signal from slow flow.

Mathematically, this b-value is such that

$$\frac{S(2\tau)}{S_0} = e^{-Db}. \tag{1}$$

Here, 2τ is the echo time and D is the diffusion coefficient from $\sigma^2 = 2Dt$ in Eq. (5.3). One can fit the signal decay for a DWI taken with a specific b-value to the above exponential to estimate D for that voxel. In terms of the MR sequence, this b-value is a function of sequence timing parameters and gradient strength as follows.

$$b = \gamma^2\delta^2\Big(\Delta - \frac{1}{3}\delta\Big)g^2. \tag{2}$$

This uses the sequence timing parameters in Fig. 5.1a and assumes a gradient strength of g. Assuming a long TR to minimize T1 effects, we can rewrite Eq. (2.3a) in complex notation as

$$\vec{M}_{xy} = M_0 e^{i\omega t} e^{-t/T2}.$$

If we normalize a diffusion-weighted image of $b > 0$ to a b_0 image with $M_{b0} = M_0 e^{-t/T2}$, we can remove the $T2$ effects, which will be done for the rest of this section.

$$\frac{\vec{M}_{xy}}{\vec{M}_{b0}} = M_0 e^{i\omega t}$$

In the rotation frame we can remove B_0 effects and solely focus on the influence of a gradient. The application of a gradient G at point $\vec{r}$ will change the precession in the previous equation to $\omega = -\gamma \vec{G} \cdot \vec{r}$.

$$\vec{M}_{xy} = M_0 e^{-i\gamma \vec{G} \cdot \vec{r} t}$$

With $\vec{}$ representing vectors and $M_{xy} = |\vec{M}_{xy}|$ as the magnitude of the vector, taking the partial derivative of both sides and integrating from 0 to t returns the following.

$$\frac{\partial \vec{M}_{xy}}{\partial t} = -i\vec{G} \cdot \vec{r} \vec{M}_{xy}$$

$$\int_{\vec{M}_{xy}(0)}^{\vec{M}_{xy}(t)} \frac{\partial_t \vec{M}'_{xy}}{\vec{M}'_{xy}} \longrightarrow \ln \vec{M}'_{xy} \Big|_{\vec{M}_{xy}(0)}^{\vec{M}_{xy}(t)} = -i\gamma \vec{r} \cdot \int_0^t \vec{G}(t' \partial t')$$

$$\vec{M}_{xy} = M_0 e^{-i\gamma \vec{r} \cdot \vec{F}(t)} \qquad \text{with } \vec{F}(t) = \int_0^t \vec{G}(t') dt'$$

Now adding diffusion to this equation with Fick's second law to predict how diffusion will change a concentration ψ over time,

$$\frac{\partial \psi}{\partial t} = D \nabla^2 \psi.$$

The Laplacian is with respect to the spatial variable along the diffusion axis. This must be added to the magnetization equation as the diffusion of magnetization leads to total a diffusion current from diffusion of both positively and negatively oriented spins. This total diffusion current composed of the difference of positive and negatively oriented spins diffusing is an increase in the magnetic moment from the equilibrium magnetization. This increase can be linearly added to the magnetization equation as described in Torrey [1956].

$$\frac{\partial \vec{M}_{xy}}{\partial t} = -i\vec{G} \cdot \vec{r} \vec{M}_{xy} + D \nabla^2 \vec{M}_{xy} \tag{3}$$

Applying boundary conditions, after the 180° pulse we know that there will be a $-2\vec{f} = -\vec{F}(\tau) = \int_0^\tau G(t')dt'$ accumulated phase that must be added to the equation. To take into account the phase before and after the 180° pulse we include $\xi = 1$ for $t < \tau$ and $\xi = -1$ for $t > \tau$ and include this phase after the pulse. This means that from $t = [0, \tau]$ the second exponent is 0, as $\vec{F}(t)$ increases from $\vec{F}(0)$ to $\vec{F}(\tau)$. First assuming diffusion is zero, the equation can be solved as follows

$$\vec{M}_{xy}(t) = M_{xy}(t)e^{-i\gamma\vec{r}\cdot[\vec{F}(t)-(\xi-1)\vec{f}]}. \tag{4}$$

In this equation, before the 180° pulse, the phase accrual is as expected, and after the pulse the spins are flipped over the axis, and so $2\vec{f}$ is subtracted. This influence of the pulse on phase accrual with and without movement is demonstrated visually in Fig. A1. In this figure both the stationary and moving spin start at a position in the gradient with $G = 1$. Assuming that $\delta = 5$, and that the 180° pulse is played immediately after the gradient is turned off,

$$F(\tau) = \int_0^\tau G(0)dt = \int_0^5 1dt = 5.$$

This means that for the stationary spin, $2\vec{f} = 2\vec{F}(\tau) = 10$, shown as the blue dashed line at the 180° pulse. In comparison, if there is motion due to diffusion, phase is accumulated at different rates over time due to its movement within the linear gradient. In this example figure, the spin travels at a speed of $+.25G/s$. In other words, per second the spin travels the linear distance needed such that the gradient strength one second later has increased by .25. This means that before that 180° pulse,

$$F(\tau) = \int_0^\tau G(0) + G(t)dt = \int_0^5 (1 + 0.25t)dt = 8.125.$$

The $-2f$ accumulation with this movement is shown as the dashed green line. Assuming that the particle is still moving at a constant velocity after the 180° pulse, with the gradient

applied again, its initial position is now greater, meaning that it will experience a different gradient strength. The accumulated phase after this pulse, for this example, is then

$$F(\tau+5) = \int_{\tau}^{\tau+5} G(\tau) + G(t)dt = \int_{\tau}^{\tau+5} (1+.25\tau) + 0.25tdt = 14.375.$$

As seen in Fig. A1, the difference between $F(\tau)$ and $F(\tau+5)$ is the phase accrued due to movement of the spin during the sequence. This is seen as the nonzero phase at the end of the sequence. In comparison, for the stationary spin, $F(\tau) = F(\tau+5)$ so the resulting phase accrual is zero.

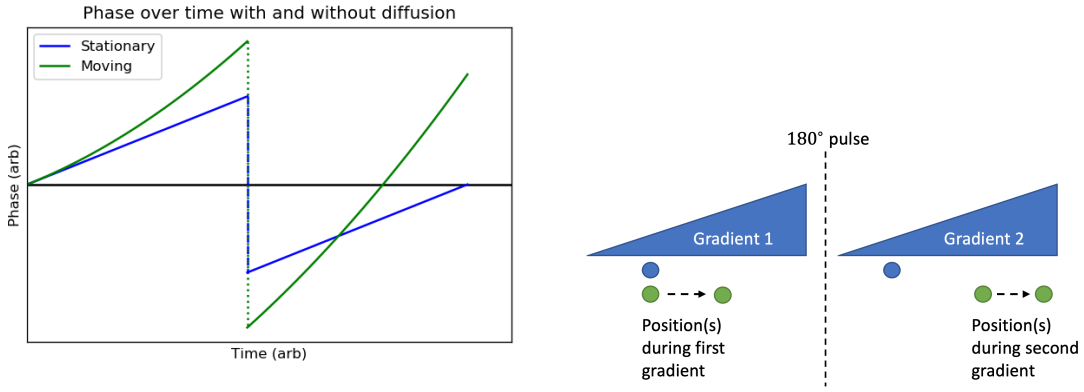

(a) Phase accrual (b) Movement in gradients

Figure A1: Phase accrual and corresponding representation of movement within the gradients before and after the 180 pulse, with and without diffusion. Green represents moving spin and blue represents stationary spin.

Continuing with this, taking the partial derivative of Eq. (4) results in

$$\begin{aligned}\frac{\partial \vec{M}_{xy}}{\partial t} = &\frac{dM_{xy}}{dt} e^{-i\gamma\vec{r}\cdot[\vec{F}(t)-(\xi-1)\vec{f}]} \\ &- M_{xy}(t) i\gamma\vec{r}\cdot\left[\frac{\vec{F}(t)}{dt} + \frac{(\xi-1)d\vec{f}}{dt}\right] e^{-i\gamma\vec{r}\cdot[\vec{F}(t)-(\xi-1)\vec{f}]}\end{aligned} \tag{5}$$

in which $\frac{d\vec{f}}{dt} = 0$ and $\frac{d\vec{F}t}{dt} = \vec{G}t$.

Now considering the diffusion part of Eq. (3) in which $M_{xy}(t)$ is solely a function of t

and the Laplacian double derivative is taken with respect to the spatial vector

$$\begin{aligned} D\nabla^2\vec{M_{xy}} &= D\nabla^2 M_{xy}(t)e^{-i\gamma\vec{r}\cdot[\vec{F}(t)-(\xi-1)\vec{f}]} \\ &= -DM_{xy}(t)\gamma^2\left(\vec{F}(t)+(\xi-1)\vec{f}\right)^2 e^{-i\gamma\vec{r}\cdot[\vec{F}(t)-(\xi-1)\vec{f}]}. \end{aligned} \tag{6}$$

Plugging Eq. (6) into Eq. (3) we can get the partial derivative of $M_{xy}(t)$ with diffusion in terms of $\vec{F}$ and M_{xy}.

$$\frac{\partial\vec{M_{xy}}}{\partial t} = -i\vec{G}\cdot\vec{r}\vec{M_{xy}} - DM_{xy}(t)\gamma^2\left(\vec{F}(t)+(\xi-1)\vec{f}\right)^2 e^{-i\gamma\vec{r}\cdot[\vec{F}(t)-(\xi-1)\vec{f}]} \tag{7}$$

This $M_{xy}(t)$ in Eq. (7) must be equal to the general equation, Eq. (5), with both diffusion effects and the 190° pulse included, so setting these equal to solve for $M_{xy}(t)$ with $\phi = -i\gamma\vec{r}\cdot[\vec{F}(t)-(\xi-1)\vec{f}]$ for simplicity we get the following.

$$\begin{aligned} &\frac{dM_{xy}}{dt}e^{\phi} - M_{xy}(t)i\gamma\vec{r}\cdot\left[\frac{\vec{F}(t)}{dt}+\frac{(\xi-1)d\vec{f}}{dt}\right]e^{\phi} \\ &\qquad = -i\vec{G}\cdot\vec{r}M_{xy} - DM_{xy}(t)\gamma^2\left(\vec{F}(t)+(\xi-1)\vec{f}\right)^2 e^{\phi} \end{aligned}$$

$$\frac{dM_{xy}(t)}{dt} = -M_{xy}(t)D\gamma^2\left(\vec{F}(t)+(\xi-1)\vec{f}\right)^2$$

Integration by separation of variables from $t=0$ to $t=\tau$ gives

$$\int_{M_{xy}(0)}^{M_{xy}(2\tau)}\frac{dM_{xy}(t)}{M_{xy}(t)} = \int_0^{2\tau} -D\gamma^2\left(\vec{F}(t)+(\xi-1)\vec{f}\right)^2 dt$$

$$\begin{aligned} \frac{1}{-D\gamma^2}\left[\ln\left(\frac{M_{xy}(2\tau)}{M_{xy}(0)}\right)\right] &= \int_0^{\tau}(\vec{F}(t)^2dt + \int_{\tau}^{2\tau}(\xi-1)\vec{f})^2dt \\ &= \int_0^{\tau}(\vec{F}(t)^2dt - 4\vec{f}\cdot\int_{\tau}^{2\tau}\vec{F}(t)dt + 4\vec{f}^2\tau. \end{aligned} \tag{8}$$

For a rectangular gradient pulse, we know the gradient strength at different times in the sequence; it is set to $G(t) = g$ when the $G_{diffusion}$ gradient is on (See Fig. 5.1a), and it is zero elsewhere. From this $\vec{F}(t) = \int_0^t G(t)dt$ can be calculated, as done by Kuchel et al. [2012], and these values can be plugged into the three right hand terms of Eq. (8) where t_1 is the time between the first RF pulse and the first gradient, δ is the duration of the gradient, Δ is the time between the start of the first diffusion gradient and the start of the second diffusion gradient, and g is the strength of the gradient.

$$\text{Term 1: } \int_0^\tau (\vec{F}(t)^2 dt = \frac{1}{3}\left[-g^2\delta^2(12t_1 + 7\delta + 9\Delta - 24\tau)\right]$$
$$\text{Term 2: } -4\vec{f}\cdot\int_\tau^{2\tau} \vec{F}(t)dt = 2(g\delta)[g\delta(2t_1 + \delta + 2\Delta - 6\tau)]$$
$$\text{Term 3: } 4\vec{f}^2\tau = 4\tau(g\delta)^2$$

Expanding these terms, combining them, and simplifying them, we get the following expression

$$\begin{aligned}
&\int_0^\tau (\vec{F}(t)^2 dt - 4\vec{f}\cdot\int_\tau^{2\tau} \vec{F}(t)dt + 4\vec{f}^2\tau \\
&= -4g^2\delta^2 t_1 - \frac{7}{3}g^2\delta^3 - 3g^2\delta^2\Delta + 8g^2\delta^2\tau + 4g^2\delta^2 t_1 + 2g^2\delta^3 + 4g^2\delta^2\Delta - 8g^2\delta^2\tau \\
&= -\frac{7}{3}g^2\delta^3 - 3g^2\delta^2\Delta + 2g^2\delta^2 + 4g^2\delta^2\Delta \\
&= -\frac{7}{3}g^2\delta^3 + g^2\delta^2\Delta + 2g^2\delta^3 \\
&= -\frac{1}{3}g^2\delta^3 + g^2\delta^2\Delta
\end{aligned}$$

Plugging this into Eq. (8),

$$\ln\left(\frac{M_{xy}(2\tau)}{M_{xy}(0)}\right) = -D\gamma^2\left[-\frac{1}{3}g^2\delta^3 + g^2\delta^2\Delta\right],$$

after rearranging terms and substituting b from Eq. (2) we get the final equation we wanted,

Eq. (5.5),

$$\begin{aligned}\frac{M_{xy}(2\tau)}{M_{xy}(0)} &= e^{-D\gamma^2\delta^2(\Delta-\frac{1}{3}\delta)g^2} \\ &= e^{-Db}.\end{aligned}$$

This shows mathematically how a larger b-value, represented previously as a steeper more sensitive gradient in Fig. 5.1b, would lead to a greater signal accrual for the same diffusion coefficient D. Fitting it to this exponential curve will then return D for a tissue. With this an MRI can image diffusion for diagnostic, prognostic, and pathologic imaging.

B. SIMULATION OF APPARENT DIFFUSION COEFFICIENT VS. MEAN DIFFUSIVITY

From diffusion tensor imaging (DTI) and diffusion weighted imaging (DWI) we get Mean Diffusivity (MD) and apparent diffusion coefficient (ADC) respectively.

$$MD = \frac{\lambda_1 + \lambda_2 + \lambda_3}{3}$$

$$ADC = \frac{(D_{xx} + D_{yy} + D_{zz})}{3}$$

If the diffusion ellipsoid axes $\vec{\epsilon_1}, \vec{\epsilon_2}, \vec{\epsilon_3}$ do not align with the standard lab frame axes $(\vec{x}, \vec{y}, \vec{z})$ is ADC a reasonable approximation of MD in non-isotropic diffusion?

$$\frac{(D_{xx} + D_{yy} + D_{zz})}{3} \approx \frac{(\lambda_1 + \lambda_2 + \lambda_3)}{3}$$

To test the validity of the claim that ADC can approximate a diffusion ellipsoid at a low resolution, ADC can be viewed as the difference between lab frame axes upon different rotations of a diffusion ellipsoid about the center point.

From Eq. (5.7) 3D anisotropic ellipsoid can be written with the Cartesian equation in a rotated frame:

$$\frac{x'^2}{2\lambda_1 t} + \frac{y'^2}{2\lambda_2 t} + \frac{z'^2}{2\lambda_3 t} = 1.$$

If the principal axes align with the three Cartesian axes, these represent the three principle diffusion directions. Therefore the eigenvectors $(\vec{\epsilon_1}, \vec{\epsilon_2}, \vec{\epsilon_3})$ are the Cartesian axes $(\vec{x}, \vec{y}, \vec{z})$, and the eigenvalues $\lambda_1, \lambda_2, \lambda_3$ are representing the strength of diffusion displacement as the Cartesian coefficients a, b, c in $\frac{x^2}{a^2} + \frac{y^2}{b^2} + \frac{z^2}{c^2} = 1$. Therefore we can get an example MD measurement in that lab frame by measuring the average diffusion from the eigenvalues of the simulated ellipsoid.

An example ADC measurement can be acquired by maintaining the global center but

rotating the ellipsoid by a random value about that center, and measuring the average diffusion along the lab frame coordinates. The lab frame coordinates will no longer necessarily be aligned with the eigenvectors, meaning the diffusion along the lab frame coordinates will now be D_{xx}, D_{yy}, D_{zz}. Therefore, creating an ellipsoid and measuring the true principal axes we can get MD.

$$MD = \frac{(\lambda_1 + \lambda_2 + \lambda_3)}{3}$$

Rotating it around its center a random amount and measuring the lab frame coordinates we get ADC.

$$ADC = \frac{(\frac{a}{2t}\widehat{x} + \frac{b}{2t}\widehat{y} + \frac{c}{2t}\widehat{z})}{3} = \frac{(D_{xx} + D_{yy} + D_{zz})}{3}$$

With this, a simulation can generate a range of expected anisotropic ellipsoids and their rotations to mimic average fractional anisotropy of whole brain $FA = 0.52 \pm 0.31$ from Kochunov et al. [2011]. The rotational angles $\theta_x, \theta_y, \theta_z$ are chosen randomly between 0 and 2π, and the eigenvalues $\lambda_1, \lambda_2, \lambda_3$ are chosen from various ranges calculated to result in a distribution of FA that is statistically similar to a human brain. These values are placed in Eq. (5.7) and rotated in the global frame by the randomly chosen angles. The values along the three Cartesian axes are retrieved and used to calculate ADC, which is then compared to the DTI from the original eigenvalues. The distribution of ADC and DTI values are compared, and the percent difference on a pair-wise basis is used to calculate average percent error. Linear regression compares the sensitivity and paired wilcoxon signed-rank compares the resulting distribution of ADC and MD.

ADC Simulation Results

For n=5000 runs, the average produced 'true' DTI MD was a normal distribution of $\mu \pm \sigma$ of 1.16 ± 0.35 while the distribution of the corresponding fit ADC was a left skewed distribution of mean $.95 \pm 0.42$ shown in Fig. B1a. This underestimation is expected, as the MD is the average of the three principal ellipsoidal axes including the major axis, while the

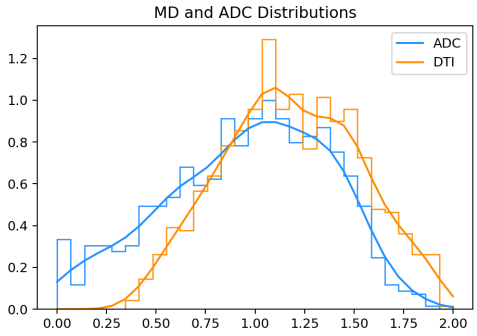

(a) MD and ADC distribution

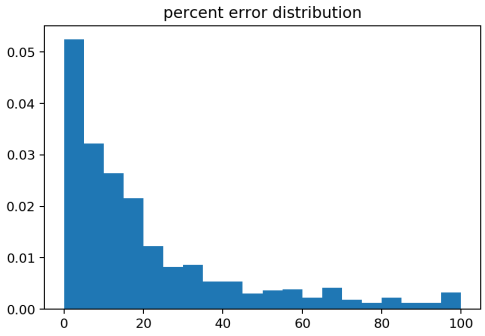

(b) ADC Percent Error Distribution

Figure B1: These figures represent the distribution of true MD from the n=1000 simulated ellipsoids and the overlay of the ADC values generated

ADC is most likely not to include the major axis. This is statistically significant difference, with wilcoxon signed-rank returning a $p = 1.24E - 125$. However, distribution of percent error shows a large majority of errors at 0, and a median of 11% error. Linear regression between MD and ADC returned slope = 1.02, intercept = 0.2, and $R^2 = 0.72$ with a $p = 0.0$.

This median of 11% underestimation of the MD is shown in Fig. B1b with the greatest number of results being 0% error, though the long tail shows there are still possibly large underestimations. However, this simulation is focused on average FA of structural tracks at high b-values. Given the general isotropic nature of perfusion on the scale of perfusion imaging and diffusion abnormalities this median underestimation of average diffusion coefficient would be much lower and is well worth the halved sequence time. Further, the longer sequence for DTI (from 5 minutes to at least 10 minutes) would increase the chance of patient motion artifacts. The varying anisotropy at different b-value sensitivities, and its effect on MD and ADC, was not explored but warrants future research.

C. ALTERNATE WATER TRANSPORT TIME DEFINITIONS

Presented here is derivation and example of two other possible definitions of WTT tested beyond 1) presented in Chapter 7. Definition 2) time for mean squared displacement to match volume of interest, and definition 3) time to leave volume of interest for a particle travelling at average velocity.

For definition 2:

Using mean squared displacement of a 3D Gaussian in Section 5.3 we know that

$$MSD = 6D^*t.$$

Therefore we can solve for a time t at which this mean squared displacement is the square of half of a cubic mm. In other words, when an instantaneous delta function in the center of a voxel has a mean displacement outside of a cubic mm:

$$WTT = \frac{MSD}{6D^*} = \frac{.5^2}{6D^*}.$$

Plugging this into the central volume equation returns the following:

$$qCBF = \frac{CBF}{WTT} = fD^* \frac{6(.79).5}{1.0g/mL} 100g \times 60s/min$$
$$\approx fD^* \times 113760.$$

For definition 3:

The water transport time can also be seen as the average time for a particle to leave the volume. This is written mathematically as the integral from 0 to ∞ over the residue function, where the residue function is the fraction of contrast remaining in the volume of tissue at time t. This returns essentially a weighted sum of times as the particles diffuse,

with the result being the average time at which the particle leaves the voxel.

$$WTT = \int_0^\infty R(t)dt$$

This residue function is the same as the 3D concentration curve in Fig. 7.2d. The integration of this function can be done analytically or numerically via a Riemann sum to return $WTT = \sum R(t)\Delta t$. Analytically this could be solved as

$$WTT = \int_0^\infty \frac{4\pi}{\sqrt{4\pi Dt}} \int_0^{.5} e^{-r^2/4Dt} r^2 dr dt.$$

This WTT would be longer than the other two types due to the tail, and also involves integral of an error function or computation via Riemann sum to return a longer WTT than expected, and so was not used. Code was written to perform the Riemann sum and compare it to the two alternate methods of calculating mean transit time in Fig. C1.

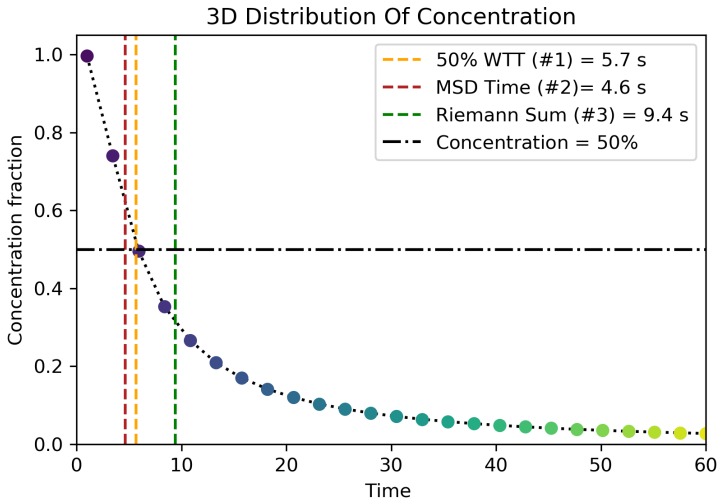

Figure C1: Three WTT types plotted on top of the concentration curve of a cubic mm over time for a hypothetical volume with a pseudo-diffusion coefficient $D^*$of 0.009. This shows the difference in the actual calculated "WTT" based on which definition is used, and its corresponding concentration. The one that this dissertation used was #1, or WTT 50% as it is the time at which the concentration is 50% of the original.

D. CONFERENCES AND PUBLICATIONS

Peer-reviewed publications

1. M. Liu, N. Saadat, Y. Jeong, S. Roth, M. Niekrasz, G. Christoforidis, T. Carroll. "Augmentation of Perfusion with Simultaneous Vasodilator and Inotropic Agents in Experimental Acute Middle Cerebral Artery Occlusion: A Pilot Study". Journal of NeuroInterventional Surgery, 2022. http://dx.doi.org/10.1136/jnis-2022-018990

2. A. Bross, E.C. Dukes, R. Ehrlich, E. Fernandez, S. Dukes, M. Gobashy, I. Jamieson, P. La Riviere, M. Liu, G. Marouard, N. Moeller, A. Pla-Dalmau, P. Rubinov, O. Shohoud, P. Vargas, T. Welch. "Tomographic Muon Imaging of the Great Pyramid of Giza". Journal for Advanced Instrumentation in Science, 2022. https://doi.org/10.31526/jais.2022.280

3. G. Christoforidis, N. Saadat, M. Liu, Y. Jeong, S. Roth, M. Niekrasz, T. Carroll. "Effect of Early SANGUINATE® (PEGylated carboxyhemoglobin bovine) Infusion on Cerebral Blood Flow to the Ischemic Core in Experimental Middle Cerebral Artery Occlusion." Journal of NeuroInterventional Surgery, 2021. http://dx.doi.org/10.1136/neurintsurg-2021-018239

4. A. Dimov, G. Christoforidis, N. Saadat, M. Liu, Y. Jeong, S. Roth, M. Niekrasz, T. Carroll. "QSM in canine model of acute cerebral ischemia: A pilot study". Mag. Reson. Med, 2020. https://doi.org/10.1002/mrm.28498

5. N. Saadat, G. Christoforidis, Y. Jeong, M. Liu, A. Dimov, S. Roth, M. Niekrasz, S. Ansari, T. Carroll. "Influence of simultaneous pressor and vasodilatory agents on the evolution of infarct growth in experimental acute middle cerebral artery occlusion." Journal of NeuroInterventional Surgery, 2020. http://dx.doi.org/10.1136/neurintsurg-2020-016539

6. M. Liu, Z. Pan, R. Basu Thakur, H. Goksu, S.Meyer, B.Benson. N.A. "Simulation and Calibration of a Compact Fourier Transform Spectrometer". OSA, Applied Optics, 2020. https://doi.org/10.1364/AO.397312

7. Z. Pan, M. Liu, R. Basu Thakur, H. Goksu, E. Rath, D. Fixsen, S. Meyer, N.A. "A Compact Millimeter-Wavelength Fourier-Transform Spectrometer". OSA, Applied Optics, 2019. https://doi.org/10.1364/AO.58.006257

Pre-prints

1. M. Liu, N. Saadat, Y. Jeong, S. Roth, M. Niekrasz, M. Giurcanu, T. Carroll, G. Christoforidis. "Quantitative perfusion and water transport time model from multi *b*-value diffusion magnetic resonance imaging validated against neutron capture microspheres" Medical Physics Arxiv, 2023. https://doi.org/10.48550/arXiv.2304.01888

Conference Presentations

1. M. Liu, C. Warioba, J. Bertini, N. Saadat, T. Carroll, G. Christoforidis. "Validation and Machine Learning of a New Method for Quantifying CBF with IVIM". ASNR 2023. (Talk)

2. M. Liu, S. Prabhakaran, J. Bertini, C. Warioba, S. Ansari, Y. Pu, T. Carroll. "Local-AIF DSC Perfusion in Intracranial Atherosclerotic Disease". ASNR 2023. (Talk)

3. J. Bertini, M. Liu, C. Warioba, YF. Chen, T. Carroll. "Cardiac-Gated Rosette Pulse Sequence Development for Off-Resonance Frequency Imaging. ISMRM 2023 (Poster)

4. M. Liu, N. Saadat, C. Warioba, T. Carroll. G. Christoforidis "IVIM quantified in

ml/100g/min with pseudo-diffusion mean transit time validated against neutron capture microspheres."ISMRM 2023 (Poster)

5. M. Liu, J. Bertini, C. Warioba, N. Saadat, D. Gorre, T. Carroll, G. Christoforidis. "Machine Learning for Quantitative IVIM (qIVIM) Cerebral Perfusion Imaging" ISMRM 2023 (Poster)

6. C.S. Warioba, M. Liu, S. Foxley, G.A. Christoforidis, T.J. Carroll. "Flow augmentation after occlusion maintains functional connectivity, mean T2* signal intensity, and mean diffusivity", ISMRM 2023 (Poster)

7. C. Warioba, M. Liu, S. Foxley, G. Christoforidis,T. Carroll. "Flow Augmentation after occlusion maintains functional connectivity and mean diffusivity" Mayo Clinic SITDP 2023 (Poster)

8. M. Liu, C. Warioba, J. Bertini, N. Saadat, T. Carroll, G. Christoforidis. "Non-contrast Perfusion MRI from the point of view of Medicine and Physics" GPMP Retreat 2023 (Flash talk)

9. C. Warioba, M. Liu, S. Foxley, G. Christoforidis,T. Carroll. "Flow Augmentation and Functional Connectivity" GPMP Retreat 2023 (Flash talk)

10. M. Liu, N. Saadat, Y. Jeong, S. Roth, M. Niekrasz, G. Christoforidis, T. Carroll. "Augmented Perfusion Quantified by MRI Depends on Collateral Recruitment in Middle Cerebral Artery Occlusion: A Pilot Study". ISMRM conference, 2023. (Power Pitch)

11. M. Liu, N. Saadat, Y. Jeong, S. Roth, M. Niekrasz, G. Christoforidis, T. Carroll. "Augmentation of Perfusion with Simultaneous Vasodilator and Inotropic Agents in Experimental Acute Middle Cerebral Artery Occlusion." ISMRM Perfusion Workshop, 2022. (Poster)

12. M. Liu, N. Saadat, Y. Jeong, S. Roth, M. Niekrasz, G. Christoforidis, T. Carroll. "Quantitative IVIM Perfusion at Normocapnia, Hypercapnia, Acute Stroke and Stroke Treatment Predicts Neutron Capture Microspheres." ISMRM Perfusion Conference, 2022. (Talk)

13. M. Liu, Y. Jeong, N. Saadat, S. Roth, M. Niekrasz, G. Christoforidis, T. Carroll. "Quantitative CBF and DWI Volume from Single MRI Scan in Stroke", Oral Presentation, 59th Annual Meeting of the American Society of Neuroradiology, 2021. (Poster)

14. M. Liu, Y. Jeong, N. Saadat, G. Christoforidis, T. Carroll. "Accuracy of Intravoxel Incoherent Motion (IVIM) for quantification of perfusion-diffusion mismatch in Acute Stroke." International Society for Magnetic Resonance in Medicine. Oral Presentation at 29th ISMRM conference in 2021. (Remote Covid-Poster)

15. Z. Pan, M. Liu, R. Basu Thakur, B. Benson, D. Fixsen, H. Goksu, E. Rath, S. Meyer. "A Compact Millimeter-Wavelength Fourier-Transform Spectrometer". CMB systematics and calibration focused workshop, 2020. (Talk)

16. M. Liu, Y. Jeong, N. Saadat, S. Roth, M. Niekrasz, G. Christoforidis, T. Carroll. "IVIM Perfusion Correlates with Quantitative CBF at Baseline, Hypercapnia, and Infarct." Oral Presentation, 58th Annual Meeting of the American Society of Neuroradiology, 2020. (Talk)

17. G. Christoforidis, N. Saadat, Y. Jeong, M. Liu, M. Niekrasz, T. Carroll. "Prediction of Leptomeningeal Collateral Recruitment in Experimental Ischemic Stroke by Cerebrovascular Reactivity to Carbon Dioxide." Poster Presentation, International Stroke Conference 2020. (Poster)

18. M. Liu. "Muon tomography simulation of sinogram space". Oral Presentation at teleconference in November 2019.

19. N. Saadat, Y. Jeong, M. Liu, S. Roth, M. Niekrasz, T. Carroll, G. Christoforidis. "Susceptibility-Weighted Imaging in Hyperacute Phase of Ischemic Stroke" RSNA. Oral Presentation at RSNA conference in 2019. (Talk)

20. A. Dimov, G. Christoforidis. N. Saadat, M. Liu, Y. Jeong, S.Roth, M. Niekrasz, T. Carroll. "Quantitative Susceptibility Mapping in acute ischemic stroke: comparison with perfusion, infarct growth rate and FMISO-PET". Poster Presentation, ISMRM, 2019. (Poster)

21. M. Liu, Y. Jeong, N. Saadat, G. Christoforidis, T. Carroll. "IVIM-based Cerebral perfusion values at rest, hypercapnia, and ischemia in an MCA occlusion model" International Society for Magnetic Resonance in Medicine. Poster Presentation at 27th ISMRM conference in 2019. (Poster)

22. Z. Pan, M. Liu, R. Basu Thakur, H. Goksu, E. Rath, D. Fixsen, B. Benson, S. Meyer. "A Compact Fourier-Transform Spectrometer". March 2019. Presented at CMB-S4 Collaboration, Fermilab. (Talk)

23. Z.Pan, R. Basu Thakur, M. Liu-Sarkar, H. Goksu, S. Meyer. "A compact millimeter-wavelength Fourier-transform spectrometer" June 18, 2018. New Perspectives 2018, Fermilab. (Talk)

24. R. Basu Thakur, H. Goksu, M. Liu-Sarkar, R. Mbarek, Z.Pan S.Meyer, B.Benson. "A Compact Fourier Transform Spectrometer". August 28, 2017. Cosmology with CMB-S4 at Harvard University. (Talk)

E. CODE AVAILABILITY

A subset of code developed and used in this dissertation is publicly available at the following github: `https://github.com/miramliu`. For access to code not publicly available yet, please contact the author, Mira Liu, with contact information available on github.

REFERENCES

S. Aja-Fernandez and G. Vegas-Sanchez-Ferrero. *Statistical analysis of noise in MRI : modeling, filtering and estimation*. Springer, Switzerland, 2016. ISBN 9783319399348 3319399349 3319399330 9783319399331. URL http://link.springer.com/10.1007/978-3-319-39934-8.

D. I. Barry. Cerebral blood flow in hypertension. *J Cardiovasc Pharmacol*, 7 Suppl 2:S94–8, 1985. ISSN 0160-2446 (Print) 0160-2446 (Linking). doi: 10.1097/00005344-198507002-00018. URL https://www.ncbi.nlm.nih.gov/pubmed/2409378.

D. I. Barry and S. Strandgaard. Acute effects of antihypertensive drugs on autoregulation of cerebral blood flow in spontaneously hypertensive rats. *Prog. Appl. Microcirc.*, 8:206–212, 1985. doi: https://doi.org/10.1159/000411599.

M. Bergamino, A. Nespodzany, L. C. Baxter, A. Burke, R. J. Caselli, M. N. Sabbagh, R. R. Walsh, and A. M. Stokes. Preliminary assessment of intravoxel incoherent motion diffusion-weighted mri (ivim-dwi) metrics in alzheimer's disease. *J Magn Reson Imaging*, 52(6):1811–1826, 2020. ISSN 1522-2586 (Electronic) 1053-1807 (Linking). doi: 10.1002/jmri.27272. URL https://www.ncbi.nlm.nih.gov/pubmed/32621405.

T. J. Carroll, H. A. Rowley, and V. M. Haughton. Automatic calculation of the arterial input function for cerebral perfusion imaging with mr imaging. *Radiology*, 227(2):593–600, 2003. URL http://www.ncbi.nlm.nih.gov/entrez/query.fcgi?cmd=Retrieve&db=PubMed&dopt=Citation&list_uids=12663823.

T. J. Carroll, S. Horowitz, W. Shin, J. Mouannes, R. Sawlani, S. Ali, J. Raizer, and S. Futterer. Quantification of cerebral perfusion using the "bookend technique": an evaluation in cns tumors. *Magn Reson Imaging*, 26(10):1352–9, 2008. ISSN 0730-725X (Print) 0730-725X (Linking). doi: 10.1016/j.mri.2008.04.010. URL https://www.ncbi.nlm.nih.gov/pubmed/18538523.

N. R. Chatterjee, S. A. Ansari, P. Vakil, S. Prabhakaran, T. J. Carroll, and M. C. Hurley. Automated analysis of perfusion weighted mri using asymmetry in vascular territories. *Magn Reson Imaging*, 33(5):618–23, 2015. ISSN 1873-5894 (Electronic) 0730-725X (Linking). doi: 10.1016/j.mri.2015.01.009. URL http://www.ncbi.nlm.nih.gov/pubmed/25601529.

G. A. Christoforidis, C. Rink, M. S. Kontzialis, Y. Mohammad, R. M. Koch, A. M. Abduljalil, V. K. Bergdall, S. Roy, S. Khanna, A. P. Slivka, M. V. Knopp, and C. K. Sen. An endovascular canine middle cerebral artery occlusion model for the study of leptomeningeal collateral recruitment. *Invest Radiol*, 46(1):34–40, 2011. ISSN 1536-0210 (Electronic) 0020-9996 (Linking). doi: 10.1097/RLI.0b013e3181f0cbc7. URL http://www.ncbi.nlm.nih.gov/pubmed/20856126.

G. A. Christoforidis, P. Vakil, S. A. Ansari, F. H. Dehkordi, and T. J. Carroll. Impact of pial collaterals on infarct growth rate in experimental acute ischemic stroke. *AJNR Am J*

Neuroradiol, 38(2):270–275, 2017. ISSN 1936-959X (Electronic) 0195-6108 (Linking). doi: 10.3174/ajnr.A5003. URL http://www.ncbi.nlm.nih.gov/pubmed/27856435.

G. A. Christoforidis, N. Saadat, M. Liu, Y. I. Jeong, S. Roth, M. Niekrasz, and T. Carroll. Effect of early sanguinate (pegylated carboxyhemoglobin bovine) infusion on cerebral blood flow to the ischemic core in experimental middle cerebral artery occlusion. *J Neurointerv Surg*, 2021. ISSN 1759-8486 (Electronic) 1759-8478 (Linking). doi: 10.1136/neurintsurg-2021-018239. URL https://www.ncbi.nlm.nih.gov/pubmed/34907008.

J. Conklin, J. Fierstra, A. P. Crawley, J. S. Han, J. Poublanc, D. M. Mandell, F. L. Silver, M. Tymianski, J. A. Fisher, and D. J. Mikulis. Impaired cerebrovascular reactivity with steal phenomenon is associated with increased diffusion in white matter of patients with moyamoya disease. *Stroke*, 41(8):1610–6, 2010. ISSN 1524-4628 (Electronic) 0039-2499 (Linking). doi: 10.1161/STROKEAHA.110.579540. URL https://www.ncbi.nlm.nih.gov/pubmed/20576954.

J. Conklin, C. Heyn, M. Roux, M. Cerny, M. Wintermark, and C. Federau. A simplified model for intravoxel incoherent motion perfusion imaging of the brain. *AJNR Am J Neuroradiol*, 37(12):2251–2257, 2016. ISSN 1936-959X (Electronic) 0195-6108 (Linking). doi: 10.3174/ajnr.A4929. URL https://www.ncbi.nlm.nih.gov/pubmed/27561834.

W. A. Copen, M. H. Lev, and O. Rapalino. Chapter 6 - brain perfusion: computed tomography and magnetic resonance techniques. In J. C. Masdeu and R. G. González, editors, *Neuroimaging Part I*, volume 135 of *Handbook of Clinical Neurology*, pages 117–135. Elsevier, 2016. doi: https://doi.org/10.1016/B978-0-444-53485-9.00006-4. URL https://www.sciencedirect.com/science/article/pii/B9780444534859000064.

A. Daoust, S. Dodd, G. Nair, N. Bouraoud, S. Jacobson, S. Walbridge, D. S. Reich, and A. Koretsky. Transverse relaxation of cerebrospinal fluid depends on glucose concentration. *Magn Reson Imaging*, 44:72–81, 2017. ISSN 1873-5894 (Electronic) 0730-725X (Print) 0730-725X (Linking). doi: 10.1016/j.mri.2017.08.001. URL https://www.ncbi.nlm.nih.gov/pubmed/28782676.

S. L. Dawson, R. B. Panerai, and J. F. Potter. Serial changes in static and dynamic cerebral autoregulation after acute ischaemic stroke. *Cerebrovasc Dis*, 16(1):69–75, 2003. ISSN 1015-9770 (Print) 1015-9770 (Linking). doi: 10.1159/000070118. URL https://www.ncbi.nlm.nih.gov/pubmed/12766365.

J. Demeestere, A. Wouters, S. Christensen, R. Lemmens, and M. G. Lansberg. Review of perfusion imaging in acute ischemic stroke: From time to tissue. *Stroke*, 51(3):1017–1024, 2020. ISSN 1524-4628 (Electronic) 0039-2499 (Linking). doi: 10.1161/STROKEAHA.119.028337. URL https://www.ncbi.nlm.nih.gov/pubmed/32008460.

J. A. Detre and D. C. Alsop. Perfusion magnetic resonance imaging with continuous arterial spin labeling: methods and clinical applications in the central nervous system. *Eur J Radiol*, 30(2):115–24, 1999. ISSN 0720-048X (Print) 0720-048X (Linking). doi: S0720-048X(99)00050-9[pii]. URL http://www.ncbi.nlm.nih.gov/pubmed/10401592.

L. Edvinsson and D. Krause. *Cerebral Blood Flow and Metabolism, Second Edition*. Lippincott Williams and Wilkins, 2001. ISBN 978-0781722599.

M. Essig, M. S. Shiroishi, T. B. Nguyen, M. Saake, J. M. Provenzale, D. Enterline, N. Anzalone, A. Dorfler, A. Rovira, M. Wintermark, and M. Law. Perfusion mri: the five most frequently asked technical questions. *AJR Am J Roentgenol*, 200(1):24–34, 2013. ISSN 1546-3141 (Electronic) 0361-803X (Linking). doi: 10.2214/AJR.12.9543. URL https://www.ncbi.nlm.nih.gov/pubmed/23255738.

C. Federau, P. Maeder, K. O'Brien, P. Browaeys, R. Meuli, and P. Hagmann. Quantitative measurement of brain perfusion with intravoxel incoherent motion mr imaging. *Radiology*, 265(3):874–81, 2012. ISSN 1527-1315 (Electronic) 0033-8419 (Linking). doi: 10.1148/radiol.12120584. URL https://www.ncbi.nlm.nih.gov/pubmed/23074258.

C. Federau, K. O'Brien, R. Meuli, P. Hagmann, and P. Maeder. Measuring brain perfusion with intravoxel incoherent motion (ivim): initial clinical experience. *J Magn Reson Imaging*, 39(3):624–32, 2014. ISSN 1522-2586 (Electronic) 1053-1807 (Linking). doi: 10.1002/jmri.24195. URL https://www.ncbi.nlm.nih.gov/pubmed/24068649.

C. Federau, M. Cerny, M. Roux, P. J. Mosimann, P. Maeder, R. Meuli, and M. Wintermark. Ivim perfusion fraction is prognostic for survival in brain glioma. *Clin Neuroradiol*, 27(4):485–492, 2017. ISSN 1869-1447 (Electronic) 1869-1439 (Linking). doi: 10.1007/s00062-016-0510-7. URL https://www.ncbi.nlm.nih.gov/pubmed/27116215.

J. C. Ferre, E. Bannier, H. Raoult, G. Mineur, B. Carsin-Nicol, and J. Y. Gauvrit. Arterial spin labeling (asl) perfusion: techniques and clinical use. *Diagn Interv Imaging*, 94(12):1211–23, 2013. ISSN 2211-5684 (Electronic) 2211-5684 (Linking). doi: 10.1016/j.diii.2013.06.010. URL https://www.ncbi.nlm.nih.gov/pubmed/23850321.

G. M. Fischberg, E. Lozano, K. Rajamani, S. Ameriso, and M. J. Fisher. Stroke precipitated by moderate blood pressure reduction. *J Emerg Med*, 19(4):339–46, 2000. ISSN 0736-4679 (Print) 0736-4679 (Linking). doi: 10.1016/s0736-4679(00)00267-5. URL https://www.ncbi.nlm.nih.gov/pubmed/11074327.

S. Fujiwara, Y. Mori, D. M. de la Mora, Y. Akamatsu, K. Yoshida, Y. Shibata, T. Masuda, K. Ogasawara, and Y. Yoshioka. Feasibility of ivim parameters from diffusion-weighted imaging at 11.7t mri for detecting ischemic changes in common carotid artery occlusion rats. *Sci Rep*, 10(1):8404, 2020. ISSN 2045-2322 (Electronic) 2045-2322 (Linking). doi: 10.1038/s41598-020-65310-8. URL https://www.ncbi.nlm.nih.gov/pubmed/32439877.

Q. Q. Gao, S. S. Lu, X. Q. Xu, C. J. Wu, X. L. Liu, S. Liu, and H. B. Shi. Quantitative assessment of hyperacute cerebral infarction with intravoxel incoherent motion mr imaging: Initial experience in a canine stroke model. *J Magn Reson Imaging*, 46(2):550–556, 2017. ISSN 1522-2586 (Electronic) 1053-1807 (Linking). doi: 10.1002/jmri.25556. URL https://www.ncbi.nlm.nih.gov/pubmed/27902857.

X. Golay, J. Hendrikse, and T. C. Lim. Perfusion imaging using arterial spin labeling. *Top Magn Reson Imaging*, 15(1):10–27, 2004. ISSN 0899-3459 (Print) 0899-3459 (Linking). doi: 10.1097/00002142-200402000-00003. URL https://www.ncbi.nlm.nih.gov/pubmed/15057170.

M. Grade, J. A. Hernandez Tamames, F. B. Pizzini, E. Achten, X. Golay, and M. Smits. A neuroradiologist's guide to arterial spin labeling mri in clinical practice. *Neuroradiology*, 57(12):1181–202, 2015. ISSN 1432-1920 (Electronic) 0028-3940 (Linking). doi: 10.1007/s00234-015-1571-z. URL https://www.ncbi.nlm.nih.gov/pubmed/26351201.

H. Gudbjartsson and S. Patz. The rician distribution of noisy mri data. *Magn Reson Med*, 34(6):910–914, 1995.

O. J. Gurney-Champion, R. Klaassen, M. Froeling, S. Barbieri, J. Stoker, M. R. W. Engelbrecht, J. W. Wilmink, M. G. Besselink, A. Bel, H. W. M. van Laarhoven, and A. J. Nederveen. Comparison of six fit algorithms for the intra-voxel incoherent motion model of diffusion-weighted magnetic resonance imaging data of pancreatic cancer patients. *PLoS One*, 13(4):e0194590, 2018. ISSN 1932-6203 (Electronic) 1932-6203 (Linking). doi: 10.1371/journal.pone.0194590. URL https://www.ncbi.nlm.nih.gov/pubmed/29617445.

S. Haller, G. Zaharchuk, D. L. Thomas, K. O. Lovblad, F. Barkhof, and X. Golay. Arterial spin labeling perfusion of the brain: Emerging clinical applications. *Radiology*, 281(2):337–356, 2016. ISSN 1527-1315 (Electronic) 0033-8419 (Linking). doi: 10.1148/radiol.2016150789. URL https://www.ncbi.nlm.nih.gov/pubmed/27755938.

M. Iima and D. Le Bihan. Clinical intravoxel incoherent motion and diffusion mr imaging: Past, present, and future. *Radiology*, 278(1):13–32, 2016. ISSN 1527-1315 (Electronic) 0033-8419 (Linking). doi: 10.1148/radiol.2015150244. URL https://www.ncbi.nlm.nih.gov/pubmed/26690990.

O. Jalnefjord, M. Andersson, M. Montelius, G. Starck, A. K. Elf, V. Johanson, J. Svensson, and M. Ljungberg. Comparison of methods for estimation of the intravoxel incoherent motion (ivim) diffusion coefficient (d) and perfusion fraction (f). *MAGMA*, 31(6):715–723, 2018. ISSN 1352-8661 (Electronic) 0968-5243 (Linking). doi: 10.1007/s10334-018-0697-5. URL https://www.ncbi.nlm.nih.gov/pubmed/30116979.

J. H. Jensen, J. A. Helpern, A. Ramani, H. Lu, and K. Kaczynski. Diffusional kurtosis imaging: the quantification of non-gaussian water diffusion by means of magnetic resonance imaging. *Magn Reson Med*, 53(6):1432–40, 2005. ISSN 0740-3194 (Print) 0740-3194 (Linking). doi: 10.1002/mrm.20508. URL https://www.ncbi.nlm.nih.gov/pubmed/15906300.

Y. I. Jeong, G. A. Christoforidis, N. Saadat, K. Kawaji, C. G. Cantrell, S. Roth, M. Niekrasz, and T. J. Carroll. Absolute quantitative mr perfusion and comparison against stable-isotope microspheres. *Magn Reson Med*, 0(0):1–11, 2019. doi: https://doi.org/10.1002/mrm.27669.

T. H. Jones, R. B. Morawetz, R. M. Crowell, F. W. Marcoux, S. J. FitzGibbon, U. DeGirolami, and R. G. Ojemann. Thresholds of focal cerebral ischemia in awake monkeys. *J Neurosurg*, 54(6):773–82, 1981. ISSN 0022-3085 (Print) 0022-3085 (Linking). doi: 10.3171/jns.1981.54.6.0773. URL http://www.ncbi.nlm.nih.gov/pubmed/7241187.

A. Z. Khawaja, D. B. Cassidy, J. Al Shakarchi, D. G. McGrogan, N. G. Inston, and R. G. Jones. Revisiting the risks of mri with gadolinium based contrast agents-review of literature and guidelines. *Insights Imaging*, 6(5):553–8, 2015. ISSN 1869-4101 (Print) 1869-4101 (Linking). doi: 10.1007/s13244-015-0420-2. URL https://www.ncbi.nlm.nih.gov/pubmed/26253982.

P. B. Kingsley. Introduction to diffusion tensor imaging mathematics: Part i. tensors, rotations, and eigenvectors. *Concepts in Magnetic Resonance Part A*, 28a(2):101–122, 2006a. ISSN 1546-6086. doi: 10.1002/cmr.a.20048. URL <GotoISI>://WOS:000236568100001.

P. B. Kingsley. Introduction to diffusion tensor imaging mathematics: Part ii. anisotropy, diffusion-weighting factors, and gradient encoding schemes. *Concepts in Magnetic Resonance Part A*, 28a(2):123–154, 2006b. ISSN 1546-6086. doi: 10.1002/cmr.a.20049. URL <GotoISI>://WOS:000236568100002.

P. B. Kingsley. Introduction to diffusion tensor imaging mathematics: Part iii. tensor calculation, noise, simulations, and optimization. *Concepts in Magnetic Resonance Part A*, 28a(2):155–179, 2006c. ISSN 1546-6086. doi: 10.1002/cmr.a.20050. URL <GotoISI>://WOS:000236568100003.

P. Kochunov, D. C. Glahn, J. Lancaster, P. M. Thompson, V. Kochunov, B. Rogers, P. Fox, J. Blangero, and D. E. Williamson. Fractional anisotropy of cerebral white matter and thickness of cortical gray matter across the lifespan. *Neuroimage*, 58(1):41–9, 2011. ISSN 1095-9572 (Electronic) 1053-8119 (Linking). doi: 10.1016/j.neuroimage.2011.05.050. URL https://www.ncbi.nlm.nih.gov/pubmed/21640837.

P. W. Kuchel, G. Pagès, K. Nagashima, S. Velan, V. Vijayaragavan, V. Nagarajan, and K. H. Chuang. Stejskal–tanner equation derived in full. *Concepts in Magnetic Resonance Part A*, 40A(5):205–214, 2012. doi: https://doi.org/10.1002/cmr.a.21241. URL https://onlinelibrary.wiley.com/doi/abs/10.1002/cmr.a.21241.

K. K. Kwong, R. C. McKinstry, D. Chien, A. P. Crawley, J. D. Pearlman, and B. R. Rosen. Csf-suppressed quantitative single-shot diffusion imaging. *Magn Reson Med*, 21(1):157–63, 1991. ISSN 0740-3194 (Print) 0740-3194 (Linking). doi: 10.1002/mrm.1910210120. URL https://www.ncbi.nlm.nih.gov/pubmed/1943674.

D. Le Bihan. What can we see with ivim mri? *Neuroimage*, 187:56–67, 2019. ISSN 1095-9572 (Electronic) 1053-8119 (Linking). doi: 10.1016/j.neuroimage.2017.12.062. URL https://www.ncbi.nlm.nih.gov/pubmed/29277647.

D. Le Bihan and M. Iima. Diffusion magnetic resonance imaging: What water tells us about biological tissues. *PLoS Biol*, 13(7):e1002203, 2015. ISSN 1545-7885 (Electronic) 1544-9173 (Linking). doi: 10.1371/journal.pbio.1002203. URL https://www.ncbi.nlm.nih.gov/pubmed/26204162.

D. Le Bihan and R. Turner. The capillary network: a link between ivim and classical perfusion. *Magn Reson Med*, 27(1):171–8, 1992. ISSN 0740-3194 (Print) 0740-3194 (Linking). URL https://www.ncbi.nlm.nih.gov/pubmed/1435202.

D. Le Bihan, E. Breton, D. Lallemand, P. Grenier, E. Cabanis, and M. Laval-Jeantet. Mr imaging of intravoxel incoherent motions: application to diffusion and perfusion in neurologic disorders. *Radiology*, 161(2):401–7, 1986. ISSN 0033-8419 (Print) 0033-8419 (Linking). doi: 10.1148/radiology.161.2.3763909. URL https://www.ncbi.nlm.nih.gov/pubmed/3763909.

D. Le Bihan, E. Breton, D. Lallemand, M. L. Aubin, J. Vignaud, and M. Laval-Jeantet. Separation of diffusion and perfusion in intravoxel incoherent motion mr imaging. *Radiology*, 168(2):497–505, 1988. ISSN 0033-8419 (Print) 0033-8419 (Linking). doi: 10.1148/radiology.168.2.3393671. URL https://www.ncbi.nlm.nih.gov/pubmed/3393671.

D. Le Bihan, R. Turner, C. T. Moonen, and J. Pekar. Imaging of diffusion and microcirculation with gradient sensitization: design, strategy, and significance. *J Magn Reson Imaging*, 1(1):7–28, 1991. ISSN 1053-1807 (Print) 1053-1807 (Linking). doi: 10.1002/jmri.1880010103. URL https://www.ncbi.nlm.nih.gov/pubmed/1802133.

A. L. Lin, Q. Qin, X. Zhao, and T. Q. Duong. Blood longitudinal (t1) and transverse (t2) relaxation time constants at 11.7 tesla. *MAGMA*, 25(3):245–9, 2012. ISSN 1352-8661 (Electronic) 0968-5243 (Print) 0968-5243 (Linking). doi: 10.1007/s10334-011-0287-2. URL https://www.ncbi.nlm.nih.gov/pubmed/22071580.

L. I. Lin. A concordance correlation coefficient to evaluate reproducibility. *Biometrics*, 45(1): 255–68, 1989. ISSN 0006-341X (Print) 0006-341X (Linking). URL https://www.ncbi.nlm.nih.gov/pubmed/2720055.

M. Liu, Y. I. Jeong, N. Saadat, G. A. Christoforidis, and T. Carroll. Ivim-based cerebral perfusion (in ml/100g/min) values at rest, hypercapnia, and ischemia in an mca occlusion model, May 2019. URL https://archive.ismrm.org/2019/3734.html.

M. Liu, N. Saadat, Y. I. Jeong, S. Roth, M. Niekrasz, T. Carroll, and G. A. Christoforidis. Augmentation of perfusion with simultaneous vasodilator and inotropic agents in experimental acute middle cerebral artery occlusion: a pilot study. *J Neurointerv Surg*, 2022. ISSN 1759-8486 (Electronic) 1759-8478 (Linking). doi: 10.1136/jnis-2022-018990. URL https://www.ncbi.nlm.nih.gov/pubmed/35803730.

G. Madelin, R. Kline, R. Walvick, and R. R. Regatte. A method for estimating intracellular sodium concentration and extracellular volume fraction in brain in vivo using sodium

magnetic resonance imaging. *Scientific Reports*, 4(1):4763, 2014. ISSN 2045-2322. doi: 10.1038/srep04763. URL https://doi.org/10.1038/srep04763.

G. Mair and J. M. Wardlaw. Imaging of acute stroke prior to treatment: current practice and evolving techniques. *Br J Radiol*, 87(1040):20140216, 2014. ISSN 1748-880X (Electronic) 0007-1285 (Linking). doi: 10.1259/bjr.20140216. URL https://www.ncbi.nlm.nih.gov/pubmed/24936980.

Y. Masutani, S. Aoki, O. Abe, N. Hayashi, and K. Otomo. Mr diffusion tensor imaging: recent advance and new techniques for diffusion tensor visualization. *Eur J Radiol*, 46(1): 53–66, 2003. ISSN 0720-048X (Print) 0720-048X (Linking). doi: 10.1016/s0720-048x(02)00328-5. URL https://www.ncbi.nlm.nih.gov/pubmed/12648802.

MATLAB. *version 9.13.0.2080170 (R2022b) Update 1*. The MathWorks Inc., Natick, Massachusetts, 2022.

R. J. McDonald, D. Levine, J. Weinreb, E. Kanal, M. S. Davenport, J. H. Ellis, P. M. Jacobs, R. E. Lenkinski, K. R. Maravilla, M. R. Prince, H. A. Rowley, M. F. Tweedle, and H. Y. Kressel. Gadolinium retention: A research roadmap from the 2018 nih/acr/rsna workshop on gadolinium chelates. *Radiology*, 289(2):517–534, 2018. ISSN 1527-1315 (Electronic) 0033-8419 (Linking). doi: 10.1148/radiol.2018181151. URL https://www.ncbi.nlm.nih.gov/pubmed/30204075.

G. McHedlishvili and N. Kuridze. The modular organization of the pial arterial system in phylogeny. *J Cereb Blood Flow Metab*, 4(3):391–6, 1984. ISSN 0271-678X (Print) 0271-678X (Linking). doi: 10.1038/jcbfm.1984.57. URL https://www.ncbi.nlm.nih.gov/pubmed/6332116.

N. H. Mehta, R.A. Suss, J. P. Dyke, N. D. Theise, G. C. Chiang, S. Strauss, L. Saint-Louis, Y. Li, S. Pahlajani, V. Babaria, L. Glodzik, R. O. Carare, and M. J. de Leon. Quantifying cerebrospinal fluid dynamics: A review of human neuroimaging contributions to csf physiology and neurodegenerative disease. *Neurobiology of Disease*, 170:105776, 2022. ISSN 0969-9961. doi: https://doi.org/10.1016/j.nbd.2022.105776. URL https://www.sciencedirect.com/science/article/pii/S0969996122001681.

J. J. Mouannes-Srour, W. Shin, S. A. Ansari, M. C. Hurley, P. Vakil, B. R. Bendok, J. L. Lee, C. P. Derdeyn, and T. J. Carroll. Correction for arterial-tissue delay and dispersion in absolute quantitative cerebral perfusion dsc mr imaging. *Magn Reson Med*, 68(2):495–506, 2012. ISSN 1522-2594 (Electronic) 0740-3194 (Linking). doi: 10.1002/mrm.23257. URL http://www.ncbi.nlm.nih.gov/pubmed/22162092.

M. G. Muhonen, P. D. Sawin, C. M. Loftus, and D. D. Heistad. Pressure-flow relations in canine collateral-dependent cerebrum. *Stroke*, 23(7):988–94, 1992. ISSN 0039-2499 (Print) 0039-2499 (Linking). doi: 10.1161/01.str.23.7.988. URL https://www.ncbi.nlm.nih.gov/pubmed/1615550.

M. G. Muhonen, G. M. Greene, D. D. Heistad, and C. M. Loftus. Mechanism of redistribution of cerebral blood flow during hypercarbia and seizures. *Am J Physiol*, 266(5 Pt 2):H2074–81, 1994. ISSN 0002-9513 (Print) 0002-9513 (Linking). doi: 10.1152/ajpheart.1994.266.5.H2074. URL https://www.ncbi.nlm.nih.gov/pubmed/8203605.

C. Neeley, M. Moritz, J. J. Brown, and Y. Zhou. Acute side effects of three commonly used gadolinium contrast agents in the paediatric population. *Br J Radiol*, 89(1063):20160027, 2016. ISSN 1748-880X (Electronic) 0007-1285 (Linking). doi: 10.1259/bjr.20160027. URL https://www.ncbi.nlm.nih.gov/pubmed/27194459.

L. Orsingher, S. Piccinini, and G. Crisi. Differences in dynamic susceptibility contrast mr perfusion maps generated by different methods implemented in commercial software. *J Comput Assist Tomogr*, 38(5):647–54, 2014. ISSN 1532-3145 (Electronic) 0363-8715 (Linking). doi: 10.1097/RCT.0000000000000115. URL https://www.ncbi.nlm.nih.gov/pubmed/24879459.

J. Overgaard and E. Skinhoj. A paradoxical cerebral hemodynamic effect of hydralazine. *Stroke*, 6(4):402–10, 1975. ISSN 0039-2499 (Print) 0039-2499 (Linking). doi: 10.1161/01.str.6.4.402. URL https://www.ncbi.nlm.nih.gov/pubmed/1154477.

A. Papoulis. *Probability, Random Variables, and Stochastic Processes*. McGraw-Hill, 3rd edition, 1991.

L. M. Parkes, W. Rashid, D. T. Chard, and P. S. Tofts. Normal cerebral perfusion measurements using arterial spin labeling: reproducibility, stability, and age and gender effects. *Magn Reson Med*, 51(4):736–43, 2004. ISSN 0740-3194 (Print) 0740-3194 (Linking). doi: 10.1002/mrm.20023. URL https://www.ncbi.nlm.nih.gov/pubmed/15065246.

A. M. Paschoal, R. F. Leoni, A. C. Dos Santos, and F. F. Paiva. Intravoxel incoherent motion mri in neurological and cerebrovascular diseases. *Neuroimage Clin*, 20:705–714, 2018. ISSN 2213-1582 (Electronic) 2213-1582 (Linking). doi: 10.1016/j.nicl.2018.08.030. URL https://www.ncbi.nlm.nih.gov/pubmed/30221622.

F. Pedregosa, G. Varoquaux, A. Gramfort, V. Michel, B. Thirion, O. Grisel, M. Blondel, P. Prettenhofer, R. Weiss, V. Dubourg, J. Vanderplas, A. Passos, D. Cournapeau, M. Brucher, M. Perrot, and E. Duchesnay. Scikit-learn: Machine learning in Python. *Journal of Machine Learning Research*, 12:2825–2830, 2011.

C. A. Potter, A. S. Vagal, M. Goyal, D. B. Nunez, T. M. Leslie-Mazwi, and M. H. Lev. Ct for treatment selection in acute ischemic stroke: A code stroke primer. *Radiographics*, 39(6):1717–1738, 2019. ISSN 1527-1323 (Electronic) 0271-5333 (Linking). doi: 10.1148/rg.2019190142. URL https://www.ncbi.nlm.nih.gov/pubmed/31589578.

M. Rogosnitzky and S. Branch. Gadolinium-based contrast agent toxicity: a review of known and proposed mechanisms. *Biometals*, 29(3):365–76, 2016. ISSN 1572-8773 (Electronic) 0966-0844 (Linking). doi: 10.1007/s10534-016-9931-7. URL https://www.ncbi.nlm.nih.gov/pubmed/27053146.

M. Rohrer, H. Bauer, J. Mintorovitch, M. Requardt, and H. J. Weinmann. Comparison of magnetic properties of mri contrast media solutions at different magnetic field strengths. *Invest Radiol*, 40(11):715–24, 2005. ISSN 0020-9996 (Print) 0020-9996 (Linking). doi: 10.1097/01.rli.0000184756.66360.d3. URL https://www.ncbi.nlm.nih.gov/pubmed/16230904.

G. G. Rowe, G. M. Maxwell, and C. W. Crumpton. The cerebral hemodynamic response to administration of hydralazine. *Circulation*, 25:970–2, 1962. ISSN 0009-7322 (Print) 0009-7322 (Linking). doi: 10.1161/01.cir.25.6.970. URL https://www.ncbi.nlm.nih.gov/pubmed/14494643.

N. Saadat, G. A. Christoforidis, Y. I. Jeong, M. Liu, A. Dimov, S. Roth, M. Niekrasz, S. A. Ansari, and T. Carroll. Influence of simultaneous pressor and vasodilatory agents on the evolution of infarct growth in experimental acute middle cerebral artery occlusion. *J Neurointerv Surg*, 2020. ISSN 1759-8486 (Electronic) 1759-8478 (Linking). doi: 10.1136/neurintsurg-2020-016539. URL https://www.ncbi.nlm.nih.gov/pubmed/32900906.

L. A. Scott, B. R. Dickie, S. D. Rawson, G. Coutts, T. L. Burnett, S. M. Allan, G. J. Parker, and L. M. Parkes. Characterisation of microvessel blood velocity and segment length in the brain using multi-diffusion-time diffusion-weighted mri. *J Cereb Blood Flow Metab*, 41(8):1939–1953, 2021. ISSN 1559-7016 (Electronic) 0271-678X (Linking). doi: 10.1177/0271678X20978523. URL https://www.ncbi.nlm.nih.gov/pubmed/33325766.

M. S. Shazeeb, R. M. King, V. Anagnostakou, Z. Vardar, A. Kraitem, J. Kolstad, C. Raskett, N. Le Moan, J. A. Winger, L. Kelly, A. Krtolica, N. Henninger, and M. J. Gounis. Novel oxygen carrier slows infarct growth in large vessel occlusion dog model based on magnetic resonance imaging analysis. *Stroke*, 53(4):1363–1372, 2022. ISSN 1524-4628 (Electronic) 0039-2499 (Linking). doi: 10.1161/STROKEAHA.121.036896. URL https://www.ncbi.nlm.nih.gov/pubmed/35306836.

H. K. Shin, M. Nishimura, P. B. Jones, H. Ay, D. A. Boas, M. A. Moskowitz, and C. Ayata. Mild induced hypertension improves blood flow and oxygen metabolism in transient focal cerebral ischemia. *Stroke*, 39(5):1548–55, 2008. ISSN 1524-4628 (Electronic) 0039-2499 (Linking). doi: 10.1161/STROKEAHA.107.499483. URL https://www.ncbi.nlm.nih.gov/pubmed/18340095.

W. Shin, T. A. Cashen, S. W. Horowitz, R. Sawlani, and T. J. Carroll. Quantitative cbv measurement from static t1 changes in tissue and correction for intravascular water exchange. *Magn Reson Med*, 56(1):138–45, 2006. URL http://www.ncbi.nlm.nih.gov/entrez/query.fcgi?cmd=Retrieve&db=PubMed&dopt=Citation&list_uids=16767742.

M. Smrcka, C. S. Ogilvy, R. J. Crow, K. I. Maynard, T. Kawamata, and 3rd Ames, A. Induced hypertension improves regional blood flow and protects against infarction during focal ischemia: time course of changes in blood flow measured by laser doppler imaging. *Neurosurgery*, 42(3):617–24; discussion 624–5, 1998. ISSN 0148-396X (Print) 0148-396X

(Linking). doi: 10.1097/00006123-199803000-00032. URL https://www.ncbi.nlm.nih.gov/pubmed/9526996.

SPM12. *Version 7771 (SPM12)*. Wellcome Centre for Human Neuroimaging, London, United Kingdom, 2022.

T. J. Steichen and N. J. Cox. A note on the concordance correlation coefficient. *The Stata Journal*, 2(2):183–189, 2002. doi: 10.1177/1536867x0200200206. URL https://journals.sagepub.com/doi/abs/10.1177/1536867X0200200206.

E. O. Stejskal and J. E. Tanner. Spin diffusion measurements: Spin echoes in the presence of a time-dependent field gradient. *Journal of Chemical Physics*, 42(1):288–+, 1965. ISSN 0021-9606. doi: Doi10.1063/1.1695690. URL <GotoISI>://WOS:A19656099500051.

S. Suo, M. Cao, W. Zhu, L. Li, J. Li, F. Shen, J. Zu, Z. Zhou, Z. Zhuang, J. Qu, Z. Chen, and J. Xu. Stroke assessment with intravoxel incoherent motion diffusion-weighted mri. *NMR Biomed*, 29(3):320–8, 2016. ISSN 1099-1492 (Electronic) 0952-3480 (Linking). doi: 10.1002/nbm.3467. URL https://www.ncbi.nlm.nih.gov/pubmed/26748572.

A. Tharwat. Independent component analysis: An introduction. *Applied Computing and Informatics*, 17(2):222–249, 2021. ISSN 2634-1964. doi: https://doi.org/10.1016/j.aci.2018.08.006.

B. B. Thomsen, H. Gredal, M. Wirenfeldt, B. W. Kristensen, B. H. Clausen, A. E. Larsen, B. Finsen, M. Berendt, and K. L. Lambertsen. Spontaneous ischaemic stroke lesions in a dog brain: neuropathological characterisation and comparison to human ischaemic stroke. *Acta Vet Scand*, 59(1):7, 2017. ISSN 1751-0147 (Electronic) 0044-605X (Linking). doi: 10.1186/s13028-016-0275-7. URL https://www.ncbi.nlm.nih.gov/pubmed/28086932.

H. C. Torrey. Bloch equations with diffusion terms. *Phys. Rev.*, 104:563–565, Nov 1956. doi: 10.1103/PhysRev.104.563. URL https://link.aps.org/doi/10.1103/PhysRev.104.563.

R. J. Traystman. Animal models of focal and global cerebral ischemia. *ILAR J*, 44(2):85–95, 2003. ISSN 1084-2020 (Print) 1084-2020 (Linking). doi: 10.1093/ilar.44.2.85. URL https://www.ncbi.nlm.nih.gov/pubmed/12652003.

C. W. Tsao, A. W. Aday, Z. I. Almarzooq, A. Alonso, A. Z. Beaton, M. S. Bittencourt, A. K. Boehme, A. E. Buxton, A. P. Carson, Y. Commodore-Mensah, M. S. V. Elkind, K. R. Evenson, C. Eze-Nliam, J. F. Ferguson, G. Generoso, J. E. Ho, R. Kalani, S. S. Khan, B. M. Kissela, K. L. Knutson, D. A. Levine, T. T. Lewis, J. Liu, M. S. Loop, J. Ma, M. E. Mussolino, S. D. Navaneethan, A. M. Perak, R. Poudel, M. Rezk-Hanna, G. A. Roth, E. B. Schroeder, S. H. Shah, E. L. Thacker, L. B. VanWagner, S. S. Virani, J. H. Voecks, N. Y. Wang, K. Yaffe, and S. S. Martin. Heart disease and stroke statistics-2022 update: A report from the american heart association. *Circulation*, 145(8):e153–e639, 2022. ISSN 1524-4539 (Electronic) 0009-7322 (Linking). doi: 10.1161/CIR.0000000000001052. URL https://www.ncbi.nlm.nih.gov/pubmed/35078371.

P. Vakil, J. J. Lee, J. J. Mouannes-Srour, C. P. Derdeyn, and T. J. Carroll. Cerebrovascular occlusive disease: quantitative cerebral blood flow using dynamic susceptibility contrast mr imaging correlates with quantitative h2[15o] pet. *Radiology*, 266(3):879–86, 2013. ISSN 1527-1315 (Electronic) 0033-8419 (Linking). doi: 10.1148/radiol.12120756. URL http://www.ncbi.nlm.nih.gov/pubmed/23297337.

L. A. van der Kleij, J. B. De Vis, J. de Bresser, J. Hendrikse, and J. C. W. Siero. Arterial co2 pressure changes during hypercapnia are associated with changes in brain parenchymal volume. *European Radiology Experimental*, 4(1):17, 2020. ISSN 2509-9280. doi: 10.1186/s41747-020-0144-z. URL https://doi.org/10.1186/s41747-020-0144-z.

J. R. Vitt, M. Trillanes, and 3rd Hemphill, J. C. Management of blood pressure during and after recanalization therapy for acute ischemic stroke. *Front Neurol*, 10:138, 2019. ISSN 1664-2295 (Print) 1664-2295 (Linking). doi: 10.3389/fneur.2019.00138. URL https://www.ncbi.nlm.nih.gov/pubmed/30846967.

J. P. Wansapura, S. K. Holland, R. S. Dunn, and Jr. Ball, W. S. Nmr relaxation times in the human brain at 3.0 tesla. *J Magn Reson Imaging*, 9(4):531–8, 1999. ISSN 1053-1807 (Print) 1053-1807 (Linking). doi: 10.1002/(sici)1522-2586(199904)9:4⟨531::aid-jmri4⟩3.0.co;2-l. URL https://www.ncbi.nlm.nih.gov/pubmed/10232510.

C. F. Westin, S. E. Maier, H. Mamata, A. Nabavi, F. A. Jolesz, and R. Kikinis. Processing and visualization for diffusion tensor mri. *Med Image Anal*, 6(2):93–108, 2002. ISSN 1361-8415 (Print) 1361-8415 (Linking). doi: 10.1016/s1361-8415(02)00053-1. URL https://www.ncbi.nlm.nih.gov/pubmed/12044998.

R. Wirestam, M. Borg, S. Brockstedt, A. Lindgren, S. Holtas, and F. Stahlberg. Perfusion-related parameters in intravoxel incoherent motion mr imaging compared with cbv and cbf measured by dynamic susceptibility-contrast mr technique. *Acta Radiol*, 42(2):123–8, 2001. ISSN 0284-1851 (Print) 0284-1851 (Linking). URL https://www.ncbi.nlm.nih.gov/pubmed/11281143.

S. M. Wong, W. H. Backes, C. E. Zhang, J. Staals, R. J. van Oostenbrugge, Crlpn Jeukens, and J. F. A. Jansen. On the reproducibility of inversion recovery intravoxel incoherent motion imaging in cerebrovascular disease. *AJNR Am J Neuroradiol*, 39(2):226–231, 2018. ISSN 1936-959X (Electronic) 0195-6108 (Linking). doi: 10.3174/ajnr.A5474. URL https://www.ncbi.nlm.nih.gov/pubmed/29217741.

W. C. Wu, Y. F. Chen, H. M. Tseng, S. C. Yang, and P. C. My. Caveat of measuring perfusion indexes using intravoxel incoherent motion magnetic resonance imaging in the human brain. *Eur Radiol*, 25(8):2485–92, 2015. ISSN 1432-1084 (Electronic) 0938-7994 (Linking). doi: 10.1007/s00330-015-3655-x. URL https://www.ncbi.nlm.nih.gov/pubmed/25693668.

M. C. Wurnig, O. F. Donati, E. Ulbrich, L. Filli, D. Kenkel, H. C. Thoeny, and A. Boss. Systematic analysis of the intravoxel incoherent motion threshold separating perfusion and

diffusion effects: Proposal of a standardized algorithm. *Magn Reson Med*, 74(5):1414–22, 2015. ISSN 1522-2594 (Electronic) 0740-3194 (Linking). doi: 10.1002/mrm.25506. URL https://www.ncbi.nlm.nih.gov/pubmed/25360990.

Y. Yao, S. Zhang, X. Tang, S. Zhang, J. Shi, W. Zhu, and W. Zhu. Intravoxel incoherent motion diffusion-weighted imaging in stroke patients: initial clinical experience. *Clin Radiol*, 71(9):938 e11–6, 2016. ISSN 1365-229X (Electronic) 0009-9260 (Linking). doi: 10.1016/j.crad.2016.04.019. URL https://www.ncbi.nlm.nih.gov/pubmed/27210244.

G. Zaharchuk. Theoretical basis of hemodynamic mr imaging techniques to measure cerebral blood volume, cerebral blood flow, and permeability. *AJNR Am J Neuroradiol*, 28(10): 1850–8, 2007. ISSN 0195-6108 (Print) 1936-959X (Electronic) 0195-6108 (Linking). doi: 10.3174/ajnr.A0831. URL https://www.ncbi.nlm.nih.gov/pubmed/17998415.

G. Zaharchuk. Arterial spin-labeled perfusion imaging in acute ischemic stroke. *Stroke*, 45(4):1202–7, 2014. ISSN 1524-4628 (Electronic) 0039-2499 (Linking). doi: 10.1161/STROKEAHA.113.003612. URL https://www.ncbi.nlm.nih.gov/pubmed/24603069.

G. Zaharchuk, I. S. El Mogy, N. J. Fischbein, and G. W. Albers. Comparison of arterial spin labeling and bolus perfusion-weighted imaging for detecting mismatch in acute stroke. *Stroke*, 43(7):1843–8, 2012. ISSN 1524-4628 (Electronic) 0039-2499 (Linking). doi: 10.1161/STROKEAHA.111.639773. URL https://www.ncbi.nlm.nih.gov/pubmed/22539548.

K. Zhang and T. J. Sejnowski. A universal scaling law between gray matter and white matter of cerebral cortex. *Proc Natl Acad Sci U S A*, 97(10):5621–6, 2000. ISSN 0027-8424 (Print) 0027-8424 (Linking). doi: 10.1073/pnas.090504197. URL https://www.ncbi.nlm.nih.gov/pubmed/10792049.

X. Zhang, E. T. Petersen, E. Ghariq, J. B. De Vis, A. G. Webb, W. M. Teeuwisse, J. Hendrikse, and M. J. van Osch. In vivo blood t(1) measurements at 1.5 t, 3 t, and 7 t. *Magn Reson Med*, 70(4):1082–6, 2013. ISSN 1522-2594 (Electronic) 0740-3194 (Linking). doi: 10.1002/mrm.24550. URL https://www.ncbi.nlm.nih.gov/pubmed/23172845.

G. Zhu, C. Federau, M. Wintermark, H. Chen, D. G. Marcellus, B. W. Martin, and J. J. Heit. Comparison of mri ivim and mr perfusion imaging in acute ischemic stroke due to large vessel occlusion. *Int J Stroke*, 15(3):332–342, 2020. ISSN 1747-4949 (Electronic) 1747-4930 (Linking). doi: 10.1177/1747493019873515. URL https://www.ncbi.nlm.nih.gov/pubmed/31480940.